Andreas Stegmeir
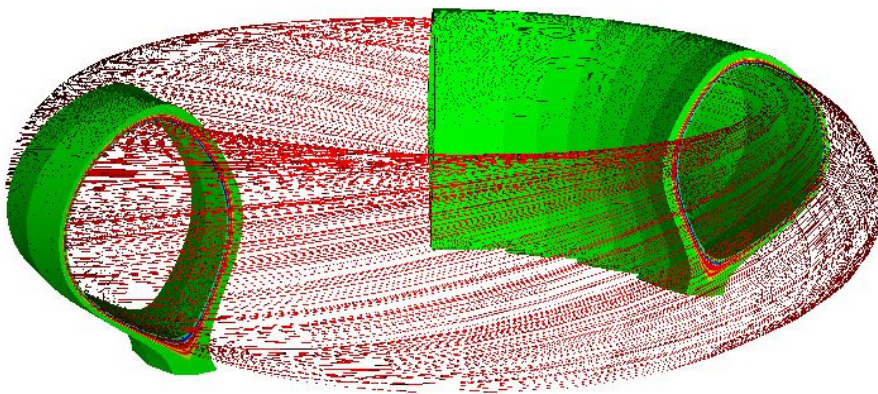
GRILLIX: A 3 D turbulence code for magnetic fusion devices based on a field line map

GRILLIX: A 3D turbulence code for magnetic fusion devices based on a field line map

Andreas Korbinian Stegmeir

TECHNISCHE UNIVERSITÄT MÜNCHEN

Max-Planck-Institut für Plasmaphysik

GRILLIX: A 3D turbulence code for magnetic fusion devices based on a field line map

Andreas Korbinian Stegmeir

Abstract

The main contribution to the (anomalous) cross field transport in tokamaks is known to be due to turbulence and numerical codes are essential tools in order to predict transport levels and understand physical mechanisms. Whereas for the interior closed field line region sophisticated turbulence codes are already quite advanced, the outer region of a tokamak, i.e. the edge and scrape-off layer (SOL), still lacks such tools to a large extent. The presence of many spatio-temporal scales and the complex geometry in diverted machines pose a huge challenge for the modelling of the edge/SOL.

In this work the newly developed code GRILLIX is presented, which is aimed to set a first milestone in the development of a 3D turbulence code for the edge/SOL. GRILLIX uses a simpli-fied physical model (Hasegawa-Wakatani), but is capable to treat the complex geometry across the separatrix. The usually employed field aligned coordinate systems are avoided by using a cylindrical grid (R, Z, φ) which is Cartesian within poloidal planes. The discretisation of per-pendicular (w.r.t. the magnetic field) operators is straight forward and parallel operators are discretised with a field line map procedure, i.e. field line tracing from plane to plane and in-terpolation. Via a grid-sparsification in the toroidal direction the flute mode character of the solutions can be exploited computationally. Ultimately, tokamak geometries with an arbitrary poloidal cross section, including a separatrix, can be treated with GRILLIX.

In non-field-aligned grids numerical diffusion, i.e. a spurious perpendicular coupling depending on parallel dynamics, arises unavoidably. This numerical diffusion can be fatal for codes, since the parallel dynamics is usually orders of magnitude faster than perpendicular dynamics in tokamaks. A new numerical scheme is developed and applied in GRILLIX which maintains the self-adjointness property of the parallel diffusion operator on the discrete level and reduces numerical diffusion drastically. Many benchmarks in several geometries are presented to validate the field line map approach in general and GRILLIX in special.

First effects of the geometry in diverted machines on drift wave turbulence were studied with GRILLIX. Field aligned structures get strongly distorted as they enter the X-point region. Their perpendicular spatial extent decreases thereby drastically towards the X-point and are thus subject to enhanced dissipation. Since ultimately close to the X-point fluctuations die out, the X-point constitutes a kind of barrier for fluctuations. This mechanism is similar to the previously found resistive X-point mode.

Zusammenfassung

Radialer (anormaler) Transport in Tokamaks wird hauptsächlich durch turbulente Prozesse getragen und numerische Simulationsprogramme sind heutzutage ein unverzichtbares Werkzeug, um Vorhersagen über das Transportlevel zu treffen und um physikalische Mechanismen zu verstehen. Während für den inneren Bereich geschlossener Feldlinien, hochentwickelte Programme bereits zur Verfügung stehen, gibt es für den äußeren Bereich (Rand und Abschälschicht) von Tokamaks kaum Ansätze. Das Vorhandensein vieler raumzeitlicher Skalen und eine komplexe Geometrie in Divertormaschinen stellen eine grosse Herausforderung beim Modellieren des Randbereiches dar.

In dieser Arbeit wurde das Simulationsprogramm GRILLIX entwickelt, welches einen ersten Meilenstein bei der Entwicklung eines 3D Turbulenzprogrammes für den Rand und die Abschälschicht setzt. GRILLIX basiert noch auf einem vereinfachten physikalischen Model (Hasegawa-Wakatani), aber kann dafür auf die komplexe Geometrie angewandt werden, z.B. sind Simulationen über die Separatrix hinweg möglich. Durch das Verwenden eines zylindrischen numerischen Gitters (R, Z, φ), welches kartesisch innerhalb poloidaler Ebenen ist, werden die üblicherweise verwendeten Feldlinien-angepassten Koordinaten umgangen. Zur Diskretisierung senkrechter (im Bezug auf die Magnetfeldlinien) Operatoren können damit Standardmethoden herangezogen werden. Die Diskretisierung paralleler Operatoren erfolgt mittels Feldlinienabbildung, d.h. Feldlinien werden von Ebene zu Ebene verfolgt und Werte an den entsprechenden Stellen interpoliert. Strukturen sind üblicherweise stark elongiert entlang Magnetfeldlinien und diese Eigenschaft wird ausgenutzt durch eine Ausdünnung des Rechengitters in toroidaler Richtung. Tokamak Geometrien mit beliebigem poloidalen Querschnitt, einschließlich einer Separatrix, können mit GRILLIX behandelt werden.

In Rechengittern, die nicht Feldlinien angepasst sind, tritt numerische Diffusion auf, d.h. eine fälschliche numerische senkrechte Kopplung, die von der parallelen Dynamik abhängt. Diese numerische Diffusion kann fatal sein für Simulationsprogramme, da die parallele Dynamik üblicherweise Größenordnungen schneller ist als die senkrechte. Ein neues numerisches Schema wurde daher entwickelt und in GRILLIX angewendet, welches die Selbstadjungiertheit das parallelen Diffusionsoperators auf der diskreten Ebene erhält und die numerische Diffusion drastisch reduziert. Viele Tests in verschiedenen Geometrien werden präsentiert, um das Konzept der Feldlinienabbildung im Allgemeinen und GRILLIX im Speziellen zu verifizieren.

Erste Geometrieeffekte in Maschinen mit Divertor auf Drift-Wellen Turbulenz wurden mit GRILLIX untersucht. Feldlininen ausgerichtete Strukturen werden stark deformiert in der Nähe des X-Punktes. Deren senkrechte Ausdehnung nimmt zum X-Punkt hin stark ab und Dissipation wird dominant. Der X-Punkt stellt letztlich eine Art Barriere für Fluktuation dar, da diese in der Nähe des X-Punktes praktisch verenden. Der Mechanismus ähnelt damit der bereits zuvor gefundenen resistiven X-Punkt Mode.

Acknowledgments

Many ideas and most strategic decisions for this work were performed in meetings among David Coster, Karl Lackner, Klaus Hallatschek and me. Hence, I want to cordially thank all three of them equally for supervising me. Karl Lackner motivated not only this work but also myself during some difficult phases. With his overview and belief in the whole project we were always able to make the right strategic decisions. I want to thank David Coster for always having an open door for me and keeping me motivated at any time with many good words (and cookies on Friday). At many problems he could help with his often pragmatic view on things from distance. As well, I was also always able to discuss the smallest details with him. I want to thank Klaus Hallatschek for his brilliant ideas contributing to this work. His detailed and critical view on results was often very helpful for the next steps and I enjoyed working with him very much.

Furthermore, Omar Maj helped me a lot at the development of the numerical scheme and his door was still open on many Fridays late. I also want to thank Matthias Hölzl for some help with the numerical scheme and his advice with the solver, Hans-Joachim Klingshirn, who helped me several times with computational issues, Michele Martone for his advice with the LIBRSB library, Andreas Kammel for exchanging his experience about the Hasegawa-Wakatani model with me and Emanuele Poli for his advice during the final stage of this work.

A very special thanks goes to my office mate and good friend Johannes Grießhammer. Not only he helped me several times with frustrating bugs in the code and other computational issues, but also we were able to answer most questions and solve most problems in our discussions. Working with him was a perfect symbiosis (Maybe, I was even slightly parasitic).

Finally, I thank my significant other Daniela Gläser for supporting me in every aspect. Not only once, she encouraged me during difficult phases. I want to thank my family for supporting and ultimately making all this possible for me.

Contents

Chapter 1.

Introduction

Feynman states in volume 1 of his famous lectures at the end of chapter 4 where he introduces the concept of energy [1, p. 4-8]:

> *"Finally, we remark on the question of where we can get our supplies of energy today. Our supplies of energy are from the sun, rain, coal, uranium, and hydrogen. The sun makes the rain, and the coal also, so that all these are from the sun. [...] We have already obtained energy from uranium; we can also get energy from hydrogen, but at present only in an explosive and dangerous condition. If it can be controlled in thermonuclear reactions, it turns out that the energy that can be obtained from 10 quarts of water per second is equal to all of the electrical power generated in the United States. With 150 gallons of running water a minute, you have enough fuel to supply all the energy which is used in the United States today! Therefore it is up to the physicist to figure out how to liberate us from the need for having energy. It can be done." [1 quart = 1/4 gallons ≈ 0.95 litres, authors annotation]*

Since this statement dating back to the 1960s the global energy problem has continued to get worse and the development of sustainable energy sources will become more and more important for humankind to raise or even just maintain its level of living. As it happens in the core of the sun, in fusion reactions of light nuclei a large amount of energy is liberated. The most promising fusion reaction for a future fusion power plant is [2]:

$$\,^2_1\text{D} + \,^3_1\text{T} \longrightarrow \,^4_2\text{He (3.5MeV)} + \,^1_0\text{n (14.1MeV)}, \tag{1.1}$$
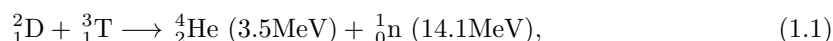
The rest mass of the products is smaller than the rest mass of the reactants and the difference is released in terms of kinetic energy of the products, denoted with the numbers given in the brackets. The fuel, i.e deuterium and tritium, can be won from water and from lithium whose amount on earth suffice for millions of years.

   The reactants must have a high temperature of several million Kelvin in order to overcome the Coulomb barrier which originates from their electrical repulsion. In such an environment the reactants are in a plasma state. A plasma consists of electrically charged particles, but is electrically neutral above a certain spatial scale. Around a small positive test charge put into a conglomerate of electrons and ions, the negatively charged electrons will accumulate and screen the extra charge above the Debye length $\lambda_D = \sqrt{T_e/(4\pi n_e e^2)}$, where T_e, n_e is the electron temperature, respectively density. Outside of a sphere with radius of a Debye length around this test particle, other particles do not feel this individual test charge but interact in a collective long ranging manner. This is what characterizes a plasma and thus one may ideally speak of a plasma if the number of charged particles within a Debye sphere is much larger than one, i.e. $n_e \lambda_d^3 \gg 1$. The spatial dimension of a plasma must be also large compared to the Debye length ($L \gg \lambda_D$). In addition, the typical frequency of plasma oscillations $\omega_{pe} = \sqrt{4\pi n_e e^2/m_e}$, which characterizes an oscillation of an electron cloud with respect to the fixed ions, must be large compared to the plasma-neutral collision frequency ($\omega_{pe}\tau \gg 1$) (see e.g. [3, 4]).

1.1. Tokamaks

In order to reach and sustain the required high temperatures, the plasma has to be confined and insulated against thermal losses. For the sun gravity acts as the confining force. On the surface of the earth, where gravity is negligible against the appearing electromagnetic forces, magnetic fields can be used to confine a plasma. In a strong homogeneous magnetic field a charged particle performs a helical orbit with a perpendicular extent of the Larmor radius $\rho_L = mcv_\perp/(|Ze|\,B)$, where Ze is the charge of the particle, m its mass and $v_\perp$ its velocity perpendicular to the magnetic field $\mathbf{B}$. Assuming that the particle has a thermal velocity of $v_\perp = \sqrt{T/m}$, leads to $\rho_L = c\sqrt{Tm}/(|Ze|\,B)$. Whereas the charged particles of the plasma can still stream freely along magnetic fields, their motion in the perpendicular direction is constrained which leads to the idea of magnetic confinement concepts.

Among various magnetic fusion concepts the tokamak (see fig. 1.1) has proven to be the most successful configuration, which utilizes magnetic fields in a toroidal topology to confine the plasma. A strong toroidal field is created by a set of planar coils. However, the resulting inhomogeneity of the toroidal magnetic field $B_{tor} \propto R^{-1}$ would cause a charge dependent vertical drift of the particles perpendicular to the magnetic field lines. The resulting electric field would in turn cause a charge independent radial drift and lead to a fast loss of the plasma. To compensate for this effect, a poloidal field is created additionally via a toroidal current induced in the plasma, which owing to its composition of charged particles, is a good electric conductor. The poloidal magnetic field component is usually much smaller than the toroidal component and the resulting magnetic field runs helically in toroidally nested flux surfaces. In such a geometry parallel compensation currents (Pfirsch-Schlüter currents) can now short-circuit the vertical electric field and the plasma remains confined. It is important to note that the whole configuration is axisymmetric. A set of vertical magnetic field coils balances the radially outwards acting hoop force and is also used for plasma shaping. The finite resistivity of the plasma requires a continuous toroidal current drive to maintain the poloidal magnetic field. This is achieved via the principle of a transformer, where the plasma column plays the role of a secondary winding. In the primary winding a rising current has to flow which constrains the whole concept to a pulsed operation (see e.g. [2, 4, 5, 6]).

a)   b)
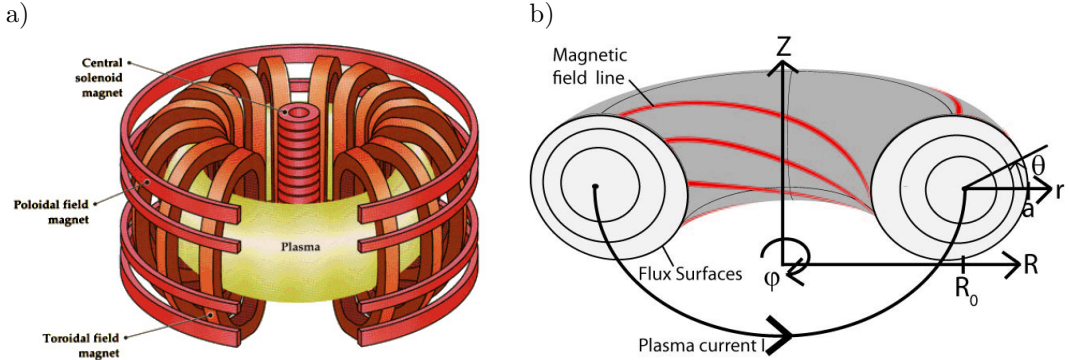
Figure 1.1.: Concept of tokamak: a) Coil system, b) geometry and magnetic field line topology

Given this qualitative picture, the macroscopic plasma behaviour is well described by Magnetohydrodynamics (MHD, see e.g. [7]), which models the plasma as a single neutral fluid which can nevertheless carry an electric current. Any confined state has to fulfil perpendicular force

balance according to MHD:

$$\mathbf{J} \times \mathbf{B} = c\nabla p, \tag{1.2}$$

i.e. a pressure gradient (∇p) can be maintained with currents ($\mathbf{J}$) perpendicular to the magnetic field. In an axisymmetric toroidal topology the force balance can be recast to the Grad-Shafranov-Schlüter equation (GSS), which is introduced in more detail in section 3.1. The solution to the GSS equation defines then the toroidally nested flux surfaces on which the pressure is constant, and in which currents and magnetic field lines run. An important quantity for tokamaks is the safety factor q which gives the numbers of toroidal turns of a magnetic field line as it turns once poloidally.

The tokamak is currently the most advanced confinement concept and the ITER [8] experiment, which is planned to start operation from the year 2020, is expected to obtain for the first time a net power output, i.e. where more energy through fusion reactions is produced than is needed to heat and sustain the plasma. Also possibilities of steady state or at least long pulse operation, where the current is driven also by alternative mechanisms, are being investigated. The demonstration power plant DEMO, which is planned to start operation around 2040, is presently also based on the tokamak concept [9].

1.2. Stability and transport

A state in which the force balance 1.2 is fulfilled does not automatically imply confinement, since also stability against perturbations has to be taken into account. Numerous types of plasma instabilities exist: Some might saturate non-linearly on a nearly constant turbulence level and cause just an increase in transport of heat and particles. A slight modification of the profiles is the result [6, 10]. Others are fatal, since they can lead to a fast collective motion of the plasma towards the first wall which might in turn be even damaged severely.

The control of macroscopic ideal MHD instabilities is mostly crucial [5]. A practical outcome of MHD stability considerations is e.g. that for suppression of fatal instabilities (disruptions) tokamaks are limited to a certain operational regime in ($q_a, \bar{n}$) parameter space, where q_a is the safety factor at the edge and $\bar{n}$ the mean electron density [11]. Moreover, tokamaks should be operated below a certain β which is defined as the ratio of plasma pressure to magnetic pressure:

$$\beta := \frac{p}{B^2/8\pi} < \beta_N \frac{I[MA]}{a[m] \cdot B_{tor}[T]}, \tag{1.3}$$

where I is the plasma current and a the minor radius of the tokamak. β_N is a numerical value for which the Troyon limit ($\beta_N = 0.028$) is common [5, 4, 11], but it can be raised by properly shaping the plasma cross section [12]. β gives also a rough estimate for the economic efficiency of a reactor and should be above ≈ 0.05, which is just realistically reachable [5, 12]. Another class of important instabilities enters as resistivity is taken into account. In contrast to ideal MHD, resistive MHD allows also a change of the magnetic field line topology, i.e. reconnection of field lines. Magnetic islands can form at low order rational surfaces ($q = m/n$) across which the profiles flatten due to the quick parallel transport. An overall degradation of confinement is the result [6, 10].

The absolute minimum cross field transport of particles and heat, which even arises in an MHD stable plasma, is caused by diffusive processes due to Coulomb collisions. MHD assumes that the plasma is always highly collisional, such that the underlying distribution function is always a local Maxwellian. However, transport processes arise from non-Maxwellian modifications to the underlying distribution function [5] and require thus a more comprehensive model to compute

the desired transport coefficients. The most prominent among them is certainly the Braginskii model [13] which will be introduced in chapter 2, but transport coefficients can also be estimated with a simple random walk model: In a magnetised plasma particles are displaced by a distance of the Larmor radius ρ_L in the perpendicular direction as they undergo an effective collision[1]. Particle diffusion (D_n) can only be caused by unlike particle collisions, whereas heat diffusion (χ_i, χ_e) is caused also among like particle collision [5, 4, 14]:

$$D_n \sim \frac{\rho_{Le}^2}{\tau_{ei}}, \quad \chi_i \sim \frac{\rho_{Li}^2}{\tau_{ii}}, \quad \chi_e \sim \frac{\rho_{Le}^2}{\tau_{ee}}, \tag{1.4}$$

where $\tau_{ii}, \tau_{ee}, \tau_{ei}$ are ion-ion, electron-electron, electron-ion effective collision times. Ion heat diffusivity is usually dominant over electron heat diffusivity. This classical transport has to be corrected for toroidal systems to the neoclassical transport if the time between collisions is sufficiently large that particles feel the global geometry of the system (banana regime). The $1/R$ dependence of the magnetic field gives rise to a magnetic mirror. A particle located at the outer low field side with a low ratio of $v_\parallel/v_\perp$ is repelled from the inner high field side of the tokamak and remains trapped on the torus outside[2]. It ultimately undergoes an orbit which is in poloidal projection shaped like a banana. Though only a small fraction of particles ($\sim \sqrt{\epsilon} := \sqrt{a/R_0}$) is trapped, their perpendicular step size (banana width) and the effective collision frequency between trapped and passing particles is enhanced. This enlarges each diffusion coefficient in expression 1.4 by a factor $q^2\epsilon^{-3/2}$ [5, 15].

However, experimental measurements of confinement times in tokamaks suggest that the transport in the electron channel greatly exceeds the neoclassical prediction and is comparable to the ion flux. The flux in the ion channel is often around a factor of $\approx 2-3$ larger than predicted by neoclassical theory [4, 14]. Hence, transport is said to be anomalous. It is now commonly accepted that the cause for the anomalous transport are microscopic fluctuations which lead to a plasma and heat exhaust by microscopic advective $\mathbf{E} \times \mathbf{B}$ flows. Moreover, turbulent flutter of magnetic field lines, along which transport takes place rapidly, can contribute to this phenomenon. The fluctuations are driven by microscopic instabilities which are in turn fed by pressure gradients. Heuristic arguments (see e.g. [16]) lead to a diffusivity coefficient, known as the Gyro-Bohm scaling:

$$D^{GB} \sim \frac{c\,T_e}{16\,e\,B}\frac{\rho_s}{L_p}, \tag{1.5}$$

where $L_p \sim p/|\nabla p|$ denotes a pressure gradient length and $\rho_s = c\sqrt{T_e M_i}/(eB)$ the sound radius which gives a rough estimate for the spatial scales of the fluctuations. ρ_s is introduced in more detail in chapter 2. For a deuterium plasma with $T_e = 1\mathrm{keV}$, $B = 2.5\mathrm{T}$ and $L_p \sim a = 50\mathrm{cm}$ one obtains $D^{GB} = 1.25\mathrm{m\,s^{-2}}$, which matches roughly experimental conditions of current tokamaks.

1.3. Turbulence basics

Although scaling laws derived from experiments can be used to predict the performance of a future fusion reactor (see e.g. [17]), a first principles prediction and understanding of anomalous transport requires computations of self consistent models. The description usually has to take into account quadratic non-linearities which give rise to turbulent dynamics. Turbulence involves many degrees of freedom and is characterised by an unpredictable behaviour which is highly

---

[1]An effective collision by $90°$ is the result of many small angle scatterings.

[2]The magnetic mirror effect can also be illustrated with the conservation of the adiabatic invariants of the particle, i.e its energy and magnetic moment, in an inhomogeneous magnetic field.

sensitive to initial and boundary conditions. However, in a saturated state, where the interactions among the various degrees of freedom are in a statistical balance, the fluctuation levels and also the transport level remain statistically stationary. This saturated transport level is what is called anomalous transport.

However, turbulence is in general a very complex and yet unsolved problem as the following citation of Horace Lamb from the year 1932 shall illustrate (see [18, p. 24]):

> "I am an old man now, and when I die and go to heaven there are two matters on which I hope for enlightenment. One is quantum electrodynamics, and the other is the turbulent motion of fluids. And about the former I am rather optimistic."

Kolmogorov's theory of 1941 (K41) is one of the few exceptions where an analytic result for the incompressible 3D Navier-Stokes equation is available. It would be beyond the scope of this thesis to give a review about turbulence theory in general and K41 in special, but due to its importance the main ideas and results of K41 are illustrated here very briefly (For a more general introduction to turbulence and K41 see textbooks like [19, 18, 20]).

A paradigm for turbulence is the incompressible Navier-Stokes equation:

$$\nabla \cdot \mathbf{v} = 0, \quad \frac{\partial}{\partial t}\mathbf{v} + \mathbf{v} \cdot \nabla \mathbf{v} = \mathbf{f} + \nu \nabla^2 \mathbf{v}, \tag{1.6}$$

where $\mathbf{v}$ is the velocity of the fluid, ν a viscosity constant and $\mathbf{f}$ some force (stirring) term which maintains the fluid motion. An important number in fluid theory is the Reynolds number which gives the ratio of inertial forces to viscous forces:

$$Re = \frac{vl_0}{\nu}, \tag{1.7}$$

with v a mean velocity and l_0 a characteristic scale length.

The basic picture behind K41 is that energy is introduced (stirring) at some large scale $k_0 \sim l_0^{-1}$ into the system. As illustrated in fig. 1.2a, large eddies then break up into two smaller eddies of comparable size which break up then again and again towards smaller and smaller scales until they are dissipated at the smallest scales k_ν. Energy is thereby transferred down in a so called Richardson Cascade. It is assumed that for sufficiently high Reynolds numbers there is an inertial range which is not affected by the details of the energy input or the dissipation. Within this inertial range it is assumed that the dynamics is statistically isotropic and the statistical behaviour of the system is uniquely determined by the spatial scale k itself and the spectral energy flux ϵ, which is statistically constant. Even in the limit of vanishing viscosity $\nu \to 0$, the rate at which energy is dissipated remains finite and is just shifted to ever smaller scales. It is equal to the energy flux and also equal to the energy which is pumped into the system. By dimensional arguments the spectral energy must then follow a remarkably simple power-law dependency (see fig. 1.2b):

$$E(k) = C\epsilon^{2/3}k^{-5/3}, \tag{1.8}$$

with C a universal constant. This result has been confirmed in experiments, but there are also other predictions of K41 concerning higher order structure functions where deviations to experiments arise.

As shown in chapter 2 simple paradigms for turbulence in tokamaks are also based on fluid models (e.g. Hasegawa-Mima or Hasegawa-Wakatani). In magnetic fusion devices the dominant $\mathbf{E} \times \mathbf{B}$ non-linearity acts in planes perpendicular to the magnetic field, such that the momentum equation looks very similar to a 2D incompressible Navier-Stokes equation. 2D incompressible
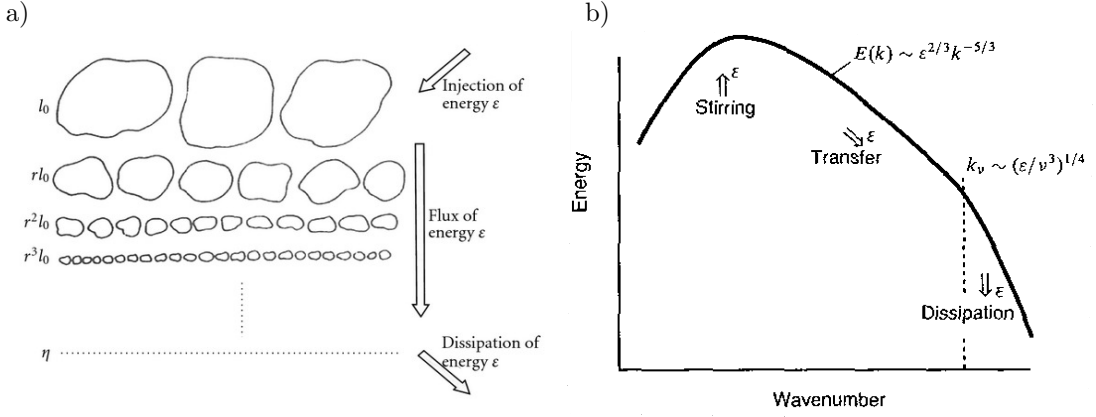
Figure 1.2.: a) Scheme of Richardson Cascade. Energy is injected at some scale $l_0 \sim k_0^{-1}$ at rate ϵ. Eddies break up in subsequent steps (r) into roughly always two eddies of comparable size. The spectral energy throughput is thereby constant and equal to ϵ. At the smallest scale eddies and energy are dissipated also at rate ϵ, independent on ν (Figure taken from [19]). b) Resulting energy spectrum predicted by Kolmogorov (K41) (Figure taken from [20]).

Navier-Stokes turbulence is quite different from 3D, since a simultaneous conservation of energy and also enstrophy[3] leads to a dual cascade in which energy is transferred at constant rate towards larger scales and enstrophy at constant rate towards smaller scales. On the other hand, the thermal energy content related with passively advected quantities (passive tracers), e.g. the density, obeys a direct cascade [20]. Without any coupling between the flow and the density they would develop apart from each other. The third dimension is now of importance, since a coupling mechanism between both quantities along the magnetic field lines leads ultimately to a common development [21].

Although analytic results for turbulence are of major importance and helpful for understanding, in practice a prediction for the absolute value of anomalous transport in magnetic fusion devices based on first principles is currently only possible with numerical simulations.

1.4. Edge and SOL

Before this work can finally be motivated, the divertor concept has to be introduced. Ideally, a fusion plasma consists only of deuterium, tritium and also helium ash which has to be removed constantly, but in reality there is also always a small fraction of impurities present. Especially, highly charged impurity concentrations have to be minimized, since they can significantly dilute the plasma and contribute substantially to radiation losses [22].

At some place the plasma has contact with a material surface, where the particles sputter impurities from the material which can then flow back into the main plasma region. In order to avoid damage of the wall during a possible disruption and to have a controlled contact with the wall, a limiter can be used at the outer boundary of the plasma (see fig. 1.3a). The outer confined region, i.e. outer flux surfaces that contain closed field lines is called edge. Magnetic field lines which have contact with the limiter form the scrape-off layer (SOL). The edge is separated

---

[3]Enstrophy is the integral of the square of vorticity: $U = 1/2 \int_V dV \, (\nabla \times \mathbf{v})^2$.

from the SOL by the separatrix, sometimes also called last closed flux surface (LCFS)[4]. Due to the fast loss of plasma along magnetic field lines to the target plates of the limiter, the perpendicular plasma density and temperatures decay roughly exponentially with a half width of $\lambda_{SOL} \sim \sqrt{D_\perp L_c / c_s}$, where $D_\perp$ is an (anomalous) cross field diffusion coefficient, L_c the connection length to the target plate and $c_s = \sqrt{T_e / M_i}$ the sound speed. λ_{SOL} is typically of the order of mm to few cm [2, 23, 22].

Modern day tokamaks and also future devices like ITER are based on the divertor concept (see fig. 1.3b). With additional coils a poloidal magnetic field null is created at one point (sometimes also two), denominated X-point and the contact with the target plates occurs remotely from the confined region. In comparison to the limiter concept the influx of impurities into the confined region is reduced. Moreover, impurities and helium ash can be removed constantly from the divertor region with additional pumps. Consequently, the confined plasma is more pure in a divertor configuration. A new mode of improved confinement, called the H-mode, has been found in 1982 for the first time at ASDEX [24] also in a divertor configuration.

As pointed out in [11], the physics of the edge and SOL is in many ways more complicated and difficult to model (see e.g. [23, 22, 25]) than the rest of the plasma. Atomic processes, radiation losses and sheath physics have to be taken into account. Parallel transport to the plates is important, leading eventually to strong gradients along magnetic field lines. Also perpendicular gradients are steep (few cm). Turbulent fluctuations are of the order of unity, i.e. $\delta n_e \sim n_e$, which prohibits a splitting into background quantities and fluctuations in the modelling. The complex geometry in diverted geometries, which is the main issue of this work, introduces additional complexities to the modelling.

On the other hand the edge and SOL is of high importance, since its influence on the core can be large. The plasma and impurity densities are often largely set by conditions in the plasma boundary [23]. Moreover, high heat fluxes on the divertor target plates of the order of 5MW m^{-2} [25] can be expected for ITER in steady state operation and a precise prediction of such numbers is from the engineering point of view of high importance.

1.5. Motivation and outline

As pointed out in the previous sections, the prediction of anomalous turbulent cross field transport and the understanding of turbulent phenomena based on first principles models is of major importance for the construction and operation of magnetic fusion devices. At present, sophisticated models and codes are available mainly for the core and to a certain extent also for the edge region. However, the edge and SOL, especially the region around the separatrix in diverted devices, is under this aspect still a rather untouched area of research. Roughly speaking, two major problems related to this region can be identified: Firstly, the physical model which has to be retained is rather complex. Secondly, the geometry which is imposed by the magnetic field is also rather complex in diverted devices. As also discussed chapter 3, the usually employed field aligned coordinates become ill defined on the separatrix in diverted devices. This makes the numerical treatment difficult.

In the past, several approaches have been dedicated to parts of these problems[5]: The SOLPS package [25] uses a 2D model where the anomalous diffusion is modelled with effective diffusion coefficients which remain an input to the model, i.e. they are not computed self consistently. Physics of impurity and radiation losses can be included in the modelling. In Tokam2D [27] and

---

[4]The nomenclature for separatrix is not definite in literature. Some might use separatrix only for diverted devices (e.g. [22]).

[5]In the following, only fluid approaches are listed without claiming to be complete.

a)   b)
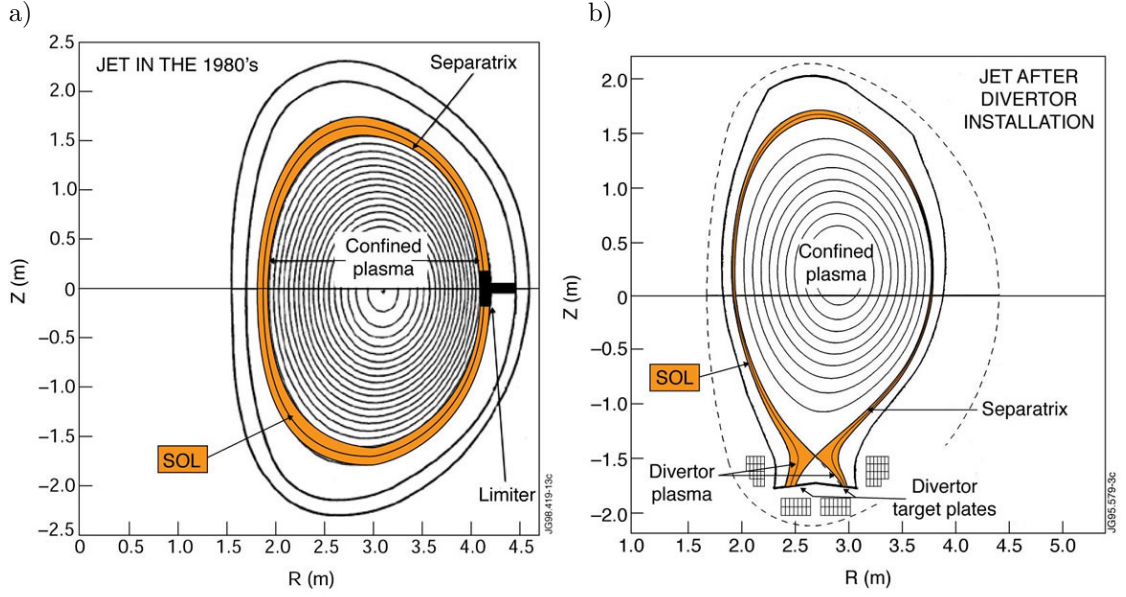
Figure 1.3.: Poloidal cross section of tokamak in limiter (a) and divertor (b) configuration. The scrape-off layer (SOL) is formed by field lines that end on limiter or divertor plates. The separatrix denotes the flux surface which is at the boundary between SOL and edge (closed field line region). In divertor configuration a null in the poloidal field determines the X-point and ensures that the first contact with the divertor plates is remote from the confined region. (Figure taken from [26]).

ESEL [28] turbulence and transport in the edge/SOL is approximated only with a 2D model where the parallel dynamics is parametrized. The GBS code [29, 30] and Tokam3D [31] simulate turbulence and transport in 3D. However, they rely still on a field aligned coordinate system. This makes simulations across the separatrix in diverted geometry impossible and only limiter configurations can be treated. A limiter configuration was also investigated with a gyrofluid model based on the GEM model [32, 33]. Open and closed field lines in a divertor configuration have been studied separately in [34]. BOUT [35, 36, 37, 38, 39, 40] is capable to treat diverted geometries by avoiding field aligned coordinate systems. However, the approach is still based on a flux aligned grid. Due to the change of topology, the X-point region remains still somewhat exceptional in this approach as illustrated in fig. 1.4. In the worst case, this might even lead to numerical artefacts. Moreover, there is a huge resolution imbalance within the poloidal plane, which is in contrast to the turbulent dynamics tending to be isotropic within poloidal planes. Several attempts have also been pursued by the stellerator community who have to deal unavoidably with complex geometries [41, 42, 43, 44, 45, 46, 47]. FINDIF [47], as one of the most recent approaches, creates the computational grid by putting grid points along magnetic field lines. However, the grid creation is cumbersome and one has only little control over the grid quality. Moreover, whereas the discretisation of parallel operators is straight forward, the numerical treatment of perpendicular operators is difficult.

This work is mainly dedicated to the development of a numerical concept which is able to accurately treat the full 3D geometry in diverted devices. The supplied numerical tools and performed tests set a first milestone for the future development of a edge/SOL turbulence code which shall ultimately retain the full geometry as well as a valid physics model. Due to the huge
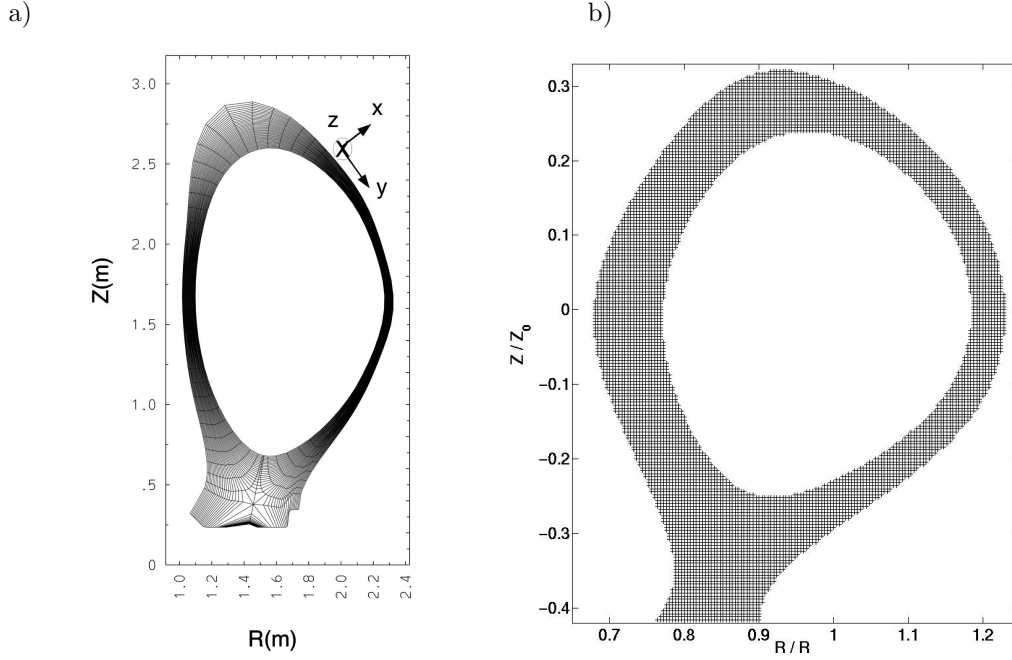
Figure 1.4.: a) Numerical grid as used in the BOUndary Turbulence code BOUT [37]. Note the special role of the X-point in the grid, which is connected to eight cells, instead as the usual four cells. Moreover there is a huge resolution imbalance between midplane and X-point region. b) Numerical grid as used in the here newly developed code GRILLIX. The X-point is treated as any other grid point and the resolution is homogeneous within poloidal planes.

complexity of such a possible future project, the developed methods are here only applied to a simple and well established turbulence model (Hasegawa-Wakatani) which is in general not valid in the edge/SOL. This approach makes sense, since later on a modification of the equations in a numerical code is usually easier then a modification of the geometry. Nevertheless, the used model is self consistent and already suited to study first effects of the complex diverted geometry on turbulence. The results here might thus also help to understand future results obtained with a more complex physical model.

In chapter 2 the target model, Hasegawa-Wakatani, is derived and its implications are discussed. It is emphasized which assumptions of the model might be broken in the edge/SOL. Starting from a kinetic model which accurately describes the plasma dynamics, each reduction is reviewed in the context of its validity in the edge/SOL region. Hence, one can trace always back to a 'more' valid model.

In chapter 3 the numerical concept is presented. As an introduction, a short review of field and flux aligned coordinates and why they fail in diverted geometries at the separatrix is given. The numerical concept is presented which is based on a field line map. The advantage of this approach over previous ones is that axisymmetric geometries with arbitrary poloidal cross sections can be treated where the X-point is treated like any other grid point and is not exceptional any more (An example numerical grid is shown in fig. 1.4b). Simultaneously, the property of the solutions to be strongly elongated along magnetic field lines is exploited computationally. The axisymmetric constraint is thereby not a general restriction of the method but used in this work

simply for convenience. A field line map approach was recently proposed [48] and applied to the FENICIA code [49, 50, 51], but as is shown in chapter 3 and appendix A their motivation for the method was initially based on field aligned coordinates which become ill defined at the separatrix. Therefore, the field line map approach is motivated in this work differently. This work was performed independently and is complementary to FENICIA which is devoted to the discretisation of the parallel gradient operator, whereas this work is mainly concerned with the parallel diffusion operator. A new scheme, which is a generalisation of [52, 53], is presented which reduces spurious numerical cross field diffusion drastically, arising unavoidably with non field aligned grids.

The numerical concept is applied in the newly developed code GRILLIX. The full set of equations which can be solved with GRILLIX are the 3D Hasegawa-Wakatani equations in tokamaks with an arbitrary poloidal cross section. Isolated benchmarks of the code on the perpendicular dynamics are presented in chapter 2 and on the parallel diffusion operator in chapter 3. Some additional benchmarks can be found in appendix B and D. In chapter 4 the code is finally presented in detail. GRILLIX is written in Fortran, MPI parallelised over the poloidal planes and OpenMP parallelised within poloidal planes. Some additional details on the implementation are also given in appendix C.

The full set of equations is applied in chapter 5 to axial circular geometry. The results of this chapter establish the basis in order to understand later results in more complex geometry. Moreover, GRILLIX can still be tested and benchmarked on analytic predictions, self consistency, convergence and against other field aligned codes. Several diagnostic tools are presented. Also a recently found parameter threshold for zonal flow production in the Hasegawa-Wakatani model is confirmed with GRILLIX.

Finally, GRILLIX is applied to the complex diverted geometry in chapter 6. The effects of an X-point are discussed with a simple model and GRILLIX is applied to a geometry where the effects of an X-point can be studied in isolation and as purely as possible. It will be shown that field aligned structures are strongly damped as they enter the X-point region and fluctuations practically die out near the X-point. Hence, the X-point tends to disconnect structures along the parallel direction.

The main result of this work is the provision of a numerical concept and numerical tools which can cope accurately with a diverted geometry. Moreover, global tokamak or even Stellerator simulations, which include also a magnetic axis, pose no substantial problems to the concept, in contrast to the widely used field and flux aligned codes.

Chapter 2.

The Hasegawa-Wakatani model

The Hasegawa-Wakatani (HW) model, a simple model for plasma turbulence, is presented. Many approximations of HW are not valid especially in the SOL of tokamaks. But since ultimately the emphasis of this work is on the complex geometry and the establishment of a rather new numerical concept, this model is chosen due to its simplicity and maturity. Containing all necessary ingredients for a self consistent description of turbulence, HW serves as a perfect first target model.

2.1. Braginskii equations

The dynamics of a plasma is accurately described with the Boltzmann equation. The distribution function $f_\alpha(t, \mathbf{r}, \mathbf{v})$ for species α is evolved in time according to electromagnetic forces created by external mechanisms like coils and fields created by the charged particles of the plasma itself. The distribution function and the fields are thereby not exactly localized quantities but smoothed entities. The interaction between the particles in a plasma is split up into a long ranging collective interaction, described with electromagnetic fields, and a short range interaction described by a collision term. The Debye length serves as a separation between both scales. The smoothed electromagnetic fields are computed self-consistently from the distribution functions with the Maxwell equations, leading to a non-linear integro differential equation [6, 54]. However, due to the non-linear nature, the high dimensionality (6D phase space) and the retention of many spatial and temporal scales the Boltzmann-Maxwell equation system is very complex to solve. Several simplifications of the system have been developed quite successfully during the recent years, e.g. Gyrokinetics (see. e.g. [55] and references therein), where the fast gyro motion is averaged away, leading to a reduced 5D phase space description. Direct numerical simulations of the plasma become possible (see e.g. [56]).

Passing to a fluid description is another simplification. In a fluid model the plasma is described by functions which only depend on space and time and which can be identified with intuitional quantities like the density $n_\alpha(t, \mathbf{r})$, the velocity $\mathbf{v}_\alpha(t, \mathbf{r})$ and the temperature $T_\alpha(t, \mathbf{r})$ of a fluid segment. They are much simpler to solve than kinetic models due to the decrease of dimensionality (6D or 5D(Gyrokinetics) $\rightarrow$ 3D). Fluid models are based on the assumption that the plasma is collision dominated and hence the distribution function is close to a Maxwellian [54]. In situations where collisions are rare, such that a particle can feel the global geometry, neoclassical effects might become important [14]. Nevertheless, in the edge and SOL of magnetic fusion devices temperatures are usually low and collisions frequent, such that many phenomena can be described accurately with fluid models.

There are two different ways to derive a self consistent fluid model: One is based on physical intuition using conservation of mass, momentum and energy (see e.g. [5]). On the other way the fluid model is derived from the kinetic model by taking velocity moments of the distribution function [13, 54]. Since in this approach the evolution equations for a finite number of moments

always depend on higher order moments, some kind of closure of the system is needed which expresses the unknown higher moments in terms of the available moments.

Based on the moment approach, a detailed derivation of a fluid model is given in [13] which is quite comprehensive, well established and often used in the fusion community. A derivation of this model here would go beyond the scope of this thesis and just the final result, the Braginskii equations, for a single component hydrogen plasma (i.e. $Z = 1$ and the species index α has been dropped) is presented.

The continuity equations for the electrons and ions express local conservation of mass:

$$\frac{\partial}{\partial t} n_i + \nabla \cdot (n_i \mathbf{v}_i) = 0, \tag{2.1}$$

$$\frac{\partial}{\partial t} n_e + \nabla \cdot (n_e \mathbf{v}_e) = 0. \tag{2.2}$$

The equations of motion express conservation of momentum:

$$M_i n_i \frac{d_i}{dt} \mathbf{v}_i = -\nabla p_i - \nabla \cdot \mathbf{\Pi}_i + e n_i \left(\mathbf{E} + \frac{1}{c} \mathbf{v}_i \times \mathbf{B} \right) - \mathbf{R}, \tag{2.3}$$

$$m_e n_e \frac{d_e}{dt} \mathbf{v}_e = -\nabla p_e - e n_e \left(\mathbf{E} + \frac{1}{c} \mathbf{v}_e \times \mathbf{B} \right) + \mathbf{R}, \tag{2.4}$$

where $d_{e,i}/dt = \partial/\partial t + \mathbf{v}_{e,i} \cdot \nabla$ is called the advective derivative. The left hand sides describe inertial forces and forces acting on the fluid segment appear on the right hand sides: A force is exerted due to a pressure gradient $p_{e,i} = n_{e,i} T_{e,i}$ within the fluid and due to electromagnetic forces, caused by external mechanisms (coils) and the smoothed long ranging collective interaction of the plasma which has to be computed self consistently. The ion stress tensor $\mathbf{\Pi}_i$ contains besides collisional terms also collisionless finite Larmor radius contributions arising from the strong anisotropy in magnetised plasmas. These terms are of importance later for the diamagnetic cancellation (section 2.2.2). The electron stress tensor is neglected. Momentum transfer between electron and ions is contained in $\mathbf{R}$. The component of this drag force along magnetic field lines (parallel) is given by:

$$R_\| = e n_e \eta_\| J_\| - 0.71 n_e \nabla_\| T_e. \tag{2.5}$$

The first term describes friction between the electron fluid and the ion fluid ($\eta_\| = 0.51 m_e \nu_e/(e^2 n_e)$, with ν_e the electron collision frequency) and the second term is a thermal force.

The heat equations express local conservation of energy:

$$\frac{3}{2} n_i \frac{d_i}{dt} T_i + p_i \nabla \cdot \mathbf{v}_i = -\nabla \cdot \mathbf{q}_i - \mathbf{\Pi}_i \cdot \nabla \cdot \mathbf{v}_i + Q_i, \tag{2.6}$$

$$\frac{3}{2} n_e \frac{d_e}{dt} T_e + p_e \nabla \cdot \mathbf{v}_e = -\nabla \cdot \mathbf{q}_e + Q_e, \tag{2.7}$$

i.e. a change of internal energy can be caused by compression of the fluid segment, heat conduction and heat sources/sinks. Explicit expressions for the heat fluxes $\mathbf{q}_{e,i}$, heat sources/sinks $Q_{e,i}$ and the gyroviscous tensor $\mathbf{\Pi}_i$ are ultimately not needed and the interested reader is referred to [13]. The electric and magnetic fields have to be computed self consistently from Maxwell's equations.

$$\nabla \cdot \mathbf{E} = 4\pi \rho_{ch}, \tag{2.8}$$

$$\nabla \cdot \mathbf{B} = 0, \tag{2.9}$$

$$\nabla \times \mathbf{E} = -\frac{1}{c} \frac{\partial}{\partial t} \mathbf{B}, \tag{2.10}$$

$$\nabla \times \mathbf{B} = \frac{4\pi}{c} \mathbf{J} + \frac{1}{c} \frac{\partial}{\partial t} \mathbf{E}, \tag{2.11}$$

with $\rho_{ch} = e(n_i - n_e)$ the charge density and $\mathbf{J} = en_i\mathbf{v}_i - en_e\mathbf{v}_e$ the current density. The Braginskii equations constitute a self consistent fluid model for collision dominated plasmas with a rather wide range of validity. However, since practically no assumptions on time and space scales of interest and the fluctuation levels have been done, this model is still rather complex. Further simplifications are advisable.

2.2. Derivation

The HW equations are derived from the Braginskii equations. At the beginning approximations are performed which are usually well justified, but towards the end of the derivation assumptions are made which are usually not satisfied in the edge/SOL region. However, the present scope of this work is the establishment and investigation of a new numerical concept derived in chapter 3. Therefore, these strong approximations are performed in order to obtain a turbulence model which is still self consistent, but as simple as possible and already well established.

2.2.1. Robust simplifications

Simplifications which are usually satisfied very well by many orders of magnitudes in fusion plasmas [5] rely on the fact that the frequencies of interest are much smaller than the characteristic frequencies of the electron motion and the frequencies of light:

$$\omega \ll \omega_{pe}, \Omega_e, ck, \tag{2.12}$$

with $\omega_{pe} = \sqrt{4\pi n_e e^2/m_e}$ the plasma frequency, which describes an oscillation of the electrons with respect to the fixed (due to their inertia) ions and $\Omega_e = eB/(m_e c)$ the electron gyro frequency, which describes the gyro-motion of the electrons around a magnetic field line. Under the assumptions 2.12 the displacement current in Maxwell's equations is neglected and the current density is divergence free. This is called the quasi-neutral approximation, since a direct consequence of $\nabla \cdot \mathbf{J} = 0$ is that for the charge density it holds that $\rho_{ch} = \nabla \cdot \mathbf{E}/4\pi \ll en_e$ and thus $n_e \approx n_i$. Another implication of 2.12 is that the inertial terms in the electron momentum equation 2.4 can be neglected.

The scale of frequencies of interest is introduced in the next section 2.2.2 (expression 2.13) and conditions 2.12 are satisfied for typical edge parameters (see e.g. section 5.1, expressions 5.3) by roughly 5 orders of magnitude.

2.2.2. Drift approximation

In this subsection a brief synopsis of the drift approximation is given, a detailed derivation and discussion can be found e.g. in [57, 58, 59] and references therein. Very close is also a model called reduced MHD [60, 61, 57], which is actually a subset of the more general two fluid drift model and contained in the presented model.

Plasma confinement in tokamaks is largely determined by low frequency drift-wave fluctuations [62, 63]. A significant non-linear interaction among the individual drift waves results in a turbulent vortical motion transporting particles and energy down the gradients. The characteristic temporal scale of these motions is the electron diamagnetic frequency which is low in comparison to the ion cyclotron frequency, and the characteristic perpendicular spatial scale is given by the drift scale, i.e.:

$$\omega \sim \frac{c_s}{L_\perp} \ll \Omega_i, \quad k_\perp^{-1} \sim \rho_s \ll L_\perp, \tag{2.13}$$

where $c_s = \sqrt{T_e/M_i}$ is the sound speed, reflecting that the electrons provide the pressure and the ions inertia. $L_\perp$ is some characteristic background gradient scale length and $\Omega_i = eB/(M_i c)$ the ion cyclotron frequency. The sound radius $\rho_s = c\sqrt{M_i T_e}/(eB)$ has the form of a Larmor radius, but keeps its relevance also in the limit of cold ions $T_i \to 0$ and massless electrons $m_e \to 0$. Due to the strong guiding field the dynamics along the magnetic field lines is much faster than the perpendicular dynamics leading to spatial scales which are strongly elongated along magnetic field lines:

$$k_\perp \gg k_\parallel. \tag{2.14}$$

This property, called flute mode character, implies that the compressional Alfvén wave, propagating in the perpendicular direction, has a much higher frequency than the shear Alfvén wave, propagating in the parallel direction. Usually, the frequency of the compressional Alfvén wave is on a much higher level than the characteristic frequency of the fluid drift motion, whereas the frequency of the shear Alfvén wave is of the same order. Another assumption of the drift approximation is that the plasma pressure should be much lower than the magnetic field pressure. Summarizing, the following ordering is used in the drift approximation:

$$\omega \sim \left[\frac{c_s}{L_\perp},\, k_\parallel v_A \right] \sim \delta \left[\Omega_i, k_\perp v_A \right], \tag{2.15}$$

$$\beta_e := \frac{4\pi p_e}{B^2} \sim \delta, \tag{2.16}$$

where $\delta \ll 1$ is introduced as an ordering parameter. Note that assumption 2.15 automatically implies $\rho_s/L_\perp \sim \delta$. Using again typical edge parameters (section 5.1, expressions 5.3) and estimating $k_\parallel \sim R_0^{-1}$, one obtains $c_s/(L_n k_\parallel v_A) \approx 0.49$, $c_s/(L_n \Omega_i) = \rho_s/L_n \approx 0.014$, $k_\parallel/k_\perp \approx 3.1 \cdot 10^{-4}$ and $\beta_e \approx 1.2 \cdot 10^{-4}$, which is consistent with the ordering 2.15 and 2.16.

Within this framework the perpendicular motion remains dynamically incompressible and a quasi-static force balance is established in the perpendicular direction, i.e. only inertia and the magnetic field inhomogeneity contribute as small corrections to the otherwise incompressible perpendicular motion. The fast dynamical perpendicular oscillations, i.e. the compressional Alfvén waves are not involved in the balancing of the perpendicular forces. The advantage of the drift approximation is that parallel and perpendicular dynamics are separated and the perpendicular dynamics can be expressed with stream functions. Instead of the partial differential equations (PDEs) 2.1-2.7 which evolve vector quantities in time, the system can be reduced to a PDE system which describes the temporal evolution of just scalar functions.

In the quasi-static perpendicular force balance the perpendicular electric field remains electrostatic and the magnetic field perturbations are perpendicular:

$$\mathbf{E}_\perp = -\nabla_\perp \phi, \quad E_\parallel = -\frac{1}{c} \frac{\partial}{\partial t} A_\parallel - \nabla_\parallel \phi. \tag{2.17}$$

To leading order in δ the inertial terms and the stress tensor can be neglected in the perpendicular ion momentum balance. Multiplying eq. 2.3 and eq. 2.4 with $c/(e n_e B^2)\mathbf{B}\times$, yields as leading terms for the perpendicular velocities:

$$\mathbf{v}_{i\perp} = \mathbf{v}_E + \mathbf{v}_{di} = \frac{c}{B^2} \mathbf{B} \times \nabla\phi + \frac{c}{e n_e B^2} \mathbf{B} \times \nabla p_i, \tag{2.18}$$

$$\mathbf{v}_{e\perp} = \mathbf{v}_E + \mathbf{v}_{de} = \frac{c}{B^2} \mathbf{B} \times \nabla\phi - \frac{c}{e n_e B^2} \mathbf{B} \times \nabla p_e. \tag{2.19}$$

The $\mathbf{E} \times \mathbf{B}$ velocity $\mathbf{v}_E$ is equal for both ions and electrons describing a common flow and $\mathbf{v}_{di,de}$ is the ion respectively electron diamagnetic velocity. By inserting the obtained zero order ion

velocities again into the ion momentum equation 2.3, the first order in δ polarisation velocity is obtained:

$$\mathbf{v}_{pol} = \frac{1}{\Omega_i}\mathbf{b} \times \left\{\left[\frac{\partial}{\partial t} + (\mathbf{v}_E + \mathbf{v}_{di} + \mathbf{v}_{pol} + \mathbf{v}_{i\parallel}) \cdot \nabla\right](\mathbf{v}_E + \mathbf{v}_{di}) + \frac{1}{n_e M_i}\nabla \cdot \mathbf{\Pi}_{i0}\right\}, \qquad (2.20)$$

where $\mathbf{\Pi}_{i0}$ denotes that the zeroth order velocities according to eq. 2.18 have to be used in the computation of the ion stress tensor. The stress tensor incorporates a collisionless finite Larmor radius term which cancels the advection with the diamagnetic velocity, i.e. $\nabla \cdot \mathbf{\Pi}_{i0} \sim -n_e M_i \mathbf{v}_{di} \cdot \nabla \mathbf{v}_i$ (diamagnetic cancellation [64, 65, 66]). This reflects the fact that the diamagnetic velocity cannot cause a guiding center drift in a homogeneous magnetic field. It is immediately obvious from expression 2.20 that $|\mathbf{v}_{pol}| / |\mathbf{v}_{i\perp}| \sim \omega/\Omega_i \sim \delta$. However, the polarisation velocity must be kept, since, although the polarisation velocity itself is small compared to the zeroth order velocities, its divergence is not. The only terms contributing to the divergence of the zeroth order flow enter through the background magnetic field gradient, which is small in tokamaks. Finally, it is noted that it seems unusual that the polarisation velocity appears also in the advection of eq. 2.20 , since it is one order lower with respect to $\mathbf{v}_E$, but it must be kept for energy conservation [58].

The net result at this stage is that the originally vector-valued velocities can be replaced in favour of scalar stream functions $\mathbf{v}_i \rightarrow p_i, \phi, v_{i\parallel}$. Analogously, the temporal evolution of the magnetic field can replaced in favour of a scalar potential $\partial \mathbf{B}/\partial t \rightarrow \partial A_\parallel/\partial t$. Obtaining now the reduced Braginskii equations is in principle straight forward, but the resulting expressions are lengthy and the interested reader is referred to [57, 58, 59, 67]. The resulting equation system consists of six partial differential equations for $n_e, \phi, A_\parallel, v_{i\parallel}, T_e, T_i$.

Certain approximations applied up to this point might become questionable in the edge/SOL region: There are e.g. objections that the distribution function in the edge/SOL is not close enough to a Maxwellian, such that a fluid approach is not justified. There are also projects like COGENT [68, 69], TEMPEST [70] and XGC1 [71, 72, 73] which are based on a full-f gyrokinetic model. However, the price of these approaches is the complexity and the computational intensity. Another objection might be that the presence of open field lines causes stronger parallel gradients, such that the flute mode ordering 2.14 breaks down.

Furthermore, a subtle point in the drift approximation is the treatment of finite Larmor radius (FLR) effects which appear somewhat hidden in the ion stress tensor $\mathbf{\Pi}_i$. Such effects are generally treated with a Taylor expansion in $k_\perp \rho_{Li}$ (see e.g. [65]) and the resulting models are only valid for $k_\perp \rho_{Li} \ll 1$. In the cold ion limit, which is taken later, this issue is automatically resolved. FLR effects are treated more naturally with a gyrofluid model where moments of the gyrokinetic equation are evolved in time. In the gyrokinetic approach the drift approximation is performed consistently already at the kinetic level, which is valid also for $k_\perp \rho_{Li} > 1$. As moments are taken of the gyrokinetic equation, FLR effects are treated automatically, in contrast to the normal fluid model where they have to be intricately reintroduced again. The final result is a gyrofluid set of equations (see e.g. [74]). A discussion of these equations would be beyond the scope of this work. Moreover, since in the cold ion limit, which will be applied later anyway, fluid and gyrofluid models agree, it is not necessary here. However, in the future, as the physical model might be extended, a gyrofluid model might be preferable.

Nevertheless, the reduced Braginskii model serves as a robust starting point to investigate transport and turbulence derived by first principles in the edge/SOL region of a tokamak. In fact, similar models are already applied in numerical codes to the edge/SOL [35, 36, 37, 38, 39, 40, 25, 27, 31, 28, 29, 30].

2.2.3. Strong approximations

The reduced Braginskii equations are still difficult to solve, and since the main emphasis of this work is on a new numerical concept and on complex geometry, a simpler model is chosen as a starting point. Therefore, the approximations presented in this section are clearly violated in the edge/SOL region, but simplify the equations significantly.

The reduced Braginskii equations can in principle describe fluctuations of order unity, which are present in the edge/SOL [75, 76]. A great simplification is to assume that the quantities can be split in a fixed background with small gradients denoted with a zero subscript and small fluctuations with strong gradients denoted by a tilde. So for some quantity, e.g. the density, we apply the ordering:

$$\frac{\tilde{n}_e}{n_{e0}} \sim \delta, \quad \nabla \tilde{n}_e \sim \nabla n_{e0}. \tag{2.21}$$

Under this ordering, direct non-linear contributions can be dropped, e.g. $n_e T_e \approx \tilde{n}_e T_{e0} + n_{e0} \tilde{T}_e$. The strong drift ordering also implies that the $\mathbf{E} \times \mathbf{B}$ advection of a perturbed quantity ($\omega \sim \mathbf{v}_E \cdot \nabla \tilde{n}_e \sim \mathbf{v}_E \cdot \nabla n_{e0}$), a quadratic non-linearity, is kept. Neglecting explicitly parallel advection ($k_\parallel c_s \ll \omega$), only the $\mathbf{E} \times \mathbf{B}$ velocity remains in the advective derivative.

$$\frac{d}{dt} = \frac{\partial}{\partial t} + \mathbf{v}_E \cdot \nabla. \tag{2.22}$$

The resulting partially linearised equation system can also be found e.g. in [58, 59].

Furthermore, magnetic induction is neglected, i.e. the dynamics is electrostatic. Magnetic induction is important for spatial scales larger than the skin depth [77]. In the collisionless regime the skin depth is determined by the electron inertia and in the collisional regime by collisions. Both regimes can be summarized in a threshold for β_e [78, 77]:

$$\beta_e \ll (k_\perp \rho_s)^2 \frac{m_e}{M_i} \quad \text{collisionless regime,} \tag{2.23}$$

$$\beta_e \ll (k_\perp \rho_s)^2 \frac{\nu_e}{\omega} \frac{m_e}{M_i} \quad \text{collisional regime.} \tag{2.24}$$

The dependence on $(k_\perp \rho_s)$ suggests that electromagnetic effects can be important for large structures even in the edge/SOL where β_e is usually very small [78]. The electrostatic limit is obtained in the limit $\beta_e \to 0$.

In the derivation of the HW equations further approximations which are applied and not necessarily valid are:

- Cold ions: The ions are assumed to be cold $T_i = 0$. The ion heat equation can be dropped. The ion diamagnetic velocity and the ion stress tensor is zero.

- Isothermal electrons: The electron temperature is assumed to be constant $T_e = const$. The electron heat equation can be dropped.

- No parallel flows: The ion parallel flow is set to zero. The parallel ion momentum equation can be dropped, the parallel current is given by $J_\parallel = -e n_e v_{e\parallel}$.

2.2.4. The equations

Under the approximations discussed in the previous sections, the HW equations can be obtained. The equations were first derived in [79].

The electron continuity equation 2.2 becomes:

$$\left(\frac{\partial}{\partial t} + \mathbf{v}_E \cdot \nabla\right)(n_{e0} + \tilde{n}_e) = -n_e \nabla \cdot \mathbf{v}_E - \nabla \cdot (n_e \mathbf{v}_{de}) - \nabla \cdot \left(n_e v_{e\parallel} \mathbf{b}\right). \tag{2.25}$$

The divergence of the $\mathbf{E} \times \mathbf{B}$ velocity can be written as:

$$\nabla \cdot \mathbf{v}_E = \nabla \cdot \left(\frac{c}{B^2}\mathbf{B} \times \nabla\phi\right) = \left(\nabla \times \frac{c\mathbf{B}}{B^2}\right) \cdot \nabla\phi =: -\mathcal{K}(\phi), \tag{2.26}$$

showing indeed as before mentioned, that the only contribution to the divergence of $\mathbf{v}_E$ is due to the slowly varying inhomogeneity of the magnetic field. $\mathcal{K}$ has been defined as the magnetic curvature operator. Similarly:

$$\nabla \cdot (n_e \mathbf{v}_{de}) = \frac{1}{e}\mathcal{K}(p_e). \tag{2.27}$$

Noting that n_{e0} is time independent the electron continuity equation becomes:

$$\frac{d}{dt}\tilde{n}_e = -\mathbf{v}_E \cdot \nabla n_{e0} + n_{e0}\mathcal{K}(\phi) - \frac{1}{e}\mathcal{K}(p_e) + \frac{1}{e}\nabla \cdot \left(J_\parallel \mathbf{b}\right). \tag{2.28}$$

To obtain now an equation for the electrostatic potential, one could use the ion continuity equation 2.1 where the divergence of the polarisation velocity must be kept or instead make use of the quasi-neutrality condition.

$$0 = \nabla \cdot \mathbf{J} = \nabla \cdot \left(J_\parallel \mathbf{b}\right) + \nabla \cdot (n_i e \mathbf{v}_{i\perp} - n_e e \mathbf{v}_{e\perp}) = \nabla \cdot \left(J_\parallel \mathbf{b}\right) + \nabla \cdot \left[n_e e\left(\mathbf{v}_{pol} - \mathbf{v}_{de}\right)\right], \tag{2.29}$$

where now as stated before the polarisation velocity,

$$\mathbf{v}_{pol} = \frac{1}{\Omega_i}\mathbf{b} \times \frac{d}{dt}\mathbf{v}_E = -\frac{M_i c^2}{eB^2}\frac{d}{dt}\nabla_\perp\phi, \tag{2.30}$$

must be kept under the divergence. $\nabla_\perp = -\mathbf{b} \times \mathbf{b} \times \nabla$ is the perpendicular gradient. Under the strong drift ordering the quasi-neutrality condition takes finally the simple expression:

$$\frac{M_i c^2 n_{e0}}{B^2}\frac{d}{dt}\nabla_\perp^2\phi = -\mathcal{K}(p_e) + \nabla \cdot \left(J_\parallel \mathbf{b}\right), \tag{2.31}$$

which is also called vorticity equation, since $\Omega := |\nabla \times \mathbf{v}_E| \approx c/B \nabla_\perp^2 \phi$ is the vorticity strength.

An expression for the parallel current follows by multiplying the ion momentum equation 2.3 with e/M_i and subtracting the electron momentum equation 2.4 multiplied with e/m_e:

$$R_\parallel = \nabla_\parallel p_e - e n_e \nabla_\parallel \phi, \tag{2.32}$$

where the electron inertia and magnetic induction has been neglected. Eq. 2.32 is Ohm's law. The friction term is given as:

$$R_\parallel = n_e e \eta_\parallel J_\parallel. \tag{2.33}$$

Inserting the parallel current density into the electron continuity equation and the vorticity equation yields two partial differential equations:

$$\frac{d}{dt}\tilde{n}_e + \mathbf{v}_E \cdot \nabla n_{e0} = n_{e0}\mathcal{K}(\phi) - \frac{T_e}{e}\mathcal{K}(\tilde{n}_e) + \frac{T_e n_{e0}}{e^2 \eta_\parallel}\nabla \cdot \left[\left(\frac{1}{n_{e0}}\nabla_\parallel\tilde{n}_e - \nabla_\parallel\frac{e\phi}{T_e}\right)\mathbf{b}\right], \tag{2.34}$$

$$\rho_s^2 n_{e0}\frac{d}{dt}\nabla_\perp^2\frac{e\phi}{T_e} = -\frac{T_e}{e}\mathcal{K}(\tilde{n}_e) + \frac{T_e n_{e0}}{e^2 \eta_\parallel}\nabla \cdot \left[\left(\frac{1}{n_{e0}}\nabla_\parallel\tilde{n}_e - \nabla_\parallel\frac{e\phi}{T_e}\right)\mathbf{b}\right]. \tag{2.35}$$

In contrast to the original equations of [79], curvature terms are included in eqs. 2.34 and 2.35 [80, 81, 82].

In order to normalise the equations, the following dimensionless quantities are defined:

$$\hat{t} := \frac{c_s}{L_\perp} t, \qquad \hat{\mathbf{x}}_\perp := \frac{\mathbf{x}_\perp}{\hat{\rho}_s}, \qquad \hat{\mathbf{x}}_\parallel := \frac{\mathbf{x}_\parallel}{L_\parallel},$$

$$\hat{\mathbf{B}} := \frac{\mathbf{B}}{B_0}, \qquad \hat{n} := \delta^{-1}\frac{\tilde{n}_e}{n_0}, \qquad \hat{\phi} := \delta^{-1}\frac{e\phi}{T_e}, \qquad (2.36)$$

where the perpendicular coordinates are measured with coordinates $\mathbf{x}_\perp$ and the parallel coordinate with $x_\parallel$. n_0 is some reference density and B_0 a reference field strength where also the value for $\hat{\rho}_s = c\sqrt{T_e M_i}/(eB_0)$ is taken. $L_\perp, L_\parallel$ are parameters reflecting perpendicular/parallel scale lengths. In addition a factor of $\delta = \hat{\rho}_s/L_\perp$ was folded into the state variables. The normalized operators become:

$$\hat{\mathbf{v}}_E := \frac{\hat{\mathbf{B}}}{\hat{B}^2} \times \hat{\nabla}\hat{\phi}, \qquad \hat{\mathcal{K}}(f) := -\left(\hat{\nabla} \times \frac{\hat{\mathbf{B}}}{\hat{B}^2}\right) \cdot \hat{\nabla} f. \qquad (2.37)$$

Moreover, the local limit is applied, i.e. the background density is assumed to be constant ($n_{e0}(\mathbf{r}) = n_0$) if it appears in front of any operator as coefficient, but in the advection the background density gradient is assumed to be finite and to have the following form:

$$\frac{\hat{\nabla} n_{e0}}{n_0} = -w_n \hat{\nabla}\rho \qquad (2.38)$$

where $\rho(\mathbf{x}_\perp)$ is some flux surface label and w_n a parameter which controls the strength of the background density gradient. The normalized HW equations are finally:

$$\frac{d}{d\hat{t}}\hat{n} = \delta^{-1} w_n \hat{\mathbf{v}}_E \cdot \hat{\nabla}\rho(\hat{\mathbf{x}}_\perp) + \delta^{-1}\hat{\mathcal{K}}(\hat{\phi} - \hat{n}) + D\hat{\nabla} \cdot \left[\hat{\nabla}_\parallel\left(\hat{n} - \hat{\phi}\right)\hat{\mathbf{b}}\right] + \nu_n \hat{\mathcal{H}}^k(\hat{n}), \quad (2.39)$$

$$\frac{1}{\hat{B}^2}\frac{d}{d\hat{t}}\hat{\nabla}_\perp^2\hat{\phi} = -\delta^{-1}\hat{\mathcal{K}}(\hat{n}) + D\hat{\nabla} \cdot \left[\hat{\nabla}_\parallel\left(\hat{n} - \hat{\phi}\right)\hat{\mathbf{b}}\right] + \nu_\phi \hat{\mathcal{H}}^k(\hat{\nabla}_\perp^2\hat{\phi}), \qquad (2.40)$$

with:

$$D := \frac{c_s/L_\perp}{0.51\nu_e}\frac{M_i}{m_e}\frac{L_\perp^2}{L_\parallel^2} \qquad (2.41)$$

as a parameter in the model. Dissipation terms $\hat{\mathcal{H}}^k$ are added to the equations. These terms model perpendicular viscosity which is needed to avoid a pile up of the spectrum at high $\hat{k}_\perp$ due to the direct cascade process (see section 1.3). However, since the real perpendicular viscosity is very small and would require very fine grids to be resolved, hyperdiffusion terms are used.

$$\hat{\mathcal{H}}^k(f) = (-1)^{k-1}\hat{\nabla}_\perp^{2k} f, \qquad (2.42)$$

with $k = 1, 2, \ldots$. These terms act as a damping only at high $\hat{k}_\perp$, but leave the intermediate and low $\hat{k}_\perp$ range practically unaffected.

If not stated differently, the hats above the quantities and operators are omitted in the following.

Since the HW equations constitute one of the simplest plasma turbulence models, it has often been analysed and numerically been solved[1]: A comprehensive analysis of HW in a 2D slab

---

[1]It is again not claimed that the following list of references is complete.

geometry with a constant parallel wave vector $k_\| = const$ can be found e.g. in [83, 84]. A modification to allow the development of zonal flows in 2D is presented in [85]. 3D drift wave turbulence without curvature effects, i.e. $\mathcal{K} = 0$ is treated e.g. in [86, 87, 88, 89, 90, 91]. 3D drift-resistive-ballooning turbulence, i.e. with $\mathcal{K} \neq 0$ is investigated in [80, 81, 82].

2.3. Linear dynamics

The main ($\mathcal{K} = 0$) linear modes of HW are called drift waves and a physical picture of these are given e.g. in [59, 63] and are discussed here briefly. The curvature terms $\mathcal{K} \neq 0$ gives rise to modes which are unstable if the pressure gradient is directed along the magnetic field gradient.

2.3.1. Drift waves

To illustrate the dynamics described by HW, a slab geometry with a uniform magnetic field $\mathbf{B} = B_0 \mathbf{e}_z$ is considered. Drift planes perpendicular to the magnetic field are spanned by the coordinates x, y. A constant density gradient pointing in the negative $x-$direction is assumed, i.e. $w_n \nabla \rho = -\rho_s/L_n \mathbf{e}_x$. Thus x can be identified with a radial coordinate in a tokamak and y with a poloidal coordinate. The setup is illustrated in fig. 2.1a.
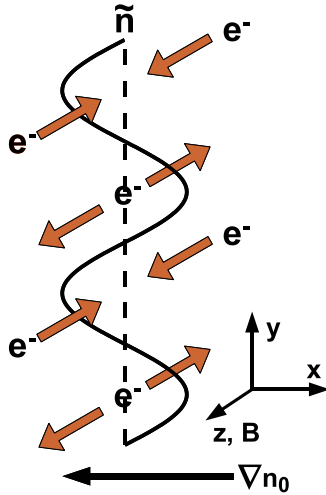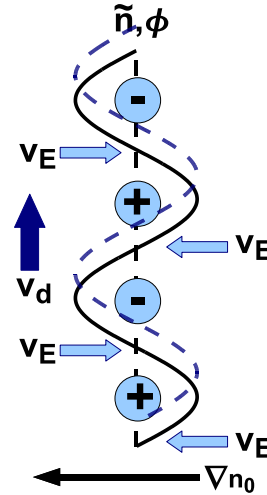
Figure 2.1.: Basic picture of a drift wave in slab model: a) A sinusoidal pressure perturbation pushes or pulls the electrons along the field lines until parallel force balance is established ($n = \phi$, normalized). b) Due to charge separation $\mathbf{E} \times \mathbf{B}$ drifts arise in the perpendicular plane. Together with the background density gradient this causes the whole structure to move with the diamagnetic velocity in the poloidal $y-$direction. Quasi-neutrality is ensured at all times by the ion polarization drift.

Consider that on some drift plane a sinusoidal pressure perturbation arises. Due to their small inertia the electrons move rapidly away from or towards the pressure perturbation along magnetic field lines. In the same process a parallel electric field is built up until parallel force

balance is established. In the adiabatic limit the motion of the electrons along the magnetic field lines is unhindered and the pressure obeys a (linearised) Boltzmann distribution:

$$\frac{\tilde{n}_e}{n_{e0}} = \frac{e\phi}{T_e} \quad \text{(unnormalized)}, \tag{2.43}$$

where due to the isothermal approximation, pressure and density can be used interchangeably. The electric field gives rise to an $\mathbf{E} \times \mathbf{B}$ drift perpendicular to the electric and magnetic field, which advects both ions and electrons equally. Simultaneously, the ion polarisation drift ensures quasi-neutrality at all times. Under the background density gradient the $\mathbf{E} \times \mathbf{B}$ advection is larger from the high density region than from the low density region, causing the whole structure to propagate in the poloidal $y-$direction (see fig. 2.1b).

To describe the drift wave phenomenon quantitatively the linearised version of eqs. 2.39 and 2.40 are used, curvature and viscosity terms are neglected and a uniform background density is assumed ($L_\perp = L_n$).

$$\frac{\partial}{\partial t} n = -\frac{\partial}{\partial y}\phi + D\frac{\partial^2}{\partial z^2}(n - \phi), \tag{2.44}$$

$$\frac{\partial}{\partial t}\nabla^2_\perp \phi = D\frac{\partial^2}{\partial z^2}(n - \phi). \tag{2.45}$$

The adiabatic limit can be obtained by letting $D \to \infty$, i.e. the electrons move unhindered along magnetic field lines which ties the potential and the density perturbation together ($n = \phi$). Finally, the system can be described by a single equation:

$$\left(1 + \nabla^2_\perp\right)\frac{\partial}{\partial t}\phi + \frac{\partial}{\partial y}\phi = 0. \tag{2.46}$$

The solution to this equation is a purely oscillating wave with a frequency of:

$$\omega = \frac{k_y}{1 + k^2_\perp}, \tag{2.47}$$

propagating in the y direction. Note that due to the ion polarization drift a dispersive character appears as a correction to the diamagnetic drift velocity[2] for small scales.

An instability, i.e. a growing drift wave, develops if the response of the electrons to the density perturbation is not instantaneous but hindered by some effect (in the HW model this is collisions, finite D). This causes a phase shift of the potential behind the density perturbation $n \sim \phi \exp(-i\alpha)$ and the shifted $\mathbf{E} \times \mathbf{B}$ advection acts now as to enhance the original pressure perturbation. To analyse this in a simple model quantitatively, we assume $\alpha \ll 1$ known and fixed. The temporal evolution of the electrostatic potential can be written with a single equation:

$$\left(1 - i\alpha - \nabla^2_\perp\right)\frac{\partial}{\partial t}\phi + \frac{\partial}{\partial y}\phi = 0. \tag{2.48}$$

The now complex frequency is:

$$\omega = \frac{k_y}{1 + k^2_\perp} + i\frac{\alpha k_y}{\left(1 + k^2_\perp\right)^2}. \tag{2.49}$$

---

[2]In unnormalized units the diamagnetic drift velocity is: $v_d = cT_e/(eBL_n)$.

In order to obtain a self consistent description, the dispersion relation of the complete system of equations 2.44 and 2.45 is considered. The solution has two roots, one which corresponds to a strongly damped mode and the other one describing the unstable drift wave (see e.g. [83, 84]):

$$\omega = \omega_R + i\gamma, \tag{2.50}$$

$$\text{with:} \quad \omega_R = \frac{\lambda}{2}\sqrt{\frac{B-1}{2}}, \quad \gamma = -\frac{\lambda}{2}\left[1 - \sqrt{\frac{B+1}{2}}\right],$$

$$\lambda = \frac{Dk_z^2(1+k_\perp^2)}{k_\perp^2}, \quad B = \sqrt{1 + \frac{16\left(Dk_z^2 k_y\right)^2}{(k_\perp\lambda)^4}}.$$

The growth rate in dependence of wave vectors for $D = 1$ is illustrated in fig. 2.2a,b. The maximum growth rate $\gamma_{max} \approx 0.15$ for $D = 1$ is roughly at $k_x = 0, k_y = 1, k_z = 0.5$. It can be seen that drift waves favour small radial mode numbers $k_x = 0$ and poloidal mode numbers of the order of $k_y = 1$.

a)   b)
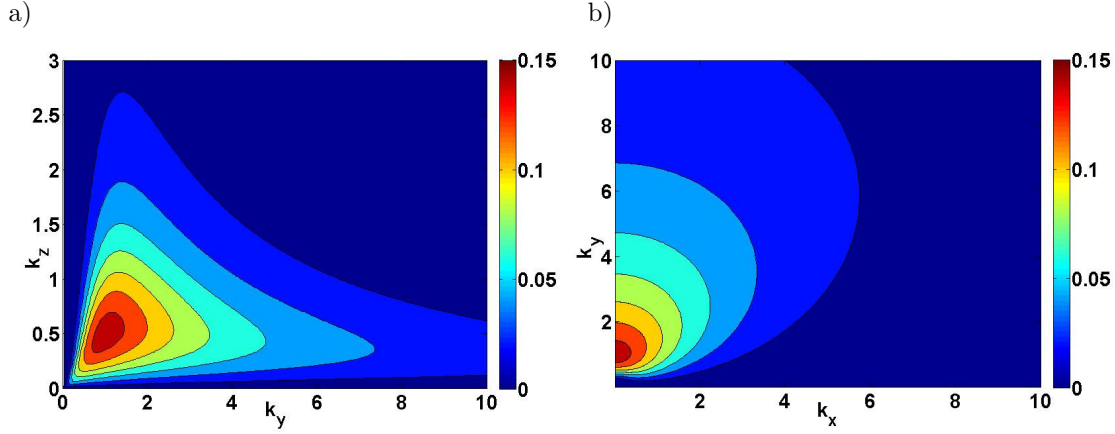
Figure 2.2.: Growth rate γ of drift wave instability in dependence of a) k_y and k_z for fixed $k_x = 0$, $D = 1$, b) in dependence of k_x and k_y for fixed $k_z = 0.5$ and $D = 1$.

2.3.2. Ideal interchange instability

In the previous section the effects of magnetic field inhomogeneities have been neglected. In this section a complementary view completes the linear analysis of the target model. We neglect collisions along magnetic field lines, so only the $k_\parallel = 0$ mode is considered, but the effects of the magnetic field inhomogeneity and background density profile is included. We assume again a slab model where the magnetic field is given as[3] $\mathbf{B} = B(x)\mathbf{e}_z$ and $\partial \log(B(x))/\partial x = -\rho_s/L_B$ and the density profile as $w_n\nabla\rho = -\rho_s/L_n\mathbf{e}_x$. Under this assumption the linearised equation system of 2.39 and 2.40 becomes:

$$\frac{\partial}{\partial t}n = -\omega_n\frac{\partial}{\partial y}\phi + \omega_B\frac{\partial}{\partial y}(\phi - n), \tag{2.51}$$

$$\frac{\partial}{\partial t}\nabla_\perp^2\phi = -\omega_B\frac{\partial}{\partial y}n, \tag{2.52}$$

---

[3]We apply again the local approximation, i.e. $B(x) = 1$ is constant but $\partial B/\partial x \neq 0$.

with $\omega_n = L_\perp/L_n$ and $\omega_B = L_\perp/L_B$ and $L_\perp$ is left as a normalisation parameter. The dispersion relation of this equation system is:

$$\omega^2 - \omega \omega_B k_y + \omega_B (\omega_n - \omega_B) \frac{k_y^2}{k_\perp^2} = 0. \tag{2.53}$$

To get more insight, we consider the large scale limit $k_\perp \ll 1$, but $k_y^2/k_\perp^2$ finite.

$$\omega^2 = \frac{k_y^2}{k_\perp^2} \omega_B (\omega_B - \omega_n). \tag{2.54}$$

Thus this mode is a growing mode if $\omega_B < \omega_n$ and $\omega_B > 0$. For an instability to be present the first condition implies that the gradient of the magnetic field must be weaker than the background density gradient. This is usually true, because else the low β assumption of the equilibrium would break down [59]. The second condition implies that an instability is present if the magnetic field gradient is aligned with the pressure gradient. This is usually the case for the outboard side of tokamaks. On the inboard side, where the magnetic field gradient is anti-parallel with respect to the density gradient, the interchange mode encounters stabilizing effects.

Following a field line in a tokamak with a finite safety factor q, the contributions from the stabilizing inboard region and the destabilizing outboard region alternate. Hence, the average curvature on a flux surface has to be considered and for $q > 1$ the interchange mode is stable [10]. However, perturbations with finite $k_\parallel$ localized on the outboard side of a tokamak, called ballooning modes, feel the fully destabilizing contribution of the curvature. This will be discussed in section 5.3.2 when the full 3D system is considered.

2.4. Fluctuation free energy theorem

In this section the energy theorem of the HW model is derived. Since the model describes fluctuations on a fixed background, the important quantity is the fluctuation free energy, which is conserved by the nonlinear terms. In contrast to global energy (see e.g. [58, 57]) it is not composed linearly from state variables (like p_0) but quadratically from fluctuation state variables ($\tilde{p}$). Background gradients appear as sources, driving the fluctuation free energy and dissipation as sinks. This is contrary to global energy which is neither created nor destroyed but just transferred, e.g. dissipation acts just as a channel from ordered motion to random motion, i.e. thermal energy [59].

The fluctuation free energy E is split into a thermal part E_n and a kinetic part E_v and is for the target model of eq. 2.39 and 2.40 (see e.g. [79, 59]):

$$E = E_n + E_v = \frac{1}{V} \int_V dV \left[\frac{n^2}{2} + \frac{\mathbf{v}_E^2}{2} \right] = \frac{1}{2V} \int_V dV \left[n^2 + \frac{1}{B^2} (\nabla_\perp \phi)^2 \right]. \tag{2.55}$$

The temporal change of the thermal part is to leading order in δ given by:

$$\frac{d}{dt} E_n = \frac{1}{V} \int_V dV \left[n \frac{\partial}{\partial t} n \right]$$

$$\approx \frac{1}{V} \int_V dV \left\{ \delta^{-1} w_n n \mathbf{v}_E \cdot \nabla \rho + \delta^{-1} n \mathcal{K}(\phi) + D n \nabla \cdot \left[\nabla_\parallel (n - \phi) \mathbf{b} \right] + \nu_n n \mathcal{H}(n) + \nabla \cdot [\cdots] \right\}. \tag{2.56}$$

Terms under the total divergence describe transport effects through the boundaries which vanish if the domain is assumed to be periodic or the quantities are assumed to be zero at the boundaries. The temporal change of the kinetic part is given as:

$$\frac{d}{dt}E_v = \frac{1}{V}\int\limits_V dV \, \frac{1}{2B^2}\frac{\partial}{\partial t}\left(\nabla_\perp \phi\right)^2 \approx \frac{1}{V}\int\limits_V dV \left\{\phi\frac{\partial}{\partial t}\left[-\frac{1}{B^2}\nabla_\perp^2\phi\right] + \nabla\cdot[\cdots]\right\}$$

$$\approx \frac{1}{V}\int\limits_V dV \left\{-\delta^{-1}n\mathcal{K}(\phi) - D\phi\nabla\cdot\left[\nabla_\parallel(n-\phi)\mathbf{b}\right] - \nu_\phi\phi\mathcal{H}(\nabla_\perp^2\phi)\right\}. \tag{2.57}$$

The complete fluctuation free energy theorem is:

$$\frac{d}{dt}E = \frac{d}{dt}(E_n + E_v) = Q + D_\parallel + D_\perp, \tag{2.58}$$

$$\text{with:} \quad Q := \frac{1}{V}\int\limits_V dV \left[\delta^{-1}w_n n\mathbf{v}_E\cdot\nabla\rho\right],$$

$$D_\parallel := \frac{1}{V}\int\limits_V dV \left\{-D\left[\nabla_\parallel(n-\phi)\right]^2\right\},$$

$$D_\perp := \frac{1}{V}\int\limits_V dV \left[\nu_n n\mathcal{H}(n) - \nu_\phi\phi\mathcal{H}(\nabla_\perp^2\phi)\right].$$

The only source for the total fluctuation free energy is the background density gradient appearing in Q. Dissipation of the parallel current $D_\parallel$ and small scale viscosity $D_\perp$ can be identified as sinks. The dissipated energy is simply lost in the model due to the isothermal approximation. The background magnetic field does not act as a source, since both terms $\delta^{-1}n\mathcal{K}(\phi)$ cancel in eq. 2.56 and 2.57 but give a transfer channel between the kinetic and the thermal part of the fluctuation free energy.

2.5. Turbulence in a box

Taking into account the non-linear $\mathbf{E}\times\mathbf{B}$ advection leads to turbulent dynamics. HW constitutes a self consistent model for turbulence. The background gradients inject via the discussed instabilities fluctuation free energy at a spatial scale of $\gtrsim \rho_s$. The quadratic non-linear $\mathbf{E}\times\mathbf{B}$ advections redistribute this energy via three wave coupling, i.e. single Fourier components $\mathbf{k}_i$ interact with each other satisfying $\mathbf{k}_1 + \mathbf{k}_2 + \mathbf{k}_3 = 0$ [59, 21]. The parallel dissipation of the current and hyperviscosity at small scales constitute energy dissipation mechanisms. Due to the vast possibility of interactions between different modes the system looses very quickly memory of its initial state and makes the dynamics unpredictable. However, if the interactions between the modes are in statistical equilibrium the system is in a statistically stationary state called saturation. In this state characteristic quantities fluctuate around a constant mean and statistical diagnostic tools can be used to describe the system. Based on the ergodic hypothesis ensemble averages can be computed with time averages [19]. Therefore, we introduce for some quantity f:

$$\langle f\rangle_e = \lim_{t\to\infty}\frac{1}{T}\int\limits_0^T dt \, f, \quad \delta f = \lim_{t\to\infty}\sqrt{\frac{1}{T}\int\limits_0^T dt \, (f - \langle f\rangle_E)^2}, \tag{2.59}$$

23

where $\langle f \rangle_e$ denotes the ensemble average of f. From the computational point of view only a finite time frame over the saturated state can be taken, of course, which should cover many correlation times.

In order to predict the performance of a fusion reactor one is mainly interested in radial fluxes. In HW only the particle flux is of interest as the convective energy flux is trivially connected to the particle flux in the isothermal approximation. The radial particle flux density is:

$$\Gamma := n\mathbf{v}_E \cdot \mathbf{e}_\rho, \tag{2.60}$$

where $\mathbf{e}_\rho$ is a unit vector which is perpendicular to flux surfaces, pointing radially outwards. The particle flux through a flux surface Γ_ρ can be obtained by integrating Γ over the flux surface and the averaged particle flux density Γ_V is defined by averaging Γ over the whole simulation domain. To predict such quantities for future reactors, numerical simulations are essential, since no general analytic solution to the relevant non-linear equations is available.

In this section numerical simulations of the HW model in slab geometry are presented, where a simplified model for the parallel dissipation was used. Although the model is unsatisfactory and has already often been analysed and discussed in literature [79, 83, 84, 85, 92], it is presented here because of two reasons: Firstly, it serves as a basis for interpretation of the results of later chapters. Secondly, the simulations were performed with the newly developed code GRILLIX and the implementation of the perpendicular dynamics can be benchmarked against several other codes. Details on the implementation of GRILLIX are described in chapter 4.

We assume again a slab model with a uniform magnetic field pointing in the z-direction and a uniform background density gradient pointing in the negative x-direction. y is identified with a poloidal direction. It is assumed that there is only one single parallel mode $k_z = const$ present. Thus the simplified two-dimensional HW model is given by:

$$\frac{\partial}{\partial t}n + [\phi, n]_{x,y} = -\frac{\partial}{\partial y}\phi + \mathcal{C}\left(\phi - n\right) + \nu_n \nabla_\perp^6 n, \tag{2.61}$$

$$\frac{\partial}{\partial t}\nabla_\perp^2 \phi + \left[\phi, \nabla_\perp^2 \phi\right]_{x,y} = \mathcal{C}\left(\phi - n\right) + \nu_\phi \nabla_\perp^6 \left(\nabla_\perp^2 \phi\right), \tag{2.62}$$

where

$$L_\perp = L_n, \quad \nabla_\perp^2 = \frac{\partial^2}{\partial x^2} + \frac{\partial^2}{\partial y^2}, \quad \text{and:} \ [f,g]_{x,y} := \frac{\partial f}{\partial x}\frac{\partial g}{\partial y} - \frac{\partial f}{\partial y}\frac{\partial g}{\partial x}.$$

The constant $\mathcal{C} = Dk_z^2$ is called the adiabaticity parameter. In the hydrodynamic limit, $\mathcal{C} \ll 1$, the system reduces to the 2D incompressible Navier-Stokes equations with the density as a passively advected quantity. In this limit the flow part obeys a dual cascade distributing energy towards larger scales, whereas the density obeys a direct cascade distributing energy towards smaller scales. Ultimately, the flow and the density separate from each other [21] (see also section 1.3). In the adiabatic regime, $\mathcal{C} \gg 1$, n remains closely tied to ϕ and the system is reduced to the Hasegawa-Mima equation [93].

In fig. 2.3 snapshots of a typical simulation with an intermediate value of $\mathcal{C} = 1$ are shown. The simulation was initialized with a small random noise (≤ 0.1) in the density perturbation. After the hyperviscosity has smoothed the initial random noise, radially elongated drift waves develop and propagate in the y direction. As soon as the amplitudes have reached a high enough level, eddies begin to tear apart due to non-linear interaction and finally a saturated turbulent state is reached. It is already apparent that the dynamics is adiabatic on a large scale ($n \sim \phi$).

In fig. 2.4a time trace diagnostics of this simulation is plotted. All quantities grow exponentially from a small amplitude until the growth is stopped non-linearly at roughly $t = 110$. After a short
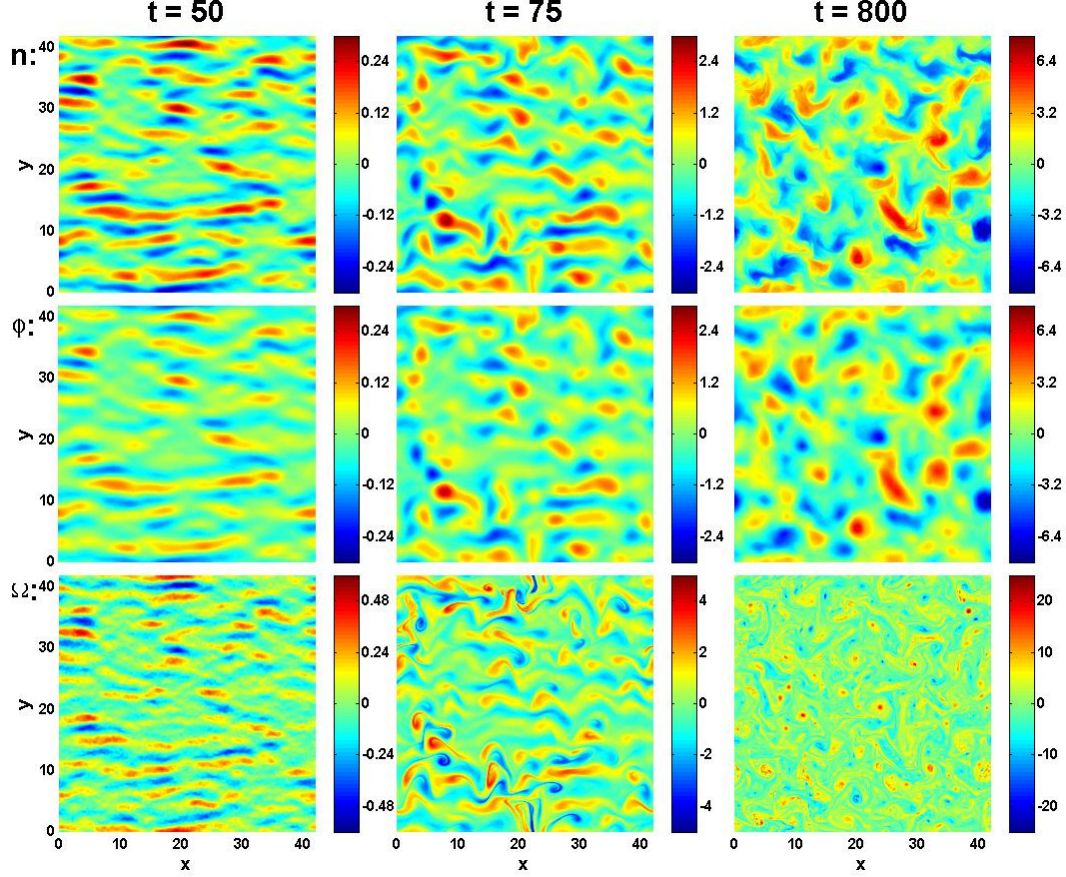
Figure 2.3.: Snapshots of a simulation in the linear phase ($t = 50$, left column) where drift waves are apparent, at the onset of the turbulence ($t = 75$, middle column) where eddy mitosis can be seen and in the saturated state ($t = 800$, right column). Shown is the density perturbation (upper row), potential (middle row) and vorticity (lower row). Parameter of the simulation are: $\mathcal{C} = 1$, $L_x = L_y = 41.89$ with $nx \times ny = 512 \times 512$ grid points, $\nu_n = \nu_\Omega = 1.0 \cdot 10^{-8}$. For units see eqs. 2.36. Time steps varied between $\Delta t = 2.0 \cdot 10^{-2}$(linear phase) and $\Delta t = 2.432 \cdot 10^{-3}$(saturated phase).

transition phase all quantities saturate and fluctuate around a mean value. As can be also seen in fig. 2.4b the temporal change of the fluctuation free energy in the saturated state is zero on average and balanced by the transport[4], the parallel and perpendicular dissipation. It is also obvious that the main dissipation mechanism in this case is the parallel dissipation.
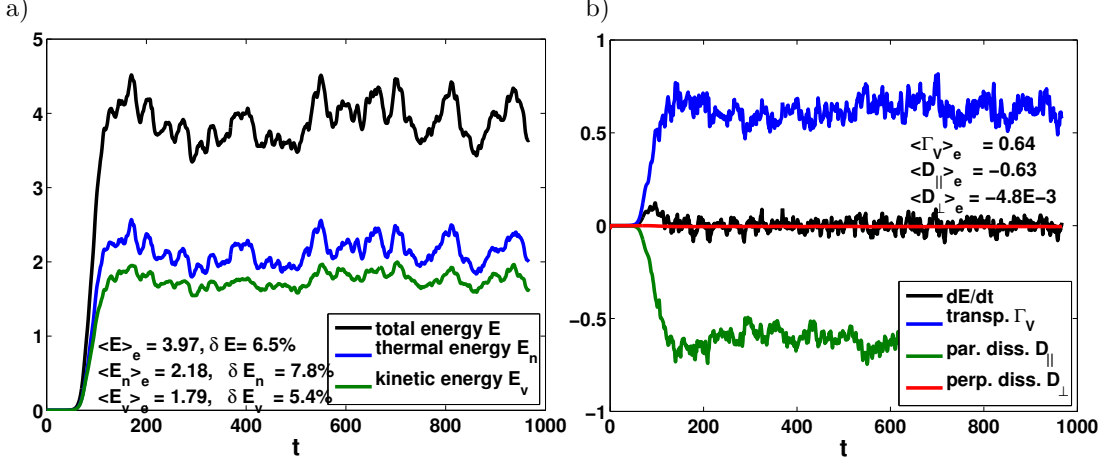
Figure 2.4.: Time trace diagnostics of simulation described in fig. 2.3. a) Total fluctuation free energy, thermal and kinetic parts. b) dE/dt, sources and sinks. The average values are obtained by temporal average between $t = 500$ and $t = 900$.

To gain more insight into the spatial structure a spectral analysis of the saturated state is performed. Since x shall mimic a radial coordinate and y a periodic poloidal coordinate, a spectral analysis along y is most natural, i.e. $f_{k_y}(x)$. However, since also in x-direction periodic boundary conditions are used and each radial position is equal, it makes sense to define only for this section also radially averaged spectra and angle averaged spectra:

$$f_{k_y} := \frac{1}{L_x} \int_0^{L_x} dx \, f_{k_y}(x), \tag{2.63}$$

$$f_k := \sum_k f_{k_x, k_y}, \quad k - \frac{k_0}{2} < \sqrt{k_x^2 + k_y^2} < k + \frac{k_0}{2}, \tag{2.64}$$

where $k_0 = 2\pi/L$ is the smallest wave number[5] allowed by the system. Besides the spectral distribution of the amplitudes itself, it is also interesting to see in which scales the fluctuation free energy of the system is distributed and at which scale the transport takes place. Therefore

---

[4]For the 2D HW model under the normalisation $L_\perp = L_n$ the rate at which fluctuation free energy is injected into the system due to the background gradient (see eq. 2.59) is equal to the transport, i.e. $Q = \Gamma_V$.

[5]Only cases for which $L := L_x = L_y$ are considered

we introduce:

$$E^n_{k_x,k_y} := \frac{1}{2} \left| n_{k_x,k_y} \right|^2, \tag{2.65}$$

$$E^v_{k_x,k_y} := \frac{1}{2}(k_x^2 + k_y^2) \left| \phi_{k_x,k_y} \right|^2, \tag{2.66}$$

$$E_{k_x,k_y} := E^n_{k_x,k_y} + E^v_{k_x,k_y}, \tag{2.67}$$

$$\Gamma_{k_x,k_y} := \left| n_{k_x,k_y} i k_y \phi^*_{k_x,k_y} \right|. \tag{2.68}$$

In fig. 2.5 the spectra of various quantities are plotted in dependence of the poloidal wave vector k_y (fig. 2.5a) and the angular wave vector k (fig. 2.5b,c). From the angular spectra can be seen that on large scales ($k < 1$) the dynamics is adiabatic, i.e. the density is tied to the potential and on smaller scales ($k > 1$) the dynamics becomes more and more nonadiabatic. The amplitudes and energy density peak around a value of $k \approx 1$, where the energy injection takes place and decays from there towards both directions. Towards high k an inertial range with power law like dependencies can be observed ($E_{k_x,k_y} \propto k^{-3.0}$). At the higher end of the k spectrum a cut off is present where the fluctuation free energy is dissipated due to hyperdiffusion. Since for the transport the cross phase between n and ϕ is important, the transport is comparably low in the adiabatic regime and peaks around $k \approx 1$ where n and ϕ begin to decouple. Comparing the angular and y amplitude spectra, an anisotropy for low k values can be observed. Since the linear growth rate is also anisotropic (see fig. 2.2), this behaviour reflects that the low k end is strongly influenced by linear dynamics, whereas the dynamics in the inertial range is isotropic as the non-linearity acts also isotropically [84].
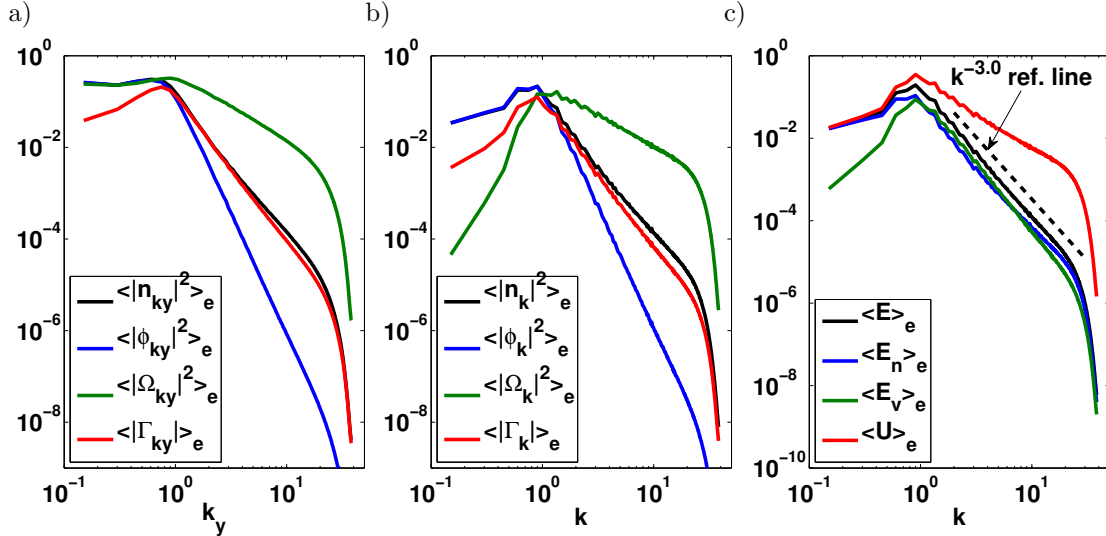
Figure 2.5.: Spectral diagnostics averaged between $t = 500$ and $t = 900$. a) y-amplitude spectra, b) angular amplitude spectra, c) angular energy spectra, total fluctuation free energy (black), thermal part (blue), kinetic part (green), enstrophy (red). A reference line (dotted black) indicates a $k^{-3.0}$ power law.

The 2D HW turbulence model can be run in the framework of GRILLIX and compared against results of other codes. Compared was against the code HW [94], which was available to me, and against [84, 88, 95]. The result of the benchmark is listed in table 2.1. Overall the agreement is

quantity	GRILLIX	HW [94]	Camargo [84]	Zeiler [88]	Numata [95]
$\mathcal{C} = 1$:					
$\langle E \rangle_e$	3.97	3.82	4.4	6.1	n.a.
$\delta E / \langle E \rangle_e$	0.065	0.068	0.16	0.082	n.a.
$\langle \Gamma \rangle_e$	0.64	0.61	0.73	0.8	n.a.
exponent	-3.0	-3.0	-2.9	n.a.	$-3.0(\mathcal{C} = 0.7)$
$\mathcal{C} = 0.1$:					
$\langle E \rangle_e$	13.43	13.33	17.9	23.8	n.a.
$\delta E / \langle E \rangle_e$	0.12	0.10	0.16	0.20	n.a.
$\langle \Gamma \rangle_e$	1.54	1.52	2.1	2.9	n.a.
exponent	-1.6	-1.6	-1.6	n.a.	-2.0
$\mathcal{C} = 5$:					
$\langle E \rangle_e$	7.18	6.91	8.3	12.6	n.a.
$\delta E / \langle E \rangle_e$	0.04	0.09	0.08	0.06	n.a.
$\langle \Gamma \rangle_e$	0.12	0.13	0.13	0.18	n.a.
exponent	-3.5	-3.5	-3.5	n.a.	$-3.9(\mathcal{C} = 10)$

Table 2.1.: Saturated values and power exponent in dependence on adiabaticity parameter, obtained with different codes (n.a. = not available).

pretty well. The closest agreement is between GRILLIX and HW, which uses similar numerical techniques. For larger values of $\mathcal{C}$ the results agree very well with Camargo's. The reason for the deviance to Camargo at $\mathcal{C} = 0.1$ might originate from the different numerical methods. Camargo uses a dealiased pseudospectral algorithm which could be better suited to resolve also the small scales.

Chapter 3.

Field line map

In the last chapter the target model HW has been derived and has already been discussed in a simple geometry, where the equations have been solved numerically for a single parallel mode $k_\parallel = const$. In this chapter the discretisation of the parallel diffusion operator arising in eqs. 2.39 and 2.40 is presented. The main requirements of the developed numerical scheme are: (1) it shall be able to treat rather general geometries with open and closed field lines present simultaneously, e.g. a diverted geometry with an X-point, and (2) it shall exploit the flute mode character ($k_\parallel \ll k_\perp$) via an appropriate anisotropic grid resolution to lower the computational costs. The main idea of the approach is to use a grid consisting of few poloidal planes and a Cartesian grid within each poloidal plane. The strong toroidal field allows one to represent perpendicular operators via a stencil within a poloidal plane. Parallel operators are discretised with a field line map. From each grid point a field line tracing towards neighbouring planes is performed and the value at the penetration points is obtained via interpolation. The parallel operators are discretised with the interpolated values. Due to the flute mode character a few poloidal planes already suffice to represent the dynamics well. Parts of this chapter have been published [96].

3.1. Field and flux aligned coordinates

Field aligned and flux aligned coordinates are essential tools for the plasma physics community. Therefore, a short overview over this topic is given here and for a general introduction the reader is referred to [97]. Such coordinates have many advantages, especially in the closed field line region of tokamaks, however, close to the separatrix they reach limits.

Any magnetic field arising from an axisymmetric ideal MHD equilibrium can be written as [97]:

$$\mathbf{B} = I(\Psi)\nabla\varphi + \nabla\Psi \times \nabla\varphi, \tag{3.1}$$

where φ is the toroidal angle and $\Psi(R, Z)$ is the poloidal flux function, a solution to the Grad-Shafranov-Schlüter (GSS) equation [98, 99]:

$$\Delta^*\Psi + I\frac{\partial I}{\partial \Psi} = 4\pi R^2 \frac{\partial p}{\partial \Psi}, \quad \text{with} \quad \Delta^* := R^2\nabla\cdot\left(\frac{1}{R^2}\nabla\Psi\right). \tag{3.2}$$

$I(\Psi)$ is proportional to the poloidal current through the surface enclosed by a flux surface and $p(\Psi)$ is the plasma pressure, which is constant on flux surfaces (see fig. 3.1a). The current and magnetic field lines run on flux surfaces.

For the moment we assume that the flux surfaces are toroidally nested. If an X-point is present, this is obviously not true and we come back to this point later. We can find an elementary toroidal coordinate system $\rho(\Psi), \theta_e, \varphi$, where ρ is any flux surface label and θ_e any angular

poloidal coordinate. The main goal is to find a bijective transformation to a coordinate system (ρ, ξ, ζ) in which the magnetic field lines are aligned along a coordinate and $\mathbf{B}$ can be written in Clebsch form [100], such that the parallel derivative becomes a derivative with respect to only one coordinate:

$$\mathbf{B} \propto \nabla\rho \times \nabla\xi \quad \rightarrow \quad \nabla_\parallel \propto \frac{\partial}{\partial\zeta}. \tag{3.3}$$

An intermediate step is to find a transformation to a coordinate system in which the field lines appear straight if rolled out on a flux surface. Due to the freedom to transform both the toroidal and the poloidal coordinate, there is no unique straight field line coordinate system $(\rho, \theta_s, \varphi_s)$ (e.g. Symmetry or Pest [97], Hamada [101], Boozer [102]), but all off them must satisfy [97]:

$$\frac{d\theta_s}{d\varphi_s} = \frac{1}{q(\rho)}, \quad \text{where} \quad q(\rho) = \frac{1}{2\pi} \int\limits_0^{2\pi} d\theta_e \frac{\mathbf{B} \cdot \nabla\varphi}{\mathbf{B} \cdot \nabla\theta_e}. \tag{3.4}$$

The safety factor q gives the number of toroidal turns as one advances along a magnetic field line one poloidal turn. In general, the obtained straight field line coordinate system is not orthogonal any more.

A field aligned coordinate system can now be obtained in two ways. One can choose the poloidal angle as the parallel angle:

$$\zeta = \theta_s, \quad \xi = \varphi_s - q\theta_s, \tag{3.5}$$

or the toroidal angle as the parallel angle:

$$\zeta = \varphi_s, \quad \xi = \theta_s - \frac{1}{q}\varphi_s. \tag{3.6}$$

The first choice 3.5 allows a truncation of the domain in the toroidal direction, i.e. not the whole flux surface has to be kept but only a fraction resulting in a flux tube which is representative for the whole flux surface. The fact that the domain can be truncated and a comparatively low resolution in the poloidal-parallel direction ζ can be used, results in a huge computational gain. However, the size of the flux tube must be chosen carefully. Furthermore, for finite shear $(dq/d\rho \neq 0)$ the flux tube becomes twisted as one follows the parallel coordinate and the parallel boundaries have to be treated with care [103, 104]. The twisting along the parallel direction also poses numerical problems, since it can result in a strong deformation of the grid, i.e. a strong variation of the metric coefficients along the ζ direction. The non-orthogonal deformation can be cured with the shifted-metric technique [105]. The topic of orthogonal deformation is treated in [106]. The grid deformation becomes especially critical close to the separatrix.

The second choice 3.6 is motivated by the fact that transformation 3.5 is ill defined at the separatrix. Since at the X-point the poloidal magnetic field vanishes, the safety factor diverges at the separatrix. Close to the separatrix the safety factor runs like [10]:

$$q(\Psi) \propto -\ln(\Psi_s - \Psi), \tag{3.7}$$

where Ψ_s is the poloidal magnetic flux at the separatrix. Since $q \to \infty$ at the separatrix, the transformation 3.5 becomes ill defined and has lead to the proposal [48] to use the toroidal angle according to 3.6 as the parallel angle, where $1/q$ is bounded at the separatrix. However, also with such a coordinate system a separatrix **cannot** be treated. The construction of a field aligned coordinate system based on the toroidal angle as the field aligned angle is not possible, because

already the construction of a straight field line coordinate system according to transformation 3.4 is not possible. Since $1/q \to 0$ at the separatrix, a transformation which fulfils eq. 3.4 cannot be bijective any more and the resulting coordinate system becomes ill defined. This can also be seen in fig. 3.1b, where the contours of the poloidal straight field line angle θ_s are sucked into the X-point. One can construct separately a straight field line coordinate system, and thus a field aligned coordinate system for the closed field line region and for the open field line region, as was done in [34], but both regions cannot be treated simultaneously with this approach.

Hence, the statement appearing in [48, 49, 50] that with such a coordinate system a separatrix can be treated is not correct by the reasons mentioned above. It is assumed in section 2 of [48] that Hamada coordinates are already available, which become ill defined at the separatrix and the failure of this coordinate system is also obvious in [51], where it is explicitly stated that the constructed poloidal straight field line angle diverges at the separatrix - However, the FENICIA code [49, 50, 51] is not based on field aligned coordinates but also on a field line map[1], as described in the next section 3.2, and therefore able to cross the separatrix. - These points are quite subtle in [48, 49, 50, 51] and a detailed analysis of these papers, regarding the therein constructed field aligned coordinate system, is therefore deferred to appendix A.

Concerning the problems of field aligned coordinate systems at the separatrix, one might give up the concept of a field aligned grid, but at least keep flux surfaces, i.e. use the elementary toroidal coordinate system ρ, θ_e, φ. As also illustrated in fig. 3.1b, the flux surfaces are strongly compressed on the outboard side of a tokamak, whereas they are stretched apart in the region near the X-point. The computational grid would finally have a resolution imbalance within the poloidal plane. Since the perpendicular operators ($\nabla_\perp^2$, $\mathbf{v}_E \cdot \nabla$) arising in typical plasma turbulence models, act mainly isotropically in planes perpendicular to the magnetic field, which are roughly poloidal planes, such a grid might not be advisable from a computational point of view. Moreover, such a grid might lead to severe constraints for time integration schemes. If the perpendicular dynamics is advanced with an explicit time stepping scheme, the very closely spaced flux surfaces in the outboard midplane region might force one to very small time steps. In addition, also in a flux aligned grid the X-point always is an exceptional grid point due to the change of topology (see again fig. 1.4). This could in the worst case even lead to numerical artefacts.

3.2. Field line map approach

However, the fact that the construction of a field aligned coordinate system across the separatrix is impossible[2] is irrelevant, since the operators are still well defined, of course. It is similar to the situation of writing e.g. the Laplacian in polar coordinates (ρ, θ). Though the polar coordinate system is ill defined at the origin, where the Jacobian vanishes, the Laplacian is still a well defined operator. One should just not use a polar coordinate system to compute the Laplacian at the origin, but e.g. a Cartesian coordinate system or a coordinate free method. Similarly one should not use field aligned coordinate systems to compute operators at the separatrix.

For a tokamak a cylindrical coordinate system (R, Z, φ) is well defined everywhere in the region of interest and we span our simulation domain with a cylindrical grid R_i, Z_j, φ_k. Within each poloidal plane k, the grid is Cartesian. It is bounded by two limiting flux surfaces Ψ_{min}, Ψ_{max}, which is the only dependence on flux surfaces of the approach. The grid is illustrated in fig. 3.2.

---

[1]This becomes clear from references [49, 51]

[2]'impossible' means here that there is not yet given in literature a way on how to construct a field aligned coordinate system in presence of an X-point. I do not touch the question after the existence of such a coordinate system in general, which is in my opinion a very academic problem. In any case, I think that from a computational point of view such a coordinate system will be always problematic.

a)

b)
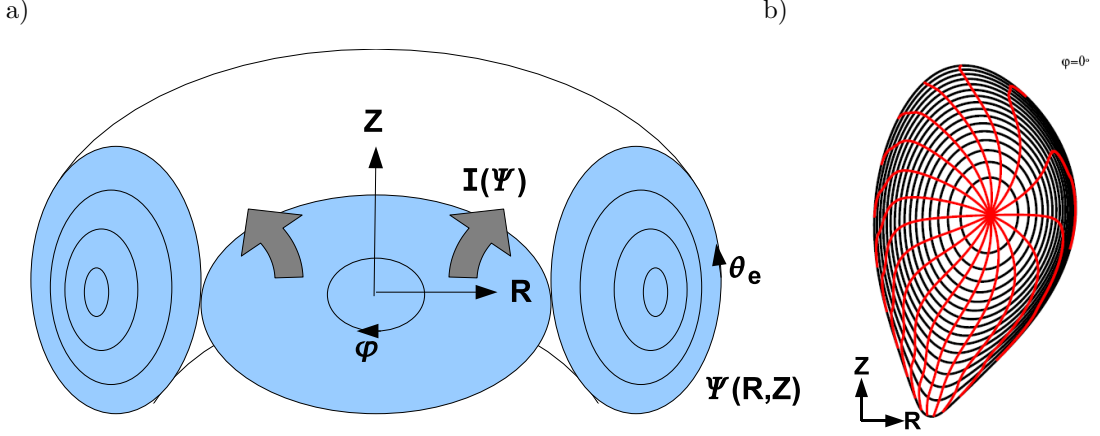
Figure 3.1.: a) Illustration of flux surfaces b) Contours of poloidal flux (black) and poloidal straight field line coordinate (red, symmetry or Pest coordinates). Close to the separatrix the contours of θ_s are sucked into the X-point. Flux surfaces are stretched apart close to the X-point, and compressed in the outboard midplane region (Figure from [107]).

Based on the assumption of a strong toroidal field, any perpendicular operator can be approximated with derivatives with respect to only R, Z, e.g. the perpendicular Laplacian is:

$$\nabla_\perp^2 = \sum_{i,j=R,Z,\varphi} \frac{1}{J} \partial_j \left[J \left(g^{ij} - b^i b^j \right) \partial_i \right] \approx \frac{1}{R} \partial_R \left(R \partial_R \right) + \partial_Z^2, \tag{3.8}$$

where $J = R$ the Jacobian of the cylindrical coordinate system and g^{ij} the metric tensor. Since the projection of the unit vector along the magnetic field on the poloidal plane is small ($b^R, b^Z \ll 1$), the derivatives with respect to φ can be neglected. The idea to neglect derivatives in the toroidal direction with respect to the poloidal directions can be transferred to any perpendicular operator, as such also the advection with the $\mathbf{E} \times \mathbf{B}$ velocity:

$$\mathbf{v}_E \cdot \nabla u \approx \frac{1}{B} \left[\phi, u \right]_{R,Z}. \tag{3.9}$$

Thus the perpendicular operators act mainly within poloidal planes. Numerically, since the grid within a poloidal plane is Cartesian, standard finite difference methods (see e.g. [108]) can be used for the discretisation of any perpendicular operator, e.g. the perpendicular Laplace operator becomes:

$$\nabla_\perp^2 u \to \frac{u_{i+1,j} - 2u_{i,j} + u_{i-1,j}}{h^2} + \frac{1}{R} \frac{u_{i+1,j} - u_{i-1,j}}{2h} + \frac{u_{i,j+1} - 2u_{i,j} + u_{i,j-1}}{h^2}, \tag{3.10}$$

where the subscript k which labels the toroidal direction has been dropped. h is the grid spacing within the Cartesian poloidal plane.

A parallel derivative is given in terms of:

$$\nabla_\parallel u = \mathbf{b} \cdot \nabla u = \lim_{h \to 0} \frac{u(\mathbf{x} + h\mathbf{b}) - u(\mathbf{x})}{h}, \tag{3.11}$$

where the last expression gives a motivation for the discretisation scheme. A parallel operator is computed via a finite difference between two values on a magnetic field line. Due to the strong toroidal field, any discrete parallel operator will connect points on neighbouring poloidal planes. A high directional accuracy, which is important, is obtained by tracing from a given grid point along a magnetic field line towards the neighbouring poloidal plane. The magnetic field is thereby assumed to be static and given (electrostatic approximation). Since the obtained penetration point does in general not coincide with another grid point, an interpolation within the neighbouring poloidal plane has to be performed.

Finally, the toroidal resolution being the main determinant for the accuracy of parallel operators and the resolution within a poloidal plane for the perpendicular operators, allows the desired scale separation for the grid resolution. Flute mode structures $k_\parallel \ll k_\perp$ are well represented on a grid with a comparatively low toroidal resolution, whereas a high resolution within the poloidal planes has to be retained.

The field line map approach here is based only on the assumption of a strong toroidal field[3]. Even if this assumption breaks down, it can be cured easily by respecting also derivatives with respect to φ in the perpendicular operators and possibly adjusting the interpolation at the discretisation of the parallel operators. In the worst case, one ends up simply with a discretisation in purely cylindrical coordinates.

It is noted that the following methods are discussed at the example of toroidal equilibria, but can also be applied to axial equilibria (x, y, z), where $z \in [0, L_{ax}]$ is a periodic axial coordinate. The transition $(R, Z, \varphi) \leftrightarrow (x, y, z)$ is trivial. It is useful to perform for this chapter the following normalisation:

$$\hat{R} := \frac{R}{R_0}, \qquad\qquad \hat{Z} := \frac{Z}{R_0}, \qquad\qquad \hat{\mathbf{B}} := \frac{\mathbf{B}}{B_0}, \qquad\qquad (3.12)$$

with $B_0 = B(R_0, Z_0)$ and define a normalized flux label:

$$\hat{\rho} := \frac{\sqrt{\Psi(R, Z) - \Psi(R_0, Z_0)}}{\sqrt{\Psi(R_x, Z_x) - \Psi(R_0, Z_0)}}, \qquad\qquad (3.13)$$

where R_x, Z_x is the position of the X-point. For axial equilibria:

$$\hat{x} := \frac{2\pi x}{L_{ax}}, \qquad \hat{y} := \frac{2\pi y}{L_{ax}}, \qquad \hat{z} := \frac{2\pi z}{L_{ax}}, \qquad \hat{\mathbf{B}} := \frac{\mathbf{B}}{B_z}, \qquad (3.14)$$

where B_z is the axial field strength assumed to be constant. For axial circular flux surfaces we define as flux label:

$$\hat{\rho} := \sqrt{\hat{x}^2 + \hat{y}^2}. \qquad\qquad (3.15)$$

If not stated differently, the hats above the quantities are omitted in the following.

3.3. Field line tracing

The first step of the field line map is a field line tracing procedure. The magnetic field is assumed to be electrostatic ($\partial_t \mathbf{B} = 0$), and therefore the field line tracing has to be performed only once at the beginning of a simulation, though this is not a principle constraint of the approach. Due

---

[3]The $k_\parallel \ll k_\perp$ is not a general assumption of the field line map approach but ultimately only exploited by choosing a coarse toroidal resolution. It can be relaxed by increasing the number of poloidal planes.

a)   b)
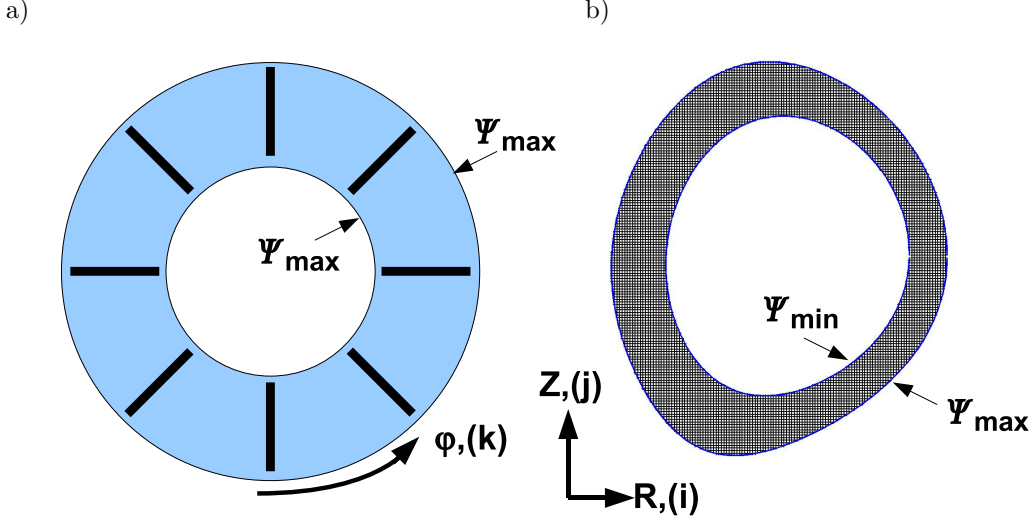
Figure 3.2.: Computational grid: a) View of tokamak from above, Planes are taken at equally spaced toroidal angles φ_k. b) Within each poloidal plane a Cartesian grid (R_i, Z_j) is used bounded by two extreme flux surfaces.

to axisymmetry, the field line tracing has to be performed only for a single plane. For 3D equilibria, which are not discussed here, a separate field line tracing for each plane would have to be performed. Starting from a grid point (R_i, Z_j) the penetration points at the neighbouring poloidal planes $\pm\Delta\varphi$ are obtained according to:

$$
R_{i,j}^{\alpha,\beta} = R_i + \int\limits_0^{\pm\Delta\varphi} d\varphi \, \frac{B^R}{B^\varphi}, \qquad\qquad Z_{i,j}^{\alpha,\beta} = Z_j + \int\limits_0^{\pm\Delta\varphi} d\varphi \, \frac{B^Z}{B^\varphi}, \qquad\qquad (3.16)
$$

where α, β denote the co/counter direction with the toroidal coordinate. The contravariant components of the magnetic field vector can be obtained from eq. 3.1 and in the following it is assumed that $I(\Psi) = const \rightarrow B^\varphi \propto R^{-2}$.

For toroidal equilibria eqs. 3.16 are integrated via a fourth order Runge-Kutta scheme [109], which has to be performed with a high accuracy in order to avoid numerical pollution. Since the parallel dynamics is orders of magnitudes faster than the perpendicular dynamics, a small erroneous displacement from the originating field line at the field line tracing process could result in spurious perpendicular dynamics. To avoid spurious perpendicular dynamics arising from the field line tracing, the following criterion must be satisfied for the erroneous displacement Δ_{trace} [47]:

$$
\Delta_{trace} \ll l_\| \sqrt{\frac{\chi_\|}{\chi_\perp}}, \qquad\qquad (3.17)
$$

where $l_\|$ is the length along a field line and $\chi_\|, \chi_\perp$ are parallel and perpendicular diffusion coefficients of interest, whose ratio can be as big as $\chi_\|/\chi_\perp \sim 10^{10}$ for heat diffusion processes in the core region of a tokamak. For axial equilibria with circular flux surfaces the penetration points can be computed analytically via a prescribed q-profile leaving thus no error due to the field line tracing. Details of the field line tracing procedure and a description of various other quantities which have to be computed for the field line map are given in appendix C.

3.4. Parallel gradient

3.4.1. Finite difference method

A sketch of the discretisation of the parallel gradient is shown in fig. 3.3a. For some quantity u the parallel gradient is computed at the positions half way along the magnetic field line towards the neighbouring poloidal planes. The general structure of the magnetic field thereby gives rise to two possible gradients according to co/counterdirection with φ denoted in the following with α, β. The values at the penetration points $u_{i,j,k}^{\alpha,\beta}$ are computed via a 2D interpolation within the poloidal plane. Currently a bilinear interpolation involving 4 points and a 3rd order polynomial interpolation involving 16 points are implemented (see appendix B.1). For some grid point (i, j, k) the discrete parallel gradients are:

$$\nabla_\parallel^\alpha u_{i,j,k} = \frac{1}{\Delta s_{i,j}^\alpha} \left(u_{i,j,k}^\alpha - u_{i,j,k} \right), \qquad \nabla_\parallel^\beta u_{i,j,k} = \frac{1}{\Delta s_{i,j}^\beta} \left(u_{i,j,k} - u_{i,j,k}^\beta \right). \tag{3.18}$$

$\Delta s_{i,j}^{\alpha,\beta}$ are distances along the magnetic field line from plane to plane and are computed during the field line tracing process (see appendix C). The parallel gradient at the grid point itself could be obtained via a further interpolation between the α, β discrete values along the magnetic field line. However, since in our target model no parallel gradient appears but a parallel diffusion, this issue is left for future work. Some results for the parallel gradient can be found in [49, 50, 51].

For interpolation techniques which are linear in the grid values the discrete parallel gradient can be expressed with a Matrix $\mathbf{Q}^{\alpha,\beta}$, which will be useful later.

$$\mathbf{u} = (u_{1,1,1}, u_{2,1,1}, \cdots)^T, \qquad \mathbf{q}^{\alpha,\beta} = \left(\nabla_\parallel^{\alpha,\beta} u_{1,1,1}, \nabla_\parallel^{\alpha,\beta} u_{2,1,1} \cdots \right)^T, \qquad \mathbf{q}^{\alpha,\beta} = \mathbf{Q}^{\alpha,\beta} \mathbf{u}. \tag{3.19}$$

3.4.2. Coordinate free representation

Later on, especially for field lines which are strongly converging/diverging another discretisation of the parallel gradient is useful based on a coordinate free representation. Instead of using expression 3.11 to motivate a finite difference expression for the parallel gradient, we can write also:

$$\nabla_\parallel u = \frac{1}{B} \nabla \cdot (\mathbf{B} u) = \frac{1}{B} \lim_{V \to 0} \frac{1}{V} \int_{\partial V} d\mathbf{S} \cdot \mathbf{B} u, \tag{3.20}$$

where V is an enclosed Volume. The surface integral can now be mimicked on the discrete level. Flux boxes around the magnetic field line are taken as discrete finite volume elements (see fig. 3.3b), such that the only contributions to the surface integral come from the toroidal ends of the flux box:

$$\nabla_\parallel^\alpha u_{i,j,k} = \frac{1}{\Delta \mathcal{V}_{i,j}^\alpha B_V} \left[\sum_{n,m} \left(u_{n,m,k+1} B_{n,m}^{tor} \Delta A_{i,j,n,m}^\alpha \right) - u_{i,j,k} B_{i,j}^{tor} h^2 \right], \tag{3.21}$$

where $\Delta \mathcal{V}_{i,j}^\alpha$ the flux box volume and B_V the magnetic field strength in the center of the flux box. $\Delta A_{i,j,n,m}^\alpha$ is the surface overlap of grid point $(n, m, k+1)$ with the toroidal end of the flux box surface of grid point (i, j, k). The β discretisation can be achieved analogously.

Due to the fact that the magnetic field is divergence free, the computation of the flux box volumes $\Delta \mathcal{V}_{i,j}^\alpha$ can be performed during the field line tracing procedure with a high accuracy (see appendix C). As illustrated in fig. 3.3b the mapped surface is obtained via field line tracing

of the four corners of the initial square. The mapping can be done in principle also with a higher accuracy by tracing more than just the four corners, yielding a polygon as mapped surface. However, this shall not be pursued here. Since the integration is a linear operation, the parallel gradient can also be written with matrices in the form of expression 3.19.

a)   b)
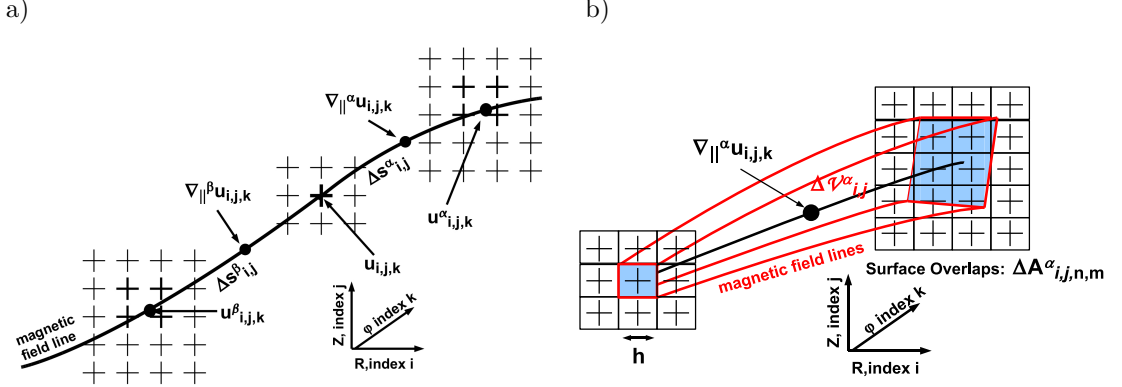
Figure 3.3.: Sketch for computation of parallel gradient: a) Finite difference method. b) Coordinate free representation (only α discretisation).

3.5. Parallel diffusion

In this section the discretisation of the parallel diffusion operator is discussed:

$$\mathcal{D}u := \nabla \cdot \left[(\nabla_\parallel u) \mathbf{b} \right]. \tag{3.22}$$

3.5.1. Naive discretisation

Only in this section for the naive discretisation the contribution of $\nabla \cdot \mathbf{b}$, which is zero in axial circular equilibria, is simply neglected. This approximation is not applied later in section 3.5.2 for the support operator method. The parallel diffusion operator can then be approximated as:

$$\mathcal{D}u \approx \nabla_\parallel^2 u, \tag{3.23}$$

which motivates a discretisation via a second application of a finite difference to the parallel gradient:

$$\nabla_\parallel^2 u_{ijk} = \frac{2}{\Delta s_{i,j}^\alpha + \Delta s_{i,j}^\beta} \left(\nabla_\parallel^\alpha u_{i,j,k} - \nabla_\parallel^\beta u_{i,j,k} \right). \tag{3.24}$$

However, it will turn out that this scheme, called here the naive discretisation, exhibits a slow convergence with respect to the poloidal resolution h.

3.5.2. Support operator method

In non-field aligned grids a directional discretisation error of the parallel diffusion operator introduces unavoidably a spurious numerical perpendicular coupling. Due to the strong anisotropy ($\chi_\parallel \gg \chi_\perp$), the thereby arising numerical perpendicular dynamics could overwhelm the real

perpendicular dynamics and lead finally to wrong results. In [52, 53] a discretisation scheme (symmetric scheme) is presented for a strongly anisotropic heat equation in a non-field aligned Cartesian grid, which gave the motivation to generalize this method to the field line map approach, where an interpolation is involved. It is stated in [52] that a basic difference between the asymmetric scheme, which causes a comparatively large numerical perpendicular transport, and the symmetric scheme with low numerical perpendicular transport is, that the symmetric scheme is self-adjoint on the discrete level. So also within the framework of the field line map approach a better discretisation of the parallel diffusion operator with respect to the naive scheme is found by conserving a 'good' property, i.e. the self-adjointness of the parallel diffusion operator on the discrete level.

Let u, v be two real valued arbitrary scalar fields, which vanish at the boundary of the domain. We define a scalar product as an integration over the whole domain:

$$\langle u, v \rangle := \int_V dV \, u \, v. \tag{3.25}$$

The self-adjointness property is obvious:

$$\langle u, \mathcal{D}v \rangle = \int_V dV \, u \nabla \cdot \left[\left(\nabla_\parallel v \right) \mathbf{b} \right] = - \int_V dV \, \nabla_\parallel u \nabla_\parallel v = - \left\langle \nabla_\parallel u, \nabla_\parallel v \right\rangle$$

$$\Rightarrow \nabla_\parallel^\dagger = -\nabla \cdot \left[\mathbf{b} \circ \right], \quad \mathcal{D}^\dagger = \mathcal{D}. \tag{3.26}$$

The method of support operators [110], which was also used in [52], gives an instruction how second order operators can be constructed which conserve certain integral equalities like eq. 3.26 on a discrete level. The idea is that a first order operator is discretised, e.g. the gradient or the divergence in general (in our case the parallel gradient) and the discrete second order operator is constructed via a discretisation of a scalar product and the demand to conserve certain integral equalities. We discuss in the following the scheme of the α discretisation. The β discretisation follows completely analogous and a fusion of both is presented at the end of this section.

We choose as prime operator the parallel gradient, whose discrete analogue $\nabla_\parallel^\alpha$ is given by expression 3.18 or 3.21, which can generally be written in matrix form according to expression 3.19 with a matrix $\mathbf{Q}^\alpha$. Scalar functions u, v (e.g. temperature) are located on the scalar's grid, i.e. the basic grid made up of poloidal planes with a Cartesian grid. Fluxes p^α, q^α are located on points half way along magnetic field lines between a grid point and the corresponding penetration point (see fig. 3.3a). The discrete parallel gradient maps from the scalar's grid (SG) to the flux's grid (FG^α).

$$\nabla_\parallel^\alpha, \mathbf{Q}^\alpha : SG \to FG^\alpha. \tag{3.27}$$

The parallel divergence $\nabla \cdot [\mathbf{b} \circ]$ as the derived operator is now constructed by requiring a conservation of the integral identity 3.26 on the discrete level. Therefore, we have to define scalar products in the discrete spaces SG and FG^α, which mimic both an integration over the same whole domain.

$$\langle u, v \rangle_{SG} := \sum_i u_i \, v_i \, \Delta V_i, \qquad \langle p^\alpha, q^\alpha \rangle_{FG^\alpha} := \sum_n p_n^\alpha \, q_n^\alpha \, \Delta \mathcal{V}_n^\alpha, \tag{3.28}$$

where in this section i, j, n, m are used as summation indices over all points and not as grid indices as in the sections before. The finite volume elements ΔV_i and $\Delta \mathcal{V}_n^\alpha$ are chosen as finite flux box volumes around a magnetic field line as illustrated in fig. 3.4. ΔV_i is a flux box ranging
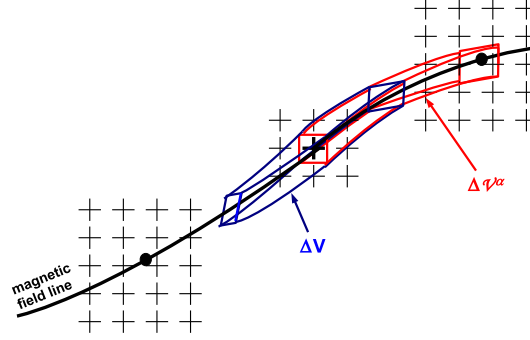
Figure 3.4.: Illustration of flux box volumes ΔV and $\Delta \mathcal{V}^\alpha$

around the field line toroidally limited by $[\varphi_k - \Delta\varphi/2, \varphi_k + \Delta\varphi/2]$ and $\mathcal{V}_n^{\alpha,\beta}$ toroidally limited by $[\varphi_k, \varphi_k \pm \Delta\varphi]$. Again, these volumes can be computed to a high accuracy during the field line tracing process. The discrete parallel divergence as the derived operator can now be derived from the discrete parallel gradient, the discrete scalar products and by requiring the integral equalities 3.26 on the discrete level. On the one hand:

$$\langle u, \mathcal{D}v \rangle \rightarrow \langle u, D^\alpha v \rangle_{SG} = \sum_{i,j} u_i \, \mathbf{D}_{ij}^\alpha \, v_j \Delta V_i, \tag{3.29}$$

with D^α (and $\mathbf{D}^\alpha$ as matrix) the discrete analogue to $\mathcal{D}$. On the other hand:

$$\langle u, \mathcal{D}v \rangle = -\left\langle \nabla_\parallel u, \nabla_\parallel v \right\rangle \rightarrow -\left\langle \nabla_\parallel^\alpha u, \nabla_\parallel^\alpha v \right\rangle_{FG^\alpha} = -\sum_{n,m,k} \mathbf{Q}_{nm}^\alpha u_m \, \mathbf{Q}_{nk}^\alpha v_k \, \Delta\mathcal{V}_n^\alpha. \tag{3.30}$$

A relabelling of the indices $m \rightarrow i, k \rightarrow j$ and requiring the equality of expression 3.29 and 3.30 for arbitrary $\mathbf{u}, \mathbf{v}$, yields finally the desired expression for the discrete parallel diffusion operator.

$$\mathbf{D}_{ij}^\alpha = -\sum_n \mathbf{Q}_{ni}^\alpha \mathbf{Q}_{nj}^\alpha \frac{\Delta\mathcal{V}_n^\alpha}{\Delta V_i}. \tag{3.31}$$

In the simplified case that all volumes are equal, this yields the simple expression

$$\mathbf{D}^\alpha = -(\mathbf{Q}^\alpha)^T \mathbf{Q}^\alpha, \tag{3.32}$$

where the self-adjointness on the discrete level is obvious. For axial equilibria the volume correction factor is negligible, since all points have the same flux box volume. However, in toroidal equilibria due to geometry and the $1/R$- dependence of the magnetic field strength the volumes are different. The volume correction factor accounts for the effects of $\nabla \cdot \mathbf{b} \neq 0$. In addition, the volume factor matters if the distances $\Delta s_{i,j}^\alpha$ along magnetic field lines vary, i.e. if the grid is non-equidistant in the parallel sense. This plays a role as parallel boundaries are taken into account (see appendix B.4).

A further important point concerns numerical stability. If the discrete parallel diffusion operator is used within a time evolution equation, e.g. a heat equation, a discretisation of the parallel diffusion operator with the support operator excludes possible instabilities arising from the interpolation, since it guarantees a strict decrease of the L^2-norm on the discrete level:

$$\langle u, D^\alpha u \rangle_{SG} = -\left\langle \nabla_\parallel^\alpha u, \nabla_\parallel^\alpha u \right\rangle_{FG^\alpha} \leq 0, \tag{3.33}$$

which is in general not fulfilled with the naive discretisation method.

Finally, a small modification is applied to the scheme. A discrete parallel diffusion operator can also be derived completely analogously by choosing the β discretisation (replace just all α's with β's), which will end also in a consistent and convergent scheme by itself. However, it is desirable that the final discrete scheme is independent on this initial arbitrary choice. To achieve this, we simply take the average between both discretisations:

$$\mathcal{D} \to \mathbf{D} := \frac{1}{2}\left(\mathbf{D}^\alpha + \mathbf{D}^\beta\right). \tag{3.34}$$

This modification does not alter the self-adjointness property on the discrete level in the sense that the scalar product for fluxes is now defined as:

$$\langle p, q \rangle_{FG} := \frac{1}{2}\left\langle p^\alpha, q^\alpha \right\rangle_{FG^\alpha} + \frac{1}{2}\left\langle p^\beta, q^\beta \right\rangle_{FG^\beta}, \tag{3.35}$$

which still mimics one integration over the same whole domain.

3.6. A simple model problem

Expression 3.31 (respectively 3.34) and 3.24 are discretisation schemes for the parallel diffusion operator in a quite general geometry. To get further insight into the difference of both schemes, a simple 2D model problem is considered.

3.6.1. Stencil

We consider a minimum non-trivial 2D problem spanned by coordinates x, z which are assumed doubly periodic. The setup is illustrated in fig. 3.5a. x plays the role of a coordinate within a poloidal plane and z the toroidal/axial direction. The magnetic field is uniform with a slight inclination with respect to the axial direction:

$$\mathbf{b} = \frac{1}{\sqrt{(fh)^2 + \Delta z^2}}\left[(fh)\mathbf{e}_x + \Delta z \mathbf{e}_z\right], \tag{3.36}$$

where on the continuous level (fh) is the distance in x-direction and Δz the distance in z-direction as one travels along a magnetic field line. The numerical grid is regular in x, z with grid spacing h and index i in the $x-$direction and grid spacing Δz and index k in the $z-$direction. Using a linear interpolation to determine the value at the penetration points, the matrix for the
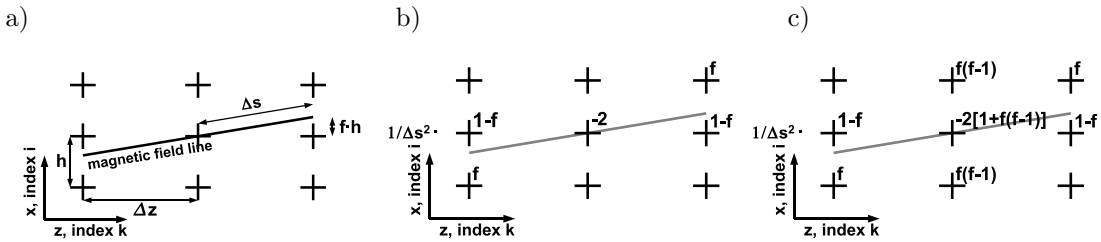
Figure 3.5.: Model problem at the example of 9 grid points. a) Setup. b) Discrete stencil of parallel diffusion operator for naive scheme, c) for support scheme.

discrete parallel gradient matrix in the 9 point example is:

$$
\mathbf{Q}^{\alpha} = -\left(\mathbf{Q}^{\beta}\right)^{T} = \frac{1}{\Delta s}
\begin{pmatrix}
-1 & & & 1-f & f & & & & \\
& -1 & & 1-f & f & & & & \\
& & -1 & [f] & & 1-f & & & \\
& & & -1 & & 1-f & f & & \\
& & & & -1 & & 1-f & f & \\
& & & & & -1 & [f] & & 1-f \\
[1-f] & [f] & & & & & -1 & & \\
& [1-f] & [f] & & & & & -1 & \\
[f] & & [1-f] & & & & & & -1
\end{pmatrix},
\tag{3.37}
$$

where the quantity $u_{i,k}$ is stored into a vector according to $\mathbf{u} = (u_{1,1}, u_{2,1}, u_{3,1}, u_{1,2}, \dots)^{T}$. Entries, which are given in square bracket arise due to the periodic boundary conditions and are of no importance for the final stencil of an inner point, which is in the example only $i = 2, k = 2$. The distance along field lines is $\Delta s = \sqrt{\Delta z^2 + (fh)^2}$. The flux box volumes are in this example all equal ($\Delta V = \Delta \mathcal{V} = h\,\Delta z$) and the discrete parallel diffusion follows immediately. The stencils of the inner grid point for the naive and support operator scheme are illustrated in fig. 3.5b,c. First, if the displacement is set to zero ($f = 0, 1$), the interpolation becomes exact, both schemes agree and yield the standard second order finite difference expression for the second derivative. For finite displacement the most striking difference is that the naive scheme has a stencil which involves the interpolating grid points in the neighbouring planes ($k-1, k+1$) and the considered grid point itself, whereas the stencil of the support scheme comprises also neighbouring points in the same plane (x-direction) as the considered grid point.

3.6.2. Numerical analysis

The discrete parallel diffusion operators are now investigated based on their action on a mode $u = \exp(ik_x x + ik_z z)$. The analytic result is:

$$
\mathcal{D}^{an} u = -\frac{\left((fh)k_x + k_z \Delta z\right)^2}{\Delta s^2} u =: -k_{\parallel}^2 u.
\tag{3.38}
$$

On the discrete level the parallel diffusion operators are:

$$
\mathbf{D}^{naive} u = \frac{2}{\Delta s^2}\left[(1-f)\cos(k_z \Delta z) + f\cos(k_x h + k_z \Delta z) - 1\right]u,
\tag{3.39}
$$

$$
\mathbf{D}^{supp} u = \frac{2}{\Delta s^2}\Big[(1-f)\cos(k_z \Delta z) + f\cos(k_x h + k_z \Delta z)
\tag{3.40}
$$
$$
- f(1-f)\cos(k_x h) - 1 - f(f-1)\Big]u.
$$

A Taylor expansion in $(k_x h, k_z \Delta z)$ yields:

$$
\mathbf{D}^{naive} u \approx \left[-k_{\parallel}^2 - \frac{f(1-f)(k_x h)^2}{\Delta s^2} + \mathcal{O}\left(\frac{(k_x h, k_z \Delta z)^4}{\Delta s^2}\right)\right]u,
\tag{3.41}
$$

$$
\mathbf{D}^{supp} u \approx \left[-k_{\parallel}^2 + \mathcal{O}\left(\frac{(k_x h, k_z \Delta z)^4}{\Delta s^2}\right)\right]u.
\tag{3.42}
$$

By comparing the numerical results 3.41 respectively 3.42 with the analytic result 3.38, it is obvious that the error of the naive scheme for finite displacement is already of the order $(k_x h)^2/\Delta s^2$, whereas the support scheme yields an error of the order $(k_x h, k_z \Delta z)^4/\Delta s^2$, indicating a faster convergence of the support scheme with the poloidal resolution h. A similar analysis using a 3rd

order polynomial interpolation (see appendix B.2) yields:

$$\mathbf{D}^{naive}u \approx \left[-k_\parallel^2 + \frac{1}{12}k_\parallel^4 \Delta s^2 - \frac{(k_x h)^4}{\Delta s^2} \frac{f(f-1)(f+1)(f-2)}{12} \right.$$
$$\left. + \mathcal{O}\left(\frac{(k_x h, k_z \Delta z)^6}{\Delta s^2} \right) \right] u, \tag{3.43}$$

$$\mathbf{D}^{supp}u \approx \left[-k_\parallel^2 + \frac{1}{12}k_\parallel^4 \Delta s^2 + k_\parallel \mathcal{O}\left(\frac{(k_x h, k_z \Delta z)^5}{\Delta s^2} \right) + \mathcal{O}\left(\frac{(k_x h, k_z \Delta z)^8}{\Delta s^2} \right) \right] u. \tag{3.44}$$

The error term $\propto k_\parallel^4$ arises due to the discretisation in the parallel direction[4] and could be eliminated by choosing a higher order discretisation of the parallel gradient along the magnetic field line. Since $k_\parallel$ is dependent on $k_x h, k_z \Delta z$, the overall error for structures with finite $k_\parallel$ is of the order $(k_x h, k_z \Delta z)^4 / ds^2$.

The dangerous error terms are those which are purely dependent on $k_x h$, since these introduce a directional error and are responsible for the numerical perpendicular transport. In tokamaks the parallel dynamics is usually much faster than the perpendicular dynamics, e.g. the heat conductivity can reach ratios up to $\chi_\perp / \chi_\parallel \sim 10^{-10}$. A small directional error of a discrete parallel operator can thus overwhelm the real perpendicular dynamics. In terms of numerical transport the support scheme with polynomial interpolation clearly performs best. Especially for modes which have $k_\parallel = 0$, the numerical error is of the order $(k_x h)^8 / \Delta s^2$.

Embedding the discrete parallel diffusion operator into a parallel diffusion equation 3.45, a mode which has initially $k_\parallel = 0$ decays numerically. This numerical decay can be quantified with a decay exponent γ_{num} of the L^2-norm. As illustrated in fig. 3.6, the above derived scalings of the decay exponent with resolution for the different schemes are perfectly obtained.
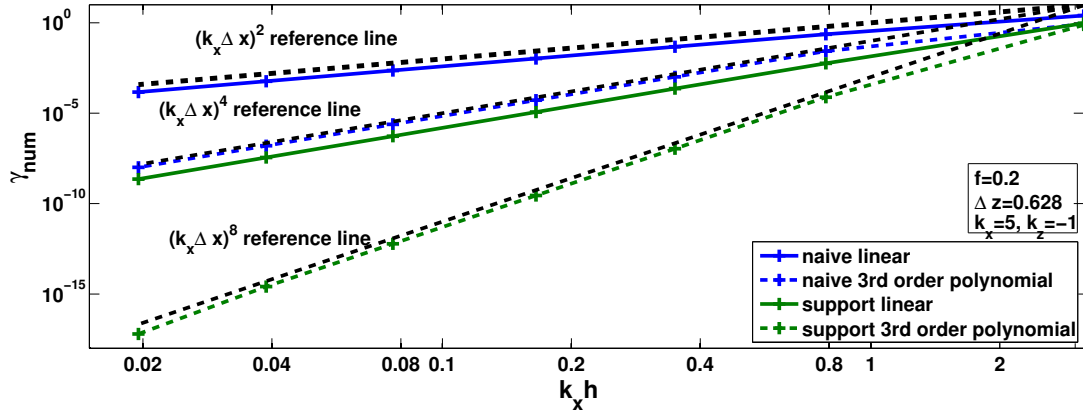
Figure 3.6.: Numerical decay exponent γ_{num} of L^2-norm in dependence of poloidal resolution h for fixed z-resolution and fixed displacement ($f = 0.2$ or $f = 0.8$). The initial state is a $k_x = 5, k_z = -1$ mode and the magnetic field pitch is $\tan\theta = k_z / k_x$, such that the parallel gradient vanishes. The simulation domain was doubly periodic $[0, 2\pi] \times [0, 2\pi]$.

---

[4] Remember that a similar analysis of the standard second order finite difference expression in 1D (coordinate x, grid spacing Δx) for the second derivative yields: $\partial_x^2 \exp(ikx) \approx \left[-k^2 + k4\Delta x^2/12 + \cdots \right] \exp(ikx)$

3.7. Benchmarks in 3D

In this section benchmarks of the parallel diffusion operator in 3D are presented. As an example problem the parallel diffusion equation serves:

$$\frac{\partial}{\partial t}u = \chi_{\parallel}\mathcal{D}u, \tag{3.45}$$

which can be run within the framework of the GRILLIX code by just switching off certain terms, i.e. it is also a direct test of the implementation. Since we are here interested in the spatial error, the time step was chosen always sufficiently small, such that the temporal discretisation error was always subdominant. Details of the temporal discretisation, the solver, computational parallelisation etc. are discussed in chapter 4. For benchmarks, performed in axial geometry with circular flux surfaces, an analytic solution is available. Let the initial state be characterised with a poloidal and axial mode number (n, m) and an arbitrary radial structure:

$$u(t = 0) = f(\rho)\sin(m\theta + nz), \tag{3.46}$$

then the analytic solution can be found via Fourier Transform methods:

$$u^{an}(t) = f(\rho)\exp(-\gamma(\rho)t), \quad \text{with:} \quad \gamma = \frac{\chi_{\parallel}}{1 + \rho^2/q(\rho)^2}\left(\frac{m}{q(\rho)} + n\right)^2. \tag{3.47}$$

Hence, a characteristic time scale is given by the inverse decay rate $t_e^{-1} = \gamma((\rho_{max} + \rho_{min})/2)$. If not stated differently, $\chi_{\parallel} = 1$, i.e. time is measured in units of $R_0^2/\chi_{\parallel}$ respectively $L_{ax}^2/(4\pi^2\chi_{\parallel})$, and the radial structure is characterised with a radial mode number r, such that:

$$f(\rho) = \sin\left(\pi r\frac{\rho - \rho_{min}}{\rho_{max} - \rho_{\min}}\right). \tag{3.48}$$

The simulation domain is a flux shell limited[5] by $\rho_{min} = 0.1$, $\rho_{max} = 0.2$. The error is measured in the L^2-norm:

$$\delta_2(t) = \frac{||u^{an}(t) - u^{num}(t)||_2}{||u^{an}(t)||_2}. \tag{3.49}$$

Five possible discretisations will be investigated:

- **N-1**: Naive scheme with bilinear interpolation.

- **N-3**: Naive scheme with 3rd order bipolynomial interpolation.

- **S-1**: Support scheme with bilinear interpolation.

- **S-3**: Support scheme with 3rd order bipolynomial interpolation.

- **S-C**: Support scheme with the parallel gradient discretised via the coordinate free representation.

---

[5]For a better match of the radial mode with the perpendicular boundaries the flux shell is actually extended about roughly one grid point, i.e. $\rho = \rho_{min} - h \cdots \rho_{max} + h$

3.7.1. Basic test $q = \infty$

For the case $q = \infty$ the magnetic field is purely axial and the penetration points coincide with grid points. The interpolation is exact, the discrete parallel gradient operator reduces to the well known standard second order finite difference expression for all schemes and the numerical error should depend on the poloidal resolution h. Hence, this case serves merely as check for the correctness of the implementation of the schemes. In fig. 3.7 the error in dependence on the number of poloidal planes (axial resolution) for a $r = 1$, $m = 0$, $n = 1$ mode is shown. The numerical error decays like N_{pol}^{-2} for all schemes, which shows the expected second order accuracy.
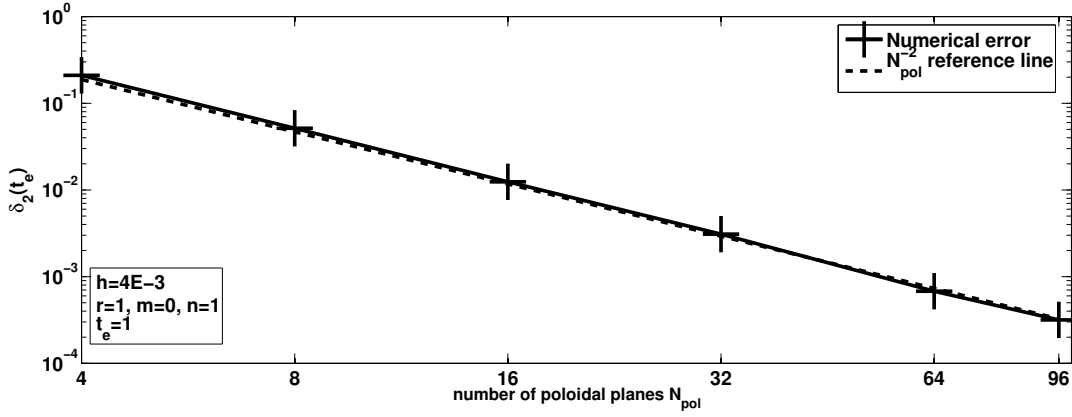

Figure 3.7.: Numerical error in dependence on number of poloidal planes for a $r = 1$, $m = 0$, $n = 1$ mode with $q = \infty$.

3.7.2. $q \neq \infty$

In the next benchmark a finite safety factor of $q = 3.4$ is chosen. The penetration points do now not coincide with grid points any more, and thus the numerical accuracy is also dependent on the poloidal resolution h and the scheme.

In fig. 3.8 the difference between the analytic solution and the numerical solution for a $m = 3$, $n = 1$, $r = 1$ mode at the axial position $z = 0$ is shown for the different schemes on the same colour scale. The basic behaviour is consistent with the predictions of the simple 2D model problem. The error is largest for the **N-1** scheme with an order of $\mathcal{O}(h^2)$. The errors of the other schemes are on a lower level $\mathcal{O}(h^4)$. However, since at the boundaries the conditions for the interpolation become worse, significant errors arise here. Especially for the **N-3** scheme the errors are significant.

The numerical error in dependence of the axial resolution for two different poloidal resolutions is shown in fig. 3.9a,b. For low axial resolutions the error is dominated by the axial resolution N_{pol} and decays like $N_{pol}^{-2} \approx \Delta s^2$, showing the second order accuracy of the schemes. For high axial resolution the error is dominated by the poloidal resolution h of the mode and deviates from the line N_{pol}^{-2} but increases. In agreement to the predictions of the simple 2D model, this transition occurs first for the **N-1** scheme and for the other schemes later at roughly the same point. In fig. 3.9c,d the numerical error in dependence on the poloidal resolution h for a fixed axial resolution N_{pol} is shown. Again, the convergence is slowest for the **N-1** scheme and for the other schemes faster. The **S-1** and **S-3** scheme perform thereby slightly better than the **N-3**

a)   b)   c)   d)
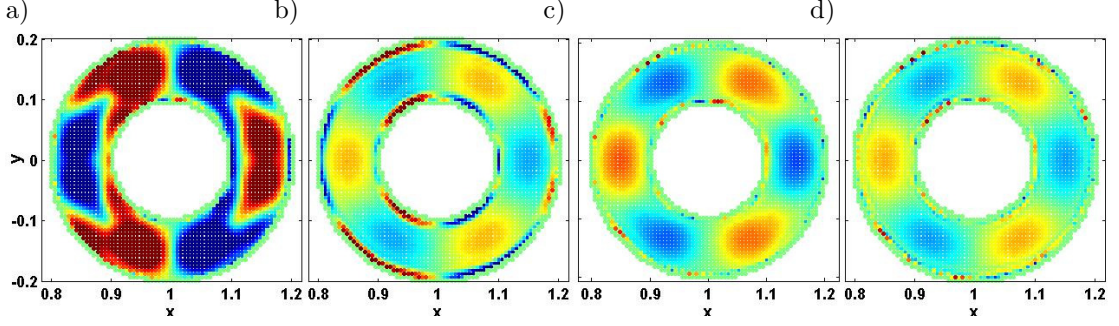
Figure 3.8.: Difference between analytic and numeric solution $u^{an}(t_e) - u^{num}(t_e)$ of a $r = 1$, $m = 3$, $n = 1$ mode ($t_e \approx 0.3$) at $z = 0$. a) **N-1**, b) **N-3**, c) **S-1**, d) **S-3**. Parameters were $q = 3.4$, $N_{pol} = 32$, $h = 6 \cdot 10^{-3}$. Colour code is from -0.01 (dark blue) to $+0.01$ (dark red).

scheme. In the end the **N-1**, **S-1** and **S-3** schemes converge to the same constant error of roughly $\delta_2 \approx 1.25 \cdot 10^{-2}$ for $N_{pol} = 32$ respectively $\delta_2 \approx 3.5 \cdot 10^{-3}$ for $N_{pol} = 64$ which is determined by the axial resolution. These values lie then again on the N_{pol}^{-2} line indicated with a red point in fig. 3.9b. As becomes especially apparent in fig. 3.9d, the **N-3** scheme initially shows also a smooth convergence to the same value as the other schemes, but then suddenly changes quite abruptly at the highest resolution. The reason for this is not yet quite clear, but might have to do with a numerical instability arising due to the interpolation process. This peculiarity is not investigated here further, since a computation at a higher resolution could not be performed presently with the available hardware and the **N-3** scheme will ultimately not be used anyway.

Having analysed the numerical accuracy of the schemes for modes with $k_{\parallel} \neq 0$, it is worth to analyse the numerical perpendicular transport for $k_{\parallel} = 0$ modes. In fig. 3.10a the temporal evolution of the error is plotted for a zonal mode ($r \neq 0$, $m = 0$, $n = 0$). It can be seen that for the **N-1** scheme the error increases rapidly until after $t \approx 1000$ the mode has decayed practically completely. For the other schemes the error first increases also quite rapidly due to effects at the boundary. After this initial transient phase the error increases on a much slower level. Due to the worse conditioning of the 3rd order polynomial interpolation at the boundaries, the initial error is slightly larger for the **S-3** scheme than for the **S-1** scheme. However, after the transient phase the numerical error increases for the **N-3** and **S-1** faster than for the **S-3** scheme. In fig. 3.10b the temporal evolution of the L^2-norm is shown. Whereas the mode has practically decayed completely for the **N-1** scheme after $t = 1000$ and a slow decay for the **N-3** and **S-1** can be seen, it remains practically stable with the **S-3** scheme. From these curves a numerical decay exponent γ_{num} can be estimated.

Finally, the numerical decay exponent in dependence on the resolution is shown in fig. 3.11a,b. By varying the resolution h and the mode number r independently, it is apparent that the numerical decay exponent is solely dependent on $k_{\rho}h$ and N_{pol}. The scalings which can be derived from the graphs are roughly:

$$\gamma_{num} = \begin{cases} (k_{\rho}h)^2 N_{pol}^2, & \text{for } \textbf{N-1}, \\ (k_{\rho}h)^4 N_{pol}^2, & \text{for } \textbf{N-3} \text{ and } \textbf{S-1}, \\ \left[A(k_{\rho}h)^8 + B(k_{\rho}h)^4 \right] N_{pol}^2, & \text{for } \textbf{S-3}. \end{cases} \tag{3.50}$$

Recalling that $N_{pol} \approx \Delta s^{-1}$, the scalings derived for the simple model problem in section 3.6.2 are obtained. Except for the **S-3** scheme, where for low poloidal resolutions is as derived $(k_{\rho}h)^8 / \Delta s^2$
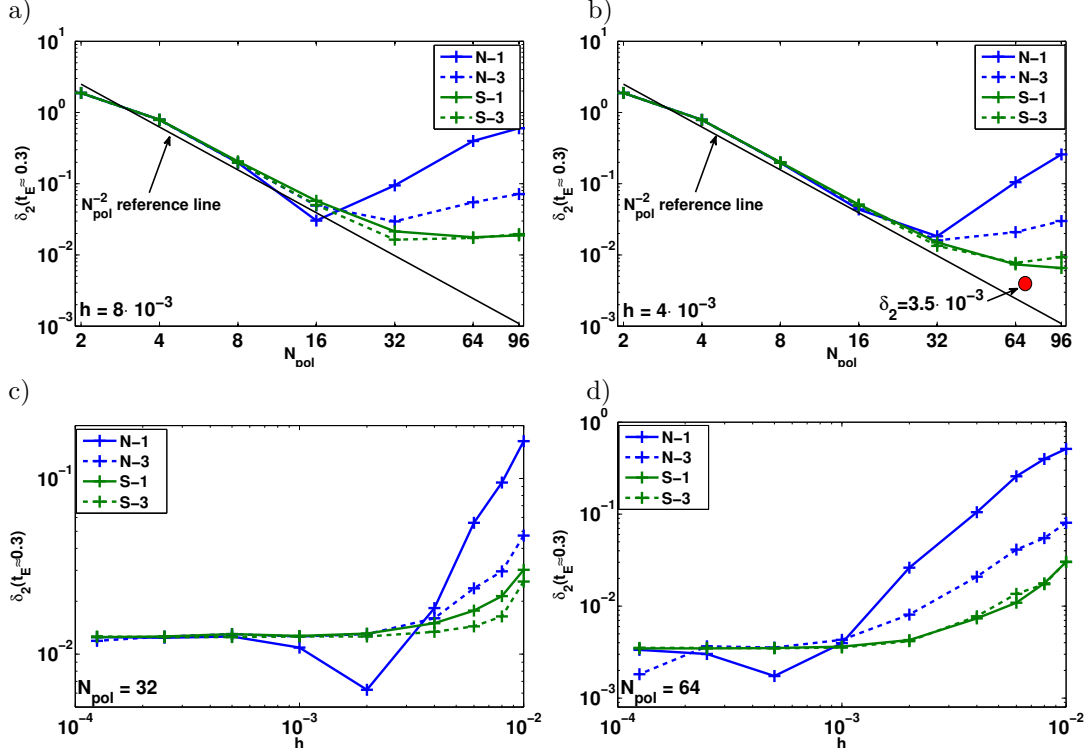
Figure 3.9.: Numerical error $\delta_e(t_e)$ of a $r = 1$, $m = 3$, $n = 1$ mode ($t_e \approx 0.3$) in dependence on resolution with $q = 3.4$. In dependence on axial resolution for fixed poloidal resolution of a) $h = 8 \cdot 10^{-3}$, b) $h = 4 \cdot 10^{-3}$. In dependence on poloidal resolution for fixed axial resolution of c) $N_{pol} = 32$ and d) $N_{pol} = 64$. The error converges against $\delta_2 \approx 3.5 \cdot 10^{-3}$, which is indicated in fig. b) with a red circle.
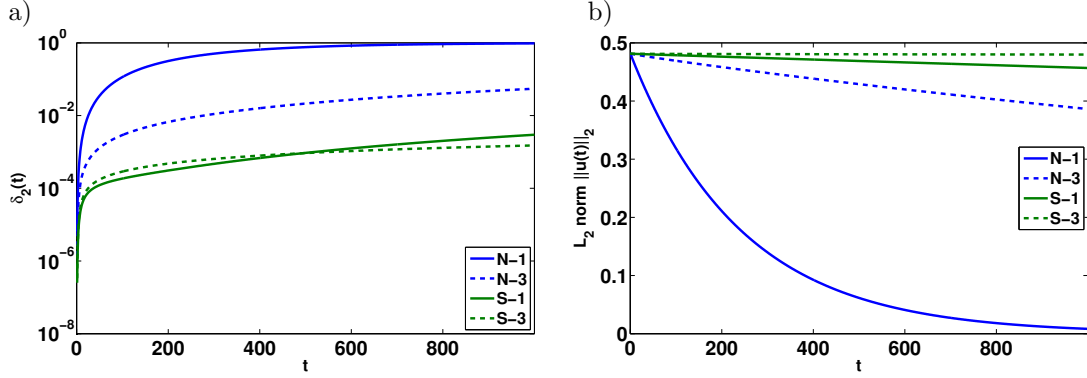
Figure 3.10.: Temporal evolution of a) error and b) L^2-norm of a zonal mode with $r = 4$, $m = 0$, $n = 0$. Resolution was $h = 4 \cdot 10^{-3}$, $N_{pol} = 2$ and $q = 3.4$.

but then changes to $(k_\rho h)^4 / \Delta s^2$. This change of scaling is again explained by the boundary conditions. It has been observed that the numerical transport is larger close to the boundaries than in the center of the flux shell. This breaks the derived scaling of the simple 2D model

problem.

a)

b)
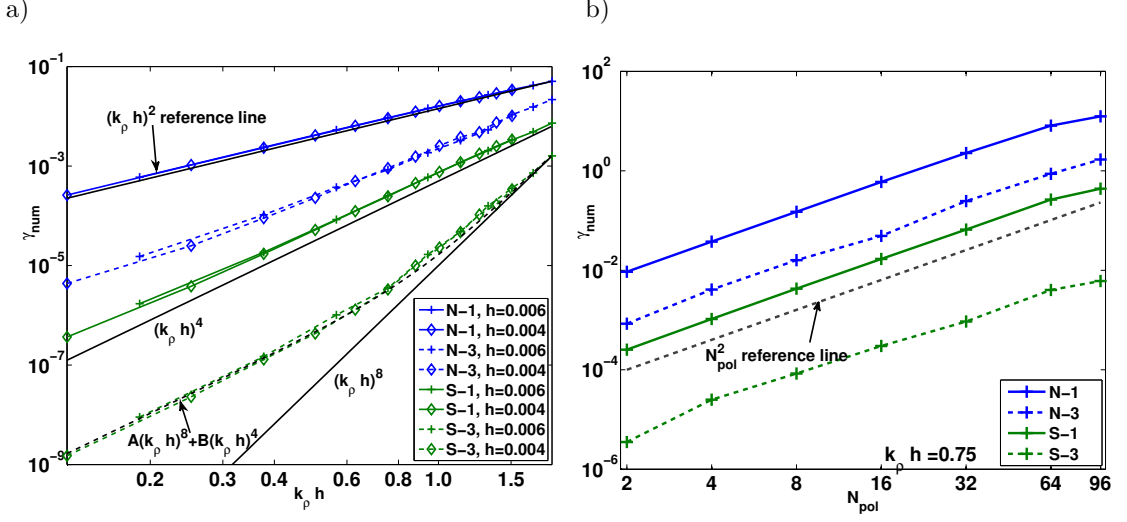
Figure 3.11.: Numerical decay exponent in dependence of a) poloidal resolution of mode $k_\rho h$ for fixed axial resolution $N_{pol} = 2$ and b) in dependence of toroidal resolution N_{pol} for fixed poloidal resolution $k_\rho h = 0.75$.

3.8. Map distortion

So far, only axial equilibria with a constant safety factor have been considered, where the magnetic field lines are still pretty simple. In realistic tokamak geometry especially in presence of an X-point, the magnetic field lines can become distorted strongly by converging in one direction, while diverging in the other direction to maintain $\nabla \cdot \mathbf{B} = 0$. As an example consider initially a square of lateral length h on a poloidal plane close to the X-point. Tracing the edges as illustrated in fig. 3.3b of this square towards e.g. the outboard midplane will distort the square such that it becomes poloidally strongly elongated but radially compressed while preserving the toroidal magnetic flux through the area. How does this distortion affect the numerical scheme?

To illustrate the effects of such a distortion, we consider a 2D example illustrated in fig. 3.12, where x shall again mimic a direction within a poloidal plane and φ the toroidal direction. Close to the separatrix the magnetic field lines behave ergodically, i.e. two field lines initially separated by the poloidal grid distance h become separated by a distance $g \propto h \exp(\varphi)$ as one advances a distance φ in the toroidal direction. Let us further assume that there is some blob with finite poloidal extent of the order of h at some plane. In reality the blob diffuses along field lines and thus spreads across many points in the neighbouring poloidal plane. For the naive scheme with any kind of interpolation this does not cause any problems, since the discrete parallel diffusion operator at some grid point is just computed by 'taking' values from neighbouring poloidal planes. However, in the support scheme a value is not just 'taken' from neighbouring but also 'sent' towards neighbouring poloidal planes. This might become clearer by recalling that the support scheme roughly involves a multiplication with the transpose matrix of the parallel gradient matrix (see eq. 3.32). If the parallel gradient is computed only via an interpolation at the penetration points, grid points which lie in between the diverged field lines are not connected

to the original points by the scheme. The blob does not spread properly over the grid points but only diffuses to points which are connected by the scheme. Finally, spurious wiggles arise in the neighbouring poloidal plane.
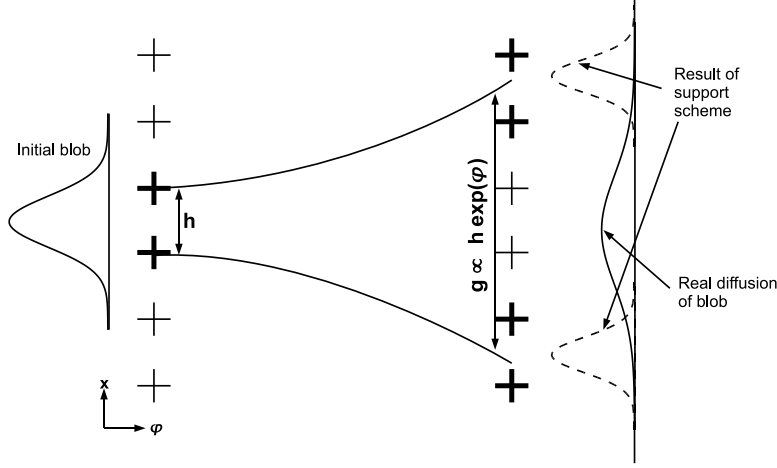
Figure 3.12.: Effects of map distortion on numerical scheme (2D). Magnetic field lines are ergodic and separate according to $g \propto h \exp(\varphi)$. In the illustration only the thick grid points are connected by the support scheme with linear interpolation (**S-1**). As a result, a blob which should in reality spread smoothly across many grid points in the next poloidal plane only diffuses to those grid points which are connected by the scheme (marked thick). Unphysical wiggles arise. With the naive discretisations this problem does not occur, since here values are only 'taken' from neighbouring poloidal planes.

As an example, in fig. 3.13 the temporal evolution of an initially Gaussian blob[6],

$$u(t = 0) = \exp \left[-\frac{(R - R_c)^2}{R_w^2} - \frac{(Z - Z_c)^2}{Z_w^2} \right] \delta(\varphi), \tag{3.51}$$

located close to the X-point is illustrated. The simulation was performed with two poloidal planes. As just described, for the **N-3** scheme the diffusion results in smooth structures, whereas for the **S-3** scheme unphysical small wiggles arise.

There are two possible remedies for the problem.

3.8.1. Remedy 1

The previous discussion suggests that the parallel gradient has to be discretised, such that the map includes those points which should be connected. This is exactly achieved via the coordinate free representation of the parallel gradient described in section 3.4.2. The result is shown in fig. 3.15a, where the same computation as in fig. 3.13 has been performed with the support scheme using the coordinate free representation for the parallel gradient (**S-C**). In the example the map was performed with quads and the wiggles vanished. If the distortion becomes even stronger, a map with quads might not suffice, but by tracing more than just the four edges of the initial square a polygon map is needed. Due to this reason and since the implementation of

---

[6]On the discrete level the δ-distribution is modelled with a Kronecker δ: $\delta(\varphi) \to N_{pol} \delta_{0,k}$.

a)   b)   c)
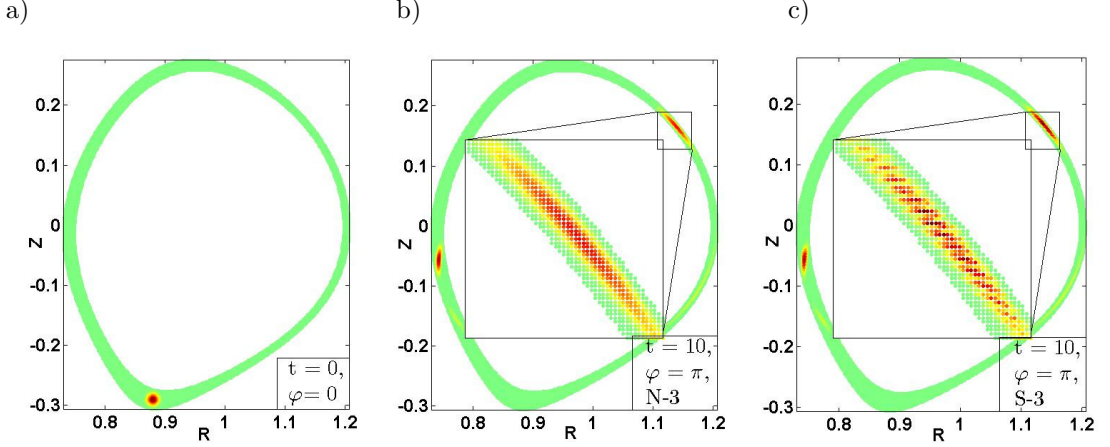
Figure 3.13.: Temporal evolution of Gaussian blob close to separatrix ($\rho_{min} = 0.9$, $\rho_{max} = 0.95$, equilibrium according to [111], see also section 4.1) with $h = 1 \cdot 10^{-3}$, $N_{pol} = 2$. a) Initial state is Gaussian blob at the first plane ($\varphi = 0$) with $R_c = 0.88$, $Z_c = -0.29$, $R_w = Z_w = 8 \cdot 10^{-3}$. b) Snapshot at $t = 10$ of the second plane ($\varphi = \pi$) computed with **N-3** scheme. Part of the domain is enlarged. c) Computed with **S-3** scheme. Due to the ergodic behaviour of the field lines, small scale wiggles arise. Colour scale green to red: a) $0 \cdots + 2$, b,c) $0 \cdots + 0.5$

the method is cumbersome, though possible as has been shown here, this method is not pursued further here. Moreover, concerning numerical transport, **S-C** has the same properties as the **S-1** scheme.

3.8.2. Remedy 2

Instead of using the **S-C** method, we define a criterion for the **S-1** and **S-3** method up to which they perform reasonably well. Starting with an initial square of lateral size h at one plane, as the edges are traced to the neighbouring planes, the mapped quads at the neighbouring planes will be distorted. Neglecting the weak dependence of B_{tor}, the area of the square is thereby preserved due to flux conservation. We can distinguish two types of distortion: A conformal distortion where the quad is stretched in one direction and squeezed in the other resulting in disparate lateral lengths, and an angular distortion where e.g. two angles become acute and the other two obtuse resulting in a parallelogram. We quantify the distortion by:

$$d_c = \max_{i,j} \frac{\text{longest side of mapped quad } i,j}{\text{shortest side of maped quad } i,j}, \tag{3.52}$$

$$d_a = \max_{i,j} \frac{\text{largest angle of mapped quad } i,j}{\text{smallest angle of maped quad } i,j}. \tag{3.53}$$

The distortion decreases as the number of poloidal planes is increased. It is evident that the **S-1** and **S-3** schemes still perform well if the mapped quad does not spread over more than two squares in each direction within the neighbouring poloidal plane. Otherwise the map might jump over grid points, which results in the appearance of the spurious wiggles and ultimately to a decrease of the effective resolution. Applying this constraint, results in a threshold for the distortion (see fig. 3.14) of $d_c \leq 4$ and $d_a \leq 3$. This threshold is based on a reasonable argument, but soft, of

course. Therefore, we require in all simulations that the toroidal resolution is sufficiently high, such that for both distortions it holds:

$$d_c, d_a \leq 4. \tag{3.54}$$

If this threshold value suffices for the individual case, could also be checked a posteriori with convergence tests in N_{pol}. Using in the example $N_{pol} = 20$ reduces the distortion below the specified threshold and the wiggles vanish (see fig. 3.15b).
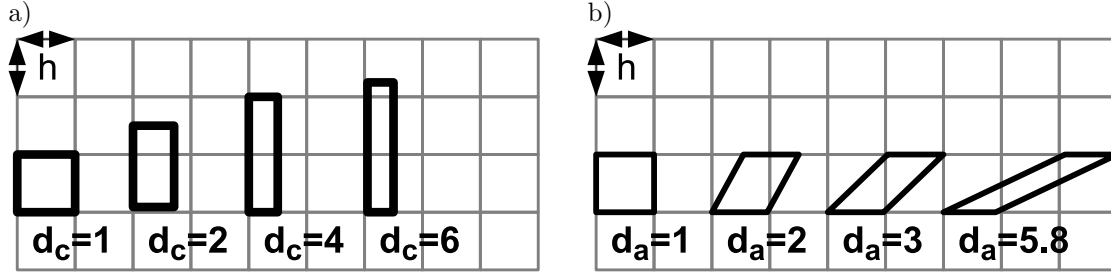
Figure 3.14.: Examples for distortion. Grey squares indicate base cells within the neighbouring poloidal plane. Black quads are examples for mapped quads. The area is thereby preserved. a) Examples for conformal distortion. A threshold of $d_c \leq 4$ ensures that the mapped quad spreads at most over 2 squares. b) Examples for angular distortion, a threshold of $d_a \leq 3$ suffices.
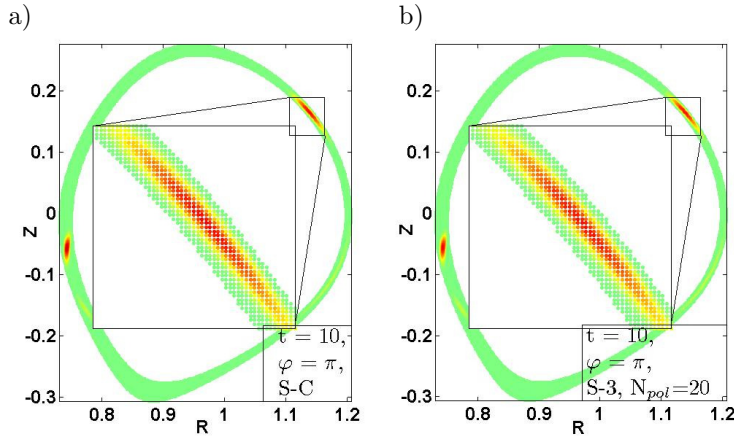

Figure 3.15.: Remedies for the map distortion: a) Same simulation as in fig. 3.13 performed with **S-C** scheme. b) Simulation performed with **S-3** and $N_{pol} = 20$ poloidal planes, i.e. the 11th plane is shown. The distortion from plane to plane is small and the wiggles vanish.

An example for the map distortion around the X-point is plotted in fig. 3.16. For $N_{pol} = 4$ (blue) the mapped quads are strongly distorted as they are squeezed in one direction and stretched in the other. With increasing number of poloidal planes, the distortion reduces drastically. This is also obvious from fig. 3.16b.

Finally, additional convergence tests which are discussed in appendix B.3 show that the support schemes also in general geometries exhibit a faster convergence and a lower numerical perpendicular transport, proving its superiority over the naive scheme.
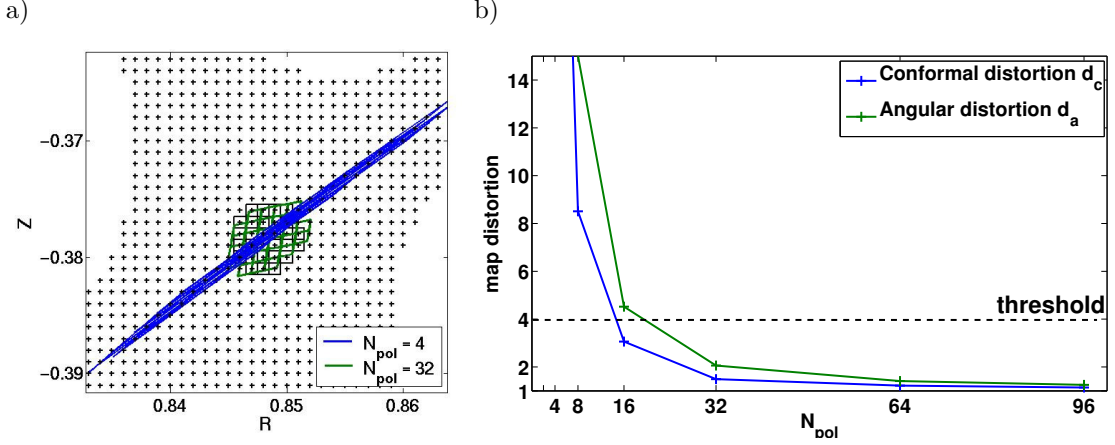
Figure 3.16.: a) Example for map distortion around X-point. Obtained mapped quads (α-direction) for toroidal resolutions $N_{pol} = 4$ and $N_{pol} = 32$. Initial squares are black. b) Map distortion as function of N_{pol} for region around X-point. A resolution of somewhat less than $N_{pol} = 32$ planes is needed to go below the desired threshold.

3.9. Conclusions

In this chapter the numerical approach has been presented. In the presence of an X-point a transformation to field aligned coordinates, as it is routinely done, is not possible since the poloidal field vanishes at the X-point. The construction of a straight field line coordinate system is not possible. Therefore, a cylindrical coordinate system (R, Z, φ) is used with a grid which is Cartesian within the poloidal planes. The discretisation of perpendicular operators is simple and straight forward, whereas for the discretisation of parallel operators a sophisticated field line map is used to exploit the flute mode character.

The main emphasis of this chapter was on the discretisation of the parallel diffusion operator. Two distinct discretisations have been presented: A naive, but at first sight plausible method, and a discretisation via the support operator method which conserves the self-adjointness on the discrete level. It has been shown both, analytically with a simple 2D model problem and by numerical measurements that the support operator method converges much faster being thus the superior method. Moreover, the numerical transport is drastically reduced with the support scheme. The origin of erroneous effects arising in a strongly distorted magnetic field have been identified and can be resolved either via an elegant discretisation of the parallel gradient or by introducing a reasonable resolution constraint. Additional topics related to the field line map approach can be found in appendix B. Parts of this chapter have been published in [96].

Chapter 4.

GRILLIX: A field line map based 3D turbulence code

In this chapter the basic work flow and some details on the implementation of the GRILLIX code is given. GRILLIX is written in Fortran and is hybrid parallelised with OpenMP and MPI. The approach with the Cartesian grid and the field line map is rather uncommon and new in the fusion community. To the knowledge of the author the only yet published code with a remotely similar approach is FENICA [50, 49], which however solves a different set of equations and only contains the parallel gradient but not the parallel diffusion. GRILLIX has been developed independently and essentially in parallel to FENICIA. Due to this new approach, GRILLIX has been developed completely from scratch by me.

4.1. Environment and data flow

The whole GRILLIX code is a closed package consisting of several programs which exchange data among each other. The single programs and the data flow is illustrated in fig. 4.1.

First the equilibrium is established which is specified by parameter in *equi_params.in*. Currently, the following equilibria can be created:

- Axial circular equilibria with prescribed q-profile.

- Axial geometry composed by superposition of a magnetic field from an axial circular geometry with prescribed q-profile and the magnetic field created by a wire in a prescribed divertor region. This results in an axial diverted magnetic configuration with an X-point (see section 6.2).

- Toroidal geometry with a magnetic field configuration which is an actual solution to the Grad-Shafranov-Schlüter equation (see eq. 3.2). The magnetic field is available in terms of analytic functions [111].

The file *equi_params.in* and *grid_params.in*, where parameters for the resolution of the grid are specified, serve as input for the program create_grid@GRILLIX, which is described separately in appendix C. create_grid@GRILLIX creates the file *grid_cart.in* where the Cartesian grid data, i.e. the position of the grid points, the results from the field line tracing, etc., is stored. Mainly for diagnostics purposes also the file *grid_polar.in* is created where grid information of a polar grid is stored. Due to axisymmetry, this data is identical for each plane.

The files *grid_cart.in* and *grid_polar.in*, together with *init_params.in* is taken as input for the program create_init@GRILLIX which creates the initial state. Several different possibilities as initial state can be created such as a random noise, Gaussian blobs, (m, n, r) modes and to a certain extent even field aligned structures. As main@GRILLIX, create_init@GRILLIX is MPI parallelised over the planes, such that each rank takes the same information from *grid_cart.in*

and *grid_polar.in* and writes its data to its own file *snapsX.out*, where *X* stands for the rank of the MPI process or the number of the plane. In addition, it creates the header of the files *diagnostics.out* and *diagnostics_radial.out* in which the diagnostics output from the program main@GRILLIX is stored.
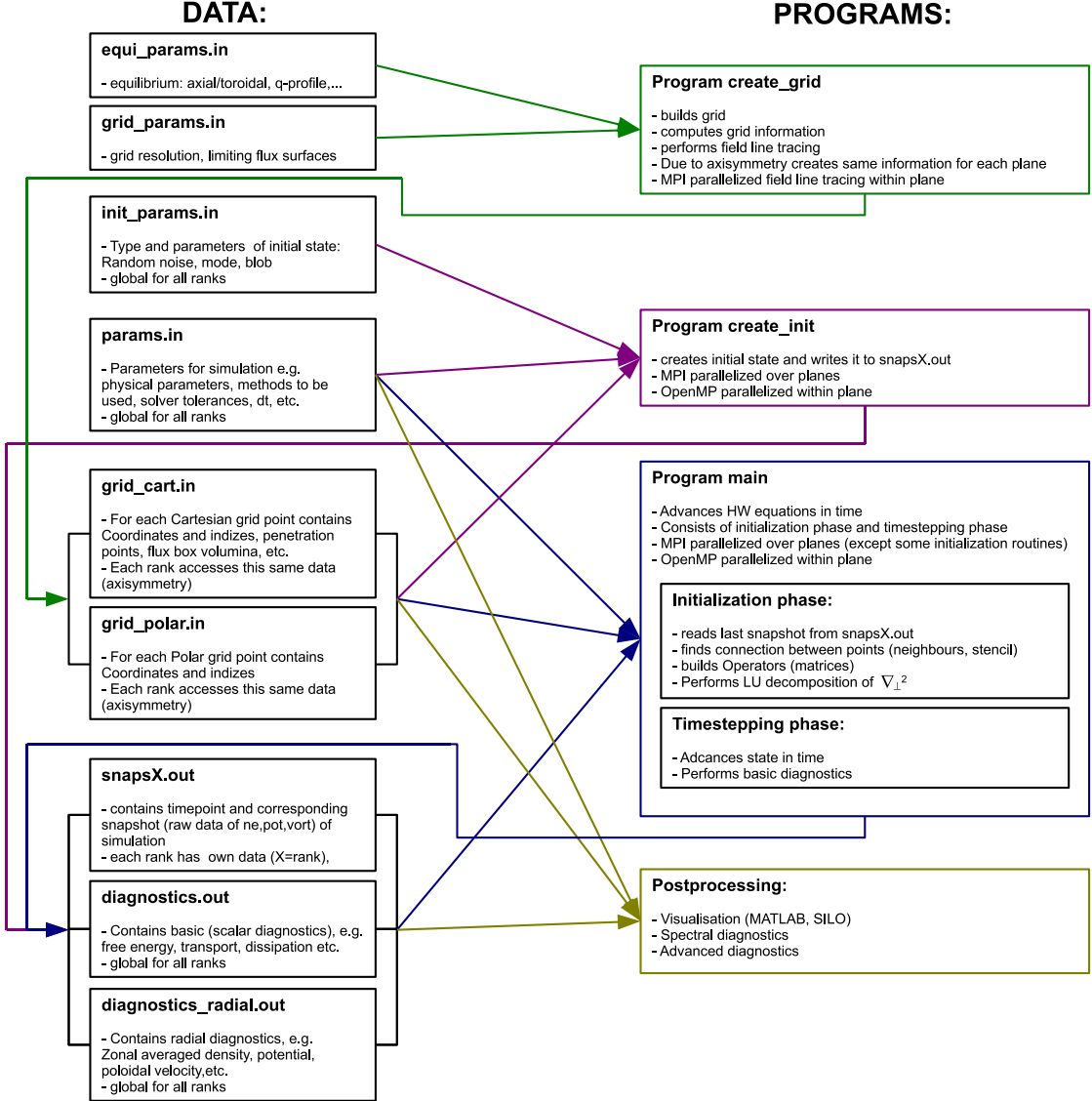
Figure 4.1.: Content of GRILLIX package and data exchange among different subprograms.

In the file *params.in* the parameters for the simulation have to be specified by the user. Besides physical constants, e.g. the adiabaticity (parameter D) or the hyperviscosities ν_n, ν_ϕ, also numerical parameters are specified, e.g. the desired size of the time step dt_{max}, dt_{min}. The maximum equation system which can be solved yet is the Hasegawa-Wakatani equations with curvature (see eqs. 2.39, 2.40). Each term can be switched off and on via parameters separately,

such that e.g. also the parallel diffusion equation or only linear dynamics can be studied.

The program main@GRILLIX consists of an initialization phase and a time stepping phase. During the initialization phase the input from *params.in* and the grid data (*grid_cart.in*, *grid_polar.in*) is read. The last frame from the file *snapsX.out* is taken as start frame, such that the simulation can be restarted at any time. In the initialization an indexing is performed where for each grid point its neighbours are found and the operators (matrices) are built, which remain constant in time.

The initialization phase is followed by the time stepping phase where the quantities are evolved in time. At certain time points, specified by the user in *params.in* via dt_{snaps}, the code writes a full snapshot of the quantities to *snapsX.out*, performs a basic (scalar) diagnostics (dt_{diag1}) and writes the result to *diagnostics.out*, or performs a zonal diagnostics (dt_{diag2}) and writes the result to *diagnostics_radial.out*.

Several post processing routines are available which perform more elaborate diagnostics, e.g. computing spectra. 2D visualisation routines are available as MATLAB [112] scripts and a separate program can transform the raw data from *snapsX.out* to the SILO [113] format, which can be visualized in 3D with e.g. VISIT [114]. All programs and diagnostics tools have been developed by me from scratch.

4.2. main@GRILLIX

In this section the program main@GRILLIX is described in more detail.

4.2.1. Paralellisation scheme

The idea of the parallelisation of main@GRILLIX (and also many other programs/tools of GRILLIX) is a MPI parallelisation over the poloidal planes, i.e. each MPI process, rank, works on its own poloidal plane. The number of MPI processes is thus constrained to the number of poloidal planes. Communication between the ranks appears only if global quantities have to be computed or if parallel operators have to be evaluated. Within each poloidal plane loops are OpenMP parallelised, respectively multi threaded libraries are used.

There are few exceptions of this parallelisation scheme in the initialisation phase. For huge grids the indexing routines which find for each grid point the perpendicular/parallel neighbours can take very long (in the worst case this can result in N^2-loops). Due to axisymmetry, this information is the same for each plane, and instead that each rank computes the same information by itself, this work is also split into chunks to the single ranks and finally gathered at all ranks.

4.2.2. Initialisation phase

A work flow of the initialisation phase of main@GRILLIX is illustrated in fig. 4.2 as a Jackson Diagram [115], as it is executed by a rank.

After the input has been read, a perpendicular indexing is performed, i.e. for each grid point the indices of the 12 next poloidal neighbours are searched. These 12 neighbours are involved in finite difference expressions for the perpendicular neighbours (perpendicular stencil). In addition, if some grid point misses at least one direct neighbour, it is indicated to be a boundary point, on which all quantities are set to zero.

Next, the matrix for the perpendicular Laplace operator $\nabla_\perp^2$ is built, which is approximated

as:

$$\nabla_\perp^2 \approx \sum_{i,j=R,Z} \frac{1}{J} \partial_j \left[J \left(g^{ij} - b^i b^j \right) \right] \partial_i, \tag{4.1}$$

with $J = 1$ for axial and $J = R$ for toroidal equilibria. $g^{ij} = \delta_{ij}$ is the metric tensor and $\mathbf{b}$ is the unit vector of the magnetic field. Due to the assumption of a strong toroidal field and the smallness of the structure, the perpendicular Laplace operator could be simplified even more to $\nabla_\perp^2 = \partial_R^2 + \partial_Z^2$. However, this approximation is not applied here, since the additional terms in eq. 4.1 do not introduce a significant complexity from the computational point of view. The derivatives are discretised via standard second order finite difference methods (9 point stencil). During the time stepping phase equations of the kind $\nabla_\perp^2 \mathbf{x} = \mathbf{z}$, with $\mathbf{z}$ known have to be solved for $\mathbf{x}$. This is easily and rapidly done via a back substitution with the LU decomposition of $\nabla_\perp^2$. The LU decomposition is done with the multi-threaded PARDISO solver from the MKL library [116]. Experience has shown that PARDISO is compared to several tested libraries fast and economic in memory with respect to the matrices used in GRILLIX. It exhibits a reasonable scaling with the number of threads even for the time critical back substitution phase.

The parallel gradient matrices can be stored as blocks on each rank. An off-diagonal block which acts on points in the neighbouring poloidal plane (on plane $k + 1$ for $\mathbf{Q}^\alpha$ and on plane $k - 1$ for $\mathbf{Q}^\beta$) and a diagonal block acting on points of the same plane. Due to axisymmetry, the blocks are identical for all ranks. Parallel neighbours, i.e. grid points which are involved in the interpolation process, are found via another indexing routine. The blocks of the parallel gradient matrices are then filled up with the interpolating coefficients (see appendix B.1). It is also possible to compute the parallel gradient matrices with the coordinate free representation. To this aim, overlaps between quads have to be computed, which is done by the routine given in [117][1]. However, the development of the coordinate free representation is still experimental and not yet optimized (at the moment for N^2 grid points the overlap is computed which is very slow). During the time stepping phase parallel gradient matrices are involved in matrix vector multiplications, i.e. $\mathbf{z} = \mathbf{Q}^{\alpha,\beta} \mathbf{x}$, with $\mathbf{x}$ known. The Recursive Sparse Block library (LIBRSB) [118] is used which performs cache efficient multi-threaded sparse matrix vector operations.

For operations in the buffer zones, close to the boundary, and for diagnostics purposes, flux surface averaged quantities have to be computed in the closed field line region [97]:

$$\langle u \rangle (\rho) = \frac{\int\limits_0^{2\pi} \int\limits_0^{2\pi} d\theta_e d\varphi \, J_e \, u}{\int\limits_0^{2\pi} \int\limits_0^{2\pi} d\theta_e d\varphi \, J_e}, \tag{4.2}$$

where $J_e^{-1} = \nabla \rho \cdot (\nabla \theta_e \times \varphi)$ is the Jacobian of an elementary toroidal coordinate system. In *grid_polar.in* the coordinates of a polar grid and the Jacobian J_e are given as computed by create_grid@GRILLIX (see appendix C). To perform flux surface averages, the quantity is mapped from the Cartesian grid to the polar grid via an interpolation. In analogy to the establishment of the parallel gradient matrix, first a polar indexing is performed, i.e. for each polar grid point the Cartesian neighbours involved in the interpolation are searched. Afterwards, the matrix $\mathbf{P}$ is filled with the interpolating coefficients. Also for the Matrix $\mathbf{P}$ the LIBRSB library is used.

---

[1]Slight errors have been found in the given source code which have been corrected.
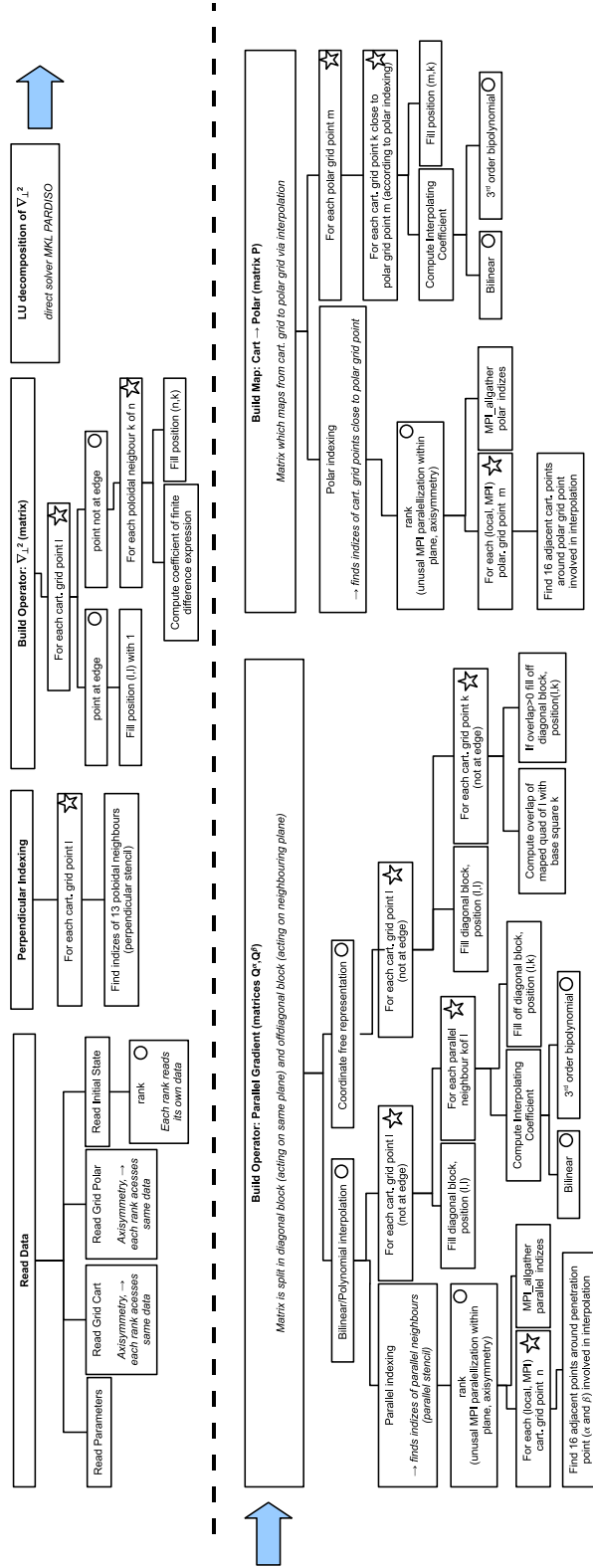
Figure 4.2.: Work flow of initialisation phase of main@GRILLIX as Jackson Diagram [115]. The program, i.e. each rank, executes the blocks from left to right. Downwards, connected with lines, substructures of a block are described. A box with a circle in the upper right corner denotes a loop. A box with a star in the upper right corner denotes an 'if' branch.

4.2.3. Time stepping phase

Time stepping scheme

The time stepping scheme was adopted from the 2D Hasegawa-Wakatani code HW [94].

For time propagation a 3rd order backward differentiation formula (BDF3) is used [119]. Tests with several other methods have shown that this scheme exhibits a robust numerical stability and energy conservation. The temporal discretisation of $\partial_t u = f(t, u)$ is expressed as:

$$u_{t+1} = \frac{18}{11}u_t - \frac{9}{11}u_{t-1} + \frac{2}{11}u_{t-2} + \frac{6}{11}\,dt\,f(t+1, u_{t+1}). \tag{4.3}$$

Hence, three time points have to be stored in memory. BDF3 is an implicit scheme, since f has to be evaluated at time point $t + 1$. Due to the non-linearity, a strict evaluation at time point $t+1$ is difficult and we split f into a part f_{imp} which is still treated strictly implicitly and a part f_{exp} which evaluates the function f at the time point $t + 1$ via a polynomial extrapolation from the three old time steps. For a constant time step dt the final method becomes:

$$u_{t+1} - \frac{6}{11}\,dt\,f_{imp}(t+1, u_{t+1}) = \frac{18}{11}u_t - \frac{9}{11}u_{t-1} + \frac{2}{11}u_{t-2} + \frac{6}{11}\,dt\,f_{exp}(t+1, u_{t+1}), \tag{4.4}$$

$$\text{with:}\quad f_{exp}(t+1, u_{t+1}) = 3\,f_{exp}(t, u_t) - 3\,f_{exp}(t-1, u_{t-1}) + f_{exp}(t-2, u_{t-2}). \tag{4.5}$$

Most terms of the HW equations are treated explicitly in f_{exp}, background gradient source, hyperviscosity, non-linear advection, curvature and sources/sinks in the buffer zones. Due to the fast dynamics along magnetic field lines, the parallel diffusion has to be treated treated implicitly in f_{imp} [120]. Especially in the vorticity equation the effective parallel diffusion coefficient can be large ($\sim D/k_\perp^2$). Introducing for notation the vector $\mathbf{y}(t) = (\mathbf{n}_t, \phi_t)^T$, where $\mathbf{n}_t$ and ϕ_t are vectors containing the discrete values of the density and the potential at the grid points at time point t, the algebraic equation system to be solved in each time step is:

$$\mathbf{A}\mathbf{y}(t+1) = \frac{18}{11}\mathbf{y}(t) - \frac{9}{11}\mathbf{y}(t-1) + \frac{2}{11}\mathbf{y}(t-2) + \frac{6}{11}\,dt\,\mathbf{f}_{exp}\left[\mathbf{y}(t), \mathbf{y}(t-1), \mathbf{y}(t-2)\right]. \tag{4.6}$$

The right hand side with $\mathbf{f}_{exp}$ can be easily evaluated and the matrix $\mathbf{A}$ has the structure:

$$\mathbf{A} = \begin{pmatrix} \mathbf{1} - \frac{6}{11}\,dt\,D\,\mathbf{D} & \frac{6}{11}\,dt\,D\,\mathbf{D} \\ -\frac{6}{11}dt D\,\mathbf{D} & \nabla_\perp^2 \end{pmatrix}. \tag{4.7}$$

Work flow

The work flow of a time propagation step of main@GRILLIX is illustrated in fig. 4.3. The temporal driver works via a reverse communication interface which controls the task. Output is written and/or diagnostics of the data are performed at fixed time intervals. The maximum allowed time step dt_{max} must be supplied by the user and must be chosen small enough to ensure numerical stability for the linear terms. During the simulation the time step is dynamically adjusted according to the maximum $\mathbf{E} \times \mathbf{B}$ velocity:

$$0.1 < \max(v_E/h)dt < 0.3. \tag{4.8}$$

With these criterions fulfilled, there was no run where a numerical instability occurred. The HW equations 2.39 and 2.40 are advanced one time step according to the algebraic equation system 4.6. First the change due to the explicitly treated dynamics is computed (f_{exp}):

- Linear advection of the background:

$$\delta^{-1} w_n \mathbf{v}_E \cdot \nabla \rho = \delta^{-1} w_n \frac{B_{tor}}{B^2} [\phi, \rho]_{R,Z} . \tag{4.9}$$

The parameter w_n can be set by the user to control the background density gradient. The Jacobi bracket is discretised with a second order Arakawa scheme [121].

- Non-linear advection:

$$\mathbf{v}_E \cdot \nabla n = \frac{B_{tor}}{B^2} [\phi, n]_{R,Z} , \tag{4.10}$$

$$B^{-2} \mathbf{v}_E \cdot \nabla \nabla_\perp^2 \phi = \frac{B_{tor}}{B^4} [\phi, \nabla_\perp^2 \phi]_{R,Z} . \tag{4.11}$$

- Hyperviscosity:

$$\nu_n \nabla^{2N} n, \quad \nu_\phi \nabla^{2N} \nabla_\perp^2 \phi, \tag{4.12}$$

with $N = 1, 2, 3$ the desired order. The computation for $N = 3$ is an application of the discrete ∇^4 comprising a 13 point stencil [108] and a successive application of the discrete ∇^2. Points involved in the stencil which are outside the grid are assumed to be zero.

- Curvature terms: For toroidal geometries only the terms arising from the $1/R$ dependence of the toroidal field are respected:

$$\delta^{-1} \mathcal{K}(f) = w_{cv} \frac{2\delta^{-1}}{B^4} \frac{B_{tor}^3}{R} \partial_Z f, \tag{4.13}$$

where $w_{cv} = \rho_s/R_0$ is left as a parameter which can be set by the user to control the strength of the curvature. For axial geometry a curvature can be modelled.

$$\delta^{-1} \mathcal{K}(f) = w_{cv} \delta^{-1} 2 \partial_Z f \tag{4.14}$$

- Buffer zones: Near the boundaries buffer zones are added in which the zonal averaged density perturbation is damped in order to maintain the profile. Also the zonal averaged potential can be damped after the solve step to avoid a spurious poloidal flow creation due to boundary effects.

$$\partial_t n = \cdots - g(\rho) \langle n \rangle, \quad \phi \to \phi - dt\, g(\rho) \langle \phi \rangle, \tag{4.15}$$

$$g(\rho) = w_{bff1} \exp\left[-\frac{(\rho - \rho_{min})^2}{(p_{bff}(\rho_{max} - \rho_{min}))^2}\right] + w_{bff2} \exp\left[-\frac{(\rho - \rho_{max})^2}{(p_{bff}(\rho_{max} - \rho_{min}))^2}\right].$$

$w_{bff1}, w_{bff2}, p_{bff}$ can be set independently by the user to control the strength of the damping for the density and the potential in the buffer zones. $\langle n \rangle$ and $\langle \phi \rangle$ are computed via the map to the polar grid and an integration along flux surfaces on the polar grid (see eq. C.11).

As the right hand side of eq. 4.6 has been computed, the linear equation system is solved. An iterative GMRES algorithm is applied from CERFACS [122]. CERFACS works as a reverse communication interface and the programmer has to supply instructions for matrix vector multiplication, preconditioning and a dot product.

The preconditioning matrix $\mathbf{M}$ is obtained simply by neglecting all terms $\propto dt$ in $\mathbf{A}$:

$$\mathbf{M} = \begin{pmatrix} \mathbf{1} & \\ & \nabla_{\perp}^2 \end{pmatrix}. \tag{4.16}$$

Thus n and ϕ are decoupled in $\mathbf{M}$, the preconditioning operation remains local on each plane and no communication between the poloidal planes is necessary. The equation $\nabla_{\perp}^2 \mathbf{x} = \mathbf{z}$, with $\mathbf{z}$ known is solved via a back substitution of the previously (initialisation phase) LU-decomposed $\nabla_{\perp}^2$ with MKL PARDISO.

For the matrix vector product $\mathbf{z} = \mathbf{A}\mathbf{x}$, with $\mathbf{x}$ known, the parallel diffusion operator has to be evaluated, which involves a communication across the poloidal planes. The parallel diffusion operator is computed stepwise and involves in total four communications of the whole data for the support scheme and two communications for the naive scheme. For the local matrix vector multiplication the multi-threaded LIBRSB library [118] is used.

The evaluation of the dot product is first computed locally on each rank and the global dot product is obtained via a call to MPI_Allreduce. If the absolute error $||\mathbf{A}\mathbf{x}-\mathbf{z}||_2$ and the relative error $||\mathbf{A}\mathbf{x}-\mathbf{z}||_2/||\mathbf{x}||_2$, with $\mathbf{z}$ known, is below a desired threshold, $\mathbf{x}$ is returned as solution.

Finally, a damping of the zonal potential ϕ_{t+1} in the buffer zones is applied and the vorticity at the time step $t+1$ is computed.

4.3. Computational resources and efficiency

Typical runs of GRILLIX were performed with up to few tens of poloidal planes $N_{pol} \sim 2 \dots 32$, and depending on resolution and size of the simulation domain around $\sim 10^6$ grid points within a poloidal plane. The time critical phase is the time stepping and the size of the time step adjusts automatically according to eq. 4.8, which was depending also on resolution around $dt \sim 1 \cdot 10^{-2}$ (in units of L_n/c_s). Typical execution times for a single time step were around $\approx 1-10$s with a reasonable number of $N_{omp} = 10$ OpenMP threads.

For the demonstration simulation presented in section 5.2.1 the execution time for a single time step was ≈ 4s with 60 cores (6 MPI processes $\times$ 10 OpenMP threads). The simulation was carried out to $t \approx 1.5 \cdot 10^4$, such that the computation took 71d, i.e. $\approx 10^5$CPU hours. The memory usage per node was ≈ 10GB. However, most simulations were only carried out to $t \approx 3000$ and a typical run required roughly $\approx 2 \cdot 10^4$CPU hours. The total spent resources within this work can only be estimated to around $\approx 3 \cdot 10^6$CPU hours, which were performed mostly on HYDRA and TOKP at Rechenzentrum Garching (RZG). Few test runs were also performed on HELIOS at the Computational Simulation Centre (CSC).

To benchmark GRILLIX on its computational efficiency, a problem of typical size as described in section 5.1 and section 5.2.1 is considered. Per plane 1 752 291 grid points are used. The time critical part in the execution is the time stepping phase which is investigated here. The performance benchmarks were executed on the TOKP cluster at RZG.

4.3.1. MPI scaling

Since the number of MPI processes is constrained to the number of poloidal planes, a strong scaling scan with respect to the MPI parallelisation cannot be performed. Instead the number of grid points per plane is kept constant and the number of poloidal planes is varied together with the number of MPI-processes (weak scaling). The number of OpenMP threads was held thereby constant ($N_{OMP} = 8$) and 2 processes per node were used.

In fig. 4.4 the execution time for various phases of the time stepping in dependence of the number of poloidal planes is shown. It is obvious that the solve phase (step implicit) is the

Figure 4.3.: Work flow of time stepping phase of main@GRILLIX as Jackson Diagram.
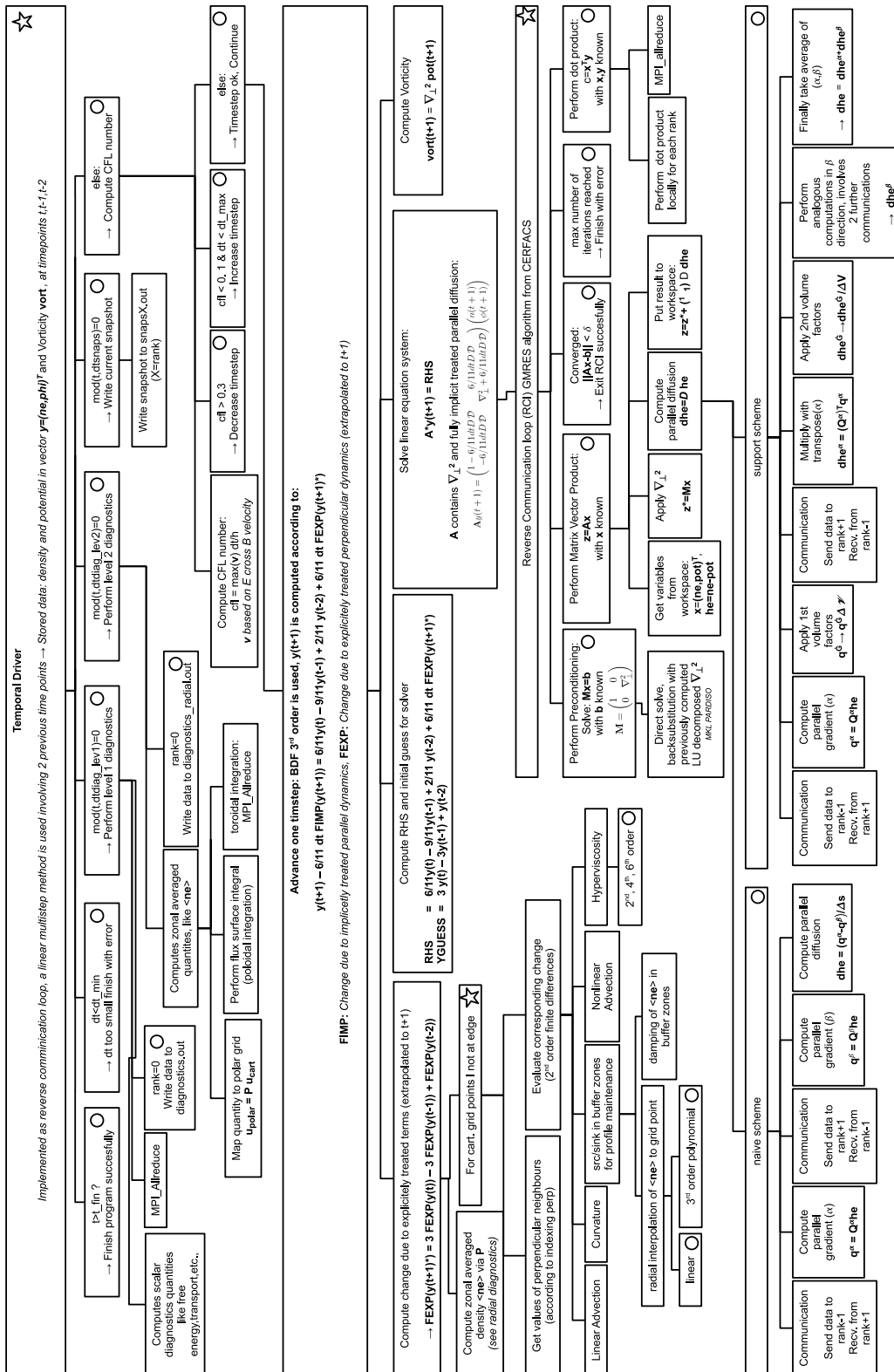
dominant contribution. With increasing number of poloidal planes, the parallel dynamics gets stiffer and the GMRES algorithm requires more iterations for convergence. Therefore, also the execution time increases with the number of poloidal planes. The execution time of the explicit terms and the single parts involved in the GMRES algorithm, i.e. preconditioning, multiplication and dot product, remain roughly constant with the number of poloidal planes, since the workload per process for a single execution of these parts remains also constant.

a)　　　　　　　　　　　　　　　　　　　　　b)
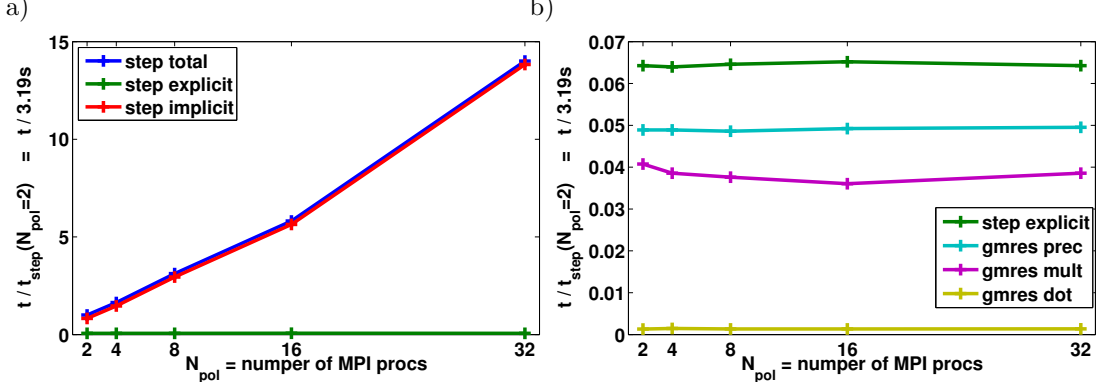
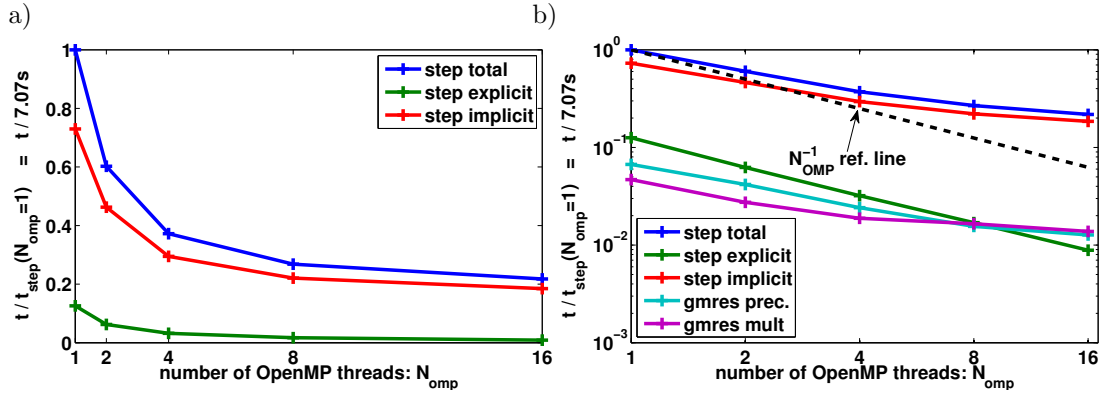**Figure 4.4.:** MPI (N_{pol}) scaling of GRILLIX for fixed grid size per poloidal plane. a) Execution time of time stepping phase. b) Execution time for explicit time stepping, and single execution time of preconditioning (back substitution), matrix vector multiplication and dot product performed within GMRES algorithm.

4.3.2. OpenMP scaling

The OpenMP parallelisation is benchmarked at fixed problem size (strong scaling). In fig. 4.5 the execution time for various phases is shown in dependence of the number of OpenMP threads N_{OMP}. Since the parallelisation of the explicit time stepping phase is trivial, a very good scaling of nearly N_{OMP}^{-1} is obtained. However, the total execution time is determined by the solve phase which scales worse. Within the GMRES algorithm the time critical parts are the preconditioning and the matrix vector multiplication. The parallelisation of the preconditioning, which constitutes a back substitution into the initially LU decomposed matrix $\mathbf{M}$, is a difficult task in principle and is left to the MKL-PARDISO library. The matrix vector multiplication $\mathbf{z} = \mathbf{A}\mathbf{x}$ involves MPI communications between neighbouring poloidal planes and local sparse matrix vector multiplications. The local multiplications are performed with LIBRSB [118] which was especially for multiplications with the transposed matrix $(\mathbf{Q}^{\alpha,\beta})^T$ up to a factor 1.8 faster then the sparse BLAS routines from MKL [123].

Figure 4.5.: OpenMP scaling of GRILLIX for fixed problem size ($N_{pol} = 2$): a) Execution time of time stepping phase. b) Execution time of time stepping phase, and single execution time of preconditioning (back substitution) and matrix vector multiplication performed within GMRES algorithm in loglog-plot.

Chapter 5.

Axial circular geometry

In this chapter results of GRILLIX turbulence simulations in axial circular geometry are presented. Phenomena of the 3D HW drift wave system are presented and illustrated with example simulations. A large part of this chapter is devoted to benchmarks and consistency checks of GRILLIX, which is still possible for such a simple geometry. Due to the rather uncommon numerical approach, many benchmarks have been performed during the development of GRILLIX. However, only the most important ones are shown in this chapter and further selected benchmarks are presented in appendix D.

5.1. Comparison with sheared slab geometry and standard parameters

Advanced results of the HW model are available for sheared slab geometry [88, 90, 91]. This geometry can be approximated in the framework of GRILLIX by using a sufficiently large flux annulus as simulation domain, i.e. $W_\rho := \rho_{max} - \rho_{min} \ll \rho_{min}$. It was found (see especially [91]) that in 3D sheared slab geometry there is only one single dimensionless parameter[1] which determines the turbulent transport as well as all other physical characteristics of HW[2].

$$C_{HW} = \frac{\rho_s}{L_{DW}}, \quad \text{with:} \quad L_{DW} := \left[\frac{M_i\, T_e\, n_0\, \eta_\parallel\, L_s^2}{e\, L_n B^3} \right]^{1/3}, \tag{5.1}$$

where L_s is the magnetic shear length. In the parameter C_{HW} all physical relevant parameters are combined $(T_e, n_0, B, L_n, \nu_e, L_s)$. In the 2D simulations performed in section 2.5 the parameter $\mathcal{C}$ was still sufficient to describe the whole system. However, as one introduces shear into the system, it is obvious that also the magnetic shear length (or something similar) must enter into such a single dimensionless parameter. Via a proper normalisation of the 3D HW equations [88] the parameter C_{HW} can then be motivated. C_{HW} can be regarded as measuring the effect of the magnetic shear or the Larmor radius.

A circular axial geometry can be mapped to sheared slab geometry by expressing the magnetic shear length as $L_s = qL_{ax}/(2\pi\hat{s})$, where $\hat{s} = \rho/q\, dq/d\rho$. The knowledge about the existence of such a single dimensionless parameter is very helpful in choosing a reasonable q-profile for first test simulations with GRILLIX. Having fixed all other parameters, the q-profile should be chosen such that the parameter C_{HW} is constant across the whole domain. With such a q-profile the turbulent transport is expected to be constant at each radial position and no initially needless complication is introduced into the system. Requiring a constant parameter C_{HW} radially across

---

[1]The original nomenclature from [88, 91] is $\hat{\rho}_s$ or $\rho = (2\pi)^{2/3}\hat{\rho}_s$ [90]. I will follow in this thesis the convention of [90], but call the parameter C_{HW} instead of ρ, since it might lead to confusion with the flux surface label.

[2]As in the original papers, SI units have to be used here for the computation of L_{DW}.

the flux annulus, leads to q-profiles of the form[3]:

$$q(\rho) = \frac{1}{1/q_0 - \alpha \ln(\rho/\rho_0)} \quad \text{with:} \quad \alpha = \frac{(C_{HW} \, \rho_s \, B)^{3/2}}{\sqrt{M_i \, T_e \, n_0 \, \eta_\parallel / (e \, L_n)} \, L_{ax}/(2\pi)}, \quad (5.2)$$

where $\rho_0 = (\rho_{max} + \rho_{min})/2$ and $q_0 = q(\rho_0)$ a desired value for the safety factor in the center of the flux shell.

If not stated differently, the following standard parameters and standard resolution are used within this chapter. This standard test case models the edge region of a tokamak with roughly the following parameters:

$$T_e = 80\text{eV}, \qquad n_0 = 4.5 \cdot 10^{13}\text{cm}^{-3}, \qquad B_0 = 2.5\text{T}, \qquad R_0 \hat{=} \frac{L_{ax}}{2\pi} = 165\text{cm},$$

$$a = 30\text{cm}, \qquad L_n = 3.65\text{cm}, \qquad M_i = 3670 m_e, \qquad q_0 = 1.5. \quad (5.3)$$

The q-profile is chosen such that the parameter $C_{HW} = 0.8$ is constant across the whole domain, which yields $\alpha \approx 0.464$. The standard resolution is $N_{pol} = 6$ poloidal planes and $h = 2/3\rho_s$. A third order hyperviscosity (∇^6) with coefficients of $\nu_n = \nu_\phi = 1 \cdot 10^{-3}$ is used. The standard radial width of the flux shell is $W_\rho = 210\rho_s$. At the radial edges of the domain (buffer zones) the zonal averaged density is damped to keep up the gradient drive. The zonal averaged potential is also damped in the buffer zones to avoid a spurious momentum input into the system due to boundary effects [91] ($w_{bff1} = w_{bff2} = 1, p_{bff} = 0.02$). The simulations were initialized with a small random noise in the density perturbation ($n < 0.1$). Flux surfaces are labelled with $\rho = \sqrt{x^2 + y^2}$ (in units of ρ_s). The background density is assumed to be constant on flux surfaces with a uniform background density gradient and the normalisation length is chosen to be equal to this density gradient length, i.e. $L_\perp = L_n$. In terms of GRILLIX parameters this yields finally $D = 2.4$ (see eq. 2.41) and $w_n = \delta = 0.014$ (see eq. 2.38). The results are presented in dimensionless units and can be translated to physical units via eqs. 2.36. By default, the simulations are performed with the **S-3** scheme for the parallel diffusion operator, i.e. support scheme with 3rd order polynomial interpolation.

It is not the goal of this chapter to supply precise quantitative results but to present the basic physical mechanisms of the 3D HW model and show that these can also be obtained with GRILLIX. Therefore, many simulations presented here were not run until a full saturated state and might be slightly under resolved. Mostly qualitative results are shown, for which in many cases a run with a moderate resolution and a moderate simulation time sufficed. Details about the convergence behaviour for a demonstration run is given in section 5.5.2. Obtaining precise quantitative results with GRILLIX would be overkill and for such geometries other codes and approaches exist which are computationally much less expensive, since these do not keep the full flux surface but only a small representative part of it.

5.2. No curvature

In this section results of simulations which were performed without curvature, $\mathcal{K} = 0$, are presented..

5.2.1. Demonstration run

Snapshots of the density perturbation and the potential at different stages of a simulation performed with the standard parameters are shown in fig. 5.1. During the initial linear phase

---

[3]Also for the computation of α SI units have to be used.

unstable drift waves develop which propagate poloidally around the annulus. The electron dia-magnetic drift direction is counter-clockwise. Due to the finite shear, the structures are not as radially elongated as in the simplified 2D model of section 2.5 (compare with fig. 2.3) but are tilted with respect to the flux surfaces, yielding crossed structures. At the boundaries of the domain all quantities are set to zero ($n = 0$, $\phi = 0$, $\nabla^2_\perp \phi = 0$), which models an impenetrable wall. Therefore, an accumulation of drift waves can be observed close to the boundaries. The final result was found to be largely independent on the effects close to the boundaries as long as the radial width of the flux shell was sufficiently large (see section 5.5.3).

At some later stage a turbulent state developed where mainly isotropic structures can be seen in the density fluctuations. In the potential already a strong shearing of the vortices is apparent yielding poloidally elongated structures. Some structures repeat along the poloidal direction, indicating resonant surfaces for which $k_\parallel \propto n - m/q \approx 0$, where m is a poloidal and n an axial mode number. This becomes clearer as spectra in section 5.2.3 are discussed.

5.2.2. Zonal flows

In the final saturated state of the simulation (fig. 5.1 lower row) a robust zonal flow has developed. Zonal flows [124, 125] are electric field fluctuations which are constant on flux surfaces, but radially varying, i.e. $m = n = 0$, $r \neq 0$, where r is a radial mode number. Zonal flows are fed or damped non-linearly by the drift wave turbulence, where the turbulence itself is fed by the background gradients. The Reynolds stress acts as a mediator between drift waves and the zonal flow. They do not contribute to the transport but may influence it by shearing the turbulent eddies apart as they propagate radially.
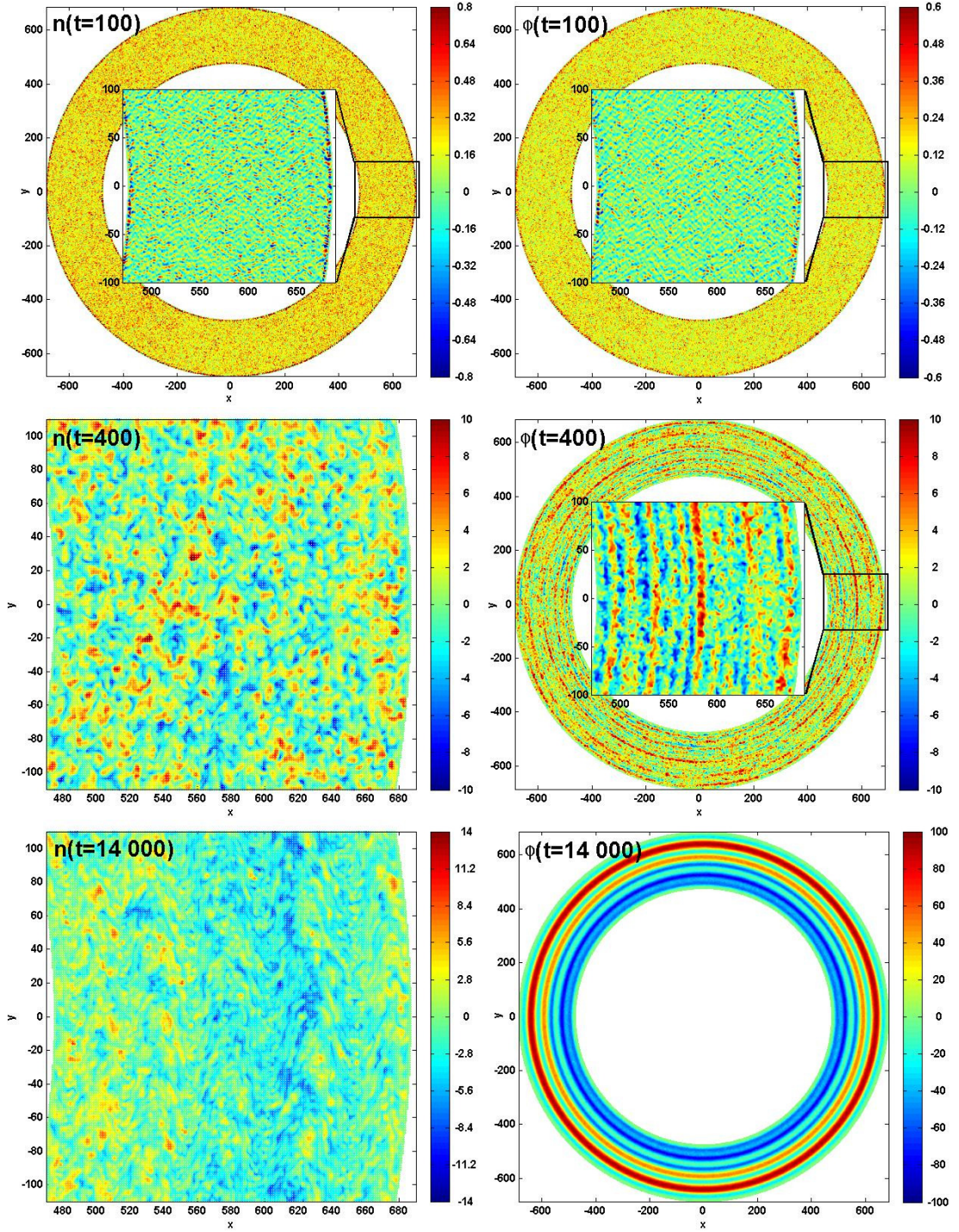
By taking the flux surface average of the vorticity equation 2.40, the temporal evolution of the zonal flow velocity in the sheared slab limit[4] can be derived as [126]:

$$\frac{\partial}{\partial t} \langle v_\theta \rangle = -\frac{\partial}{\partial \rho} \langle v_\theta v_\rho \rangle + (-1)^{k-1} \nu_\phi \frac{\partial^{2k}}{\partial \rho^{2k}} \langle v_\theta \rangle, \tag{5.4}$$

where ρ, θ are polar coordinates and $v_\theta = \partial \phi / \partial \rho$ and $v_\rho = -\rho^{-1} \partial \phi / \partial \theta$. The quantity $\Pi_{\rho\theta} := \langle v_\theta v_\rho \rangle$ is called the Reynolds stress. The right term describes collisional dissipation of the flow. Within the HW model, anisotropic velocity fluctuations can cause an acceleration or deceleration of a large scale poloidal flow. Since the advective derivative, the origin of the force term for the poloidal velocity, does not act as an energy source/sink but merely as a transfer of energy between different modes, this mechanism can be viewed as a transfer process for energy from the turbulence to the zonal flow and back. Hence, in an ad hoc model the turbulence/zonal-flow system is described by a 0-D predator-prey model (Lotka-Volterra equations) [127, 128], where the interaction is described with scalar parameters. A sketch of the turbulence/zonal-flow system is illustrated in fig. 5.2a.

Under the influence of a radially sheared poloidal flow, a radially propagating eddy is stretched and distorted since different parts of the eddy are advected at different velocities (see fig. 5.2b). This may result in a breakup of the eddy reducing its radial extent and a stronger coupling to small scale dissipation. The correlation length of the eddy is reduced and thus the effective step size of turbulent transport [124, 129]. It is this quenching of turbulent transport which drives a large interest of the fusion community into zonal flow research, being a crucial element in the transition from the low confinement regime (L-mode) to the high confinement regime (H-mode) in tokamaks [130].

---

[4]Taking the circular shape of the flux surfaces into account yields: $\frac{\partial}{\partial t} \langle v_\theta \rangle = -\frac{1}{\rho^2} \frac{\partial}{\partial \rho} \left[\rho^2 \langle v_\theta v_\rho \rangle \right] +$ $(-1)^{k-1} \nu_\phi \frac{\partial}{\partial \rho} \langle \nabla^{2k-2} \nabla^2_\perp \phi \rangle$.

Figure 5.1.: Snapshots of density perturbation n (left column) and potential ϕ (right column) of demonstration simulation. Upper row: Late linear phase ($t = 100$), middle row: turbulent phase ($t = 400$), lower row: saturated final state ($t = 14000$). For units see eqs. 2.36 and 5.3.

a)
b)
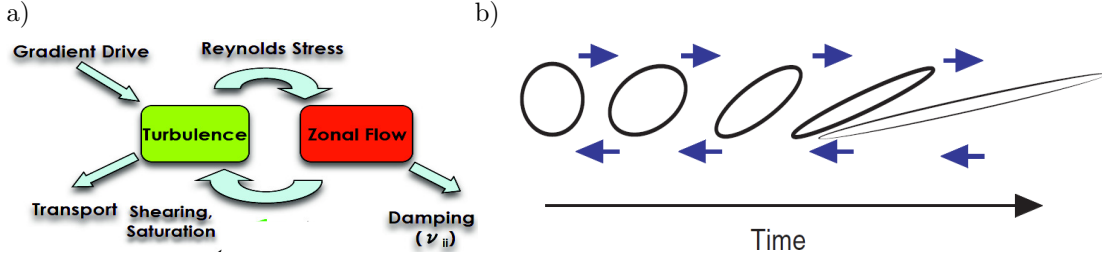
Figure 5.2.: a) Paradigm of zonal flow drift wave turbulence. Figure taken from [131]. b) Shearing of vortex, figure taken from [124].
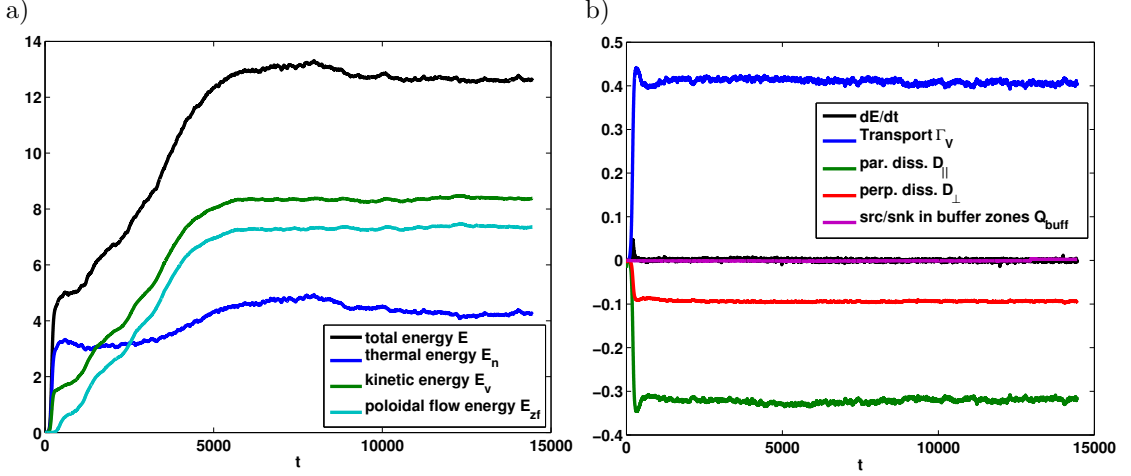
5.2.3. Diagnostics

The simulations of GRILLIX can be diagnosed with several tools. In fig. 5.3a the evolution of the fluctuation free energy of the system is plotted, which can be split into a thermal and a kinetic part (see eq. 2.55). The kinetic part can again be split up into kinetic energy contained in the zonal flow and kinetic energy contained in the turbulence. The fluctuation free energy rises initially due to the linear instability until the non-linear terms cause a stop of the growth. Shortly after this transition the zonal flow energy rises. The turbulent kinetic energy is the difference between total kinetic energy and the zonal flow energy. On a very long time scale energy is continuously pumped from the gradient source into the turbulence into ultimately the zonal flow until at roughly $t = 5000$ a stationary saturated state has been reached. The thermal part of the fluctuation free energy remains roughly on the same level after the first transition and only a small evolution of the density profile was be observed.

In fig. 5.3b the temporal evolution of the time rate of the fluctuation free energy is plotted. It is balanced by transport (= gradient drive), parallel/perpendicular dissipation (see eq. 2.59) and sources/sinks which have been added in the buffer zones (see eq. 5.11). The transport rises until $t \approx 300$ during the linear phase, drops slightly with the rise of the zonal flow and saturates quickly. The fact that the transport is saturated, while the zonal flow energy still rises shows that the zonal flow does not contribute to the transport. As discussed in the previous section, the zonal flow might merely influence the transport by shearing the drift wave eddies apart, therefore the shear of the poloidal flow velocity $\partial v_\theta / \partial \rho$ being of importance for the final transport level. The flow shear saturated also on a comparable time scale as the transport.

To gain more insight into the development of the zonal flow and its saturation, we consider the temporal evolution of the zonal flow velocity in fig. 5.4a. In an early phase the zonal flow is small in amplitude but has a large radial mode number. The zonal flows subsequently merge together to form structures of lower radial mode number storing a larger kinetic energy. The flow shear is not appreciably altered during this process explaining the fast saturation of the transport. In fig. 5.4b zonal averages of various quantities are shown at the final time point of the simulation. The radial dependence of the zonal averaged flow shear ($\langle dv_\theta/d\rho \rangle$) is sawtooth like, and it can be deduced that the zonal flows have steep minima and broad maxima. This characteristic asymmetric zonal flow shape was also found previously [90, 91] with a flux aligned code. It is explained by a self-focusing mechanism where drift waves are repelled from negative (with respect to the electron diamagnetic drift direction) flows and attracted by positive flows. The zonal averaged density perturbation is more irregular but a slight density corrugation in accordance with the zonal flow pattern can be seen. Moreover, $\langle n \rangle$ is slightly hollow, which reflects a small transport imbalance between the inside and outside of the flux shell. This might be an effect of the circular geometry (finite shell width) which is not taken into account in the

a)

b)

Figure 5.3.: Scalar diagnostics for demonstration simulation: a) Components of fluctuation free energy, b) temporal change of fluctuation free energy, transport, dissipation, sources/sinks. For units see again eqs. 2.36 and 5.3.

parameter C_{HW}. Even hollower profiles for $\langle n \rangle$ were obtained in annuli with larger ratios of W_ρ / ρ_0, where the effects of the circular geometry are stronger.

a)

b)
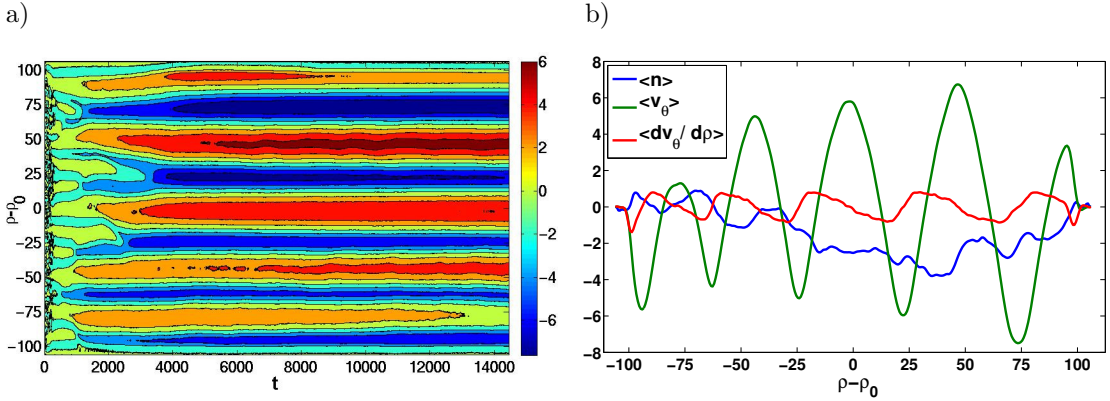
Figure 5.4.: a) Temporal evolution for radial profile of zonal averaged poloidal flow velocity. b) Flux surface averaged quantities at the end of the simulation $t = 14\,448$.

In fig. 5.5a the amplitude spectrum of the potential taken along the poloidal direction is plotted in dependence of the flux label. Peaks in the spectrum can be seen clearly in accordance with resonant surfaces, i.e. at the center of the flux shell for example $q = 3/2$ and therefore structures with a poloidal mode number of $m = 3, 6, 9, \ldots$ are dominant. These modes represent structures with $k_\parallel \approx 0$ which encounter only weak parallel dissipation. Accordingly also at other low rational surfaces peaks arise. In fig. 5.5b amplitude spectra are shown for the central flux surface where $q = 3/2$. Clearly, the $k_\parallel \approx 0$ structures are visible for all quantities. At higher k_θ these resonant modes are weaker, but rudimentary an inertial range is visible where the spectra might follow power law like dependencies. However, due to the low resolution of only $2/3\rho_s$, the energy

input range and the viscous range might not be well separated, such that an inertial range might not have developed sufficiently. There could be still a significant contribution of the even smaller scales to the transport, which peaks around $\approx \rho_s$ and falls off only slowly towards high k_θ. The spectra are a first indication that the field line map works. In contrast to field aligned codes, the computational grid of GRILLIX has no information about the magnetic field line structure. The autonomous development of field aligned structures, which are also radially well resolved, is a consequence of the discrete parallel diffusion operator, which gives qualitatively the expected result.

a)

b)
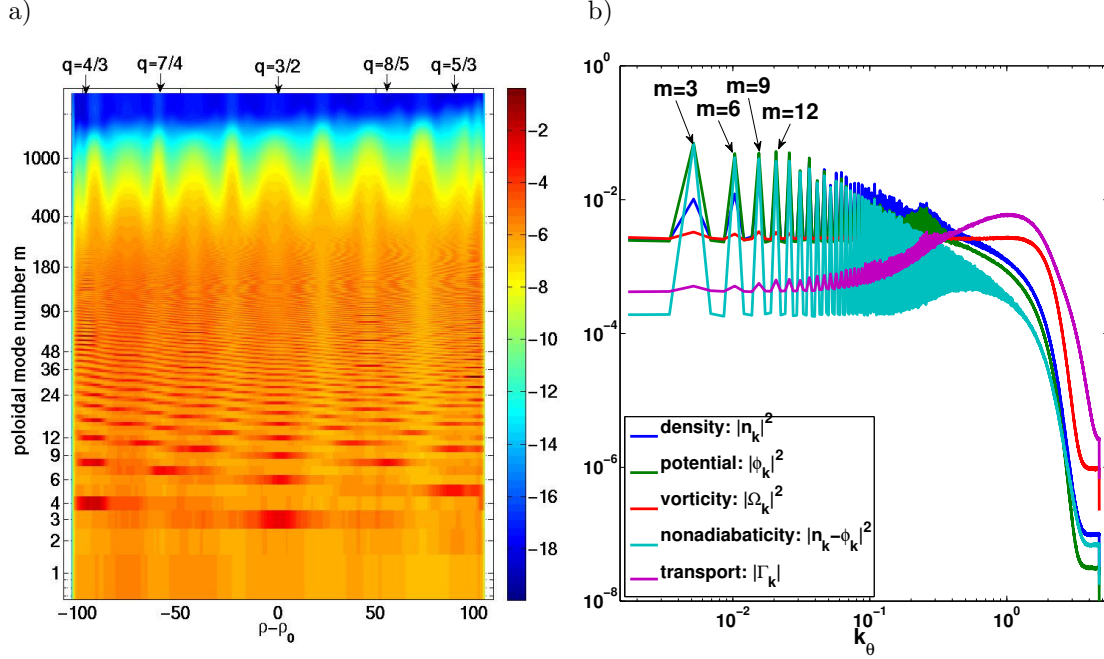
Figure 5.5.: Poloidal amplitude spectra of demonstration simulation averaged between $t = 10\,000 - 14\,000$ over 801 snapshots. a) Poloidal spectrum of potential, $\log |\phi_{k_\theta}|^2$, in dependence on flux surface label. b) Poloidal amplitude spectra at center of flux shell ($\rho = \rho_0$).

The structures can also be illustrated along the parallel direction. In fig. 5.6 the fluctuating part of the nonadiabaticity $(n - \phi - \langle n - \phi \rangle)$ is plotted on flux surfaces, i.e. at fixed ρ in dependence on the axial coordinate z and the geometrical poloidal angle θ. For the establishment of these plots the quantities were assumed to be piecewise constant along magnetic field lines half way towards neighbouring poloidal planes. The transition between poloidal planes is indicated with dotted black lines. It is obvious that the nonadiabaticity is smooth along magnetic field lines and there are no jumps at the transition between neighbouring planes. This shows that the field line map does not introduce any numerical artefacts, but the field alignment happens automatically during the simulation. On rational surfaces (fig. 5.6b) the structures seem to be slightly broader in the poloidal direction than on irrational surfaces (fig. 5.6a). This might be explained again by the fact that on rational surfaces poloidally smooth structures with $k_\parallel \approx 0$ can develop which encounter only weak parallel dissipation.

In fig. 5.7 the fluctuating nonadiabaticity is plotted along a sample magnetic field line running

in an irrational surface. For the establishment of this plot a magnetic field line was traced a fixed distance and at every intersection with a poloidal plane the value is interpolated, which is indicated with crosses. Note again that the structure is smooth (in the numerical sense) along the magnetic field line.

a)

b)
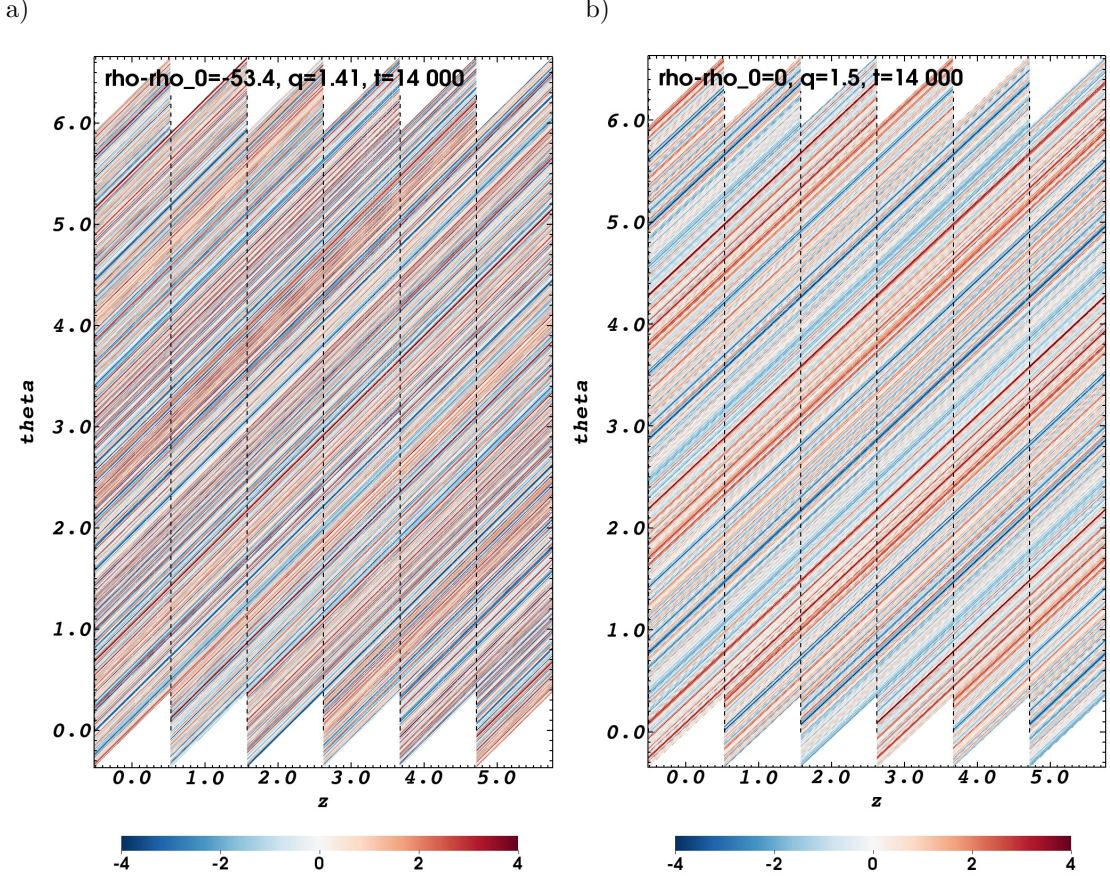
Figure 5.6.: Fluctuating part of nonadiabaticity $(n - \phi - \langle n - \phi \rangle)$ on flux surfaces at $t = 14\,000$ on a) irrational surface $\rho - \rho_0 = -53.4$, $q = 1.41$ and b) on rational surface $\rho = \rho_0$, $q = 1.5$. Dashed lines indicate transitions between poloidal planes.

5.2.4. Parameter scan over C_{HW}

To show the qualitative behaviour of the system in dependence of the parameter C_{HW}, the q-profile is modified according to:

$$q(\rho) = \frac{1}{1/q_0 - \alpha \ln(\rho/\rho_0)} + \beta \left(\rho - \rho_0 \right), \tag{5.5}$$

such that the parameter C_{HW} is not radially constant across the flux shell but varies. In fig. 5.8a,b the temporal evolution of the zonal averaged density perturbation and the poloidal flow velocity is shown for a simulation with $\alpha = 0.464$ and $\beta = -4$. For all other quantities the standard
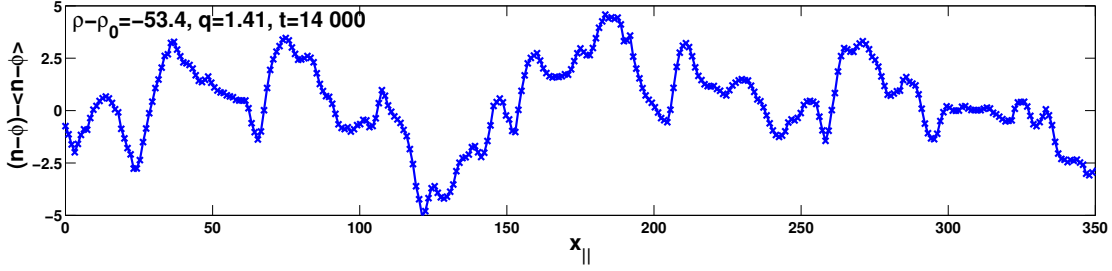
Figure 5.7.: Fluctuating part of nonadiabaticity along sample magnetic field line running in $\rho - \rho_0 = -53.4$, $q = 1.41$ flux surface at $t = 14\,000$. The parallel coordinate $x_{\parallel}$ is measured in $L_{\parallel} = L_{ax}/(2\pi)$ (see eqs. 2.36).

parameters were used, except for $N_{pol} = 12$, which makes no difference for a qualitative discussion. The parameter C_{HW} varies from 0.39 at the inner limiting flux surface to 0.62 at the outer limiting flux surface. It is immediately apparent that in the region of low C_{HW} there are no zonal flows produced or at least their growth is strongly impeded. This result is consistent with the findings of [90, 91] where a bifurcation in the parameter C_{HW} was found via numerical simulations. Starting a simulation from initial random noise, below a critical value of $C_{HW} = 0.4$, no zonal flows were produced, whereas for larger values zonal flows were produced. As shown in the previous section, for $C_{HW} = 0.8$ a regular zonal flow was obtained also with GRILLIX. The result of this section together with the result of appendix D.1, where simulations with different but radially constant C_{HW} are shown, indicate also a bifurcation in C_{HW} at a value of around $\approx 0.4 \ldots 0.5$, which is in very good agreement.

Moreover, the zonal averaged density perturbation develops towards a positive bump. The turbulent radial transport on the inside of the flux shell, where C_{HW} is small, is larger, whereas it is smaller on the outside of the flux shell, where C_{HW} is bigger and the density perturbations pile up to a positive bump. This picture is also consistent with the findings of [88, 90, 91] which found a larger turbulent transport[5] for lower C_{HW}. It is also supported by the results of appendix D.1. Since the evolution of the density profile is a process which takes place on a long time scale, the simulation is not run until complete saturation but only trends are shown here.

5.3. Curvature

The major contribution to the curvature in a tokamak is usually due to the $1/R$ dependence of the dominant toroidal field. We model this curvature in axial circular geometry without affecting the geometry. Therefore, still the same axial circular equilibrium with $B_z = 1$ is used to compute the field line map (parallel operators), but the curvature term $\mathcal{K}$ is modelled as obtained from a $1/R$ dependence of the toroidal field. This leads to a curvature term of

$$\mathcal{K}(f) = 2w_{cv}\frac{\partial}{\partial y}f, \tag{5.6}$$

where $w_{cv} = L_{\perp}/R_0$ with R_0 the major radius of the tokamak to be modelled.

---

[5]Actually, according to [88, 90, 91] the turbulent particle flux increases with decreasing C_{HW} in units of $D_{DW} := L_{DW}/t_0 \propto L_s^{2/3}$ (see [90] for definition of t_0). Leaving all parameters except the shear length L_s constant, as was done here, yields also a larger turbulent particle flux at lower $C_{HW} \propto L_s^{-2/3}$ in physical units and also in GRILLIX units (L_s does not enter the normalisation 2.36).

a) n:

b) $\langle v_\theta \rangle$:
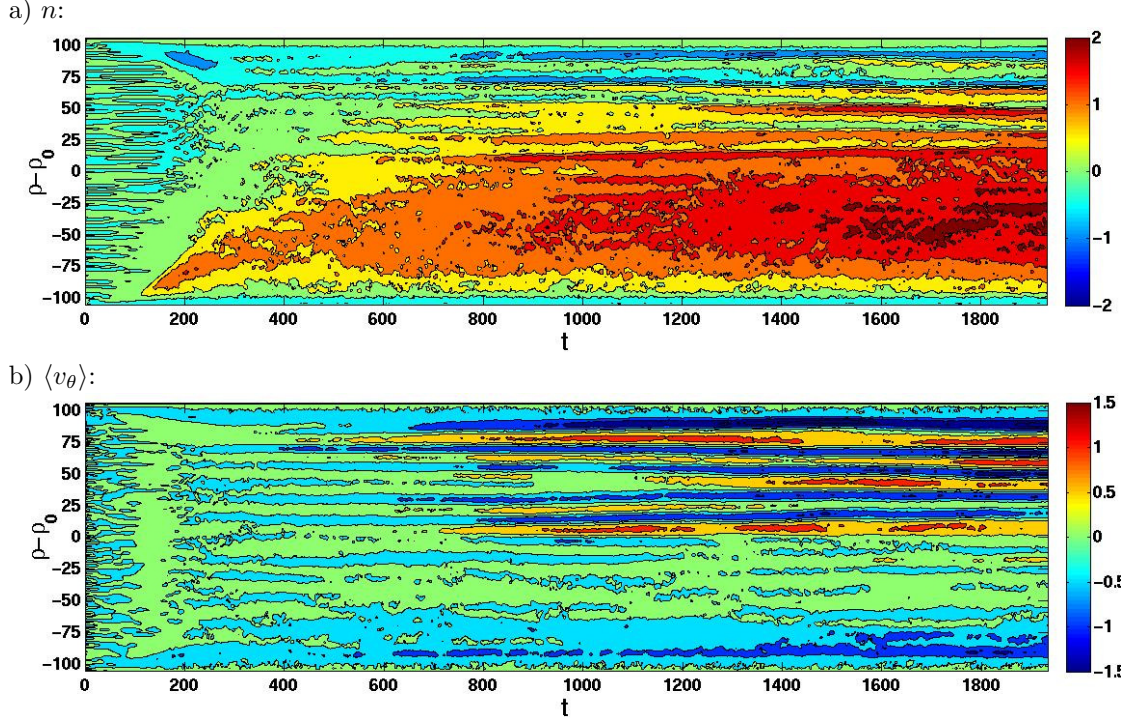
Figure 5.8.: Zonal averaged density perturbation (a) and poloidal flow velocity (b) of simulation performed with $\alpha = 0.464$, $\beta = -4$. The parameter C_{HW} varies from ≈ 0.39 at the inner limiting flux surface to ≈ 0.62 at the outer limiting flux surface.

5.3.1. Geodesic acoustic mode

The geodesic part of the curvature introduces a coupling of the zonal flow to pressure perturbations, which leads to an oscillation between kinetic and thermal energy, called the Geodesic Acoustic Mode (GAM) [132]. The dispersion relation of this mode is derived in the framework of the HW model. Therefore, we consider the linearised HW equations in the limit of a large thin annulus, where poloidal derivatives (∂_θ) are neglected against radial derivatives (∂_ρ), and assume that the electrons are adiabatic. This yields the model [133, 134]:

$$\frac{\partial}{\partial t}\left[n - \frac{\partial}{\partial \rho^2}\phi\right] = -2\sin\theta\frac{\partial}{\partial \rho}\phi, \quad n = \phi - \langle\phi\rangle, \quad \langle n \rangle = 0, \tag{5.7}$$

where $L_\perp = R_0$ is now used as normalisation scale length. We write the system in Fourier mode representation, i.e. $n, \phi \sim n_m, \phi_m \exp(ik_\rho\rho + im\theta + ik_z z + i\omega t)$, where only the mode subscript m is kept in the Fourier coefficients, since the geodesic curvature causes a coupling of adjacent poloidal modes:

$$\phi_m = a_m\left(\phi_{m+1} - \phi_{m-1}\right), \quad \text{with: } a_m = \begin{cases} -i\frac{1}{\omega k_\rho} & \text{for: } m = 0, \\ -i\frac{k_\rho}{\omega(1+k_\rho^2)} & \text{for: } m \neq 0, \end{cases} \tag{5.8}$$

All poloidal modes m are involved in principle, but in the limit $k_\rho \ll 1$ it follows that $a_0 \gg a_m, m \neq 0$ and therefore it is a good approximation to cut off the spectrum at some finite m.

An expansion to order k_ρ^2 where modes up to $m = \pm 2$ are kept, yields as dispersion relation:

$$\omega \approx \sqrt{2}\left(1 - \frac{k_\rho^2}{4}\right), \quad \text{for: } k_\rho \ll 1. \tag{5.9}$$

This result agrees with [133, 134] where the exact analytic result is obtained as[6] $\omega = 2(2+k_\rho^2)^{-1/2}$.

Physically, due to the geodesic curvature the zonal flow encounters a compression, which causes a density perturbation at the top/bottom of the tokamak proportional to $-\nabla \cdot \mathbf{v}$. These pressure perturbations create a diamagnetic current which cause a charge separation and acts to reverse the electric field [132]. Ultimately, an oscillation between kinetic energy and thermal (perturbation) energy takes place at the GAM frequency (in physical units: $\omega_{GAM} = \sqrt{2}c_s/R_0$).

To verify the implementation of the curvature terms in GRILLIX, this GAM mechanism has been benchmarked in a thin cylinder with $\rho_0 = 623$ and $W_\rho = 32$. Only Dirichlet boundary conditions in the perpendicular directions are available in GRILLIX and therefore a Gaussian structure of $\phi(\rho) = \exp\left[-(\rho - \rho_0)^2/(0.2W_\rho)^2\right]$ for the potential was chosen as initial state. Non-linear terms, density gradient and perpendicular viscosity were switched off. A run with perfect adiabaticity ($D \rightarrow \infty$) is not possible within GRILLIX, but simply a high value of $D = 100$ was chosen and the q-profile was set constant to $q = 3.4$. In fig. 5.9a the temporal evolution of the zonal flow velocity is shown. Besides a dominant oscillation at the GAM frequency, a radial dispersion of the Gaussian structure can be observed. The evolution of a single radial mode r is studied in appendix D.2 with the flux aligned code GRILLIX_FA, where also periodic boundary conditions are available. A comparison between GRILLIX and GRILLIX_FA proves then that the distortion of the structure in fig. 5.9 happens due to dispersion and not due to some numerical artefact.
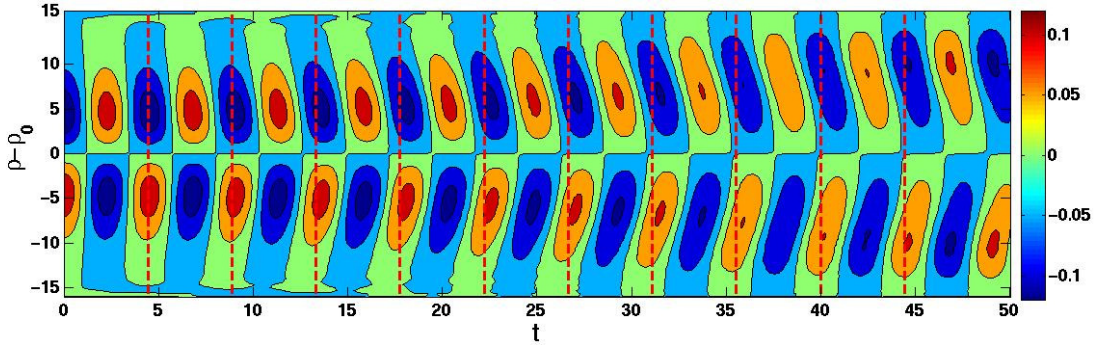
Figure 5.9.: Zonal averaged poloidal velocity in GAM benchmark. t is here given in units of $L_{ax}/(2\pi c_s)$ (see eqs. 2.36 with $L_\perp = L_{ax}/(2\pi)$). Dashed red lines indicate periods with angular frequency ω_{GAM}, i.e the analytically predicted oscillation in the limit $k_\rho \rightarrow 0$.

5.3.2. Ballooning

For a demonstration simulation with curvature again the standard parameters 5.3 were used, except that the toroidal resolution was increased to $N_{pol} = 12$ and the radial width of the flux shell was decreased by a factor of 2/3 to $W_\rho = 140\rho_s$. The curvature strength models a tokamak

---

[6]In [133, 134] the curvature strength is modelled without the factor of 2 in eq. 5.7. Therefore, the cited dispersion relation has been multiplied by a factor of 2 here.

of major radius $R_0 = 165$cm. The normalisation scale length was again set to $L_\perp = L_n$ yielding a value for $w_{cv} = 0.022$, respectively $\omega_{GAM} = 0.031$ in units of c_s/L_n.

In fig. 5.10 a comprehensive summary of the simulation is shown. In the linear phase the perturbations are stronger on the outside of the torus in the region of unfavourable curvature and weaker on the inside as expected from the simple 2D model of section 2.3.2. During the simulation the zonal flow drive, i.e. the zonal averaged divergence of the Reynolds stress, is balanced by perpendicular dissipation (see eq. 5.4) and the geodesic transfer to $m = \pm 1$ pressure perturbations, which are in turn depleted by non-linear transfer of energy back to turbulence [135]. Thus, in contrast to simulations performed without curvature, zonal flows are strongly suppressed and simulations with curvature saturate faster. The final transport level is slightly higher than for the case without curvature.

To illustrate the ballooning character of the turbulence, the root mean square (RMS) of the density perturbation averaged over time and the axial coordinate is shown in fig. 5.11. If the curvature terms are switched off, the turbulence is independent of the poloidal angle and lower in amplitude, whereas for increasing strength of the curvature a ballooning towards the outboard side can be seen. For a curvature strength of twice the nominal curvature ($w_{cv} = 0.044$) the zonal flows died out completely.

5.4. Limiter

GRILLIX can also be applied to a situation where a limiter is present. A thin axisymmetric limiter was introduced half way radially into the domain at the bottom. Dirichlet boundary conditions (perpendicular and parallel) were set at the limiter plates ($n = 0$, $\phi = 0$, $\nabla^2_\perp \phi = 0$). Again, all other simulation parameters were standard parameters, as described in section 5.1, except that $N_{pol} = 12$ poloidal planes were used. Curvature terms were again switched off.

A snapshot of the simulation is shown in fig. 5.12. Though the computational grid is not aligned with the flux surfaces, a clear and sharp distinction between the open and closed field line region is evident. In the closed field line region (edge) zonal flows develop, which is similar to the previous simulations where no limiter was present (compare with fig. 5.1). In the open field line region (SOL) no zonal structures can be observed any more but a variation of the structures with the poloidal angle can be seen. Starting from the limiter and following the electron diamagnetic drift direction, i.e. counter-clockwise, drift waves develop and the perturbations are small in amplitude. Going further on in the poloidal direction, the structures become isotropic within the poloidal plane indicating isotropic turbulent dynamics. Finally, the eddies impound in front of the limiter plate (left side), which is modelled as an impenetrable wall, and are ultimately dissipated.

A conspicuous feature is an early and rather strong development of a negative potential dip just inside the last closed flux surface (LCFS) indicating a positive (with respect to the electron diamagnetic drift direction) poloidal flow. A strong radial variation of the Reynolds stress across the LCFS drives the poloidal flow. The abrupt change of the parallel dynamics from open to closed field lines is responsible for anisotropic velocity fluctuations which caused a strong variation of the Reynolds stress across the LCFS. Ultimately, edge and SOL and a sharp transition became apparent by itself as a consequence of the field line map. Poloidal flows just inside the LCFS were also obtained from more sophisticated models [136, 137, 33], but the mechanisms described therein might differ. One has to keep in mind that the HW model used here is a too poor approximation to the situation.
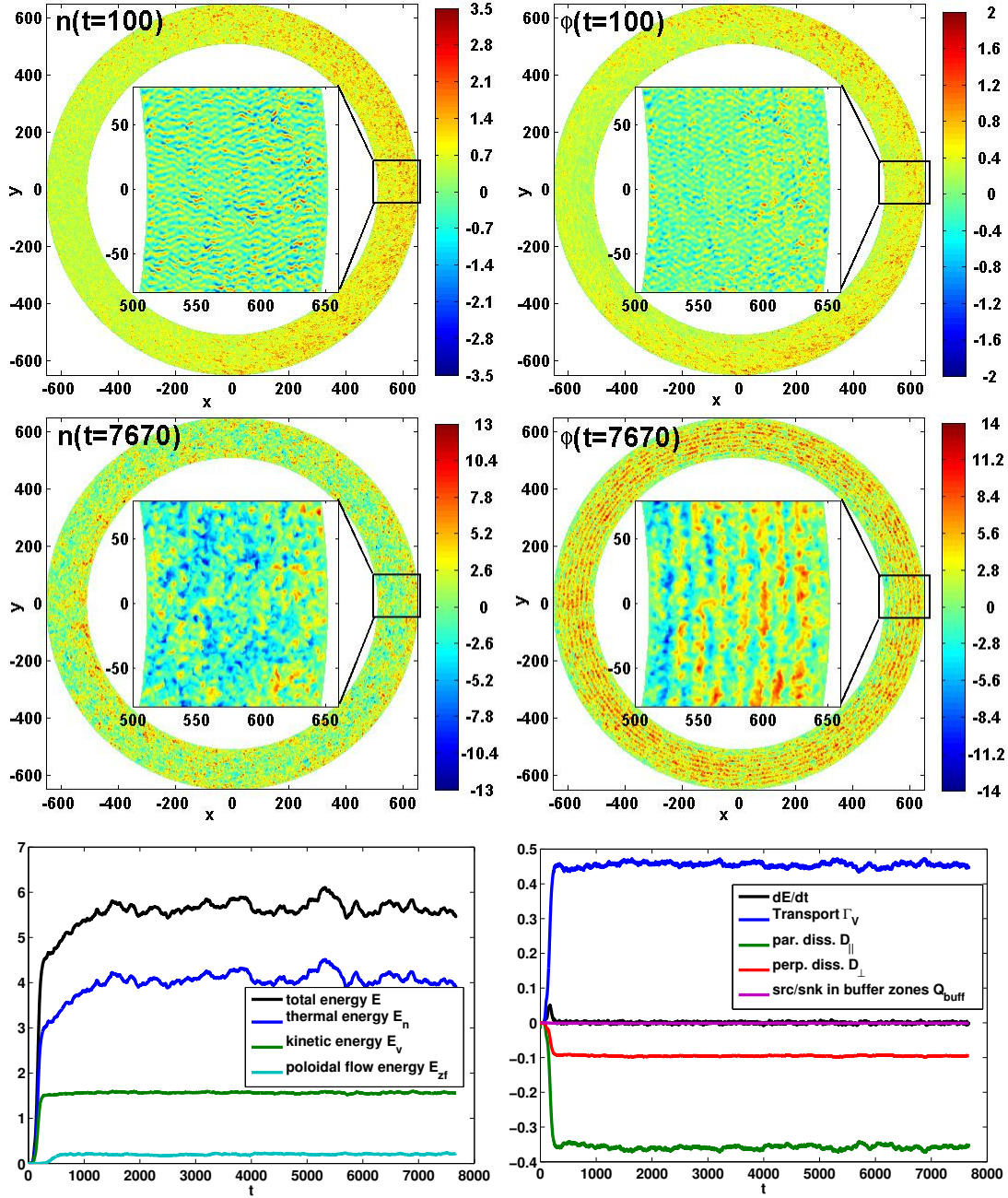
Figure 5.10.: Simulation with curvature $w_{cv} = 0.022$. Upper and middle row: Snapshots of density perturbation (left) and potential (right) in late linear phase at $t = 100$ (upper row) and in saturated state at $t = 7670$ (middle row). Lower row: Temporal evolution of fluctuation free energy (left) and temporal evolution of energy change, transport, sources and sinks of system (right). For units see again eqs. 2.36 and 5.3.
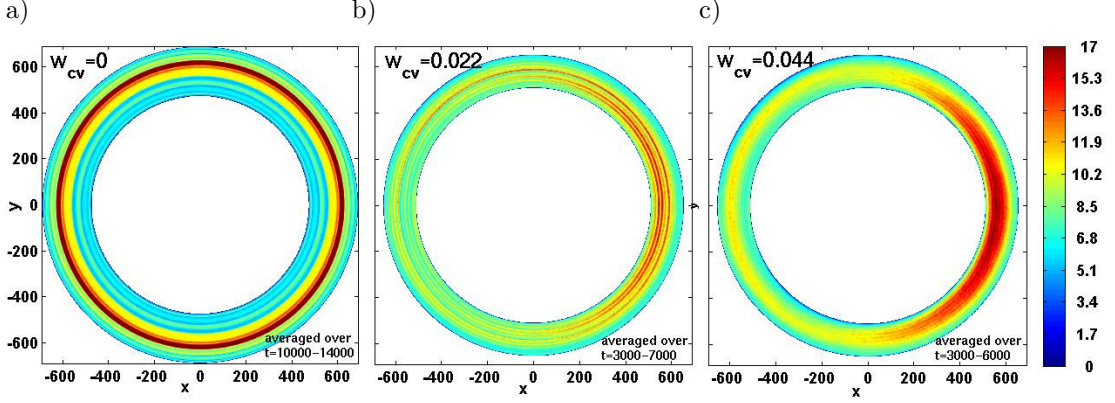
Figure 5.11.: Root mean square density fluctuation level averaged over time and axial coordinate. a) No curvature effects ($w_{cv} = 0$), b) nominal curvature ($w_{cv} = 0.022$), c) twice the nominal curvature ($w_{cv} = 0.044$).
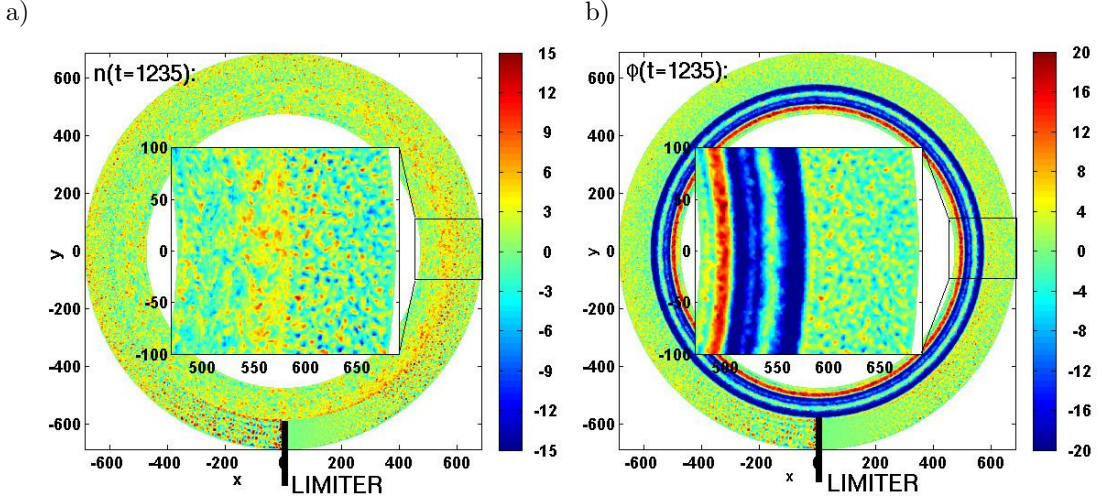
Figure 5.12.: Snapshot of GRILLIX simulation performed without curvature and with axisymmetric limiter ranging radially half way into the domain. a) Density perturbation, b) electrostatic potential. For units see again eqs. 2.36 and 5.3.

5.5. Benchmarks

Before GRILLIX is applied to more complex geometries, several intrinsic benchmarks and convergence checks are performed for the circular geometry. These benchmarks comprise intrinsic consistency checks, i.e. the conservation of integral properties, convergence checks and effects of the boundaries.

5.5.1. Consistency checks
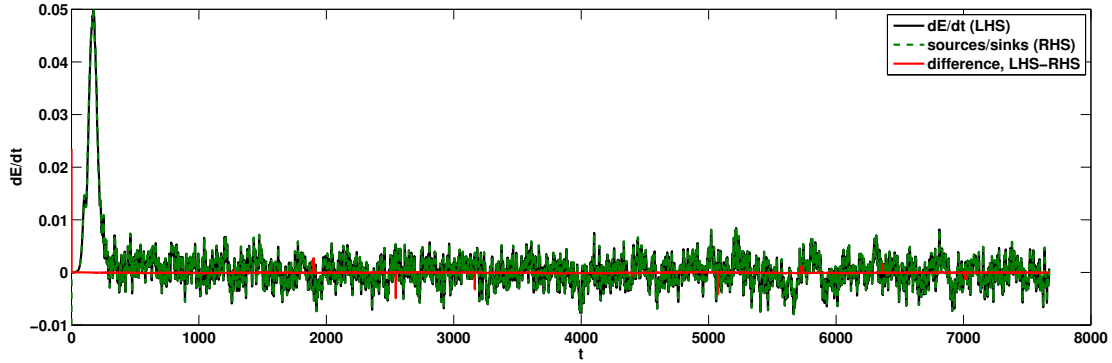
Fluctuation free energy

To check the fluctuation free energy theorem, its temporal change was computed by a finite difference between two time steps (LHS) and compared against the sources/sinks of the system (RHS).

$$\frac{dE}{dt} = Q + D_{\parallel} + D_{\perp} + Q_{buff}, \tag{5.10}$$

where Q, $D_{\parallel}$, $D_{\perp}$ are defined in eq. 2.59 and Q_{buff} is a source/sink term due to the damping of the zonal averaged density perturbation and the zonal averaged potential in the buffer zones (see eq. 4.15):

$$Q_{buff} = \int\limits_{V} dV \left[-g(\rho)n \langle n \rangle - \frac{1}{2B^2} \nabla_{\perp} \left(g(\rho) \langle \phi \rangle \right) \cdot \nabla_{\perp} \phi \right] \tag{5.11}$$

In fig. 5.13 the temporal change of the fluctuation free energy computed directly (LHS) and computed by sources/sinks (RHS) is shown for the demonstration simulation from section 5.3.2 (Fig. 5.10). Except for some spikes, which indicate positions where the simulation was restarted, both curves agree very well. At start or continuation of a simulation, the temporal change was not computed self consistently, due to the lack of previous time points. The numerical error which is defined here as the difference between LHS and RHS divided by the root mean square averaged over time of the LHS was always below 1% (except at restarts of simulation).

Figure 5.13.: Check of fluctuation free energy theorem with demonstration simulation. For simulation details refer to section 5.3.2 (fig. 5.10).

Zonal flow drive and numerical diffusion

For simulations performed without curvature the integral equation. 5.4 for the zonal flow drive (corresponding footnote 4 on page 65) can be checked. In fig. 5.14 the temporal change of the poloidal flow velocity, computed via a finite difference between two time steps (LHS), and the drive/dissipation of the poloidal flow (RHS) is plotted for the demonstration simulation from section 5.2.1 at three different time points. Except from the buffer regions, where additional contributions to eq. 5.4 due to the sources/sinks have not been taken into account, the agreement between both curves is good. A substantial mismatch between both curves could indicate spurious

effects of the field line map, like a wrong implementation or a too high numerical diffusion. The mismatch here however, might very well also arise from the discretisation of perpendicular operators. In section 5.5.3 it is shown that the same shape and size of zonal flows were obtained also with a flux aligned code. Moreover, as also shown in appendix D.3, zonal flows with similar size and shape have been obtained in a simulation performed with doubled resolution within the poloidal plane. This suggests that the numerical diffusion indeed is negligibly small for this case and had no effect on the simulation.

Also different schemes for the parallel diffusion were tried (see appendix D.3). With the **S-1** scheme similar results were obtained as with the standard **S-3** scheme. No zonal flows were produced with the **N-1** scheme and only smaller zonal flows with the **N-3** scheme. This shows the need and the superiority of the developed support schemes.

a) $t = 300$:
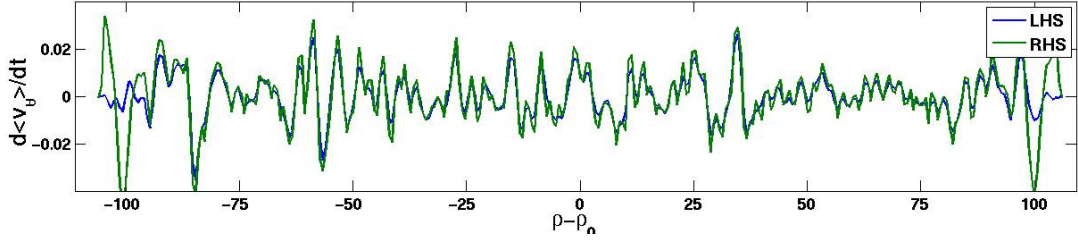
b) $t = 1000$:
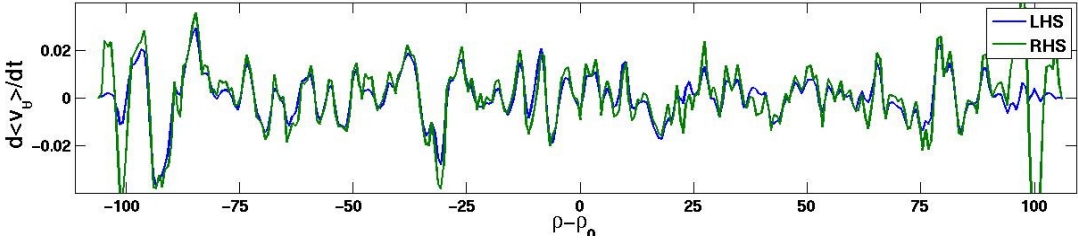
c) $t = 10\,000$:
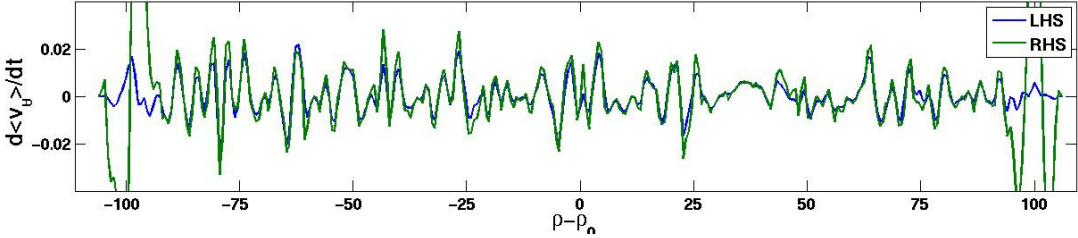
Figure 5.14.: Check of zonal flow drive with demonstration simulations from section 5.2.1 at time a) $t = 300$, b) $t = 1000$ and c) $t = 10\,000$.

5.5.2. Convergence

The achievement of saturation for simulations without curvature is very elaborate, since it requires very long run times and a large radial width of the domain for the condensation of zonal flows. Moreover, the final state is dependent on the initial state also in a statistical sense [91, 90]. Therefore, convergence checks with respect to resolution were only performed for a simulation with curvature where zonal flows are suppressed. The convergence behaviour with respect to

resolution and domain size were performed only for the transport, since it is the quantity one is usually most interested in, in practice. It is noted that among all the simulations performed at different resolutions, no qualitative but just quantitative differences were observed.

Standard parameters were used with a curvature strength of $w_{cv} = 0.022$. For the convergence studies the radial width of the domain W_ρ, the number of poloidal planes N_{pol} and the poloidal grid resolution h were varied. The strength of the hyperviscosity was adapted to the poloidal grid resolution to damp always only the smallest scales ($\nu_{n,\phi}(h = 0.66) = 1 \cdot 10^{-3}$, $\nu_{n,\phi}(h = 0.33) = 1 \cdot 10^{-4}$, $\nu(h = 0.17) = 1 \cdot 10^{-6}$).

In fig. 5.15 the time trace of the transport computed with various resolutions is plotted. The blue group of lines show the convergence with the toroidal resolution N_{pol}. Since the curves with $N_{pol} = 24$ and $N_{pol} = 30$ are very close, a good convergence was achieved here. To save computational resources further resolution scans were performed with $N_{pol} = 12$ poloidal planes, which is already close to the converged result. The green group of lines shows the convergence with respect to the radial width of the domain. The agreement between the $W_\rho = 140$ and $W_\rho = 210$ is very good and only a small difference to $W_\rho = 70$ can be seen, such that further resolution scans were performed with $W_\rho = 70$ to save again computational resources. The red group shows the convergence with the poloidal resolution h. A good agreement between $h = 0.33$ and $h = 0.17$ proves convergence also with respect to h. Among the curves, there is also a noticeable difference during the transitional phase. Curves with low toroidal resolution and high poloidal resolution exhibit a small overshoot or bump of the transport, whereas other curves rise in a more monotonic manner. However, the saturated value is again close among all curves.

5.5.3. Boundary effects

Another peculiarity of GRILLIX is that the (perpendicular) boundaries of the Cartesian grid do not coincide with the limiting flux surfaces but are only approximated stepwise by the grid points. A priori it is not clear if this mismatch of the boundary introduces spurious numerical effects. As apparent from fig. 5.1 (at $t = 100$) there is a dubious accumulation of small scale eddies close to the boundaries. Thus, it has to be investigated if these wiggles are caused by the shape of the boundaries or by the physical boundary conditions ($n = 0$, $\phi = 0$, $\nabla_\perp \phi = 0$) itself and which effect these wiggles might have on the overall simulation.

To accomplish this, another completely new code GRILLIX_FA has been developed by me from scratch which solves the HW equations on a polar flux aligned grid in a circular axial geometry (ρ, θ, z). Therefore, the shape of the boundaries matches exactly with the limiting flux surfaces. GRILLIX_FA uses the same numerical techniques as GRILLIX (time stepping scheme, perpendicular operators) and can thus be directly compared to GRILLIX. The parallel diffusion operator is also discretised with the support scheme, but the interpolation is reduced to a 1D interpolation within a flux surface. In GRILLIX_FA there is no spurious numerical coupling across flux surfaces by parallel derivatives. Hence GRILLIX_FA is also a very useful tool for benchmarking GRILLIX.

A simulation with GRILLIX_FA with the same parameters and comparable resolution as to the standard case was performed. A direct comparison between both codes as a snapshot of the density perturbation during the late linear phase is shown in fig. 5.16a,b. The agreement between both codes is excellent. The accumulation of drift waves at the boundaries is observed also with GRILLIX_FA, which shows that not the shape of the boundaries but the boundary condition itself, being an impenetrable wall, caused the wiggles. Therefore, the already discussed buffer zones were introduced. Also the development of zonal flows is in good agreement between both codes as illustrated in fig. 5.16c,d and the obtained saturated transport level is with both
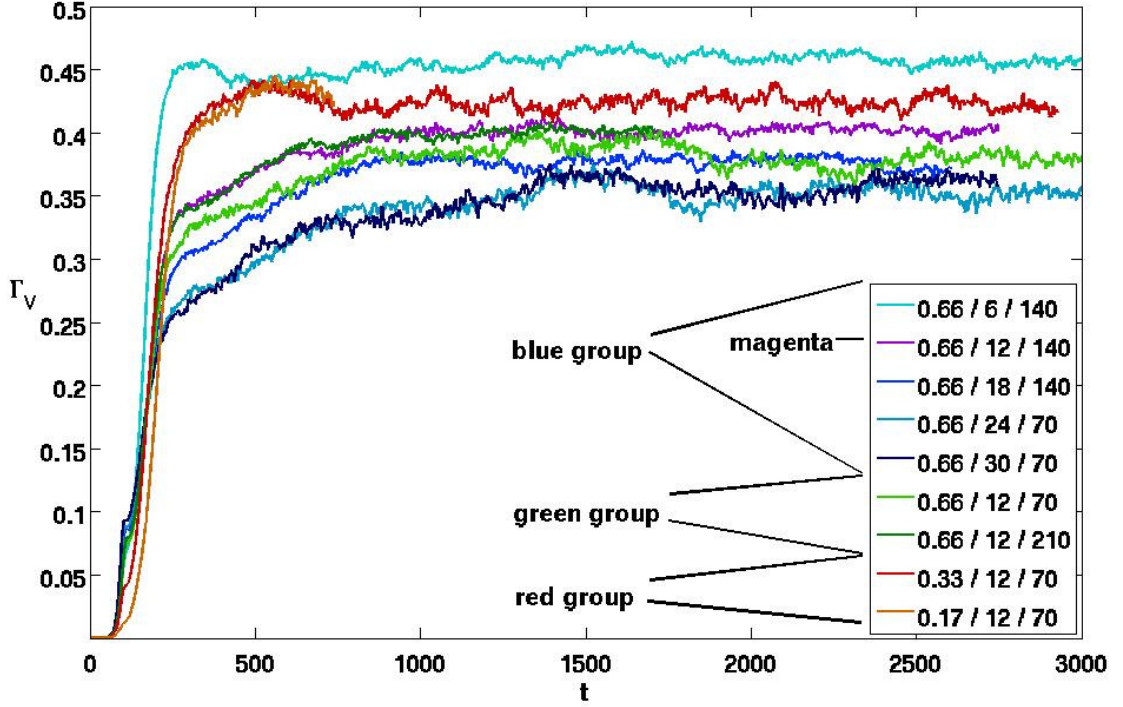
Figure 5.15.: Time trace of transport computed with various resolutions. The nomenclature of the legend is poloidal grid distance in units of ρ_s, number of poloidal planes and radial width of the domain in units of ρ_s (h / N_{pol} / W_ρ). For other simulation parameters see text. Blue group + magenta: Scan in N_{pol}, green group + magenta: Scan in radial width, red group + magenta: scan in h)

codes $\Gamma_V = 0.41$. This suggests that the numerical diffusion, which would manifest itself in a difference between both codes, is so low that it did not affect the simulations in any manner.

5.6. Conclusions

In this chapter the application of GRILLIX to a circular axial geometry has been presented. The basic physical mechanisms of 3D resistive drift wave (ballooning) turbulence in the presence of shear have been discussed and could also be obtained with GRILLIX. Several diagnostics tools have been implemented to analyse the simulations.

In the sheared slab limit, which is approximated as a large thin annulus with GRILLIX, the results are in very good agreement to the results obtained with field aligned codes aimed for a sheared slab. The previously found parameter C_{HW} is here also the single dimensionless parameter of the system and roughly the same onset for zonal flow production at $C_{HW} \approx 0.4$ has been verified with GRILLIX and the correct behaviour of the transport with C_{HW}. The implementation of the (artificial) curvature terms has been tested with the analytically predicted GAM oscillation that was also obtained with GRILLIX. In the presence of curvature, zonal flows are suppressed and the well known ballooning behaviour has been obtained. The introduction of an axisymmetric limiter into the system caused an abrupt change of the dynamics between the open and closed field line region. Zonal structures dominate the edge, whereas the dynamics in
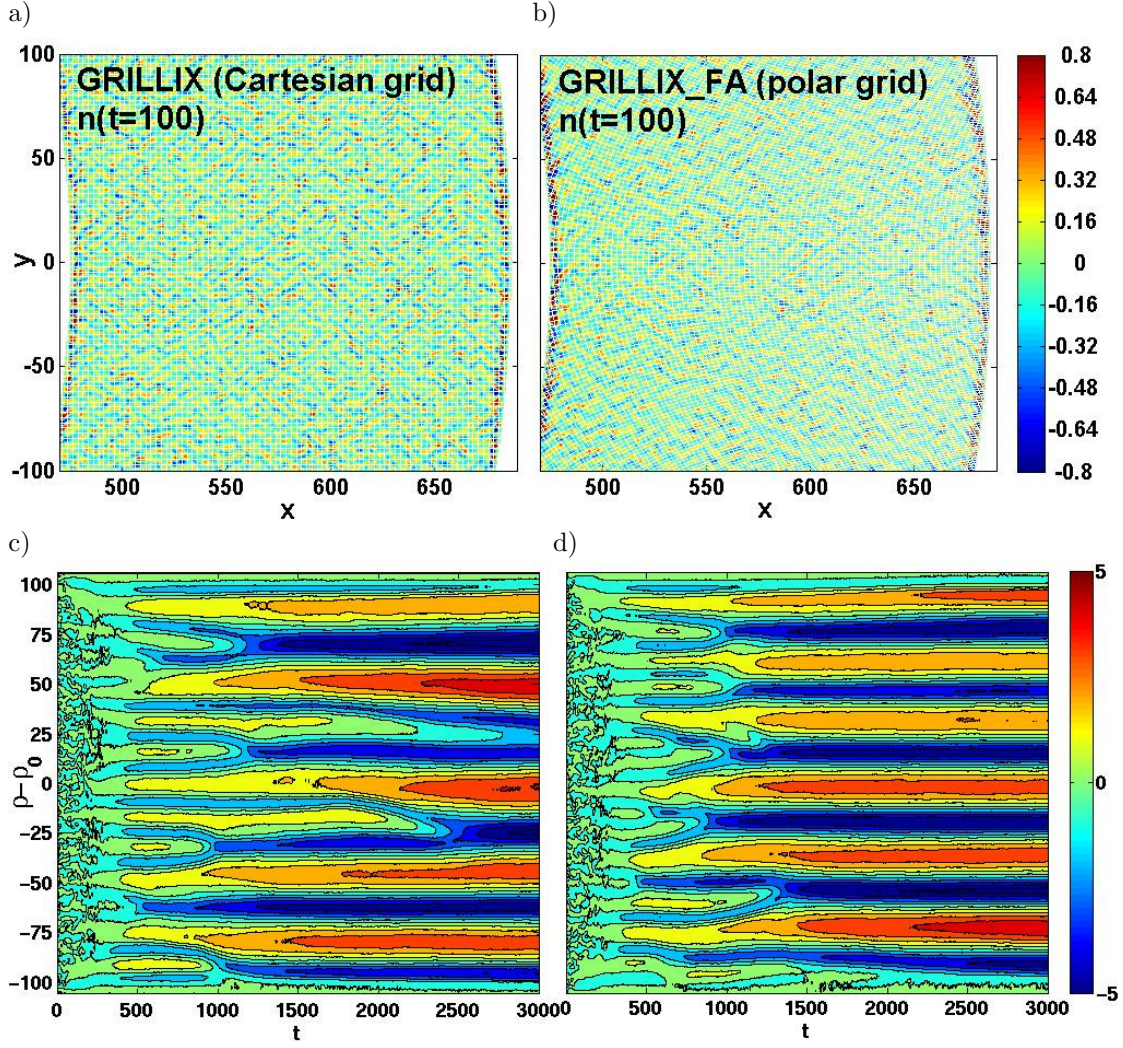
Figure 5.16.: Snapshot of simulation performed with a) GRILLIX (Cartesian grid) and with b) GRILLIX_FA (flux aligned grid) at a comparable resolution. Temporal evolution of poloidal flow velocity with GRILLIX (c) and GRILLIX_FA (d).

the SOL region is described by drift waves propagating in the electron diamagnetic direction.

Several benchmarks showed that GRILLIX intrinsically conserves important integral relations, like energy conservation and zonal flow drive. By use of the newly developed support schemes for the discretisation of the parallel diffusion operator, the numerical diffusion was always low enough at the used resolutions to not affect the results. It has also been shown that possible spurious effects arising from the mismatch of the boundaries were of no importance. The convergence at least for one simulation has been analysed. However, due to constraints of the available hardware many results of this chapter might not be converged quantitatively but only qualitatively, i.e. the main effects were captured correctly.

All in all, this proves that the Hasegawa-Wakatani equations have been correctly implemented in GRILLIX and that the numerical scheme, i.e. the field line map, works. The same results as

with a flux aligned codes are obtained. Hence, GRILLIX is now ready to be applied to more complex geometry for which it was designed and where only few results are available.

Chapter 6.

Diverted geometry

Having benchmarked GRILLIX extensively in the previous chapters, it is finally applied to diverted geometry where the simulation domain covers a region across the separatrix. As already pointed out, the separatrix cannot be simulated with most present turbulence codes or is only treated poorly, in the sense that the X-point is an exceptional grid point, which might in the worst case even lead to numerical artefacts. Within GRILLIX the X-point is treated naturally as any other point.

The aim of this chapter is to discuss and validate effects of the complex geometry, even though the underlying turbulence model is not suited to model the edge/SOL of fusion devices accurately. Since the region of interest is rather large, the presented simulations might again be not well resolved due to constraints of computational resources. However, at this early stage one is anyway mainly interested in qualitative and not quantitative results, for which the used resolutions suffice. Therefore, convergence checks only in a qualitative sense have been performed.

6.1. Theoretical background

To illustrate the effects of an X-point, we consider a model geometry [138] illustrated in fig. 6.1a, where x, y label directions perpendicular to a reference field line and z a coordinate parallel. The reference field line is assumed to start at $z = 0$ somewhere in a nominal region, like outboard midplane of a tokamak, and approaching with increasing z the X-point which is at $z = \infty$. Along z we separate the domain in two regions, $z < z_x$, where the magnetic field lines are practically unaffected by the X-point and a region $z > z_x$ where the magnetic field lines are influenced by the X-point. At the X-point the poloidal flux function has a saddle point and for the X-point region we use the lowest order approximation for the poloidal magnetic field [139, 140]:

$$\mathbf{B} = B_z \mathbf{e}_z + [\alpha x \mathbf{e}_x - \alpha y \mathbf{e}_y] \Theta(z - z_x), \qquad (6.1)$$

where Θ is the Heavyside step function and α a constant. A flux box around the reference magnetic field line becomes strongly distorted as it enters the X-point region.

$$w_x(z) = w_0 \exp\left(-\alpha \xi(z)\right), \quad w_y(z) = w_0 \exp\left(\alpha \xi(z)\right), \qquad (6.2)$$

where w_x, w_y are the perpendicular lateral lengths of the flux box and ξ measures the penetration length into the X-point region, i.e. $\xi(z) = (z - z_x)\Theta(z - z_x)$. w_0 is the lateral length of the initial square and its cross section area is preserved along z. In reality a small distortion of the flux box occurs also without X-point due to the canonical shear for $z < z_x$, which is not taken into account here. The affinity of this simple model to the tokamak geometry becomes clear by fig. 6.1b, where the distortion of the flux box cross section is shown within the poloidal plane. The initial circular cross section becomes strongly distorted, as the flux box enters the X-point region.

a)

b)
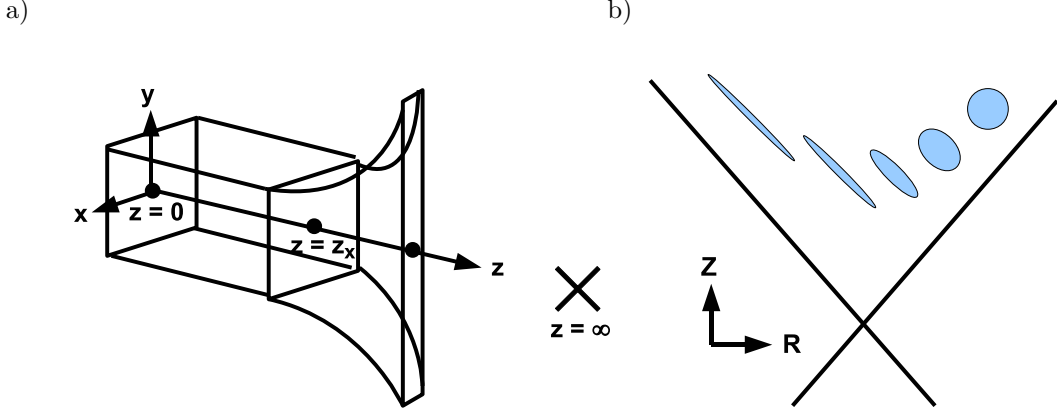
Figure 6.1.: a) Scheme of simple X-point model. b) Distortion of cross section of flux tube entering with a circular shape the X-point region.

Consequently, a flute mode perturbation will encounter the same distortion along the magnetic field lines and its perpendicular wave number will change along the parallel direction according to:

$$k_x \to k_x(z) = k_{0_x} \exp\left(\alpha\xi(z)\right), \quad k_y \to k_y(z) = k_{0_y} \exp\left(-\alpha\xi(z)\right), \tag{6.3}$$

where k_{0_x}, k_{0_y} are perpendicular wave numbers at $z = 0$. Note also that $k_\perp^2$ increases drastically as a field aligned structure enters the X-point region.

$$k_\perp^2(z) = k_{0_x}^2 \exp\left(2\alpha\xi(z)\right) + k_{0_y}^2 \exp\left(-2\alpha\xi(z)\right) \xrightarrow[\xi \gg \alpha^{-1}]{} k_{0_x}^2 \exp\left(2\alpha\xi(z)\right). \tag{6.4}$$

One may thus anticipate that within the framework of the HW model perpendicular dissipation becomes dominant in the X-point region as it scales with $k_\perp^6$. Even if the strong $k_\perp^6$ dependence arises from the ad hoc introduced hyperdiffusion model, the perpendicular dissipation is for large $k_\perp$ also in reality the dominant term ($\propto k_\perp^2$).

Based on this observation, also Farina et al. [139] (see also [141]) conclude that flute mode like perturbations cannot penetrate the X-point region, since their spatial extent in one perpendicular direction can easily become smaller than the ion gyration radius and is thus subject to dissipation.

Myra et al. [142, 143, 144] use a reduced Braginskii model which takes into account electromagnetic effects to derive the resistive X-point mode. This mode is mainly driven on the midplane outboard side of a tokamak, the region of unfavourable curvature, and has there characteristics of an electromagnetic ideal MHD mode. As the mode approaches the X-point, it becomes electrostatic with the resistivity being dominant. The mode is damped in the X-point region, which leads to an enhancement of the parallel wave vector. Since the X-point resistively disconnects structures along the parallel direction, the mode does not encounter the stabilizing effect from the inboard side (good curvature). In cases of a configuration with a second upper X-point in the near SOL the mode remains even confined on the outboard side between both X-point regions. The resistive X-point mode is thus the result of synergism between resistivity and X-point geometry. It has also been validated numerically with the BOUT code and found to be dominant for typical parameters [37, 38, 40]. However, the BOUT code uses a flux aligned grid, where the X-point is an exceptional point, and might ultimately thus not be the best approach to investigate dynamics around the separatrix. On the other hand, GRILLIX is capable of treating

the X-point geometry accurately as will be shown, but its physical model is yet insufficient to describe these modes, since electromagnetic effects are not taken into account. This will be a goal of future investigations. But as will be shown in section 6.3 with linear runs, there seems to be a remote analogue also within the HW model. Drift waves are found to be most unstable in regions of strong density gradients, i.e. where flux surfaces are closely spaced. The fluctuations are then distributed via the parallel current along the magnetic field lines also to regions of reduced density gradient. At the X-point these perturbations encounter a strong perpendicular dissipation, which also damps the mode towards the X-point, leading to a disconnection of the modes across the X-point.

Assuming the prescribed dependence 6.3 for $k_\perp(z)$, also reduced models were proposed [144, 145, 146, 138] which treat the outboard midplane and the X-point region with separate models. The idea is that fluctuations are mainly created in the outboard midplane region constant along magnetic field lines. Fluctuations in the X-point region are driven due to the parallel current and the strong shear is taken into account via an ordering procedure according to the z-dependence of the perpendicular operators. Ultimately, effective boundary conditions can be formulated at some intermediate z coordinate which could be used for an effective $2D$ outboard midplane model.

6.2. Axial diverted configuration

GRILLIX could be applied now to a realistic toroidal equilibrium, as obtained from a solution of the Grad-Shafranov-Schlüter equation 3.2 or even from an experimental input. This is only performed in section 6.5 as a proof of ability of GRILLIX. However, at this stage this approach would be pointless, since due to the lack of data and the poor turbulence model the results for such complicated equilibria would be questionable and very hard to interpret. Instead, it is highly desirable to study the effects of an X-point in isolation as purely as possible and to be able to compare the results against available results. To this aim a simpler magnetic field configuration was established which fulfils these requirements. This magnetic field configuration is not necessarily an equilibrium in the sense of MHD but just a solution to Ampere's law, which suffices as input for GRILLIX.

To obtain such a diverted magnetic field configuration, the magnetic field of an axial circular equilibrium with prescribed q-profile was taken and superposed with the magnetic field created by a wire located in the divertor region. Performing this for the logarithmic q-profile described in section 5.1 and a wire located at $(x = 0, y = y_{wire})$, one obtains as poloidal flux function:

$$\Psi(x,y) = \left(\frac{1}{2q_0} + \frac{\alpha}{4}\right)\rho^2 - \frac{\alpha}{2}\rho^2\ln\left(\frac{\rho}{\rho_0}\right) + \frac{c_{wire}}{2}\ln\left(1 - \frac{2y}{y_{wire}} + \frac{\rho^2}{y_{wire}^2}\right), \qquad (6.5)$$

where the parameter c_{wire} is proportional to the current through the wire. The magnetic axis is an extreme point of Ψ and the X-point a saddle point. The resultant poloidal flux function, which was created based on the standard parameters of section 5.1 with some reasonable choice for c_{wire} and y_{wire}, is shown in fig. 6.2a. The magnetic configuration is simple in the sense that it exhibits a left-right symmetry and at the position opposite to the X-point (top) the flux surfaces are nearly circular. Furthermore, far enough inside the closed field line region the equilibrium is similar to the simple axial-circular equilibrium which allows comparisons to the results from chapter 5. The resulting q-profile is shown in fig. 6.2b. Far enough inside the separatrix the q-profile runs similar to the axial circular equilibrium, but approaching the separatrix ($\rho = 1$) a logarithmic divergence [10] appears.

$$q(\rho) \propto -\ln(1-\rho) \quad \text{for: } \rho \lesssim 1. \qquad (6.6)$$

a)   b)
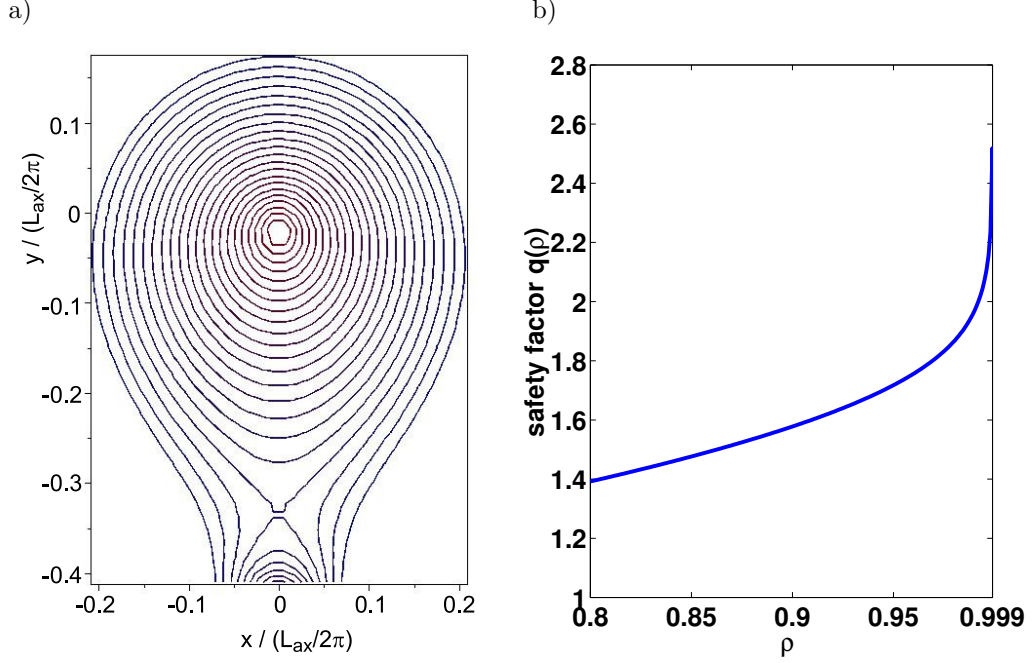
Figure 6.2.: a) Contours of poloidal flux function of axial diverted configuration. Parameters are (in units of $L_{ax}/2\pi$): $\rho_0 = 0.182$, $q_0 = 1.5$, $\alpha = 0.464$, $c_{wire} = 0.015$, $y_{wire} = -0.45$. Coordinates of magnetic axis are $x_o = 0$, $y_o = -0.021$ and of X-point $x_x = 0$, $y_x = -0.333$. b) Corresponding q-profile in the edge region.

For the aim of comparison to the axial circular cases, similar parameters as the standard test case given in section 5.1 were used. However, some things must be respected: The flux label ρ is now defined to range from 0 at the magnetic axis to 1 at the separatrix according to eq. 3.13. The background density was assumed to be constant on flux surfaces and the radial background density gradient is not homogeneous any more. To allow for a comparison, the background density profile was modelled to match roughly the circular axial one at the top where the flux surfaces are nearly circular. The perpendicular normalisation length was chosen to be equal to the background density gradient length at the top, i.e. $L_\perp = L_n(top)$. Concerning resolution, a higher toroidal resolution had to be chosen to meet the requirements 3.54. With $N_{pol} = 18$ planes the distortion remained below the threshold of 4, except for a few grid points in the deep private flux region which exceeded this limit slightly. It was also checked qualitatively for map distortion effects by doubling the resolution to $N_{pol} = 36$.

6.3. Linear runs

6.3.1. Isolated blob

To elucidate the distortion of a vortex near the separatrix, a linear simulation was performed with an initial nonadiabatic Gaussian blob located at the top of the equilibrium on the separatrix. Sources/sinks in the buffer zones were switched off and all other parameters were as described in section 6.2. The result is shown in fig. 6.3.

The snapshot at $t = 0.5$ as an overlay of the planes shows nicely the expected behaviour.

The initial nonadiabatic blob at the top (position 0) drives rapidly fluctuations along the field lines via the parallel current. The blob becomes only slightly distorted due to the canonical shear towards the left and right sides. As the structure enters the X-point region (bottom), it becomes strongly distorted increasing its $k_\perp^2$ (Compare also with fig. 6.1b). Due to the enhanced perpendicular dissipation and the infinite (parallel) distance, the blob is not able to pass or even reach the X-point but lingers close to it. On flux surfaces close to the separatrix, the blob is hardly able to pass the X-point with drastically reduced amplitude. On a much slower time scale the blob also propagates in the electron diamagnetic drift direction.

In fig. 6.3b the nonadiabaticity is shown on a flux surface which is very close to the separatrix. In the X-point region (around $\theta = 3\pi/2$) the structure is bent along the axial direction and is damped drastically. It is not able to pass through the X-point region. For the establishment of this figure the quantity was assumed to be piecewise constant along magnetic field lines within two poloidal planes, i.e. between two black lines. Thus, the obvious smoothness of the structure between two vertical black lines is constructed, but across the black lines is a result of the numerics (field line map). The interpolation at the evaluation for the discrete parallel operators did not introduce spurious wiggles or any other numerical artefacts, which proves that the field line map approach works very well even in such complex geometry.

Finally, in fig. 6.3c the nonadiabaticity as a function of the distance along a magnetic field line is shown at various times. The considered field line starts at $x_\parallel = 0$ at the top (position 0) just inside the separatrix goes to the left and at roughly $x_\parallel = 7$ the field line passes at the bottom the X-point, where it lingers long and comes back up on the right at roughly $x_\parallel = 12$. Due to the enhanced perpendicular dissipation, the structure cannot pass the X-point region and loses its Gaussian structure.

6.3.2. Most unstable mode

In order to figure out where the fluctuations are mainly created and how they are distributed along the magnetic field lines, a linear simulation with a small random noise in the density perturbation as initial state was performed. Non-linear terms and source/sink terms in the buffer zones were again switched off. The result is shown in fig. 6.4 and it might be worth to compare it against the linear mode structure in axial circular geometry (fig. 5.1, upper row). It is apparent that the structures are regular at the top, i.e. the drift waves are elongated perpendicular to the flux surfaces. This is the region of the largest background density gradient, since the flux surface are most closely spaced here. Hence, perturbations are created mostly in this region and distributed via the parallel current towards the sides, where they become slightly sheared due to the canonical shear but are still comparable in amplitude. On flux surfaces still far enough inside the separatrix the perturbations, though lower in amplitude, can still exist at the bottom and have a very fine grained chequerboard pattern there that can hardly be resolved by the grid. The chequerboard pattern is the footprint of the regular structures at the top and a result of the already strong local shear in that region. A similar fine grained chequerboard pattern has also been obtained with double resolution in the axial direction, i.e. $N_{pol} = 32$ and is thus not a numerical artefact of the map distortion. Moreover, Hariri [49] has performed also with a field line map approach a parallel sound wave propagation across the separatrix in absence of any dissipation mechanisms. Also in these simulations appear very fine grained chequerboard structures as a result of the footprint of the modes to the X-point which could not be resolved with the available poloidal resolutions. Near the X-point the perturbations practically die out completely due to the infinite connection length to the top and the enhanced perpendicular dissipation.

In fig. 6.5 the nonadiabaticity along a field line running close to the separatrix in the flux
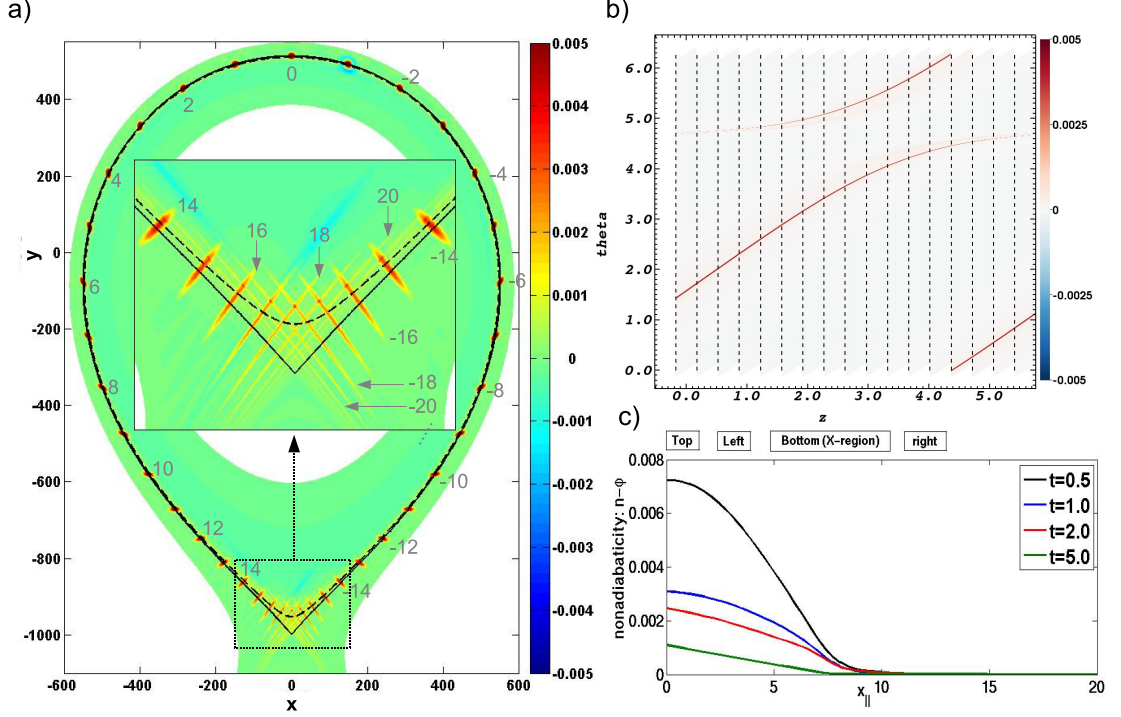
Figure 6.3.: a) Snapshot of drift wave blob (nonadiabaticity $n - \phi$) at $t = 0.5$. For units see eqs. 2.36 with parameters given in expressions 5.3 (For further simulation details see also last paragraph of section 6.2). Initial state was nonadiabatic blob at top (position 0). Picture shows overlay of all ($N_{pol} = 18$) poloidal planes, where the grey numbers n indicate the position along the axial coordinate, i.e. $z = (n \mod 18) \cdot 2\pi/18$. Black lines indicate separatrix (solid: $\rho = 1$) and $\rho = 0.996$ surface (dashed). b) Illustration on flux surface $\rho = 0.996$. Dashed black lines indicate transition between neighbouring planes. c) Nonadiabaticity at different times in dependence of length along field line, starting from the top (position 0). Corresponding poloidal positions are indicated with text in boxes.

surface $\rho = 0.996$ is shown. A clear correlation between the nonadiabaticity and the geometry is obvious. Whenever the field line passes close to the X-point, the nonadiabaticity is damped practically to zero and the mode remains confined from one side of the X-point to the other. Also an abrupt change in the slope of the curve in the X-point region shows that the X-point virtually disconnects the structures. This is somewhat similar to the resistive X-point mode (compare e.g. fig. 3b in [143]) which remains also confined between X-points, though the physical mechanisms of driving and damping here is different.

6.4. Non-linear runs

Next, non-linear terms were switched on to allow turbulence. An imperfect zonal average operator has been implemented only for diagnostic purposes also for the open field line region but it might be not suited for computational purposes. Therefore, the source/sink term in the buffer zones was only switched on for the inner closed flux surface region. This will be improved in future.
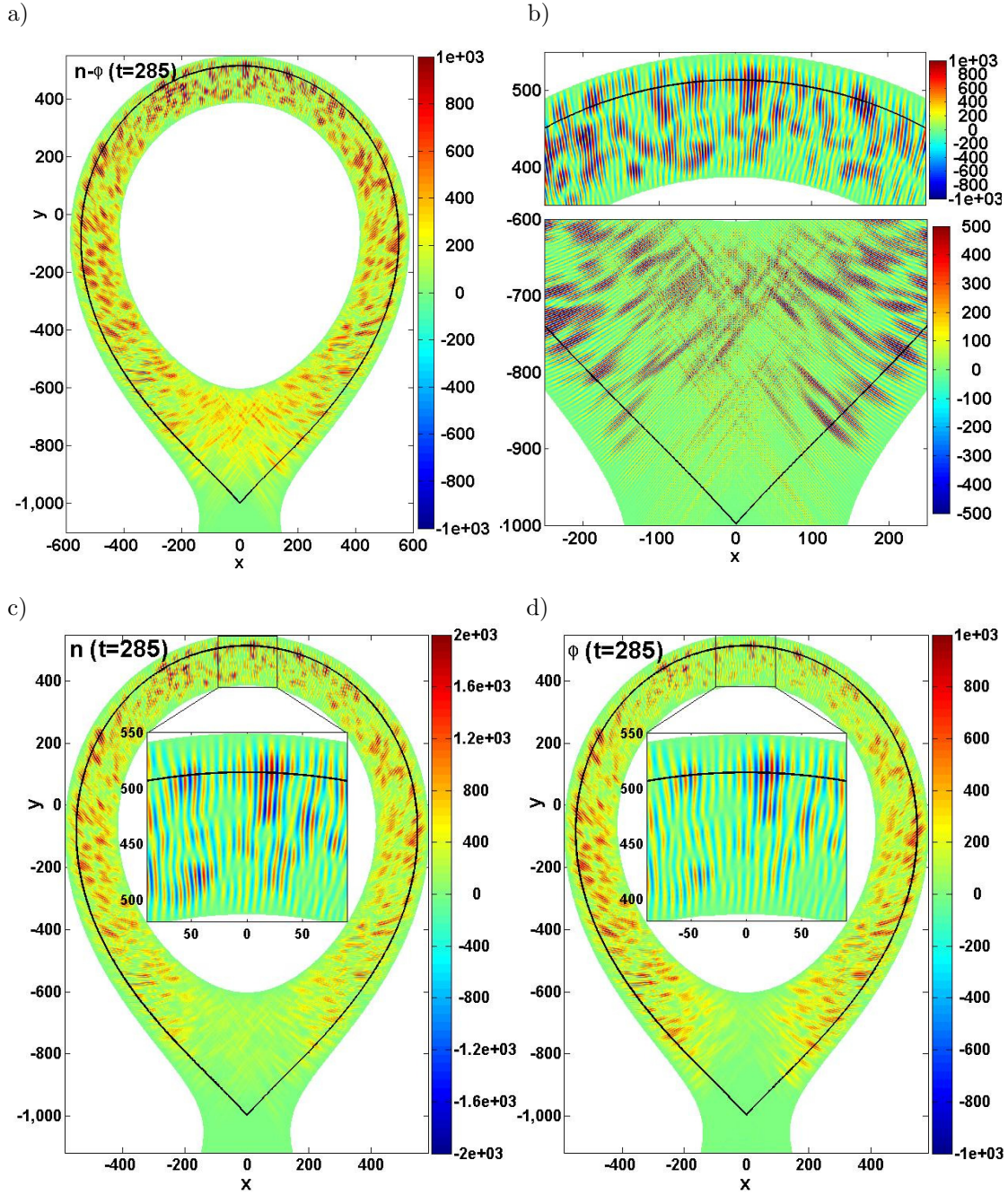
Figure 6.4.: Snapshot at $z = 0$ and $t = 285$ of linear simulation initialized with random noise. a) Nonadiabaticity $n - \phi$, b) nonadiabaticty enlarged (note the different colour scales). c) Density perturbation n and d) potential ϕ.

The buffer zones are mainly important for the approach towards a fully saturated state where the density profile and the zonal flows have fully developed. This requires long simulation times,
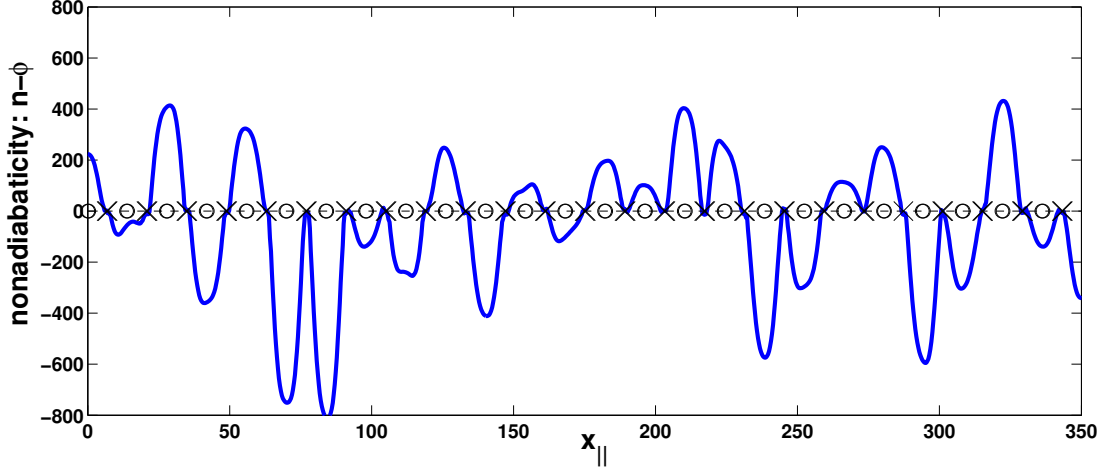
Figure 6.5.: Nonadiabaticity of linear simulation at $t = 285$ along magnetic field line which runs in $\rho = 0.996$ flux surface starting at the top. Transitions through X-point region are marked with crosses and transition through top region are marked with circles

a large domain and also high resolution for quantitative statements, which might be hard to achieve presently with GRILLIX for the used geometry. Moreover, in the open field line region an implementation of better parallel boundary conditions which take into account Debye sheath physics instead of buffer zones might make more sense.

At this early stage we are mainly interested in the shape and the structure of turbulent eddies in the presence of a separatrix. For such a rough qualitative discussion, some robust turbulent state, dominated by non-linear dynamics, suffices. A snapshot of such a turbulent state is shown in fig. 6.6a,b. On a rough scale the picture looks similar to the limiter case (compare fig. 5.12). Within the closed flux surface region zonal structures develop and again a negative potential dip just inside the separatrix is present. Note again that the computational grid does not know about flux surfaces or the X-point at all. The automatic development of flux surface aligned structures, the appearance of the X-point and the sharp transition between open and closed flux surfaces is a consequence of the field line map, which produces very well the expected result. In the open field line region drift wave type structures propagate in the electron diamagnetic direction and accumulate in front of the left divertor plate. No perturbations arise in the private flux region[1] which is dominated by the parallel boundaries. In fig. 6.6c the evolution of the fluctuation free energy of the system is shown. The simulation is not yet saturated and the density profile and the zonal flows still develop. Fig. 6.6d shows zonal averages of various quantities at $t = 1500$. A sharp transition at the separatrix is obvious. In the closed field line region zonal flows develop with the characteristic steep minima and broad maxima (see section 5.2.3) and in accordance density corrugations. The potential exhibits a deep dip just inside the separatrix. In the open field line region also the zonal nonadiabaticity $\langle n - \phi \rangle$ is small, since the parallel boundary conditions tie also the zonal density to the zonal potential. Due to the absence of a sink for the perturbations on the outside, the turbulence screens its drive, the background density gradient, and a shallow density profile develops in the open flux surface region.

In fig. 6.7a the nonadiabaticity is shown on a flux surface well in the closed field line region. The structures are very elongated along the magnetic field lines even through the near X-point

---

[1]There is also a background density gradient in the private flux region present in the simulation.
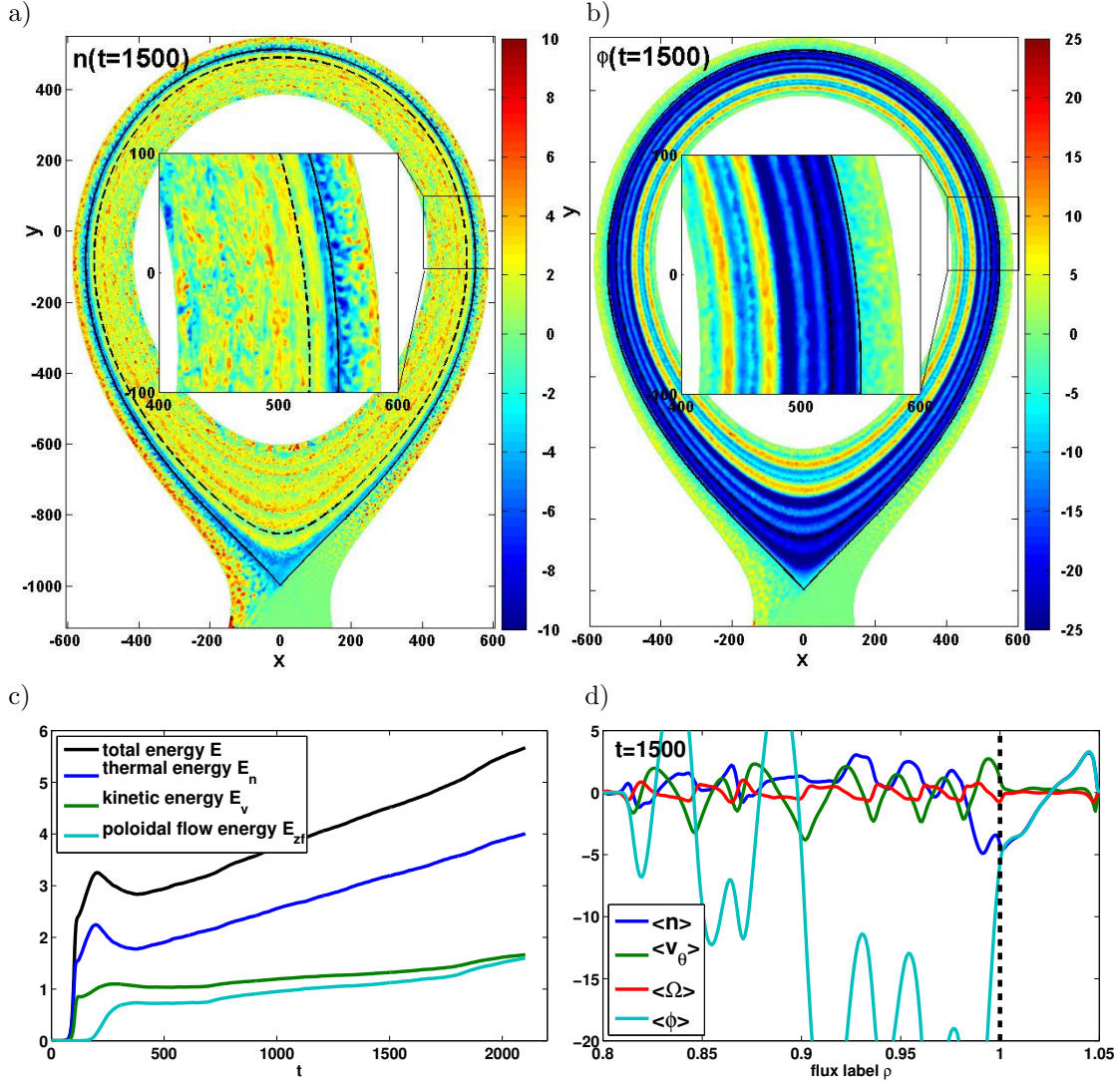
Figure 6.6.: Comprehensive summary of turbulence simulation in axial diverted geometry. For units see again eqs. 2.36 with parameters given in expressions 5.3 (For further simulation details see also last paragraph of section 6.2). Snapshot of a) density perturbation and b) electrostatic potential in the turbulent phase at $t = 1500$. c) Temporal evolution of energies of system. d) Zonal averages of density perturbation, poloidal flow velocity, vorticity and potential at $t = 1500$.

region, where a small bending of the field lines in the axial direction can be observed. On a flux surface very close to the separatrix (fig. b) the structures cannot pass the X-point region but are disconnected. Figs. c,d show correspondingly the nonadiabaticity along a magnetic field line running in these surfaces. On the inner surface the structures can pass often unaffected (undamped) the X-point region. On near separatrix surfaces the structures are always strongly damped in the X-point region which leads to a disconnection across the X-point region. Note again that in all cases the structures are smooth (in numerical sense) along magnetic field lines..
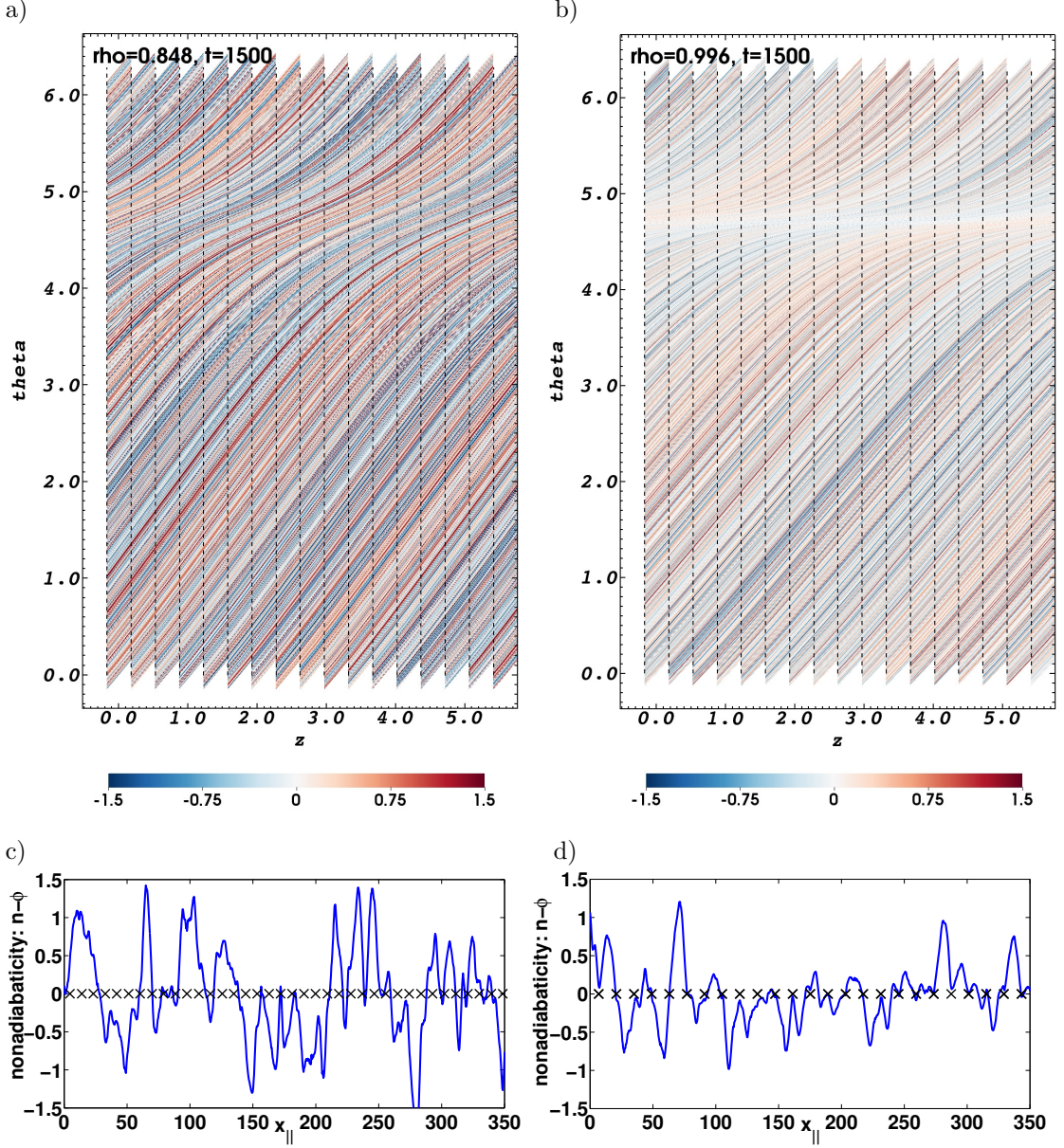
Figure 6.7.: a) Nonadiabaticity $n - \phi$ on flux surface ($\rho = 0.848$) at $t = 1500$ well inside the separatrix. b) For $\rho = 0.996$ close to separatrix. c) Nonadiabaticity along magnetic field line running in c) $\rho = 0.848$, and d) $\rho = 0.996$ flux surface. Black crosses mark regions where magnetic field line passes X-point region.

6.5. Full toroidal geometry

Finally, just as a proof of ability, GRILLIX was applied to a more realistic toroidal geometry. For the equilibrium an analytic solution to the Grad-Shafranov-Schlüter equation with dissimilar source functions [111] was used which models roughly ASDEX Upgrade ($q(\rho = 0.95) = 1.93$).

The background density was assumed to be constant on flux surfaces, which have now a complex shape. The perpendicular scale for normalisation was again the background density gradient, which was taken at the outboard midplane side, i.e. $L_\perp = L_n(om)$. The used parameters again mimic the standard parameters given in expressions 5.3, except that the resistivity was doubled to save computational resources which yielded $D = 1.2$ in terms of GRILLIX parameters (This reduced the stiffness of the problem). Curvature terms were still switched off. To further save computational resources for this simulation, which covered a large domain, a resolution of only $h = 4\rho_s/3$ with $\nu_n = \nu_\phi = 0.01$ was used. $N_{pol} = 20$ poloidal planes were used to bring the map distortion below the desired threshold. To also emphasize the work done at the visualisation a 3D snapshot of this simulation at some robust turbulent state is shown in fig. 6.8. At most planes an amplitude filter was applied, which shows only the strongest structures. Again open and closed flux surfaces and the X-point are apparent. The structures are obviously field aligned across the poloidal planes.
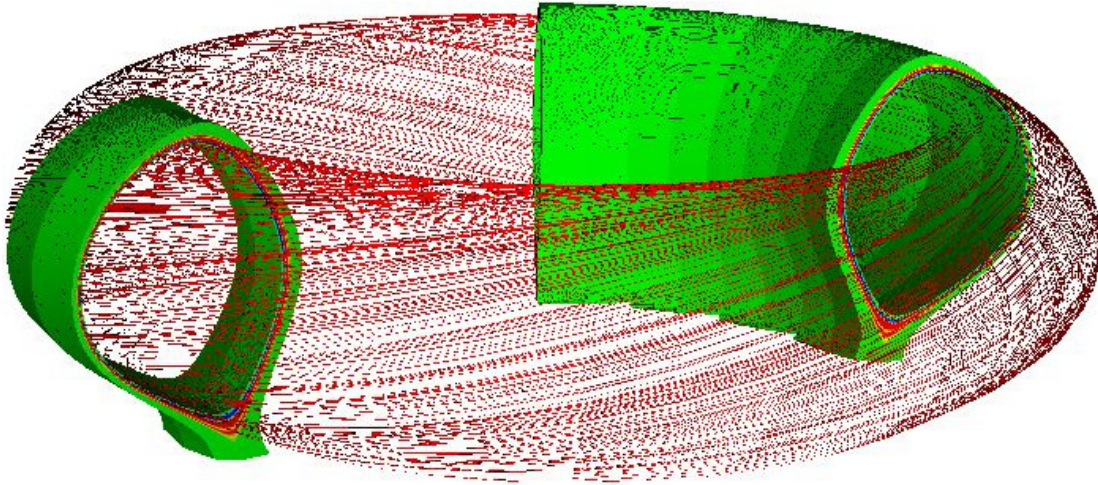
Figure 6.8.: 3D snapshot of nonadiabaticity $n - \phi$ at $t = 400$ of simulation performed in realistic geometry. On most planes an amplitude filter is applied, which shows only the highest values. Colourscale is from blue (low) to red (high).

6.6. Conclusions

In this chapter the effects of an X-point in the domain have been discussed. A flux tube approaching the X-point encounters an exponential compression in one perpendicular direction and an exponential expansion in the other conserving its cross section. For field aligned structures this results in a strong increase of $k_\perp^2$ towards the X-point region and within the HW model the perpendicular dissipation becomes dominant near the X-point.

GRILLIX has then been applied to a domain which spans across the separatrix. A particular simple magnetic field configuration was created to validate and study the effects of an X-point in isolation as purely as possible. The expectations discussed in advance have been validated with GRILLIX. Structures cannot pass or even reach the X-point, since the X-point is infinitely far away (parallel direction) and the structures become strongly distorted near the X-point and are thus subject to an enhanced perpendicular dissipation. They remain ultimately confined from one side of the X-point to the other, which is remotely similar to the resistive X-point mode,

though details of the mechanism differ.

A simulation also with non-linearities switched on has been performed. Though the computational grid is neither field nor flux aligned, the X-point and flux surfaces, with a sharp transition between edge and SOL, became apparent by itself. The structures were at all times smooth (in numerical sense) along magnetic field lines across the poloidal planes, which showed that the field line map, especially the interpolation, did not introduce any numerical artefacts even in such complicated geometry. On a rough scale the result seemed not to differ significantly from the limiter case. Under the influence of turbulence non-zonal perturbations died also out near the X-point. Just as a proof of ability an application to a more realistic equilibrium with a complicated shape of flux surfaces has been presented.

All results are yet qualitative in nature. A short term target which does not need significant further development of GRILLIX could comprise parameter scans in the parallel resistivity and the background density gradient to possibly define a threshold when X-point effects become significant. Also effects of curvature could be studied in the near future. The perturbations are then expected to be driven strongest on the midplane outboard side and the X-point disconnects these modes from the good curvature region. Since the curvature breaks poloidal symmetry it would then be of importance where the X-point is located poloidally.

Chapter 7.

Summary and outlook

7.1. Summary and conclusions

The new 3D turbulence code GRILLIX based on the Hasegawa-Wakatani equations has been developed by me from scratch. The main goal was to build a proof of concept for a turbulence code aimed to investigate and predict anomalous transport in the edge and scrape-off layer in diverted magnetic fusion devices, which pose a special numerical challenge due to the complex geometry. With the exception of FENICIA, which uses a different physical model and which has been developed independently and essentially in parallel to GRILLIX, all present turbulence codes are either not able to cross the separatrix or treat the X-point, as an exceptional grid point, poorly. GRILLIX has been designed to cope with these complex geometries and as such has been shown to be successful and to fulfil the desired requirements.

In chapter 3 the numerical approach, i.e. the field line map, has been presented. A Cartesian grid within poloidal planes is used and the character of the solutions, namely being elongated along magnetic field lines, is exploited by a sparsification of the grid in the toroidal direction and a field line following discretisation of parallel operators. Field or flux aligned coordinate systems, which become ill defined in the presence of a separatrix, are thereby avoided. In contrast to [48, 49, 50], who initially motivated the field line map approach still via a field aligned coordinate system which becomes ill defined at the separatrix, the field line map approach has been motivated here by the observation that the existence of a field aligned coordinate system is irrelevant, since the operators are anyway well defined. This achievement removes possible confusion. Within the field line map approach the flute mode character is exploited at the discretisation step by allowing a lower toroidal resolution without relying on a complicated coordinate system. For the evaluation of parallel operators an interpolation within the perpendicular directions has to be performed, which introduces unavoidably spurious perpendicular coupling. To reduce these spurious effects the parallel diffusion operator has been discretised to maintain its self-adjointness on the discrete level. This was achieved via the application of the method of support operators, which was also previously applied in [52, 53], but in a much simpler environment. A numerical analysis and code benchmarks showed the superiority of this newly developed scheme with which the numerical diffusion can be brought below controllable limits. Effects of a strong map distortion on the numerical scheme have been identified and elegant remedies to these problems have been formulated. Parts from chapter 3 of this thesis have been published [96].

In chapter 5 GRILLIX was applied to axial circular geometry. This simple geometry allowed for extensive benchmarks and comparisons against available codes. The benchmarks have all been passed successfully. Perpendicular operators were benchmarked successfully already in section 2.5 in a periodic box against many other available codes. The support operator method guaranteed that numerical diffusion was subdominant and zonal flows were obtained correctly. The bifurcation of zonal flow production ($C_{HW} = 0.4$), which was recently found with a flux aligned slab code, could also be reproduced with GRILLIX. With a separate also newly developed flux aligned code GRILLIX_FA spurious effects arising from the specific shape of the boundaries

were found to be irrelevant and it could be shown once more that numerical diffusion is well controlled.

Finally, in chapter 6 effects of an X-point were discussed and validated with GRILLIX. For the first time the X-point was investigated systematically with a turbulence code, where the X-point was not treated as an exceptional point. Due to the strong shear near the X-point, the absolute perpendicular wave number increases drastically as a field aligned structure enters the X-point region. Hence, within the Hasegawa-Wakatani model perpendicular dissipation plays the dominant role around the X-point, which led to a confinement of the structures from one side of the X-point to the other. Although the numerical grid of GRILLIX has no knowledge about field lines at all, the X-point and flux surfaces with a sharp transition between open and closed flux surfaces became apparent by itself. Structures which are smooth along magnetic field lines developed automatically also in these complex geometries as a consequence of the field line map. This indicates that the field line map approach is very well suited for studies of this region.

All in all, this proves that the field line map approach in general and GRILLIX in particular are successful. This work sets a milestone for the development of codes whose goal it is to simulate magnetic fusion devices with a separatrix present. Moreover, global tokamak or even stellarator simulations which include also a magnetic axis pose no substantial problems to the field line map approach, in contrast to the widely used flux and field aligned codes.

7.2. Outlook

As has been shown, GRILLIX is already fully able to study effects of a complex geometry on a simple turbulence model. A continuation of this study in a more quantitative manner, which could involve also different kinds of equilibria (e.g. two X-points), is ready to be started. The effects of curvature within the HW model is also left here as a short term target.

For a realistic prediction of anomalous transport in the edge/SOL, the physical model has to be extended. As discussed in detail in chapter 2, a possible target model could be the reduced Braginskii equations which take into account electron/ion temperature fluctuations and which can cope with strong gradients and perturbations of order unity. Moreover, a gyrofluid model (total-f) might be even better suited as a target model, in order to account for small structures ($k_\perp > \rho_{Li}^{-1}$).

The work presented here puts a basis for such a longer term project, since it provides already many of the necessary numerical tools and numerical investigations. Additionally, results for the parallel gradient operator and a parallel advection type equation, which has not been touched here, can be found in [49, 50, 51]. The discretisation of any perpendicular operator is straight forward and simple. But it is e.g. not yet clear how to handle electromagnetic effects in detail, which would lead to a temporal change of the field line map. However, since a temporal variation of the magnetic field does not pose a fundamental problem to the field line map approach, an elegant solution to this problem can certainly be found. It might also be worth to invest some effort to treat the shape of the perpendicular boundaries in a cleaner way, although it did not seem to have big effects on the final result. This could allow also other boundary conditions in the radial direction (e.g. Neumann).

In parallel, continuous work at the algorithms has to be performed. The current constraint of binding the number of MPI processes to the number of planes, might have to be given up at some point. In terms of memory and computational effort, a domain decomposition also within poloidal planes might be inevitable for grids of realistic size. A domain decomposition according to flux surfaces would be on the one hand advantageously to reduce the communication at the evaluation of parallel operators, but on the other hand cumbersome to implement for the

Cartesian grid. Moreover, a better preconditioning which also takes into account the implicitly treated parallel dynamics would be a huge gain. First tests showed already that the number of GMRES iterations could be reduced, by using a preconditioning matrix, where the parallel operators are approximated with just one and the same plane. However, the LU-decomposition and the back substitution of this preconditioning matrix turned out to be too costly. Eventually, this could be resolved automatically by abandoning direct solvers at all. A multigrid method for the solution of the elliptic problem in each time step arising from the vorticity equation, could lead to a substantial improvement. Ongoing work on this problem can already found, e.g. in [147], which take into account also non-Boussinesq flows.

Hence, there is still a lot of work ahead in order to establish a field line map based code which can compute anomalous transport from first principles for the edge/SOL of magnetic fusion devices in complex geometry. Concrete plans to address various of the discussed problems are already on the way at IPP Garching. CPU time at the computer centre IFERC-CSC in Japan has already been applied for and a collaboration with the NMPP division (Numerical Methods in Plasma Physics) and the HLST (High Level Support Team) might be started (partly also continued) in the near future.

Appendix A.

A detailed analysis of references [48,50] with regard to the therein constructed coordinate system at the separatrix

In references [48, 49, 50] it is claimed that the therein constructed coordinate system can deal with diverted magnetic field configurations where a separatrix is present. It has already been discussed in section 3.1 that this statement is not correct, but it shall again be pointed out that the FENICIA code [49, 50, 51] does not rely on the constructed coordinate system, but is ultimately also based on a field line map. Hence, the results presented in [49, 50, 51] are valid and FENICIA is able to treat diverted geometries with a separatrix present. In section 2 of [51] the approach of FENICIA with a field line map is presented.

Nevertheless, to avoid possible confusion in future related to the field line map approach, these papers are analysed here in detail. As was already pointed out in section 3.1, their constructed field aligned coordinate coordinate system becomes ill defined at the separatrix, since already the underlying straight field line coordinate system is ill defined at the separatrix. In section 2 of [48] it is assumed that the coordinates (r, φ, θ) are already available as a set of straight field line coordinates (Hamada), which are ill defined at the separatrix. They propose then a transformation to a field aligned coordinate system[1] according to:

$$\xi = \theta - \frac{1}{q(r)}\varphi, \quad s = \varphi, \quad \rho = r. \tag{A.1}$$

Thus, the parallel gradient becomes $\nabla_\parallel = \partial/\partial s$. It is claimed that this coordinate system can be applied across the separatrix, since the transformation now involves $1/q$, which is bounded at the separatrix. However, this coordinate system is ill defined at the separatrix, since already the poloidal straight field line angle θ is ill defined. This manifests itself as one considers the metric tensor of the coordinate system, which is not discussed in these papers. The radial derivative becomes (eq. 9 of [48], eq. 10 in [50]):

$$\frac{\partial}{\partial r} = \frac{\partial}{\partial \rho} - \frac{q\prime(r)}{q^2(r)}\varphi\frac{\partial}{\partial \xi}. \tag{A.2}$$

This derivative is ill defined since the factor $q\prime/q^2$ diverges at the separatrix. Close to the separatrix the safety factor runs like [10]:

$$q(r) \propto -\ln(r_s - r), \tag{A.3}$$

---

[1]The transformation which they actually propose involves several local coordinate systems N_φ at different toroidal positions φ_k. However, for a strict mathematical treatment we can assume without loss of generality $N_\varphi = 1$ and $\varphi_1 = 0$.

where r_s is the flux label at the separatrix. Applying L'Hospital's rule yields:

$$\lim_{r \to r_s} \frac{q'(r)}{q^2(r)} = \lim_{r \to r_s} \frac{(r_s - r)^{-1}}{(\ln(r_s - r))^2} = \lim_{r \to r_s} \frac{1}{2(r_s - r)} \to \infty, \tag{A.4}$$

which shows that A.2 is ill defined and with such a coordinate system no derivatives can be computed at the separatrix.

In appendix A of [48], section 4 of [50] and section 2.2 of [49] the construction of a field aligned coordinate system based on a flux coordinate independent approach is presented. Similarly also this coordinate system is ill defined at the separatrix, which is shown in the following. An axisymmetric magnetic field of the form:

$$\mathbf{B} = \mathbf{B}_{pol}(x, y) + \mathbf{e}_z \tag{A.5}$$

is considered, where (x, y, z) is a Cartesian reference frame and the magnetic field strength is normalized to the uniform axial magnetic field strength. The poloidal magnetic field is given in terms of a flux function:

$$\mathbf{B}_{pol} = \nabla \times (\Psi(x, y)\mathbf{e}_z) = \frac{\partial \Psi}{\partial y}\mathbf{e}_x - \frac{\partial \Psi}{\partial x}\mathbf{e}_y. \tag{A.6}$$

The parallel gradient is $\nabla_\parallel = \mathbf{B} \cdot \nabla + \partial/\partial z$. A transformation is proposed:

$$\xi^\alpha = V^\alpha(x, y) + C^\alpha(x, y)z, \quad s = z, \tag{A.7}$$

where $\alpha = 1, 2$ and the coefficients V^α and C^α are yet undetermined. In the new coordinate system the parallel gradient becomes:

$$\nabla_\parallel = B_{pol}^\beta \frac{\partial V^\alpha}{\partial x^\beta} \frac{\partial}{\partial \xi^\alpha} + s B_{pol}^\beta \frac{\partial C^\alpha}{\partial x^\beta} \frac{\partial}{\partial \xi^\alpha} + C^\alpha \frac{\partial}{\partial \xi^\alpha} + \frac{\partial}{\partial s}, \tag{A.8}$$

where a summation over α, β is assumed. The coefficients V^α and C^α are chosen such that the fast varying derivatives vanish, i.e. $\nabla_\parallel \to \partial/\partial s$. One must satisfy for this:

$$C^\alpha = [\Psi, V^\alpha], \quad [\Psi, C^\alpha] = 0, \tag{A.9}$$

where $[a, b] = \partial_x a \partial_y b - \partial_y a \partial_x b$. It can be further summarized as:

$$[\Psi, [\Psi, V^\alpha]] = 0, \tag{A.10}$$

Next they consider a function $\chi(x, y)$, such that

$$[\Psi, \chi] = 1. \tag{A.11}$$

This is the critical point in the derivation. At the X-point the poloidal magnetic field vanishes ($\nabla \Psi = 0$) and it is obvious that for condition A.11 to be valid $(\nabla \chi)^2 \to \infty$. Since χ plays ultimately the role of a poloidal straight field line angle, this illustrates that the problem at the X-point is the construction of a straight field line coordinate system. However, if one assumes that the function χ can be found, the field aligned coordinate system is given as:

$$\xi^\alpha = f^\alpha(\Psi) + h^\alpha(\Psi)(\chi + z), \quad s = z, \tag{A.12}$$

where g^α and h^α are arbitrary functions which only depend on Ψ. At this point references [48, 49, 50] do not investigate if the coordinate system is well defined, which is done in the following. The Jacobian of the transformation is:

$$J^{-1} = \nabla s \cdot (\nabla \xi^1 \times \nabla \xi^2) = (A^1 h^2 - A^2 h^1)[\Psi, \chi] = A^1 h^2 - A^2 h^1, \tag{A.13}$$

100

with $A^\alpha = f^{\alpha\prime} + h^{\alpha\prime}(\chi + z)$. The metric tensor is given as:

$$g^{\alpha\beta} = A^\alpha A^\beta (\nabla\Psi)^2 + (A^\alpha h^\beta + A^\beta h^\alpha)\nabla\Psi \cdot \nabla\chi + h^\alpha h^\beta \left[1 + (\nabla\chi)^2\right], \qquad (A.14)$$

$$g^{\alpha 3} = g^{3\alpha} = h^\alpha, \quad g^{33} = 1. \qquad (A.15)$$

For a finite Jacobian it must at least hold for one of the coefficients $h^\alpha \neq 0$. Since at the X-point $(\nabla\chi)^2 \to \infty$, this results in at least one divergent entry in the metric tensor $g^{\alpha\alpha} \to \infty$ and thus the coordinate system is ill defined. E.g. a construction of the Laplacian, in which the metric coefficients enter is not possible.

In section 4.2 of reference [50] and section 2.2.1 of [49] they claim to have obtained a solution for the function χ for an X-point configuration where the poloidal flux is chosen such that $\Psi(x,y) = \Psi_0(x) + A\cos(k_y y)$. Actually, in a recent paper [51] this solution is shown. Taking $A = 1, k_y = 1$ and $\Psi_0(x) = x^2$, there are X-points at $x = 0, y = 0$ and $x = 0, y = 2\pi$ and a magnetic axis at $x = 0, y = \pi$. Indeed the function χ can be obtained in terms of elliptic integrals as:

$$\chi(x,y) = \frac{1}{\sqrt{1 - \Psi(x,y)}} F\left(\frac{x}{\sqrt{1 + \Psi(x,y)}}, \sqrt{\frac{-(1 + \Psi(x,y))}{1 - \Psi(x,y)}}\right), \qquad (A.16)$$

with F the incomplete elliptic integral of the first kind. The condition for a point (x,y) to be on the separatrix is $\Psi(x,y) = 1$. Hence, it becomes apparent that the function χ diverges on the whole separatrix, which is also noted in section 5 of [51]. In fig. A.1 the contours of the poloidal flux function Ψ and of the function χ are plotted. Similarly to fig. 3.1b in chapter 3 the contours of the straight poloidal field line angle are sucked into the X-points and χ is not well defined at the separatrix.
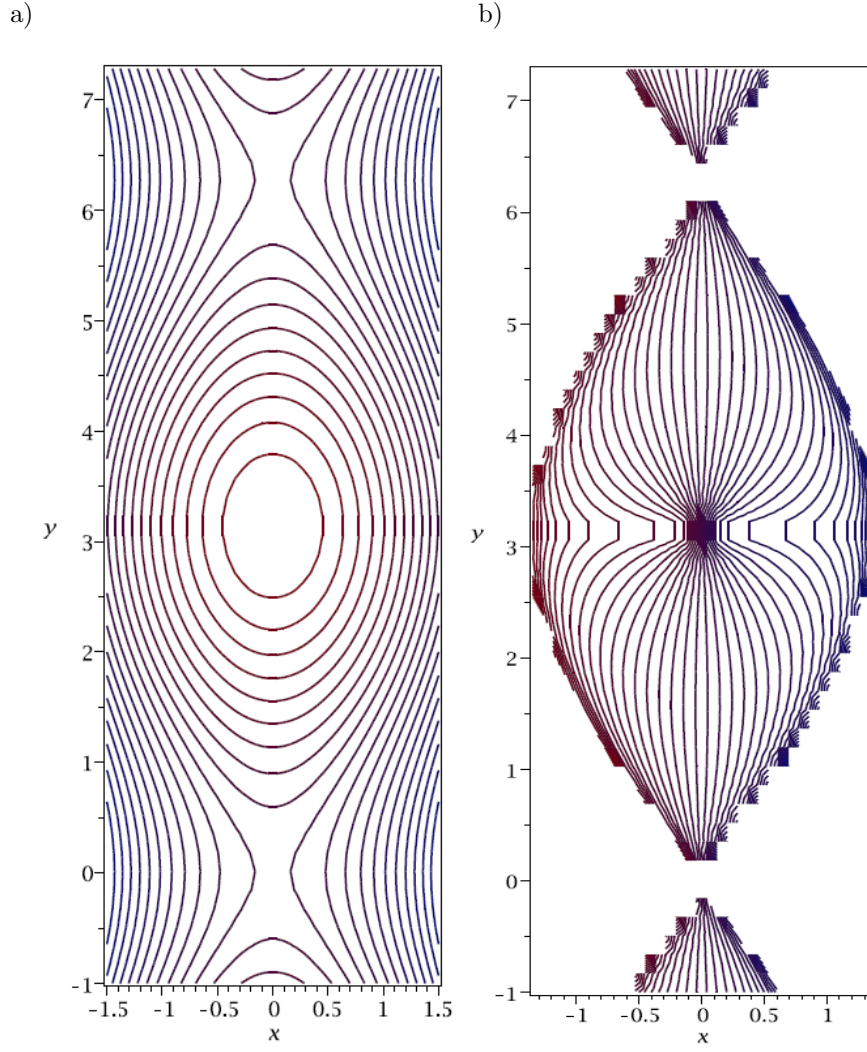
Figure A.1.: a) Contours of potential for problem posed in section 4.2 of reference [50] with $A = 1, k_y = 1$. b) Contours of corresponding function χ which fulfils $[\Psi, \chi] = 1$.

Appendix B.

Supplements to field line map

B.1. Interpolation

For the computation of the parallel gradient described in section 3.4.1 the values of the quantity at the penetration points $(R^{\alpha,\beta}, Z^{\alpha,\beta})$ are computed via a bilinear or a 3rd order polynomial interpolation. This section describes the interpolation process (see also e.g. [109]).

As shown in fig. B.1, the interpolation involves 2×2 neighbouring grid points around the penetration points for bilinear respectively 4×4 for 3rd order polynomial interpolation. The collocation points for each penetration point is found by a separate routine (see block Parallel Indexing in work flow of GRILLIX, fig. 4.2) by evaluating the distance to the penetration point[1] (R, Z). For some penetration point we label the collocation points with the indices $u_{n,m}$, with $n, m = 1, 2$ respectively $n, m = 1 \ldots 4$.

a)

b)
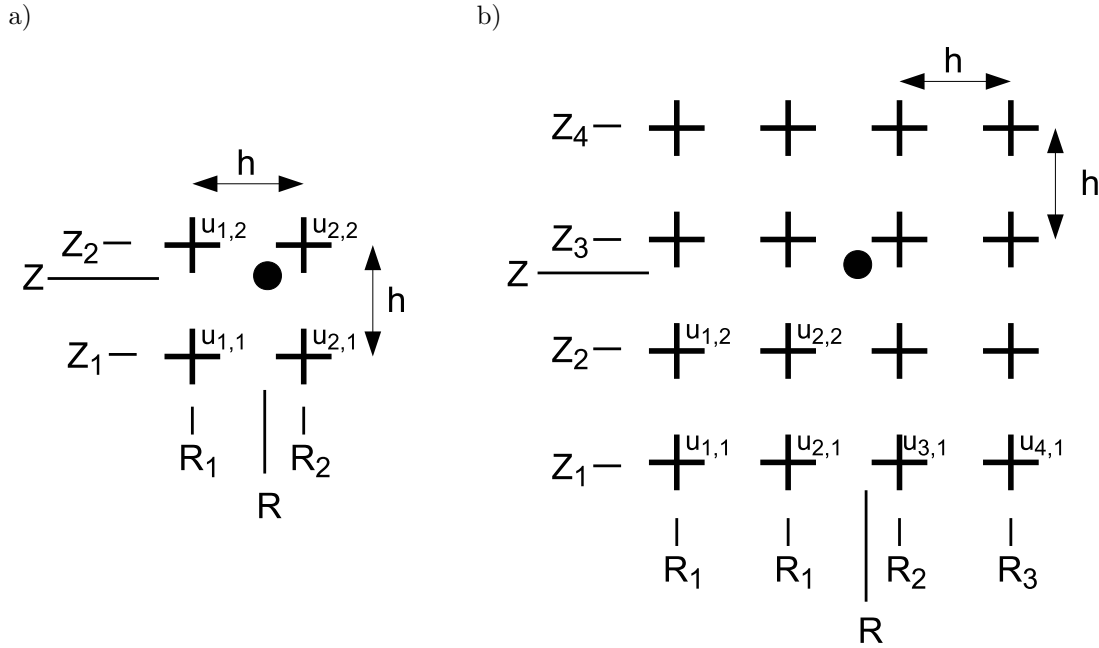
Figure B.1.: a) Interpolation grid for bilinear interpolation, b) for 3rd order bipolynomial interpolation.

---

[1] The superscript α, β is dropped in the following. The subsequent discussion is valid for both.

A bilinear interpolation consists of two interpolations along one direction (R):

$$u(R, Z_1) = \frac{1}{h} \left[(R_2 - R) \, u_{1,1} + (R - R_1) \, u_{2,1} \right], \tag{B.1}$$

$$u(R, Z_2) = \frac{1}{h} \left[(R_2 - R) \, u_{1,2} + (R - R_1) \, u_{2,2} \right], \tag{B.2}$$

followed by one interpolation along the other direction:

$$u(R, Z) = \frac{1}{h} \left[(Z_2 - Z) \, u(R, Z_1) + (Z - Z_1) \, u(R, Z_2) \right] \tag{B.3}$$

resulting in:

$$
\begin{aligned}
u(R, Z) = & \frac{(R - R_2)(Z - Z_2)}{h^2} u_{1,1} - \frac{(R - R_1)(Z - Z_2)}{h^2} u_{2,1} \\
& - \frac{(R - R_2)(Z - Z_1)}{h^2} u_{1,2} + \frac{(R - R_1)(Z - Z_1)}{h^2} u_{2,2}.
\end{aligned} \tag{B.4}
$$

It is obvious that the interpolation is linear in the collocation points and can thus be written as matrix with the interpolating coefficients as entries. Therefore, the parallel gradient can also be written in matrix form $\mathbf{Q}^{\alpha,\beta}$ as proposed in eq. 3.19.

In a similar way also the 3rd order bipolynomial interpolation is conducted. First four 3rd order polynomial interpolations in R-direction are performed to the positions $u(R, Z_m)$ and finally one 3rd order interpolation along the Z-direction, which finally yields:

$$u(R, Z) = \sum_{n=1}^{4} \sum_{m=1}^{4} \left[(-1)^{n+m} \frac{c_{n,m}}{h^6} \prod_{\substack{i=1, \\ i \neq n}}^{4} \prod_{\substack{j=1, \\ j \neq m}}^{4} (R - R_i)(Z - Z_j) \right] u_{n,m}. \tag{B.5}$$

Again, this expression is linear in the collocation points with the expression in brackets being the interpolating coefficients. The constants $c_{n,m}$ are given according to:

$$c_{1,1} = c_{1,4} = c_{4,1} = c_{4,4} = \frac{1}{36}, \tag{B.6}$$

$$c_{1,2} = c_{1,3} = c_{2,1} = c_{2,4} = c_{3,1} = c_{3,4} = c_{4,2} = c_{4,3} = \frac{1}{12}, \tag{B.7}$$

$$c_{2,2} = c_{2,3} = c_{3,2} = c_{3,3} = \frac{1}{4}. \tag{B.8}$$

Finally, it is noted that if a point of the interpolating grid is missing, which is the case for field lines close to the boundaries, ghost points with a value zero are implicitly assumed for the missing points.

B.2. 2D model problem with polynomial interpolation

Similarly to section 3.6.1 the stencil for the support scheme with a 3rd order polynomial interpolation is derived. Since more points than for the bilinear interpolation are involved, the minimum problem which contains at least one inner point is a $n_x \times n_z = 7 \times 3$ grid. The indexing is as in section 3.6.1 with $\mathbf{u} = (u_{1,1}, u_{2,1}, \cdots u_{7,1}, u_{1,2} \cdots)^T$, and the only inner point is $u_{4,2}$. The

parallel gradient matrix is:

$$
\mathbf{Q}^{\alpha} = -\left(\mathbf{Q}^{\beta}\right)^{T} = \frac{1}{\Delta s}
\begin{pmatrix}
-1 & & & & & & & c & b & a & & & & & [d] & & & & \\
& -1 & & & & & & d & c & b & a & & & & & & & & \\
& & -1 & & & & & & d & c & b & a & & & & & & & \\
& & & -1 & & & & & & d & c & b & a & & & & & & \\
& & & & -1 & [a] & & & & & d & c & b & & & & & & \\
& & & & & -1 & [b] & [a] & & & & & d & c & & & & & \\
& & & & & & -1 & & & & & & c & b & a & & & [d] \\
& & & & & & & -1 & & & & & & d & c & b & a & \\
& & & & & & & & -1 & & & & & & d & c & b & a \\
& & & & & & & & & -1 & & & & & & d & c & b & a \\
& & & & & & & & & & -1 & [a] & & & & & d & c & b \\
& & & & & & & & & & & -1 & [b] & [a] & & & & d & c \\
[c] & [b] & [a] & & & & [d] & & & & & & -1 & & & & & \\
[d] & [c] & [b] & [a] & & & & & & & & & & -1 & & & & \\
& [d] & [c] & [b] & [a] & & & & & & & & & & -1 & & & \\
& & [d] & [c] & [b] & [a] & & & & & & & & & & -1 & & \\
& & & [d] & [c] & [b] & [a] & & & & & & & & & & -1 & \\
[a] & & & & [d] & [c] & [b] & & & & & & & & & & & -1 \\
[b] & [a] & & & & [d] & [c] & & & & & & & & & & &
\end{pmatrix}
$$
(B.9)

with:

$$
a = \frac{f^{2}(f-1)}{6}, \quad b = -\frac{f(f+1)(f-2)}{2}, \quad c = \frac{(f^{2}-1)(f-2)}{2}, \quad d = \frac{f(f-1)(f-2)}{6}, \quad \text{(B.10)}
$$

and the rectangular brackets denote a connection across the periodic boundaries of the domain. Again, the stencil for the naive scheme and the support scheme follow immediately for the inner grid point and is illustrated in fig. B.2a,b Observe again that if the displacement is zero

Figure B.2.: Stencil for the 2D minimum non-trivial problem with 3rd order polynomial interpolation: a) Naive scheme, b) support scheme.

$(f = 0, 1)$ both schemes yield the standard finite difference expression for the second derivative. Again, the naive method involves only the considered grid point itself and points involved in the interpolation at the neighbouring poloidal planes, whereas the support scheme has a big stencil covering many points also within the considered plane.

B.3. Benchmarks of field line map in shaped geometry

For general shaped geometry an analytic solution to the parallel diffusion equation is in general not available. Moreover, rigorous convergence checks in the interesting region close to the sep-

aratrix are elaborate due to the complex field line structure and computationally costly due to the size of the domain. Therefore, only rough convergence tests are performed here.

For the first benchmark the blob as described in section 3.8 with a δ-peak in the toroidal direction is considered as the initial state.

$$u(t = 0) = \exp\left[-\frac{(R - R_c)^2}{R_w^2} - \frac{(Z - Z_c)^2}{Z_w^2}\right]\delta(\varphi). \tag{B.11}$$

Some snapshots which illustrate the diffusion of the blob can also be found in section 3.8 (fig. 3.13 and fig. 3.15). Convergence is checked by simply evaluating the obtained maximum value of u at the toroidally opposed plane at the time $t = 10.0$ ($\|u(t = 10.0, \varphi = \pi)\|_\infty$) in dependence on resolution and the numerical scheme. The time step was held constant at $\Delta t = 1E - 2$ regardless of spatial resolution. It is noted that as discussed in section 3.8 for resolutions $N_{pol} \lesssim 8$ spurious wiggles are observed with the **S-1** and **S-3** scheme, which vanish for higher toroidal resolution resulting in smooth structures.

In fig. B.3a the maximum value at the opposed plane is plotted against the toroidal resolution N_{pol} for fixed poloidal resolution and in fig. B.3b in dependence on poloidal resolution h for fixed toroidal resolution. Similar to the results obtained in simple cylindrical geometry in section 3.7.2, the convergence for the support schemes is faster. Both **S-1** and **S-3** converge for the fixed toroidal resolution quickly against the same value of ~ 0.4. Since the naive schemes discretise $\nabla_\parallel^2$, whereas the support schemes discretise $\nabla \cdot \left[\mathbf{b}\nabla_\parallel\right]$, we expect a convergence against slightly different values for the naive schemes. Thus the **N-3** scheme firstly shows a smooth convergence against a slightly different value of roughly ~ 0.43. Again, at the highest resolutions an abrupt jump is present which might arise from some numerical instability and is not yet fully understood. For the **N-1** scheme a convergence could not be achieved with the available hardware, but the curve tends also to converge against a slightly higher value of ~ 0.43.

a)

b)
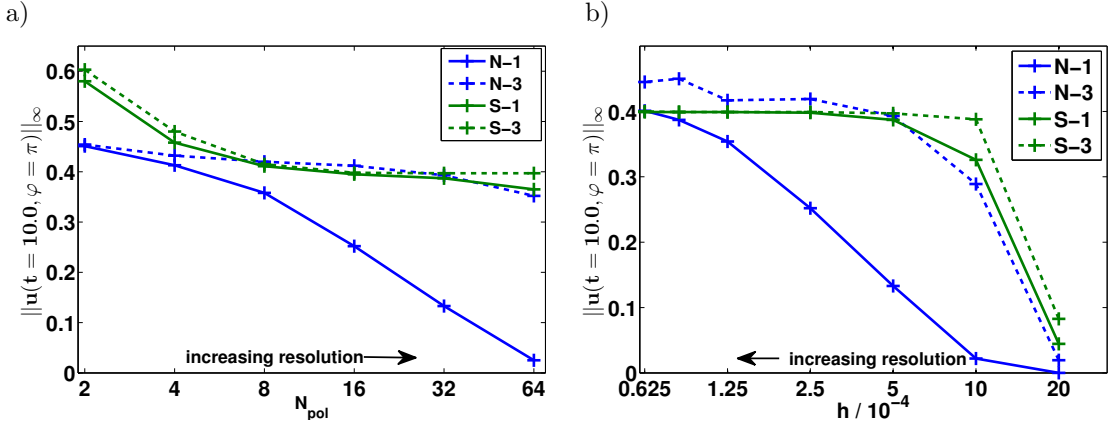
Figure B.3.: Convergence test with blob. The maximum value at the opposed plane $\|u(t = 10.0, \varphi = \pi)\|$ of the initial blob ($R_c = 0.88, Z_c = -0.29, R_w = Z_w = 8 \cdot 10^{-3}$) is plotted against resolution. a) In dependence on toroidal resolution for fixed poloidal resolution of $h = 5 \cdot 10^{-4}$, b) in dependence on poloidal resolution for fixed toroidal resolution of $N_{pol} = 32$. Time step was held constant at $\Delta t = 1 \cdot 10^{-2}$. For snapshots which illustrate the diffusion of this blob see also figs. 3.13 and 3.15 in section 3.8.

The second benchmark addresses the numerical decay of zonal modes. In fig. B.4 the error in dependence of time is shown for a zonal mode located at the edge. The toroidal resolution was

chosen $N_{pol} = 32$, such that the map distortion is well below the desired threshold. Basically, the same behaviour as was obtained for axial equilibria (see section 3.7.2, fig. 3.10) is shown. After a very short time the mode has decayed practically completely for the **N-1** scheme. For the **N-3** scheme the decay is slower due to the higher interpolation order and the decay is even a bit slower for the **S-1** scheme. Due to boundary effects for the **S-3** scheme, the error is first slightly higher as compared to the **S-1** scheme, but then the mode decays on a much slower level.
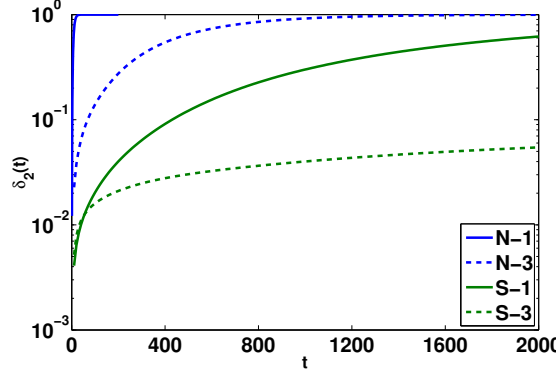
Figure B.4.: Temporal evolution of error $\delta_2(t)$ for a zonal mode $r = 2, m = 0, n = 0$. The simulation domain covered $\rho = 0.9 \ldots 0.95$. The simulations were resolved with $N_{pol} = 32$ and $h = 5 \cdot 10^{-4}$ being roughly 20 points per radial wavelength at the LFS and roughly 40 points at the HFS. Time step was $\Delta t = 1.0$

We pass on a scan of the numerical decay rate γ_{num} with poloidal/toroidal resolution, since it is computationally very expensive. The decay rate for the **S-3** scheme exhibits a very strong scaling with poloidal resolution. The determination of the decay rate thus requires extremely long run times with a large grid. The results shown here should be evidence enough that the support operator method is by far the superior with respect to the naive method also in shaped geometry.

B.4. Parallel boundary conditions

For open field lines hitting divertor or limiter plates parallel boundary conditions at the intersection of the field line with the plates have to be supplied. At present Dirichlet boundary conditions $u|_{plate} = 0$ are available.

Field lines which hit divertor plates are identified during the field line tracing procedure. In each integration step it is checked if field lines intersect with the divertor plates. At the parallel boundaries the discrete parallel gradient is computed at the position half way along a magnetic field line between the considered grid point and the plates via a finite difference. For the naive scheme the parallel diffusion operator follows as usual via a further finite difference between the parallel gradients (α and β).

For the support scheme the situation is a bit more cumbersome and is illustrated in fig. B.5. For closed field lines the $\mathbf{D}^\alpha$ and $\mathbf{D}^\beta$ discretisation of the parallel diffusion operator are equally valid and both scalar products $\langle p^\alpha, q^\alpha \rangle_\alpha$ and $\langle p^\beta, q^\beta \rangle_\beta$ cover the same domain. Thus for the final parallel diffusion operator just the average is taken $\mathbf{D} = 1/2 \left(\mathbf{D}^\alpha + \mathbf{D}^\beta \right)$ (see expression 3.34). However, in the presence of a parallel boundary field lines end in plates and the scalar products in α and β cover a different volume. Hence, the combined scalar product for fluxes, according to

eq. 3.35 has to be modified:

$$\langle p, q \rangle_{FG} := \sum_i f_i^\alpha q_i^\alpha p_i^\alpha \Delta \mathcal{V}_i^\alpha + f_i^\beta q_i^\beta p_i^\beta \Delta \mathcal{V}_i^\beta, \tag{B.12}$$

where $f_i^{\alpha,\beta} = 1/2$ if the field line originating from grid point i in α, β direction does not intersect with a plate and $f_i^{\alpha,\beta} = 1$ if it intersects with a plate. Accordingly, the parallel diffusion operator for some point i changes to:

$$\mathbf{D}_{ij} = f_i^\alpha \mathbf{D}_{ij}^\alpha + f_i^\beta \mathbf{D}_{ij}^\beta. \tag{B.13}$$

As can be also seen in fig. B.5, the distinction of the domain which is counted once or twice is not perfect, but an error remains only for single grid points. In the limit $h \to 0$ the flux box volumes reduce essentially to lines and the distinction becomes perfect showing indeed the convergence of this approach.
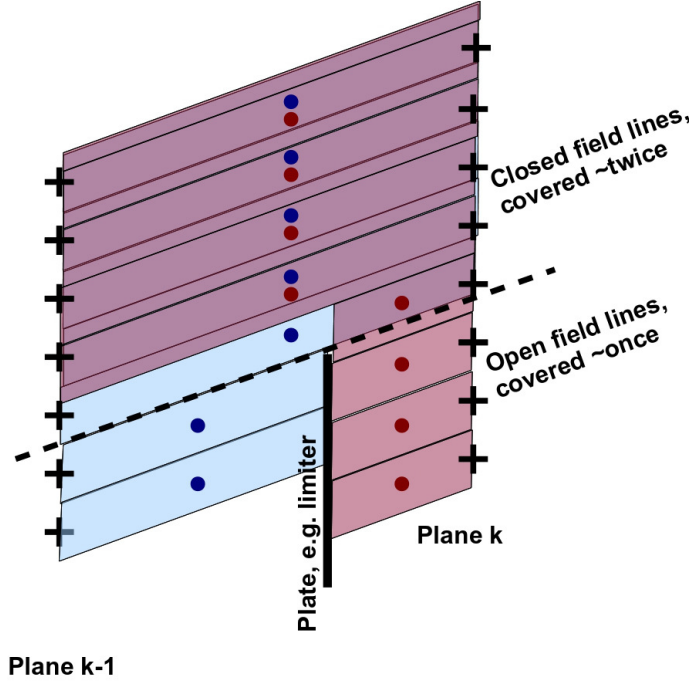
Figure B.5.: Sketch of field line map with parallel boundary conditions. Illustrated are two planes (2D) with a plate in between, e.g. a limiter plate. The magnetic field lines are assumed for simplicity straight. Blue (red) points indicate positions where the parallel gradient α (β) is computed for plane $k-1$ (k). Blue (red) boxes indicate flux box volumes around parallel gradients $\Delta \mathcal{V}^\alpha$ ($\Delta \mathcal{V}^\beta$) belonging to plane $k-1$ (k). Note that more or less the closed field line region is covered twice (red + blue) by the flux box volumes, whereas the open field line region is covered only once (either red or blue).

To perform a benchmark of the boundary conditions, an axial equilibrium is considered with a toroidally axisymmetric limiter at the poloidal angle $\theta = 0$. The limiter extends radially into the whole domain and is assumed to be infinitely thin in the poloidal direction. An approximate analytic solution can be found. We imagine the magnetic field lines rolled out from the one side

of the limiter to the other side as illustrated in fig. B.6a. $x_\parallel$ shall be a coordinate along a field line starting from a limiter plate and $\mathbf{x}_\perp$ coordinates perpendicular to the magnetic field line. The parallel diffusion equation reduces then to a simple 1D diffusion equation along $x_\parallel$. Let the initial state be characterised by a parallel wave number $n_\parallel$, i.e.:

$$u(t=0) = u(\mathbf{x}_\perp)\sin\left(\frac{n_\parallel \pi}{L_\parallel}x_\parallel\right), \tag{B.14}$$

where $L_\parallel(\rho) = 2\pi q(\rho)\sqrt{1 + \rho^2/q(\rho)^2}$ is the connection length from plate to plate. The representation of such a structure on the GRILLIX grid is shown in fig. B.6b,c. The solution of the parallel diffusion equation can again be found via Fourier transform methods:

$$u(t) = u(t=0)\exp(-\gamma t), \quad \text{with: } \gamma(\rho) = \frac{n_\parallel^2 \pi^2 \chi_\parallel}{L_\parallel(\rho)^2}. \tag{B.15}$$

For the benchmark a constant safety factor is assumed and the width of the flux shell is assumed to be small such that in a good approximation $\gamma(\rho) \approx \gamma((\rho_{max} + \rho_{min})/2)$ can be assumed.
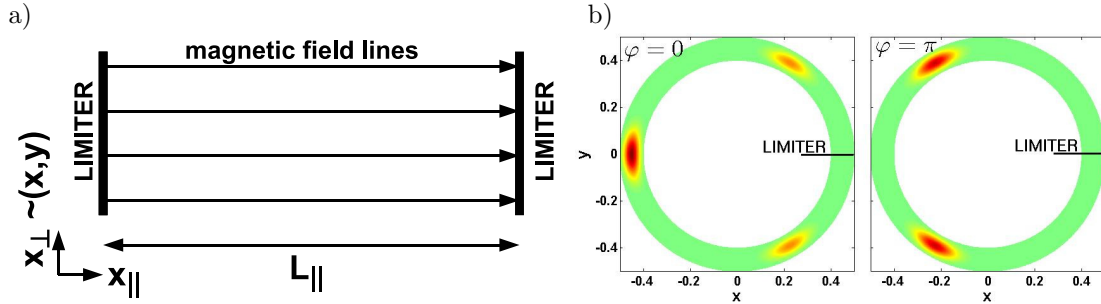

Figure B.6.: a) Sketch of rolled out field lines in presence of an axisymmetric limiter. b) Example of a $n_\parallel = 1$ mode on the GRILLIX grid at $\varphi = 0$ and $\varphi = \pi$. The structure is in the perpendicular direction a Gaussian of size $w_\rho = 0.03$, $w_\theta = 0.2$, centred around a magnetic field line, which runs from plate to plate. The safety factor is $q(\rho) = 3$ with $\rho = 0.4 \ldots 0.5$.

In fig. B.7 the relative error of the numerically obtained decay exponent is plotted in dependence on toroidal resolution N_{pol} for two different parallel mode numbers. Due to the fact that the analytic solution is only approximate, the finite poloidal resolution and the non-equidistant grid (in the parallel sense), the error does not follow a straight line but is slightly irregular. Overall the error goes down and scales somewhat in between N_{pol}^{-1} and N_{pol}^{-2} in contrast to the benchmarks performed in section 3.7.2 for closed field lines (see fig. 3.9), where the error scaled like N_{pol}^{-2} for a sufficiently high poloidal resolution. The reason for this break of scaling here is that the presence of the limiter breaks the equidistant property of the grid, i.e. $\Delta s^\alpha \neq \Delta s^\beta$ for grid points next to the plates, and in the worst case only a first order accuracy can be expected [110].

A final test concerns the simultaneous presence of open and closed field lines. An axial equilibrium with an axisymmetric limiter half way radially into the flux shell is considered. A zonal mode extending across the separatrix ($r = 1$, $m = 0$, $n = 0$) flows in the open field line region to the limiter plates and decays there, whereas in the closed field line region it should remain stable. Finally, a jump at the LCFS remains. This behaviour is obtained also in a simulation performed with the **S-3** scheme (see fig. B.8). Due to the interpolation, the jump across the
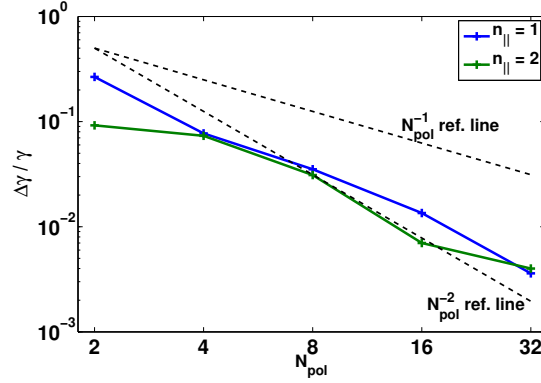
Figure B.7.: Numerical error $\Delta\gamma/\gamma = |\gamma_{num} - \gamma_{an}| \,/\, |\gamma_{an}|$ of a $n_\parallel = 1$ and $n_\parallel = 2$ mode in dependence on toroidal resolution N_{pol} for fixed poloidal resolution $h = 5 \cdot 10^{-4}$ computed with **S-3**. Perpendicular structure of initial state was a Gaussian ($w_\rho = 0.02$, $w_\theta = 0.2$, see fig. B.6) around a magnetic field line. Other parameters: $q = 3$, $\rho_{min} = 0.4$, $\rho_{max} = 0.5$, $dt = 2 \cdot 10{-}4$. $\gamma_{an}(n_\parallel = 1) = 2.72 \cdot 10^{-2}$, $\gamma_{an}(n_\parallel = 2) = 0.109$.

LCFS is not perfectly obtained, of course. In fig. B.9 the values of the grid points cut radially trough the domain ($x < 0$, $y = 0$, $z = 0$) are shown at an intermediate time and at a late time, where the mode has decayed nearly completely in the open field line region. For the **N-1** scheme the region around the LCFS becomes smeared out and the numerical perpendicular transport in this region is high resulting in a fast decay of the overall mode. For the **N-3**, **S-1** and **S-3** scheme in the region around the LCFS over swings arise due to the interpolation of a discontinuity. For the regions well away from the LCFS the structures are smooth and the mode remains stable in the closed field line region. The numerical transport is lowest for the **S-3** scheme and thus the jump is steepest for this scheme. For practical applications a finite physical perpendicular transport/diffusion process will always smooth structures in the region around the LCFS.
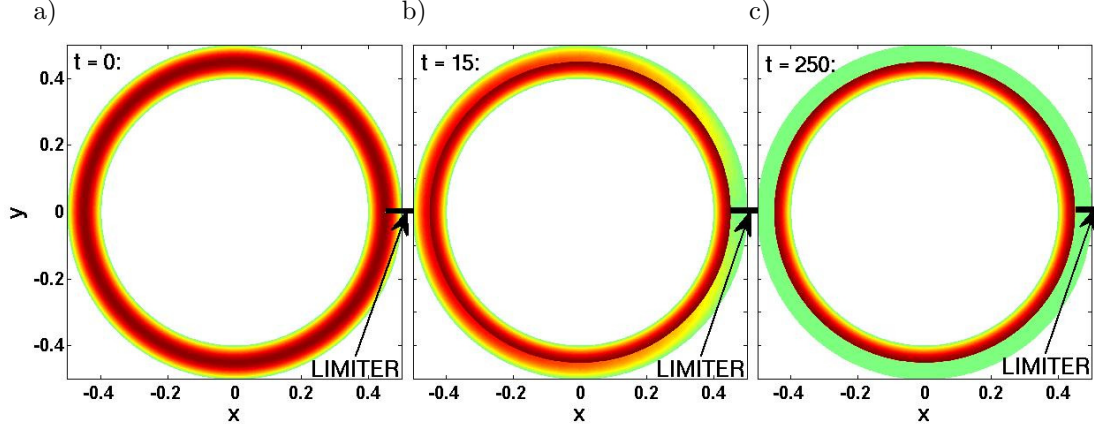
Figure B.8.: Snapshots of a simulation (**S-3** scheme performed with $N_{pol} = 16$, $h = 5 \cdot 10^{-4}$, $\rho_{min} = 0.4$, $\rho_{max} = 0.5$, $dt = 1 \cdot 10^{-2}$, here shown plane $z = 0$) with an axisymmetric limiter ranging radially half way into the domain. The initial state (a) decays in the open field line region (b). In the final state (c) the mode has decayed completely in the open field line region, whereas it remains stable in the closed field line region leaving a jump in the radial direction.
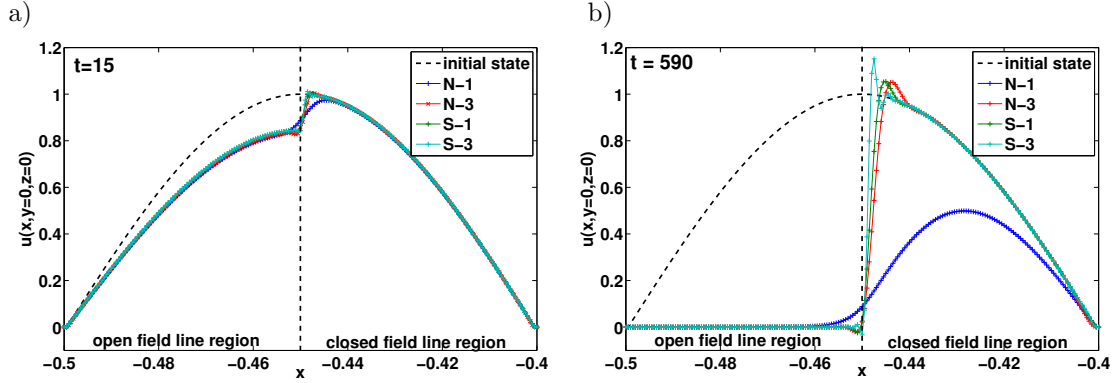
Figure B.9.: Values of quantity u on grid points at x, $y = 0$, $z = 0$ (radial cut at opposed position to limiter at a) $t = 15$, b) $t = 590$. Simulation details as in fig. B.8

Appendix C.

Field line tracing and grid creation

In this appendix the field line tracing procedure and the creation of the grids is described. The creation of the grids is performed with the program create_grid@GRILLIX which is run in a advance to main@GRILLIX. The input of create_grid@GRILLIX is the file *equi_params.in*, where parameters of the equilibrium are set (axial or toroidal, q-profile,...), and the file *grid_params.in*, where parameters of the grid (resolution, limiting flux surfaces,...) are set. The output are two files, *grid_cart.in*, where grid information for the Cartesian grid is stored, and *grid_polar.in*, where grid information for a polar grid is stored which is mainly needed for diagnostic purposes (see fig. 4.1). Due to axisymmetry the information is identical for each plane.

Within the poloidal plane only one grid index l is used for the Cartesian grid going from the lower left point of the grid to the upper right grid point. The information which is established and stored in *grid_cart.in* is:

- Position of the grid points: R_l, Z_l.

- Cartesian indices of the grid points to find poloidal neighbours: i_l, j_l.

- Flux label: ρ_l.

- Magnetic field: $B_{R\,l}, B_{Z\,l}, B_{tor\,l}$ and its derivatives with respect to R, Z.

- The penetration points and lengths along field lines towards neighbouring poloidal planes: $R_l^{\alpha,\beta}, Z_l^{\alpha,\beta}, \Delta s_l^{\alpha,\beta}$.

- The flux box volumes: $\Delta V_l, \Delta \mathcal{V}_l^{\alpha,\beta}$.

- To compute the distortion and for the coordinate free representation of the parallel gradient, the four edges of the mapped quad.

Given $R_{min}, R_{max}, Z_{min}, Z_{max}$, a Cartesian rectangular grid R_i, Z_j with given grid spacing h is established. For each point the flux label is computed via a given function $\rho(R, Z)$. Only those grid points are kept for which $\rho_{min} < \rho(R_i, Z_j) < \rho_{max}$, where ρ_{min}, ρ_{max} are the flux labels of the limiting flux surfaces. From this results the basic grid $R_l, Z_l, i_l, j_l, \rho_l$, with l the index running within the poloidal plane.

For each point the magnetic field $B_{R\,l}, B_{Z\,l}, B_{tor\,l}$, normalized to the magnetic field strength at the magnetic axis is computed. For toroidal geometries the computation of the poloidal field components is performed via derivatives from a given poloidal flux function $\Psi(R, Z)$ (see eq. 3.1).

$$B_R = -\frac{1}{R}\frac{\partial \Psi}{\partial Z}, \quad B_Z = \frac{1}{R}\frac{\partial \Psi}{\partial R}. \tag{C.1}$$

The derivatives of Ψ are given as an analytic function. The toroidal field is approximated with the vacuum field $B_{tor} = 1/R$. For axial circular geometry the axial field is assumed constant and

uniform $B_z = 1$ and the poloidal field components are computed via a given q-profile

$$B_x = -\frac{\rho \sin(\theta)}{q(\rho)}, \quad B_y = \frac{\rho \cos(\theta)}{q(\rho)}, \tag{C.2}$$

where $\rho = \sqrt{x^2 + y^2}$ the radial coordinate and $\tan\theta = y/x$ the poloidal angle. For axial geometry with an X-point the magnetic field is obtained by superposition of the axial circular field, prescribed by a q-profile and the magnetic field $\mathbf{B}_{wire}$ created by a wire in the divertor region.

$$B_{wire\,x} = -\frac{c_{wire}}{x^2 + (y - y_{wire})^2}(y - y_{wire}), \quad B_{wire\,y} = \frac{c_{wire}}{x^2 + (y - y_{wire})^2}x, \tag{C.3}$$

where c_{wire} is a constant proportional to the current through the wire and y_{wire} is the y-position of the wire. x_{wire} is assumed to be zero. The computations of the derivatives of $\mathbf{B}$ with respect to R, Z (x, y for axial geometry) is straight forward.

For axial circular geometries the computation of the penetration points $(x^{\alpha,\beta}, z^{\alpha,\beta})$ needed for the field line map can be performed analytically. For each grid point l the corresponding radial coordinate and poloidal angle ρ_l, θ_l is computed. Going a distance Δz along a field line only changes the value of the poloidal angle to:

$$\theta_l^{\alpha,\beta} = \theta_l \pm \frac{\Delta z}{q(\rho_l)}. \tag{C.4}$$

The penetration points are obtained by a back transformation from the polar coordinate to the Cartesian coordinate $(\rho_l, \theta_l^{\alpha,\beta}) \rightarrow (x^{\alpha,\beta}, z^{\alpha,\beta})$. The lengths along the magnetic field lines are $\Delta s_l^{\alpha,\beta} = \Delta z\sqrt{1 + (\rho_l/q(\rho_l))^2}$ and the flux box volumes are all constant $\Delta V_l = \Delta \mathcal{V}_l^{\alpha,\beta} = h^2\Delta z$.

For more general geometries (toroidal, axial-diverted) the field line tracing has to be performed numerically. To obtain the penetration points the following ordinary differential equations have to be solved:

$$R_l^{\alpha,\beta} = R_l + \int_0^{\pm\Delta\varphi} d\varphi\, R\frac{B_R}{B_{tor}}, \qquad\qquad Z_l^{\alpha,\beta} = Z_l + \int_0^{\pm\Delta\varphi} d\varphi\, R\frac{B_Z}{B_{tor}} \tag{C.5}$$

for toroidal geometry, respectively for axial geometry:

$$x_l^{\alpha,\beta} = x_l + \int_0^{\pm\Delta z} dz\, \frac{B_x}{B_z}, \qquad\qquad y_l^{\alpha,\beta} = y_l + \int_0^{\pm\Delta z} dz\, \frac{B_y}{B_z} \tag{C.6}$$

The integration of these equations is performed with a 4th order Runge-Kutta scheme (see e.g. [109]). The routines D02PVF and D02PCF from the NAG library [148] are used. The lengths along the magnetic field lines can be computed similarly according to:

$$\Delta s^{\alpha,\beta} = \int_0^{\pm\Delta\varphi} d\varphi\, R\sqrt{1 + \left(\frac{B_R}{B_{tor}}\right)^2 + \left(\frac{B_Z}{B_{tor}}\right)^2} \tag{C.7}$$

for toroidal geometry, respectively for axial geometry:

$$\Delta s^{\alpha,\beta} = \int_0^{\pm\Delta z} dz\, \sqrt{1 + \left(\frac{B_x}{B_z}\right)^2 + \left(\frac{B_y}{B_z}\right)^2} \tag{C.8}$$

Due to $\nabla \cdot \mathbf{B} = 0$, the magnetic flux through the initial square is conserved as one goes along a magnetic field line, i.e. $B_{tor}(s)A(s) = const$, where s is a coordinate along a magnetic field line. Based on this fact, the flux box volumes can be computed as:

$$\Delta V(\varphi) = \int\limits_0^\varphi d\varphi \, \frac{\Psi_0^{tor}}{B_{tor}(s)} \frac{\mathbf{e}_\varphi}{|\mathbf{e}_\varphi|} \cdot d\mathbf{s}(\varphi), \tag{C.9}$$

where $\mathbf{s}$ is the curve along a magnetic field line and $\Psi_0^{tor} = B_{tor}(s = 0)h^2$ the toroidal flux through the initial square at the start of the field line tracing. The flux box volumes can be computed to high accuracy by recursive addition of volumes in each integration step during the field line tracing procedure: $V_0 = 0$, $V_t = V_{t-1} + \Psi_0^{tor}/(B_{tor}(R_t, Z_t))R_t d\varphi$, where R_t, Z_t are the coordinates of the position during the field line tracing at integration step t and $d\varphi$ the step size of integration.

The computation of the mapped quads which are given by the penetration points of the corners of the square around a grid point (see fig. 3.3b) is simple as a field line tracing algorithm is available. The computation of the distortion of the mapped quads is also straight forward.

Mainly for diagnostic purposes also a polar grid ρ, θ is established for closed field lines. The needed information, which is stored in the file *grid_polar.in*, is:

- Position of polar grid points: $R_{ip,jp}, Z_{ip.jp}$.

- The Jacobian for the polar grid: $J_{ip,jp}$.

The polar grid is chosen to be equidistant in ρ in between $\rho_{min} < \rho_{ip} < \min(\rho_{max}, 0.99\rho_{separatrix})$ and equidistant in the geometrical polar angle θ in between $0 < \theta_{jp} < 2\pi$ and is thus logically rectangular with grid indices ip, jp. The grid distances $d\rho, d\theta$ are chosen, such that the resolution of the grid points corresponds roughly to the resolution of the Cartesian grid. For each point ip, jp the position $R_{ip,jp}, Z_{ip,jp}$ is computed. A map between the Cartesian and the polar grid is ultimately achieved via an interpolation.

For axial circular geometry the Jacobian of the polar coordinate system is simply $J = \rho$. For complex geometry it is obtained by locally computing the coefficients of the metric tensor and computing the determinant. The Jacobian is needed to compute the flux surface average which is actually a volume average [97]:

$$\langle f \rangle (\rho) = \frac{\int\limits_0^{2\pi} \int\limits_0^{2\pi} d\varphi d\theta \, J \, f}{\int\limits_0^{2\pi} \int\limits_0^{2\pi} d\varphi d\theta \, J}, \tag{C.10}$$

which becomes on the discrete level:

$$\langle f \rangle (\rho_{ip}) \rightarrow \frac{\sum\limits_{jp,k} f_{ip,jp,k} \, J_{ip,jp}}{\sum\limits_{jp,k} J_{ip,jp}}, \tag{C.11}$$

where $f_{ip,jp,k}$ is the function mapped from the Cartesian grid to the polar grid via interpolation.

Appendix D.

Further results for axial circular geometry

In this appendix selected additional results of GRILLIX simulations for axial circular geometry are shown which support the results of chapter 5.

D.1. Bifurcation in C_{HW}

As stated in section 5.2.4, a bifurcation was found in [90, 91] in the parameter C_{HW}. Starting a simulation from small random noise no zonal flow was produced for $C_{HW} < 0.4$ and above it was produced. This non-trivial[1] result was also obtained with GRILLIX as is presented in the following.

In contrast to the magnetic configurations used in chapter 5 where a $q = 3/2$ surface was present in the center of the domain, resonant surface effects have been excluded in [90, 91], i.e. the turbulent eddies had no opportunity to bite their tails. For low C_{HW} (< 0.4) an exponential growth of a poloidal flow at resonant surfaces was obtained with GRILLIX and also by A. Kammel [149] which is different from the usual zonal flow picture and is not investigated here further on. Hence, to reproduce the bifurcation result of [90, 91] with GRILLIX a non or at least less resonant surface with $q_0 = 19/7$ is chosen in the center of the domain and the parameter α is accordingly adjusted to yield the desired value of C_{HW}. Otherwise standard parameters are used according to the details given in section 5.1, except for the toroidal resolution which was increased to $N_{pol} = 12$ and the radial width of the domain which was reduced to $W_\rho = 140\rho_s$.

In fig. D.1 the temporal evolution of the poloidal flow velocity for three different values of C_{HW} is shown. For $C_{HW} = 0.6$ a robust zonal flow was developing continuously. For $C_{HW} = 0.3$ no zonal flows was produced within the available simulation time and for $C_{HW} = 0.5$ a transitional regime was found where zonal flows were partly produced and broke up again from time to time. Fig. D.2 supports this result where the temporal evolution of the ratio of zonal flow energy divided by the total kinetic energy is shown.

The values of the transport, which saturates comparably fast, are roughly:

$$\Gamma_V(C_{HW} = 0.3) \approx 1.9, \quad \Gamma_V(C_{HW} = 0.5) \approx 0.8, \quad \Gamma_V(C_{HW} = 0.5) \approx 0.6.$$

The trend is in good agreement with the results in [88, 90, 91], though we pass on a quantitative comparison, since the absolute value of the transport might be very sensitive to resolution. The task of a direct code comparison, as it is elaborate work and involves a close collaboration between the authors of the different codes, is left for future work.

Hence, also with GRILLIX the same non trivial result as in [90, 91], a bifurcation in C_{HW}, was found. The onset for zonal flow production is around $C_{HW} = 0.4 \dots 0.5$ which is in very good agreement.
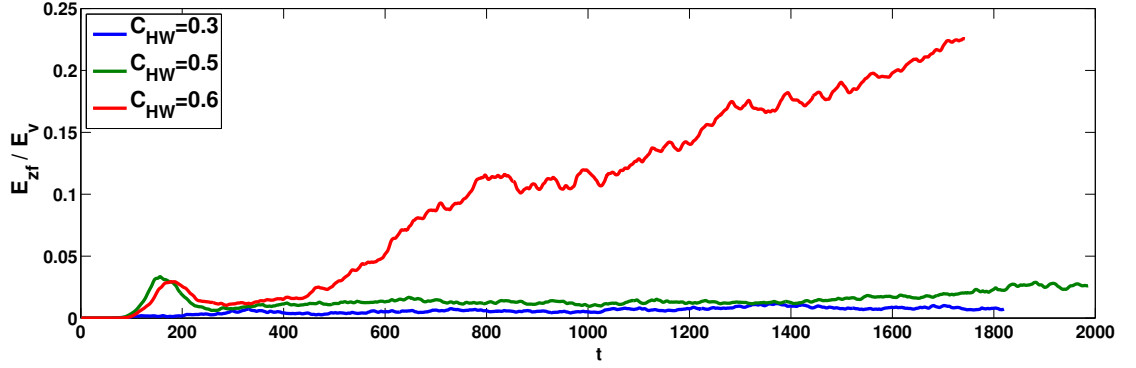
---

[1] 'Non-trivial', because it could only be obtained from numerical simulations.

a) $C_{HW} = 0.3$ b) $C_{HW} = 0.5$ c) $C_{HW} = 0.6$
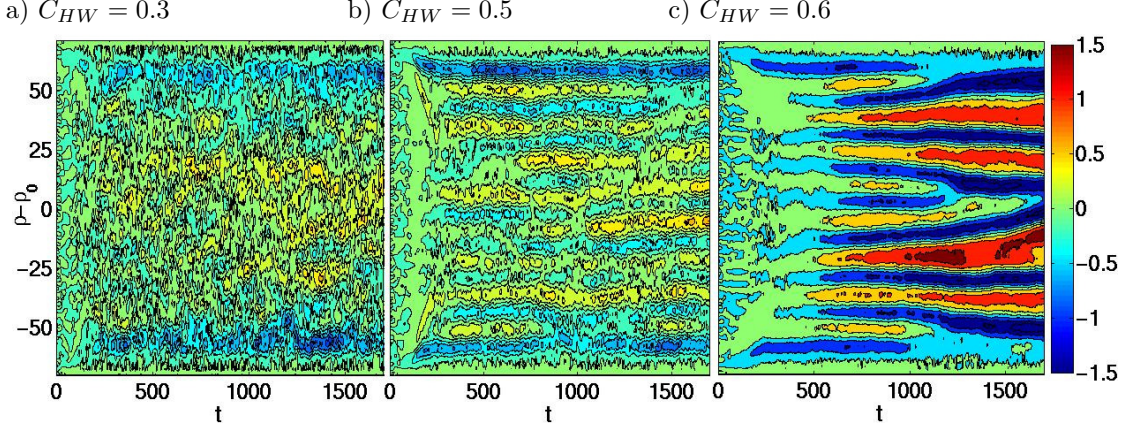
Figure D.1.: Temporal evolution of zonal flow velocity for a) $C_{HW} = 0.3 \, (\alpha = 0.1065)$, b) $C_{HW} = 0.5 \, (\alpha = 0.2291)$ and c) $C_{HW} = 0.6 \, (\alpha = 0.3013)$.

Figure D.2.: Ratio of kinetic energy contained in the zonal flow to total kinetic energy in dependence on time for different values of C_{HW}.

D.2. GAM benchmark

In section 5.3.1 the GAM oscillation is presented as a benchmark for the correct implementation of the curvature terms in GRILLIX. The benchmark in section 5.3.1 was not performed with a pure radial mode r, but with a Gaussian structure in the radial direction to be in accordance with the Dirichlet boundary conditions. A Gaussian structure involves many modes r, which led to a distortion of the structure due to dispersion. To show that really dispersion was the cause for the distortion of the structure and not a wrong implementation or a misunderstood numerical effect, this issue is investigated here in more detail. The flux aligned code GRILLIX_FA is a very useful tool for this investigation, since it can be run also with periodic boundary conditions in the ρ-direction.

GRILLIX_FA is used with the same parameters as described in 5.3.1. In order to test the pure GAM oscillation, periodic boundary conditions in the radial direction were used and a radial mode $r = 2$ ($k_\rho \approx 0.197$) was used for the potential as initial state. The temporal evolution of the zonal flow velocity is shown in fig. D.3a. Red dashed line indicate periods of the GAM oscillation without finite k_ρ corrections and and green dashed lines indicate periods with finite

k_ρ correction (see eq. 5.9). The obtained oscillation is in perfect agreement with the analytic prediction and therefore, GRILLIX_FA has passed the GAM benchmark

The same simulation as presented in section 5.3.1, where a Gaussian

$$\phi(\rho, t = 0) = \exp\left[-\frac{(\rho - \rho_0)^2}{(0.2W_\rho)^2}\right]$$

was used as initial state, was repeated with GRILLIX_FA. The result is shown in fig. D.3. In comparison the result of GRILLIX is shown again in fig. D.3c (fig. D.3c is the same as fig. 5.9). A distortion of the mode due to dispersion is obvious and the agreement between GRILLIX and GRILLIX_FA is very good. This shows in conclusion that the curvature terms are implemented correctly in GRILLIX and also the GAM mechanism is obtained correctly with GRILLIX.
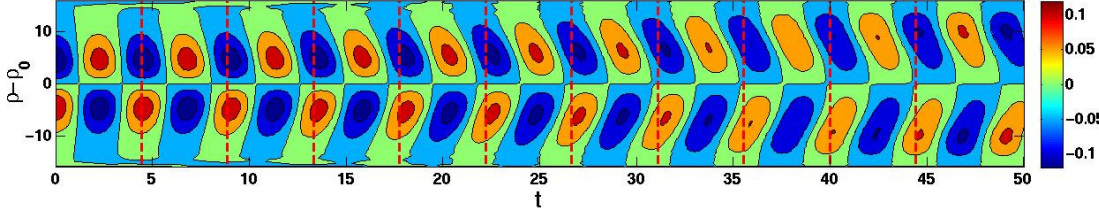
a) GRILLIX_FA, periodic boundary conditions, $r = 2$ mode:
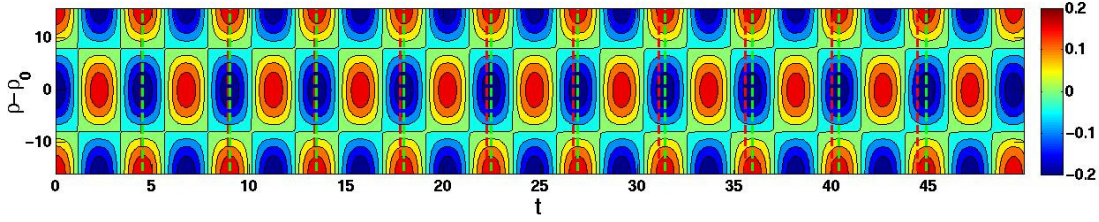
b) GRILLIX_FA, Dirichlet boundary conditions, Gaussian:
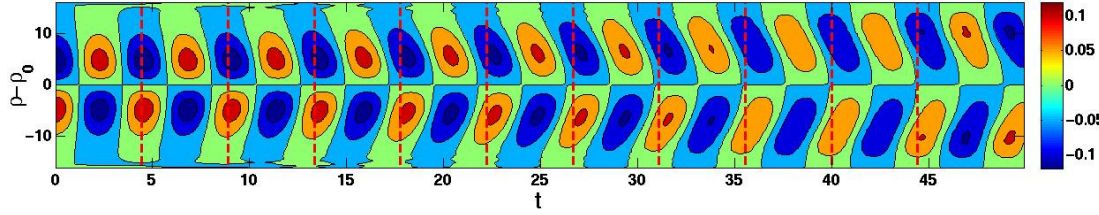
c) GRILLIX, Dirichlet boundary conditions, Gaussian:

Figure D.3.: Benchmark of GAM oscillation. a) Poloidal flow velocity simulated with GRILLIX_FA, periodic boundary conditions in ρ, $r = 2$ ($k_\rho \approx 0.197$) mode. Red dashed line indicate periods of $\omega = \omega_{GAM} = \sqrt{2}$, green dashed lines indicate periods of $\omega = \omega_{GAM}(1 - k_\rho^2/4) \approx 0.990\sqrt{2}$, i.e. with finite k_ρ correction. Poloidal flow velocity simulated with GRILLIX_FA (b) and GRILLIX (c) with Dirichlet boundary conditions and Gaussian as initial state.

D.3. Simulations with different schemes

The results of turbulence simulation obtained with the different schemes for the parallel diffusion operator is presented. Curvature terms were switched off. The standard parameters (see section

5.1) were used for simulations with the **N-1**, **N-3** and **S-1**, except for the radial width of the flux shell which was reduced to $W_\rho = 140\rho_s$. The simulation with the non-standard schemes can be compared directly to the simulation of section 5.2.1, where the **S-3** scheme was used.
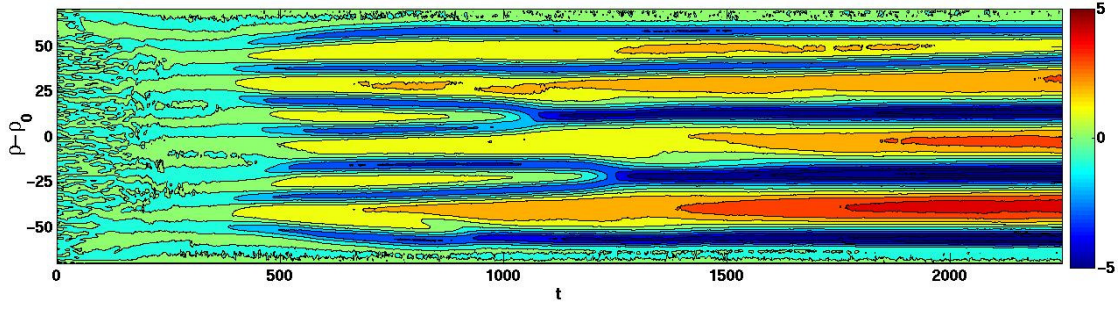
The temporal evolution of the zonal flow velocities for the different schemes is shown in fig. D.4. With the **N-1** scheme the numerical diffusion is too high and no zonal flows were produced. The agreement among the **N-3**, **S-1** and **S-3** scheme is good. However, for the **S-1** and **S-3** schemes, the zonal flows seem to merge a bit stronger together towards larger radial structures at later times. Since larger radial structures exhibit a stronger parallel damping within the HW model, this might indicate already an effect of the numerical diffusion on the **N-3** scheme. To check further on effects of numerical diffusion the same simulation is repeated for the **S-3** scheme with double resolution within the poloidal plane ($h = 1/3$ instead of $h = 2/3$). The result is shown in fig. D.5 and no qualitative difference to the results obtained with the **S-1** and **S-3** scheme with lower poloidal resolution (fig. D.4c,d) can be observed.

Overall this shows again the superiority of the newly developed support schemes over the naive schemes. At the available resolutions the numerical diffusion is such high for the naive schemes to affect the results qualitatively, which shows also the need for the superior support schemes.
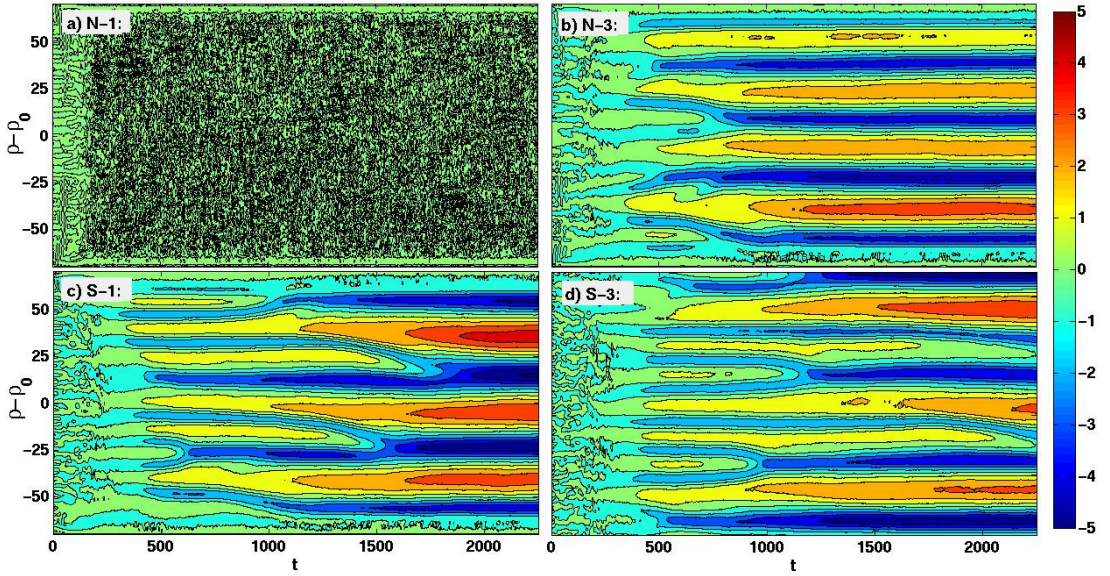
Figure D.4.: Temporal evolution of poloidal flow velocity as obtained with different numerical schemes for the parallel diffusion operator. a) **N-1**, b) **N-3**, c) **S-1** and d) **S-3** ($W_\rho = 210\rho_s$).

Figure D.5.: Temporal evolution of poloidal flow velocity as obtained with **S-3** scheme and high resolution ($h = 1/3\rho_s$) within poloidal planes. No qualitative difference to fig. D.4c,d can be observed.

Appendix E.

List of publications

1   A. Stegmeir, *Anwendung der Beam Tracing Methode zur Diagnostik von Fusionsplasmen*, diploma thesis, Technische Universität München, 2011.

2   A. Stegmeir, *Diagnostics of fusion plasmas with the Beam Tracing Method*, IPP TOK Seminar, Garching, Germany, 15th January, 2011, (talk).

3   A. Stegmeir, G. D. Conway, E. Poli and E. Strumberger, *Analysis of ITER low field side reflectometer employing the Beam Tracing method*, Fusion Engineering and Design, 86:2928, 2011.

4   G. D. Conway, A. Stegmeir, E. Poli and E. Strumberger, *Optimization studies of Doppler reflectometry on ITER*, Proceedings of the 10th International Reflectometry Workshop - IRW10, Padova, Italy, 4-6th May, 2011.

5   E. Poli, A. Stegmeir, G. D. Conway and E. Strumberger, *Application of the paraxial beam-tracing method to the diagnostics of fusion plasmas*, 14th European Fusion Theory Conference, 26-29th September, 2011, (poster).

6   A. Stegmeir, *Anomalous transport in the Scrape off Layer*, HEPP Kick-off Colloquium, Garching, Germany, 26-28th October, 2011, (poster).

7   A. Stegmeir, D. Coster, K. Hallatschek, O. Mai and K. Lackner, *Numerical simulations of edge and scrape of layer: diffusion and outlook to turbulence*, HEPP Colloquium, Greifswald, Germany, 26-28th September, 2012, (poster).

8   A. Stegmeir, *Development of a Turbulence Code for the SOL*, IPP Ringberg Theory Meeting, 14th November, 2012, (talk).

9   A. Stegmeir, *Development of a 3d turbulence code with a flux surface independent approach*, HEPP Colloquium, Strausberg, Germany, 16-19th September, 2013, (talk).

10 A. Stegmeir D. Coster, O. Maj and K. Lackner, *Development of a 3d turbulence code with a flux surface independent grid*, 14th International Workshop on Plasma Edge Theory in Fusion Devices, Cracow, Poland, 23-26th September, 2013, (poster).

11   A. Stegmeir D. Coster, O. Maj and K. Lackner, *Numerical Methods for 3D Tokamak Simulations Using a Flux-Surface Independent Grid*, Contributions to Plasma Physics, 54:549, 2014.

12   A. Stegmeir, D. Coster, O. Maj, K. Hallatschek and K. Lackner, *Development of a 3d turbulence code with a flux surface independent grid*, 78th Annual Meeting of the DPG and DPG Spring Meeting, Berlin, Germany, 17-21st March, 2014, (poster).

13   A. Stegmeir, *Development of a 3D turbulence code with a flux surface independent approach*, IPP TOK Seminar, Garching, Germany, 7th and 8th May, 2014, (talks).

Bibliography

[1] Richard P. Feynman, Robert B. Leighton, and Matthew Sands. *The Feynman Lectures on Phyiscs*, volume I: Mainly Mechanics, Radiation, and Heat. Basic Books, the new millenium edition, 2011.

[2] John Wesson. *Tokamaks*. Oxford University Press, 1987.

[3] Francis F. Chen. *Introduction to Plasma Physics*. Plenum Press, 1974.

[4] Uwe Schumacher. *Fusionsforschung*. Wissenschaftliche Buchgesellschaft, 1993.

[5] Jeffrey P. Freidberg. *Plasma Physics and Fusion Energy*. Cambridge University Press, 2007.

[6] Michael Kaufmann. *Plasmaphysik und Fusionsforschung*. B. G. Teubner, 2003.

[7] Jeffrey P. Freidberg. *Ideal Magnetohydrodynamics*. Plenum Press, 1987.

[8] http://www.iter.org/, 2014.

[9] http://en.wikipedia.org/wiki/DEMO, 2014.

[10] Dieter Biskamp. *Nonlinear Hydrodynamics*. Cambridge Monographs on Plasma Physics. Cambridge University Press, 1993.

[11] M. R. O'Brian and D. C. Robinson. Tokamak experiments. In Richard O. Dendy, editor, *Plasma Physics: an Indroductory Course*. Cambridge University Press, Cambridge, 1993.

[12] wikipedia.org/wiki/Beta_(plasma_physics), 2014.

[13] S. I. Braginskii. Transport processes in a plasma. In Acad. M. A. Leontovich, editor, *Reviews of Plasma Physics*, volume 1. Consultants Bureau, 1965.

[14] Per Helander and Dieter J. Sigmar. *Collisional Transport in Magnetized Plasmas*. Cambridge Monographs on Plasma Physics. Cambridge University Press, 2002.

[15] T. E. Stringer. Transport in magnetically confined plasmas. In Richard. O. Dendy, editor, *Plasma Physics: an Indroductory Course*. Cambridge University Press, Cambridge, 1993.

[16] John A. Krommes. Fundamental statistical descriptions of plasma turbulence in magnetic fields. *Physics Reports*, 360:1, 2002.

[17] Robert J. Goldston. Energy confinement scaling in tokamaks: some implications of recent experiments with ohmic and strong auxiliary heating. *Plasma Physics and Controlled Fusion*, 26:87, 1984.

[18] P. A. Davidson. *Turbulence: An Introduction for Scientist and Engineers*. Oxford University Press, 2004.

[19] Uriel Frisch. *Turbulence.* Cambridge University Press, 1995.

[20] Geoffrey K. Vallis. *Atmospheric and Oceanic Fluid Dynamics.* Cambridge University Press, 2006.

[21] Bruce D. Scott. Introduction to Turbulence in Magnetised Plasmas. In Andreas Dinklage, Thomas Klinger, Gerrit Marx, and Lutz Schweikhard, editors, *Plasma Physics*, volume 670 of *Lecture Notes in Physics.* Springer, 2005.

[22] G. McCracken. Boundary plasmas. In Richard. O. Dendy, editor, *Plasma Physics: an Indroductory Course.* Cambridge University Press, Cambridge, 1993.

[23] P. C. Stangeby and G. M. McCracken. Plasma boundary phenomena in tokamaks. *Nuclear Fusion*, 30:1225, 1990.

[24] F. Wagner, G. Becker, K. Behringer, D. Campbell, A. Eberhagen, et al. Regime of Improved Confinement and High Beta in Neutral-Beam-Heated Divertor Discharges of the ASDEX Tokamak. *Physical Review Letters*, 49:1408, 1982.

[25] R. Schneider, X. Bonnin, K. Borrass, D. P. Coster, H. Kastelewicz, et al. Plasma Edge Physics with B2-Eirene. *Contributions to Plasma Physics*, 46:3, 2006.

[26] http://www.efda.org/fusion/focus-on/limiters-and-divertors/, 2014.

[27] Y. Sarazin and Ph. Ghendrih. Intermittent particle transport in two-dimensional edge turbulence. *Physics of Plasmas*, 5:4214, 1998.

[28] O. E. Garcia, V. Naulin, A. H. Nielsen, and J. Juul Rasmussen. Turbulence and intermittent transport at the boundary of magnetized plasmas. *Physics of Plasmas*, 12:062309, 2005.

[29] P. Ricci, F. D. Halpern, S. Jolliet, J. Loizu, A. Mosetto, et al. Simulation of plasma turbulence in scrape-off layer conditions: the GBS code, simulation results and code validation. *Plasma Physics and Controlled Fusion*, 54:124047, 2012.

[30] Paolo Ricci and B. N. Rogers. Plasma turbulence in the scrape-off layer of tokamak devices. *Physics of Plasmas*, 20:010702, 2013.

[31] P. Tamain, Ph. Ghendrih, E. Tsitrone, V. Grandgirard, X. Garbet, et al. TOKAM-3D: A 3D fluid code for transport and turbulence in the edge plasma of Tokamaks. *Journal of Computational Physics*, 229:361, 2010.

[32] Bruce D. Scott. Free-energy conservation in local gyrofluid models. *Physics of Plasmas*, 12:102307, 2005.

[33] T. T. Ribeiro and B. Scott. Gyrofluid turbulence studies of the effect of the poloidal position of an axisymmetric Debye sheath. *Plasma Physics and Controlled Fusion*, 50:055007, 2008.

[34] Tiago Tamissa Ribeiro. *Turbulence Studies in the Scrape-Off Layer of Tokamak Plasmas by Three-Dimensional Gyrofluid Simulations.* PhD thesis, Universidade Tècnica de Lisboa, 2005.

[35] X.Q. Xu and R. H. Cohen. Scrape-Off Layer Turbulence Theory and Simulations. *Contributions to Plasma Physics*, 38:158, 1998.

[36] X.Q. Xu, R. H. Cohen, G. D. Porter, J. R. Myra, D. A. D'Ippolito, et al. Turbulence in boundary plasmas. *Journal of Nuclear Materials*, 266-269:993, 1999.

[37] X. Q. Xu, R. H. Cohen, T. D. Rognlien, and J. R. Myra. Low-to-high confinement transition simulations in divertor geometry. *Physics of Plasmas*, 7:1951, 2000.

[38] X. Q. Xu, R. H. Cohen, G. D. Porter, T. D. Rognlien, D. D. Ryutov, et al. Turbulence studies in tokamak boundary plasmas with realistic geometry. *Nuclear Fusion*, 40:731, 2000.

[39] XU Xue-qiao. The BOUT Project; Validation and Benchmark of BOUT Code and Experimental Diagnostic Tools for Fusion Boundary Turbulence. *Plasma Science & Technology*, 3:959, 2001.

[40] X. Q. Xu, W. M. Nevins, R. H. Cohen, J. R. Myra, and P. B. Snyder. Dynamical simulations of boundary plasma turbulence in divertor geometry. *New Journal of Physics*, 4:53.1, 2002.

[41] R. Schneider, M. Borchardt, J. Riemann, A. Mutzke, and S. Weber. Concept and Status of a 3D SOL Fluid Code. *Contributions to Plasma Physics*, 40:340, 2000.

[42] M. Borchardt, J. Riemann, R. Schneider, and X. Bonnin. W7-X edge modelling with the 3D SOL fluid code BoRiS. *Journal of Nuclear Materials*, 290-293:546, 2001.

[43] Y. Feng, F. Sardei, and J. Kisslinger. 3D fluid modelling of the edge plasma by means of a Monte Carlo techique. *Journal of Nuclear Materials*, 266-269:812, 1999.

[44] A. Runov, S. Kasilov, J. Riemann, M. Borchardt, D. Reiter, et al. Benchmark of the 3-Dimensional Plasma Transport Codes E3D and BoRiS. *Contributions to Plasma Physics*, 42:169, 2002.

[45] A. Runov, S. Kasilov, D. Reiter, N. McTaggart, X. Bonnin, et al. Transport in complex magnetic geometries: 3D modelling of ergodic edge plasmas in fusion experiments. *Journal of Nuclear Materials*, 313-316:1292, 2003.

[46] A. Runov, S. Kasilov, R. Schneider, and D. Reiter. Extensions of the 3-Dimensional Plasma Transport Code E3D. *Contributions to Plasma Physics*, 44:18, 2004.

[47] Oleksandr Kalentev. *A Finite Difference Code for 3D Plasma Edge Modeling*. PhD thesis, Ernst-Moritz-Arndt-Universität, 2008.

[48] M. Ottaviani. An alternative approach to field-aligned coordinates for plasma turbulence simulations. *Physics Letters A*, 375:1677, 2011.

[49] Farah Hariri. *FENICIA: A Generic Plasma Simulation Code Using a Flux-IndepENdent FIeld-Aligned CoordInate Approach*. PhD thesis, Aix-Marseille University, 2013.

[50] F. Hariri and M. Ottaviani. A flux-coordinate independent field-aligned approach to plasma turbulence simulations. *Computer Physics Communications*, 184:2419, 2013.

[51] F. Hariri, P. Hill, M. Ottaviani, and Y. Sarazin. The flux-coordinate independent approach applied to X-point geometries. *Physics of Plasmas*, 21:082509, 2014.

[52] S. Günter, Q. Yu, J. Krüger, and K. Lackner. Modelling of heat transport in magnetised plasmas using non-aligned coordinates. *Journal of Computational Physics*, 209:354, 2005.

[53] S. Günter, K. Lackner, and C. Tichmann. Finite element and higher order difference formulations for modelling heat transport in magnetised plasmas. *Journal of Computational Physics*, 226:2306, 2007.

[54] Karl-Heinz Spatschek. *Theoretische Plasmaphysik*. B. G. Teubner, 1990.

[55] A. J. Brizard and T. S. Hahm. Foundations of nonlinear gyrokinetic theory. *Reviews of Modern Physics*, 79:421, 2007.

[56] X. Garbet, Y. Idomura, L. Villard, and T. H. Watanabe. Gyrokinetic simulations of turbulent transport. *Nuclear Fusion*, 50:043002, 2010.

[57] J. F. Drake and T. M. Antonsen Jr. Nonlinear reduced fluid equations for toroidal plasmas. *Physics of Fluids*, 27:898, 1984.

[58] A. Zeiler, J. F. Drake, and B. Rogers. Nonlinear reduced Braginskii equations with ion thermal dynamics in toroidal plasma. *Physics of Plasmas*, 4:2134, 1997.

[59] Bruce Scott. Low Frequency Fluid Drift Turbulence in Magnetised Plasmas. Habilitation at Heinrich-Heine-Universität, 2000.

[60] H. R. Strauss. Nonlinear, three-dimensional magnetohydrodynamics of noncircular tokamaks. *Physics of Fluids*, 19:134, 1976.

[61] H. R. Strauss. Dynamics of high β tokamaks. *Physics of Fluids*, 20:1354, 1977.

[62] Wendell Horton. Nonlinear drift waves and transport in magnetized plasma. *Physics Reports*, 192:1, 1990.

[63] W. Horton. Drift waves and transport. *Review of Modern Physics*, 71:735, 1999.

[64] F. L. Hinton and C. W. Horton Jr. Amplitude Limitation of a Collisional Drift Wave Instability. *Physics of Fluids*, 14:116, 1971.

[65] Zuoyang Chang and J. D. Callen. Generalized gyroviscous force and its effect on the momentum balance equation. *Physics of Fluids B*, 4:1766, 1992.

[66] Bruce D. Scott. Tokamak edge turbulence: background theory and computation. *Plasma Physics and Controlled Fusion*, 49:S25, 2007.

[67] Andrei N. Simakov and Peter J. Catto. Drift-ordered fluid equations for field-aligned modes in low-β collisional plasma with equilibrium pressure pedestals. *Physics of Plasmas*, 10:4744, 2003.

[68] M. A. Dorf, R. H. Cohen, M. Dorr, T. Rognlien, J. Hittinger, et al. Simulation of neoclassical transport with the continuum gyrokinetic code cogent. *Physics of Plasmas*, 20:012513, 2013.

[69] M. A. Dorf, R. H. Cohen, M. Dorr, J. Hittinger, and T. D. Rognlien. Progress with the COGENT Edge Kinetic Code: Implementing the Fokker-Planck Collision Operator. *Contributions to Plasma Physics*, 54:517, 2014.

[70] X. Q. Xu, Z. Xiong, M. R. Dorr, J. A. Hittinger, K. Bodi, et al. Edge gyrokinetic theory and continuum simulations. *Nuclear Fusion*, 47:809, 2007.

[71] C. S. Chang, S. Ku, P. H. Diamond, Z. Lin, S. Parker, et al. Compressed ion temperature gradient turbulence in diverted tokamak edge. *Physics of Plasmas*, 16:056108, 2009.

[72] C. S. Chang. Full-f gyrokinetic simulation in realistic diverted tokamak geometry. Presentation at JET Task Force E1/E2 Meeting, March 2014.

[73] Mark F. Adams, Seung-Hoe Ku, Patrick Worley, Ed D'Azevedo, Julian C. Cummings, et al. Scaling to 150K cores: recent algorithm and performance engineering developments enabling XGC1 to run at scale. *Journal of Physics: Conference Series*, 180:012036, 2009.

[74] M. A. Beer and G. W. Hammet. Toroidal gyrofluid equations for simulations of tokamak turbulence. *Physics of Plasmas*, 3:4046, 1996.

[75] A. J. Wootton, B. A. Carreras, H. Matsumoto, K. McGuire, W. A. Peebles, et al. Fluctuations and anomalous transport in tokamaks. *Physics of Fluids B*, 2:2879, 1990.

[76] T. D. Rognlien. Understanding of edge plasmas in magnetic fusion energy devices. *Plasma Physics and Controlled Fusion*, 47:A283, 2005.

[77] A. V. Chankin and G. F. Matthews. Finite beta Electro-Magnetic Effects at the Edge and the Role of the Scrape-off Layer in the L-H Transition. *Contributions to Plasma Physics*, 38:177, 1998.

[78] B. Scott. Three-dimensional computation of drift Alfvén turbulence. *Plasma Physics and Controlled Fusion*, 39:1635, 1997.

[79] Akira Hasegawa and Masahiro Wakatani. Plasma Edge Turbulence. *Physical Review Letters*, 50:682, 1983.

[80] Hideo Sugama, Masahiro Wakatani, and Akira Hasegawa. Study of resistive drift and resistive interchange modes in a cylindrical plasma with magnetic shear. *Physics of Fluids*, 31:1601, 1988.

[81] P. N. Guzdar, J. F. Drake, D. McCarthy, A. B. Hassam, and C. S. Liu. Threedimensional fluid simulations of the nonlinear drift-resistive ballooning modes in tokamak edge plasmas. *Physics of Fluids B*, 5:3712, 1993.

[82] A. Zeiler, D. Biskamp, J. F. Drake, and P. N. Guzdar. Three-dimensional fluid simulations of tokamak edge turbulence. *Physics of Plasmas*, 3:2951, 1996.

[83] A. E. Koniges, J. A. Crotinger, and P. H. Diamond. Structure formation and transport in dissipative drift-wave turbulence. *Physics of Fluids B*, 4:2785, 1992.

[84] Suzana J. Camargo, Dieter Biskamp, and Bruce D. Scott. Resistive drift-wave turbulence. *Physics of Plasmas*, 2:48, 1995.

[85] Ryusuke Numata, Rowena Ball, and Robert L. Dewar. Bifurcation in electrostatic resistive drift wave turbulence. *Physics of Plasmas*, 14:102312, 2007.

[86] Akira Hasegawa and Masahiro Wakatani. Self-Organization of Electrostatic Turbulence in a Cylindrical Plasma. *Physical Review Letters*, 59:1581, 1987.

[87] D. Biskamp and A. Zeiler. Nonlinear Instability Mechanism in 3D Collisional Drift-Wave Turbulence. *Physical Review Letters*, 74:706, 1995.

[88] A. Zeiler, D. Biskamp, and J. F. Drake. Three-dimensional collisional drift-wave turbulence: Role of magnetic shear. *Physics of Plasmas*, 3:3947, 1996.

[89] S. B. Korsholm, P. K. Michelsen, V. Naulin, J. Juul Rasmussen, L. Garcia, et al. Reynolds stress and shear flow generation. *Plasma Physics and Controlled Fusion*, 43:1377, 2001.

[90] K. Hallatschek and A. Kammel. Zonal flow induced bifurcations in first principles sheared-slab resistive drift wave turbulence simulations. Preprint, 2014.

[91] Andreas Kammel. *Analysis of zonal flow bifurcations in 3D drift wave turbulence simulations*. PhD thesis, Technische Universität München, 2012.

[92] Joseph Michael Dewhurst. *Statistical Description and Modelling of Fusion Plasma Edge Turbulence*. PhD thesis, University of Warwick, 2010.

[93] Akira Hasegawa and Kunioki Mima. Stationary Spectrum of Strong Turbulence in Magnetized Nonuniform Plasma. *Physical Review Letters*, 39:205, 1977.

[94] Bruce D. Scott. The code HW was available to me.

[95] R. Numata, R. Ball, and R. L. Dewar. Nonlinear simulation of drift wave turbulence. http://rnumata.org/research/materials/turb_ws_jan2006.pdf, Jan. 2006. Presentation at Workshop on Turbulence and Coherent Structures.

[96] A. Stegmeir, D. Coster, O. Maj, and K. Lackner. Numerical Methods for 3D Tokamak Simulations Using a Flux-Surface Independent Grid. *Contributions to Plasma Physics*, 54:549, 2014.

[97] W. D. D'haeseleer, W. N. G. Hitchon, J. D. Callen, and J. L. Sohet. *Flux Coordinates and Magnetic Field Structure*. Springer Series in Computational Physics. Springer, 1990.

[98] H. Grad and H. Rubin. Hydromagnetic Equilibria and Force-Free Fields. In *Proceedings of the 2nd UN Conf. on the Peaceful Uses of Atomic Energy*, volume 31, page 190, Geneva, 1958. IAEA.

[99] V. D. Shafranov. Plasma equilibrium in a magnetic field. In Acad. M. A. Leontovich, editor, *Reviews of Plasma Physics*, volume 2. Consultants Bureau, 1965.

[100] M. D. Kruskal and R. M. Kulsrud. Equilibrium of Magnetically Confined Plasma in Toroid. *Physics of Fluids*, 1:265, 1958.

[101] S. Hamada. Hydromagnetic equilibria and their proper coordinates. *Nuclear Fusion*, 2:23, 1962.

[102] Allen H. Boozer. Plasma equilibrium with rational magnetic surfaces. *Physics of Fluids*, 24:1999, 1981.

[103] M. A. Beer, S. C. Cowley, and G. W. Hammet. Field-aligned coordinates for nonlinear simulations of tokamak turbulence. *Physics of Plasmas*, 2:2687, 1995.

[104] B. Scott. Global consistency for thin flux tube treatments of toroidal geometry. *Physics of Plasmas*, 5:2334, 1998.

[105] B. Scott. Shifted metric procedure for flux tube treatments of toroidal geometry: Avoiding grid deformation. *Physics of Plasmas*, 8:447, 2001.

[106] Tiago Tamissa Ribeiro and Bruce D. Scott. Conformal Tokamak Geometry for Turbulence Computations. *IEEE Transactions on plasma science*, 38:2159, 2010.

[107] Figure created by E. Strumberger, 2012.

[108] William F. Ames. *Numerical Methods for Partial Differential Equations.* Academic Press, 3rd edition, 1992.

[109] William H. Press, Saul A. Teukolsky, William T. Vetterling, and Brian P. Flannery. *Numerical Recipes.* Cambridge University Press, 3rd edition, 2007.

[110] Mikhail Shashkov. *Conservative Finite-Difference Methods on General Grids.* CRC Press, 1996.

[111] P. J. Mc Carthy. Analytic solutions to the Grad-Shafranov equation for tokamak equilibrium with dissimilar source functions. *Physics of Plasmas*, 6:3554, 1999.

[112] The MathWorks, Inc. *MATLAB.* http://www.mathworks.de/.

[113] Lawrence Livermore National Laboratory. *SILO.* https://wci.llnl.gov/codes/silo/.

[114] Department of Energy, Advanced Simulation and Computing Initiative. *Visit.* https://wci.llnl.gov/codes/visit/.

[115] http://de.wikipedia.org/wiki/Jackson-Diagramm.

[116] Intel. *Intel Math Kernel Library (MKL).* https://software.intel.com/en-us/intel-mkl.

[117] John M. Zerzan. Overlap: A fortran program for rapidly evaluating the area of overlap between two polygons. *Computers & Geosciences*, 15:1109, 1989.

[118] Michele Martone. *librsb : A shared memory parallel sparse matrix computations library for the Recursive Sparse Blocks format.* http://librsb.sourceforge.net/.

[119] Uri M. Ascher and Linda R. Petzold. *Computer Methods for Ordinary Differential Equations and Differential-Algebraic Equations.* SIAM, 1998.

[120] Bruce D. Scott. An Implicit Simulation of Drift-Wave Turbulence in a Sheared Magnetic Field. *Journal of Computational Physics*, 78:114, 1988.

[121] Akio Arakawa. Computational Design for Long-Term Numerical Integration of the Equations of Fluid Motion: Two-Dimensional Incompressible Flow. Part I. *Journal of Computational Physics*, 135:103, 1997.

[122] Valèrie Frayseè, Lue Giraud, Serge Gratton, and Julien Langou. *A Set of GMRES Routines for Real and Complex Arithmetics on High Performance Computers.* CERFACS. Technical Report TR/PA/03/3.

[123] Michele Martone. Private communication: I supplied M. Martone with typical matrices from GRILLIX for benchmarks., June 2013.

[124] P. H. Diamond, S.-I. Itoh, K. Itoh, and T. S. Hahm. Zonal flows in plasma-a review. *Plasma Physics and Controlled Fusion*, 47:R35, 2005.

[125] K. Itoh, S.-I. Itoh, P. H. Diamond, T. S. Hahm, A. Fujisawa, et al. Physics of zonal flows. *Physics of Plasmas*, 13:055502, 2006.

[126] P. H. Diamond and Y. B. Kim. Theory of mean poloidal flow generation by turbulence. *Physics of Fluids B*, 3:1626, 1991.

[127] J. N. Leboeuf, L. A. Charlton, and B. A. Carreras. Shear flow effects on the nonlinear evolution of thermal instabilities. *Physics of Fluids B*, 5:2959, 1993.

[128] P. H. Diamond, Y.-M. Liang, B. A. Carreras, and P. W. Terry. Self-regulating Shear Flow Turbulence: A Paradigm for the L to H Transition. *Physical Review Letters*, 72:2565, 1994.

[129] P. W. Terry. Suppression of turbulence and transport by sheared flow. *Reviews of Modern Physics*, 72:109, 2000.

[130] F. Wagner. A quarter-century of H-mode studies. *Plasma Physics and Controlled Fusion*, 49:B1, 2007.

[131] Lothar Schmitz. Zonal flows,predator-prey oscillations, and tokamak confinement transitions, January 2012. Presentation slides for CMTFO Winter School.

[132] Niels Winsor, John L. Johnson, and John M. Dawson. Geodesic Acoustiv Waves in Hydrodynamic Systems. *Physics of Fluids*, 11:2448, 1968.

[133] Robert Hager and Klaus Hallatschek. Radial propagation of geodesic acoustic modes. *Physics of Plasmas*, 16:072503, 2009.

[134] Robert Hager. *Radial propagation of geodesic acoustic modes*. PhD thesis, Technische Universität München, 2011.

[135] B. Scott. The geodesic transfer effect on zonal flows in tokamak edge turbulence. *Physics Letters A*, 320:53, 2003.

[136] H. Y. W. Tsui. Formation of a velocity shear layer in confined plasmas. *Physics of Fluids B*, 12:4057, 1992.

[137] D. R. McCarthy, J. F. Drake, P. N. Guzdar, and A. B. Hassam. Formation of the shear layer in toroidal edge plasmas. *Physics of Fluids B*, 5:1188, 1993.

[138] Timothy James Stoltzfus-Dueck. *Tokamak edge turbulence and the approach to adiabatic response*. PhD thesis, Princeton University, 2009.

[139] D. Farina, R. Pozzoli, and D. D. Ryutov. Effect of the magnetic field geometry on the flute-like perturbations near the X point. *Nuclear Fusion*, 33:1315, 1993.

[140] J. R. Myra, D. A. D'Ippolito, X. Q. Xu, and R. H. Cohen. MHD and Fluid Instabilities at the Plasma Edge in the Presence of a Separatrix and X-point. *Contributions to Plasma Physics*, 40:352, 2000.

[141] R. H. Cohen and D. D. Ryutov. Phenomenology of Flute-Like Perturbations in the Divertor Region. *Contributions to Plasma Physics*, 36:161, 1996.

[142] J. R. Myra, D. A. D'Ippolito, X. Q. Xu, and R. H. Cohen. Resistive X-point modes in tokamak boundary plasmas. *Physics of Plasmas*, 7:2290, 2000.

[143] J. R. Myra, D. A. D'Ippolito, X. Q. Xu, and R. H. Cohen. Resistive modes in the edge and scrape-off layer of diverted tokamaks. *Physics of Plasmas*, 7:4622, 2000.

[144] J. R. Myra and D. A. D'Ippolito. Edge instability regimes with applications to blob transport and the quasicoherent mode. *Physics of Plasmas*, 12:092511, 2005.

[145] J. R. Myra, D. A. Russell, and D. A. D'Ippolito. Collisionality and magnetic geometry effects on tokamak edge turbulent transport. I. A two-region model with application to blobs. *Physics of Plasmas*, 13:112502, 2006.

[146] R. H. Cohen, B. LaBombard, D. D. Ryutov, J. L. Terry, M. V. Umansky, X. Q. Xu, et al. Theory and fluid simulations of boundary-plasma fluctuations. *Nuclear Fusion*, 47:612, 2007.

[147] B. D. Dudson, A. Allen, G. Breyiannis, E. Brugger, and J. Buchanan. BOUT++: Recent and current developments. *arXiv*, 1405:7905, 2014.

[148] The Numerical Algorithms Group Ltd. *NAG Numerical Libraries.* http://www.nag.co.uk/.

[149] A. Kammel. Private communication, June 2014.